UNIVERSITEIT VAN PRETORIA
UNIVERSITY OF PRETORIA
YUNIBESITHI YA PRETORIA

INFLUENCE OF CIRCUMFERENTIAL SPANS OF HEAT FLUX DISTRIBUTIONS ON SECONDARY FLOW, HEAT TRANSFER AND FRICTION FACTORS FOR A LINEAR FOCUSING SOLAR COLLECTOR TYPE ABSORBER TUBE

by

IZUCHUKWU FRANCIS OKAFOR

Submitted in partial fulfilment of the requirements for the degree of
Doctor of Philosophy

In the Department of Mechanical and Aeronautical Engineering
Faculty of Engineering, Built Environment and Information Technology

University of Pretoria, South Africa

Supervisors: Prof. J. Dirker and Prof J. P. Meyer

2017

ABSTRACT

Title : Influence of Circumferential Spans of Heat Flux Distributions on Secondary Flow, Heat Transfer and Friction Factors for a Linear Focusing Solar Collector Type Absorber Tube

Author: Izuchukwu Francis Okafor

Supervisors: Prof. Jaco Dirker

Co-supervisor: Prof. Josua P. Meyer

Department: Mechanical and Aeronautical Engineering

University: University of Pretoria, Pretoria, South Africa.

Degree: Doctor of Philosophy

Solar collector absorber tubes play a critical role in converting incident solar heat flux into absorbed thermal energy and transferring it to a heat transfer fluid. In this study a single horizontally orientated absorber tube was investigated numerically in terms of the influence of different circumferential spans of symmetrical and asymmetrical heat flux distributions on buoyancy-driven secondary flow, internal heat transfer and friction factor characteristics. Three types of circumferential heat flux boundaries were considered, namely fully uniform, partial uniform and sinusoidal non-uniform heat flux distributions. Both gravitational symmetry and asymmetry for non-uniform heat flux distributions were investigated to cover symmetry angles in terms of the gravitational field (g) of 0° (symmetrical case), 20°, 30°, 40° and 60°.

Different sized stainless steel absorber tubes having a length of 10 m, and inner diameters of 62.7 mm, 52.5 mm, 40.9 mm and 35.1 mm were considered. Three dimensional steady-state simulations were performed for water as working fluid, covering laminar flow Reynolds numbers ranging from 130 to 2200, as well as for turbulent flow Reynolds numbers ranging from 3030 to 202 600. Buoyancy effects, temperature dependent fluid thermal properties, tube-wall heat conduction and the external wall heat losses by convection and radiation were taken into consideration. Average internal heat transfer coefficients, local internal heat transfer coefficients, Richardson numbers and overall

friction factors were obtained for different angular spans of incident heat flux, inlet fluid temperatures, heat flux intensities and outer wall thermal conditions

Laminar flow results indicated that the angular span, angular position, and intensity of the applied external heat flux all have significant influences on the buoyancy induced mixed convection inside the tube. This resulted in significant variations in the internal heat transfer coefficients and the friction factor which are not well described by classical empirical correlations. Buoyancy induced secondary flow significantly enhanced the internal heat transfer coefficient and significantly increased the friction factor compared to forced convection cases. Higher heat transfer coefficients and friction factors were obtained for non-uniform heat flux distributions compared to uniform heat flux distributions and were found to be dependent on the angle span and position of the heat flux. Higher inlet temperatures resulted in increased Nusselt numbers and lower friction factors, while higher external heat loss resulted in lower Nusselts numbers and lower friction factors. An increase in the asymmetry of the heat flux distribution resulted in a reduction of the Nusselt number and friction factor.

Even though turbulent flow cases with a Reynolds number range of approximately 3000 to 9000 were also influenced by buoyancy driven secondary flow, and followed the same parameter trends, it occurred to a lesser extent compared to the laminar flow cases. Turbulent flow cases with Reynolds numbers higher than 9100, exhibited little dependence on secondary flow effects and indicates the suitability of classical fully uniform heat flux heat transfer and friction factor correlations for highly turbulent flow irrespective of the distribution or intensity of the heat flux.

Keywords: linear focusing solar collector absorber tubes, symmetrical uniform and non-uniform heat flux distributions, asymmetrical non-uniform heat flux boundary, secondary flow, heat transfer coefficients, friction factors

DEDICATION

This work is dedicated to the Creator of the Universe,

The giver of wisdom and knowledge and to my

Wife and my little kids for their endurance.

ACKNOLEDGEMENT

Undertaking my PhD programme in this University offered me a wonderful experience that strongly fortified my career in engineering profession and the successful completion of this programme was achieved through the inspirations and guidance from several people who highly deserved my special gratitude.

My special appreciations are firstly to my supervisor, Professor Jaco Dirker for his tremendous guidance, advice and critical reviews of my research work at various stages. I remain very grateful for all his inputs in grooming me as his first PhD candidate and he impacted so much on my intellect. My special appreciations are also to my co-supervisor, Head of Department and Chair of the School of Engineering, Professor Joshua Meyer, for his wonderful guidance and financial supports that aided the successful completion of this programme. I remain grateful for the privileges and the international exposures he offered me and other postgraduate students in participating in international conferences and workshop trainings. I am also indebted to all the members of Thermofluid Research Group - Prof. Ken Craig, Prof. Johan Slaber, Prof. Nico Theron, Prof. Sharifpur Mohsen, Dr Lexmond Axel, Dr Inglis Helen, Dr. Mehdi Mehrab, Dr. W. G. Le Roux and others for their great commitments in cutting-edge research and academic excellence and to Ms Tersia Evans, the confidential secretary and Mrs Ilka Meyer, the departmental administrator for their continual diligence.

It is my great pleasure to acknowledge the former Vice Chancellor, University of Nigeria Nsukka, Prof. Bath. Okoro and the Director, National Centre for Energy Research and Development, Prof. P. E. Ugwuoke for approving my permission to travel to South Africa for my PhD programme at the University of Pretoria, Pretoria. It is also my great pleasure to acknowledge Prof. A. O. Odukwe, Prof. C. I. Ezekwe, Prof. D. C. Onyejekwe, Prof. S. O. Onyegegbu, Prof. V. O. Ekechukwu, Prof. G. O. Unachukwu and Prof. S. O. Enibe, Department of Mechanical Engineering for their great contributions in training me in energy and power technology, and energy management and environment. I am also indebted to Prof. C. C. Ihueze, Production Engineering, Nnamdi Azikiwe University, Awka

and Prof. J. C. Agunwamba, Civil Engineering, University of Nigeria Nsukka, for their guidance and consistent encouragements throughout my study years.

I wish to acknowledge with great appreciation all those who contributed in one way or the other towards the successful completion of this work. I am really very grateful for all their assistance, encouragement and understanding, especially Dr. Olabode Olakoyejo, Dr. Adelaja Adekunle, Dr. Aggrey Mwesigye, Dr. Saheed Adio, Dr. Noah Olugbenga, Dr. Adewumi Yinka, Engr. Daniel Ewim and Engr. A. Sogo, who were my colleagues in Thermofluids Research Group, Department of Mechanical and Aeronautical, Univerisity of Pretoria. At this juncture, I wish to express my profound gratitude to my colleagues, Engr. S. Ugwu, Dr. C. Megbemena, Dr, S. Nwanya, Dr. Howard Njoku, Dr. N. Eke and Mr. Ikechukwu Obi in the Department of Mechanical Engineering and Dr. C.N. Anynwu, Dr. S. N. Agbo, Engr. G. Akubue, Mr. M. Nnaji, Dr. C. Ibeto, Mr. K. Agbo, Mr. I. O. Imuoh, Engr. O.O. Nwoke and Mr. Innocent Obi at the National Centre for Energy Research and Development, University of Nigeria Nsukka. I am especially indebted to Dr. P. M. Ejikeme (Pure and Industrial Chemistry) and Dr. Denis, Dept. of Mathematics, University of Nigeria Nsukka, Sir. Orji Udemezue, Engr. Ben Orabueze and Engr. Ezeani Tochukwu for all their assistance and Rev. N. Aniefuna, Mr. Ifenna Anuamdi, Mr. Emeka Obi and Mr. O. C. Sam Jinwa and other friends of mine who have been my source of inspirations and emotional support over the years.

My special thanks go to my beloved parents, Mr. and Mrs. Frederick Okafor, my wife Mrs. Joy Okafor and my son Odinakachukwu Okafor, my uncles Mr. James Atuchukwu (Late), who motivated me to go for my postgraduate studies, may his Soul rest in peace, and Sir Emma Atuchukwu, and my brothers, Mr. Edwin Okafor, Mr. Innocent Okafor and my sisters for their emotional and financial supports and encouragements from my undergraduate to postgraduate studies. I am really very grateful for all their assistance.

Finally, the funding received from the Advanced Engineering Centre of Excellence at the University of Pretoria, NRF, TESP, NAC, and SOLAR Hub with the Stellenbosch University, EEDSM Hub and CSIR is highly acknowledged and duly appreciated.

TABLE OF CONTENTS

LIST OF FIGURES

LIST OF TABLES

NOMENCLATURE

A	surface or cross sectional area, m^2
c_p	specific heat of the fluid at constant pressure, J/kg K
C_μ, C_1, C_2	empirical turbulence constants
e	air-gap width, m
f	Darcy friction factor
g	acceleration due to gravity, m/s^2
G_B	generation of turbulent kinetic energy due to buoyancy, kg/ms^3
G_k	generation of turbulent kinetic energy due to the mean velocity gradients, kg/ms^3
Gr	Grashof number
Gz	Graetz number
$h, \overline{h}$	heat transfer coefficient and average heat transfer coefficient, W/m^2K
I	turbulence intensity at inlets and outlets, or number of heated divisions
i	heated division number
k	thermal conductivity, W/m K
L, L_{TOT}	axial dimension and total axial length of tube, m
M	total number of the axial divisions
$\dot{m}$	mass flow rate, kg/s
(m, n)	numerical surface location in the axial and circumferential directions
N	total number of the circumferential divisions
Nu, $\overline{\mathrm{Nu}}$	Nusselt number and average Nusselt number
P	pressure, Pa
p	centre-to-centre distance, m
$\dot{P}$	pumping power, kW
Pr	Prandtl number
q	heat transfer rate, W
q''	heat flux, W/m^2
R	thermal resistance, K/W

r	radial co-ordinate, m
Ra	Rayleigh number
Re	Reynolds number
Ri	Richardson number
S_φ	source term of φ
$\bar{S}_\varphi$	average value of S_φ
T, $\bar{T}$	temperature and average temperature, K
t	tube wall thickness, m
U	overall heat transfer coefficient, W/m^2 K
V	kinetic viscosity, m^2/s
v, $\bar{v}$	velocity and average velocity, m/s
W	collector aperture, m
x	axial co-ordinate, m
y	distance from the wall to the cell centre
y$^+$	dimensionless wall coordinate

Greek letters

α	angle span of the heated segment of the tube, °
α_w	absorptivity of tube surface
β	thermal expansion coefficient of the heat transfer fluid, K^{-1}
γ	gravity inclination in terms of the heat flux symmetry plane,°
ε	turbulent kinetic energy dissipation
ε_{tu}	emissivity of the tube-wall surface
ε_g	emissivity of glass surface
η	thermal efficiency
κ	turbulent kinetic energy generation
$\Re$	radius, m
μ	fluid viscosity at fluid bulk temperature, kg/ms

μ_{ed}	turbulent eddy viscosity of the heat transfer fluid, kg/ms
μ_{ef}	total effective viscosity of the heat transfer fluid, kg/ms
μ_{l}	laminar viscosity of the heat transfer fluid, kg/ms
μ_{sur}	fluid viscosity at boundary surface, kg/ms
ρ	density of the heat transfer fluid, kg/m^3
σ_{ε}	Prandtl number kinetic energy dissipation
σ_{k}	Prandtl number kinetic energy generation
σ_{ed}	k- ε turbulence model constant
σ_{SB}	Stefan-Boltzmann constant, W/m^{2}K^4
Γ	diffusion coefficient
φ	conservation variable
ϕ	angle span of each circumferential division, °, or tangential dimension
θ_c	collector half acceptance angle, °
ϕ_{in}	incident angle, °,
τ_g	transmittivity of glass cover
τ_w	wall shear stress, N/m^2

Subscripts

a	free stream air or aperture
atm	atmospheric
b	bulk fluid property
col	collector
conv	convection
D_i	referring to the inner diameter
ed	turbulent eddy
f	fluid, non-uniform temperature factor
FP	flat plate
g	glass
i	inner surface
m	at position m

max	maximum
n	at position n
o	outer surface or reference value
PT	parabolic trough
r	in radial direction
rad	radiation
s	solar
tu	tube
x	in axial direction
w	wall
W	referring to width
ϕ	in tangential direction
∞	radiant surroundings

Abbreviations

CFD	Computational Fluid Dynamics
CPC	Compound Parabolic Collectors
CLFC	Compact linear Fresnel concentrator
COP	Coefficient of Performance
DSG	Direct Steam Generation
HCE	Heat Collector Element
HTF	Heat Transfer Fluid
LFSC	Linear Fresnel Solar Concentrator
LFSR	Linear Fresnel Solar Reflector
MCRT	Monte Carlo Ray-Trace
NREL	National Renewable Energy Laboratory
PTC	Parabolic Trough Concentrator
SIMPLEC	Semi-Implicit Method for Pressure Linked Equations-Consistent
TPFC	Theoretical Pure Forced Convection
UHF	Uniform Heat Flux Boundary Conditions
UWT	Uniform Wall Temperature Boundary Conditions

JOURNALS PUBLICATIONS AND CONFERENCE PROCEEDINGS

The following are the lists of publications in conference proceedings and journals that were produced in the course of this research work.

International Journal Publications:

1.) I. F. Okafor, J. Dirker and J. P. Meyer, Influence of Circumferential Solar Heat Flux Distribution on the Heat Transfer Coefficients of Linear Fresnel Collector Absorber Tubes, Solar Energy 107 (2014), 381-397.
2.) I. F. Okafor, Jaco Dirker and Josua P. Meyer, Influence of Non-Uniform Heat Flux Distributions on the Secondary flow, Convective Heat Transfer and Friction Factors for a Parabolic Trough Solar Collector Type Absorber Tube, Renewable Energy Journal 108 (2017), 287-302.
3.) I. F. Okafor, J. Dirker and J. P. Meyer, Asymmetrical Non-uniform Heat Flux Distributions for Laminar Flow Heat Transfer with Mixed Convection in a Horizontal Circular Tube, Heat Transfer Engineering, Published online: 16 Jan 2018.

Papers presented at International peer reviewed conferences:

4.) I. F. Okafor, J. Dirker and J. P. Meyer; Turbulent Mixed Convection Heat Transfer for Non-Uniform Heat Flux Distributions on a Horizontal Circular Tube, 12th International Heat Transfer, Fluid Mechanics and Thermodynamics Conference, Paper ID 1570246462, 11-13 July 2016, Costa del Sol, Spain.
5.) I. F. Okafor, J. Dirker and J. P. Meyer "Laminar Flow Heat Transfer for Asymmetrical Non-Uniform Heat Flux Distributions on Horizontal Circular Tubes" Proceedings Third Southern African Solar Energy Conference 11 – 13, May 2015, Kruger National Park, South Africa.
6.) I. F. Okafor, J. Dirker and J. P. Meyer; Numerical study of heat transfer characteristics for different solar flux distributions on linear Fresnel collector absorber tubes in laminar flow, Proceedings, IHTC 15-9221, Kyoto, Japan, August 10-15, 2014

7.) I. F. Okafor, J. Dirker and J. P. Meyer; Numerical simulation of absorber tubes with non-uniform circumferential heat flux distributions, Proceedings of the Second Southern African Energy Conference, Paper 10, Port Elizabeth, 27-29 January 2014.

CHAPTER ONE: INTRODUCTION

1.1Background of Study

The increasing rate of depletion of fossil fuel resources along with environmental concerns regarding the use of fossil fuels as primary energy sources, have impelled for its replacement with alternatives that are more environmentally-friendly and sustainable [1]. Fig.1.1 shows the global share of total primary energy supply in 2014. It indicates that fossil fuels (oil, coal and gas) accounted for 81.1% of the total global energy supply, while renewable energy sources accounted for only 18.9 % [2]. Also, Fig.1.2 shows that carbon dioxide (CO_2) emission from the fossil fuel usage account for 65% of total global greenhouse gas emissions in 20014, associated with the global warming [3]. Renewable energy resources such as solar thermal, photovoltaic, hydropower, geothermal and wind energy etc. can provide viable solutions to part of the problems associated with energy production and consumption of fossil fuel resources [1].

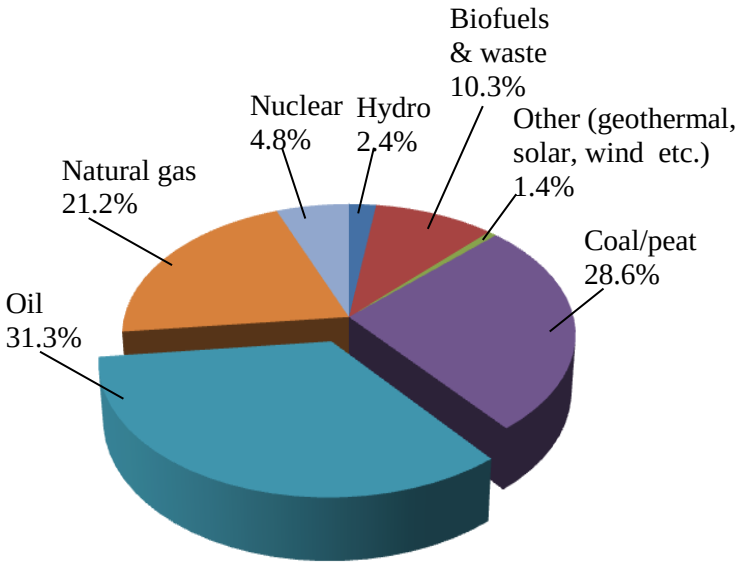

Fig. 1.1 Global share of total primary energy supply [2].

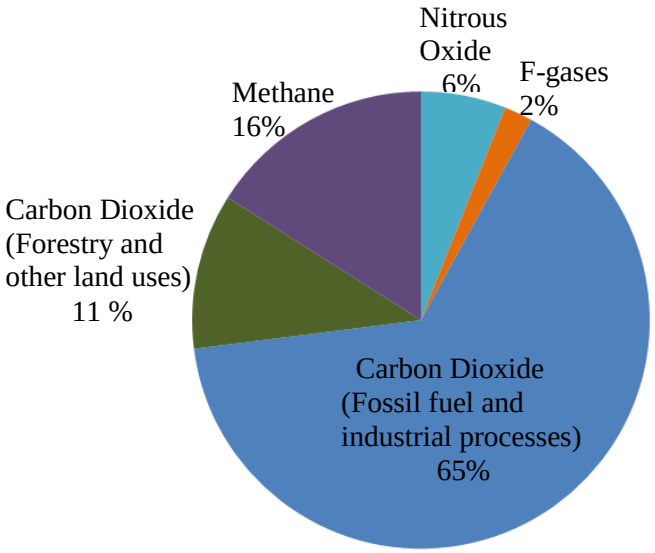

Fig. 1.2 Global anthropogenic greenhouse gas emissions in 2014 [3]

Solar thermal energy has been proposed as a viable option to lower the over-dependence on fossil fuels due to its significant potential to satisfy energy demand. This is particularly true in the Sunbelt region, where the direct solar radiation varies between 2000 and 3200 kWh/m^2/year [4]. Two basic types of solar thermal collector systems have been developed over the years. They are non-concentrating or stationary collector types and concentrating collector types. The non-concentrating solar collector types include flat plate collectors, evacuated tube collectors and solar chimneys. The concentrating collector types include linear focusing concentrators such as parabolic trough and linear Fresnel solar collectors etc., and point focusing concentrators such as parabolic dish and central tower receiver collectors [5].

The parabolic trough solar collector is the most popular type of a linear focusing solar thermal concentrator and has successfully been used in several power generation schemes such as in the Mojave Desert of Southern California in the late 1980s [6-8]. The linear Fresnel solar collector type has also received a considerable attention for power generation applications [8] due to its low construction cost with low wind loads, low maintenance and operating costs, and its higher land use efficiency [9]. A solar thermal power plant based on the linear Fresnel solar concentrator with a capacity of 1.4 MW$_e$ was installed in Puerto

Errado, Spain [6]. The linear focusing solar thermal collectors have also been considered as important options for direct steam generation power plants [10]. Mills and Morrison [11] presented the first results from the linear Fresnel solar collector installation of 1 MW_{th} at the Liddell power station completed in 2004. The direct steam generation systems eliminate the need for using expensive thermo-oil and complex heat exchangers and superheated steam can be generated directly using the concentrating collector. Apart from steam generation needed for electric power generation, the linear focusing solar collector systems are also suitable for industrial process heat generation, solar cooling, and institutional and domestic hot water system [5]. Besides hot water systems for domestic and institutional uses, several industrial applications require hot water temperatures below 100 °C [12], which makes the investigation of single phase liquid water in solar thermal collector absorber tubes very essential. The fluid flow regime could be turbulent or laminar depending on the application and operating conditions.

The earlier design and development of linear focusing solar collector systems such as parabolic trough or linear Fresnel solar collectors were focused on large-scale applications suitable for power generation [13], where the collectors are operated in the turbulent flow regime to increase the effective fluid side heat transfer coefficient, which assists in improving the thermal efficiency of the collector system. However, opportunities also exist to take advantage of buoyancy-driven secondary flow effects, which can greatly enhance heat transfer coefficients in the laminar or weak turbulent flow regimes, by increasing the thermal mixing of the heat transfer fluid, thereby improving the thermal performance of the solar collector system. Often, the commercial, institutional and domestic solar water heating systems are developed to operate as active systems at high or low mass flow rates or as passive systems (e.g. thermosyphons) without the need of a mechanical pump [14] , which inevitably reduces the fluid mass flow rate.

Of particular interest in this study is a linear focusing solar collector system such as a parabolic trough or a linear Fresnel collector type application where space restriction could exist. Shown in Fig 1.3(a), is a parabolic trough solar collector layout, for instance, which consists of a single fluid tube heated from below via concentrated solar rays reflected by a

parabolic surface. This system could be a viable alternative to traditional flat-plate collectors which usually are connected in arrays for a large volume hot water generation. Flat plat collectors have many advantages, such as simplicity of design, but they also have weaknesses. They are seldom equipped with sun-tracking systems due to the excessive weight of the heat transfer fluid in the collector tubes, making it difficult to alter the orientation of the plate collector. Because they usually suffer from high thermal losses due to their larger absorber surface areas required for intercepting the solar radiation, they exhibit poorer thermal performances compared to other solar collector types, such as evacuated tube collectors, compound parabolic collectors, linear Fresnel collectors, parabolic trough collectors and cylindrical trough collectors [15]. By contrast, the adaption of a parabolic trough solar collector system intercepts and concentrates the solar radiation on a smaller absorber surface area. The smaller surface area can offset the increase in the heat loss rate due to higher elevated surface temperatures that are obtained (due to the concentrated nature of the incident heat flux) and hence lower thermal losses and result in higher thermal efficiency.

As shown in Fig.1.3, the concentrated solar heat flux impinges on the collector tube from below, thereby resulting in circumferential non-uniform heat flux distributions around the tube-wall. The temperature differential due to the non-uniform heat flux distributions around the tube-wall could result in density differential in the heat transfer fluid. Under the influence of a gravitational field, buoyancy-induced secondary flow can arise due to the density differential within the heat transfer fluid [16]. In the laminar or weak turbulent flow regime, the non-uniform heat flux incident on the collector tube from below will result in a significant buoyancy-driven secondary flow component within the tube and this will increase the thermal mixing rate of the fluid. Hereby the fluid that is heated at the lower edge of the tube is forced upward and replaced by colder fluid drawn down by gravity effect. Therefore, increased internal heat transfer coefficients and friction factor characteristics are obtained. The increased internal heat transfer coefficient could improve the thermal efficiency of the collector system. Unlike with the case of a traditional flat-plate collector, the induced secondary flow effects are very much reduced due to heating occurring from the top surface

of the tubes and where the gravitational force component is not able to induce significantly strong secondary flow circulation in the fluid.

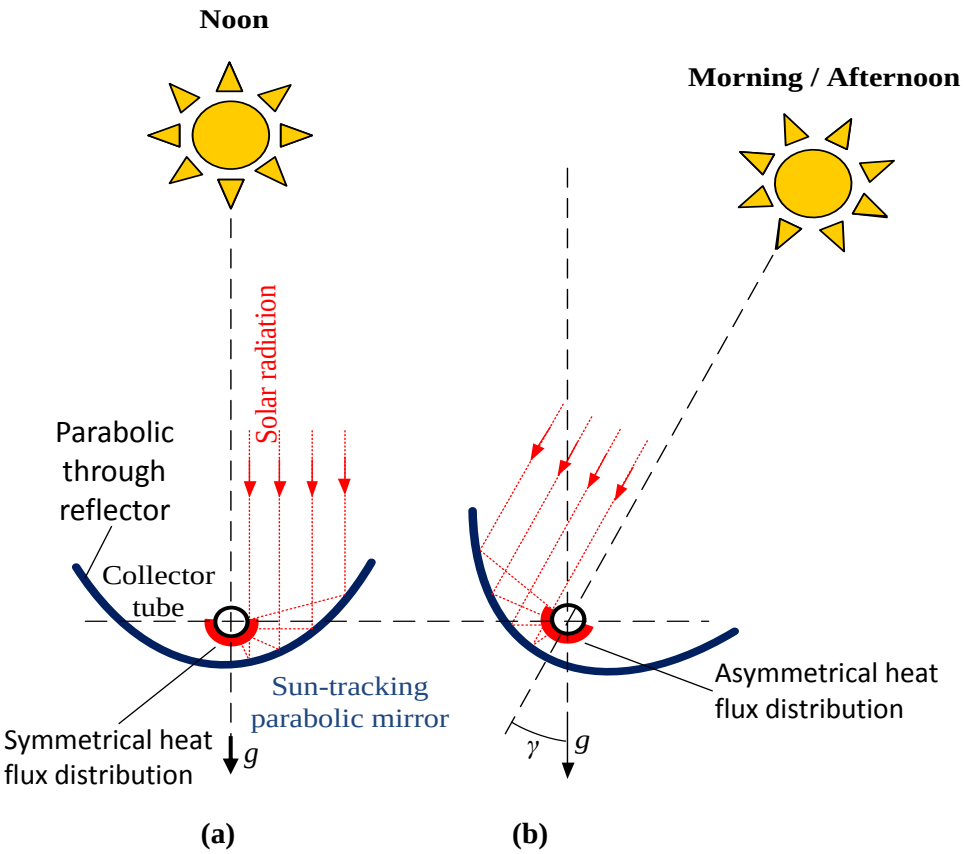

Fig. 1.3 Parabolic trough solar collector layout indicating: (a) symmetrical heat flux axis and (b) asymmetrical heat flux axis with the gravitational field.

Depending on the flow regime and the heat flux distribution boundary, a mixed convection heat transfer state can occur where the influence of the induced secondary flow component becomes comparable with the forced convection heat transfer process. The impact of the induced secondary flow on the internal heat transfers and friction factors of the collector tube can differ when the circumferential surface of the absorber tube exposed to the incident heat flux are varied, as well as the heat flux intensities and whether the heat flux distributions boundary is symmetrical or not with the gravity direction.

Comparably little to no information could be found in literature that would be useful to thermal design engineers that could indicate the effects of buoyancy-induced secondary flow

and the mixed convection heat transfer performance cases where heat flux is non-uniform in the laminar or weak turbulent flow regime. Further to this, fully developed flow at the inlet of a heat transfer tube is seldom present in real world applications.

The limited amount of information could be due to the difficulties encountered when attempting to reproduce non-uniform thermal boundary conditions in an experimental set-up, or the complexity required when attempting to integrate the interaction between ray-tracing software and the numerical modelling software [17]. Also, when considering the buoyancy-driven secondary flow phenomenon, the classical heat transfer correlations found for uniform heating condition could be inappropriate for determining the internal heat transfer and friction factor characteristics of such a horizontal absorber tube due to non-uniform circumferential heating. For instance, the heat transfer analysis and modeling of a parabolic trough solar receiver by Forristall [18] assumed uniform heat fluxes, thermodynamic properties and temperatures around the circumference of the tube for laminar and turbulent flow conditions and buoyancy-driven secondary flow effects were not investigated. A parametric study by Manikandan *et al.* [19] on a parabolic trough solar collector system was also based on uniform heat flux, while buoyancy-driven secondary flow was not considered. He *et al.* [17] considered non-uniform heat flux boundaries for a parabolic trough collector at higher turbulent flow regimes where buoyancy induced flow is not significant enough to take into consideration. Li *et al.* [20] numerically studied fully-developed mixed convection heat transfer of super-heated steam in the vacuum receiver tube of parabolic trough solar collector for a direct steam generation system under uniform and non-uniform heat flux boundary conditions. They found that fRe and Nu for laminar mixed flow varied with the heat flux distributions and should not be neglected in analysing fluid flow in a solar receiver tube. They proposed empirical correlations for fully developed fRe and Nuselt number to predict flow resistance and heat transfer rate in practical application. The experimental studies by Pino *et al.* [21, 22] and numerical studies by Velázquez *et al.* [23] and Abbas *et al.* [24] on thermal performance of linear Fresnel collector absorber tubes were based on uniform heat flux distributions assumption for convenience, which is not actually so as revealed in a number of optical designs and ray tracing simulation results. For instance, the ray tracing simulation results by Haberle *et al.* [25] indicated that the solar radiation intensity was evenly

distributed on the lower part and very low on the upper part of the absorber tube, indicating non-uniform radiation heat flux distributions on tube. The study by Eck *et al.* [26] also indicated that the heat flux distribution was at maximum at the bottom of the outer surface of the absorber tube followed by the sides and then decreased to the top portion of the tube. The studies by Goswami *et al.* [27] and Mathur *et al.* [28] on the linear Fresnel collector optical designs also revealed that flux distributions on the outer-wall surface of the absorber tube had a peak at the central portion from underneath and decreased rapidly on both sides of the tube. These studies were focused on large-scale solar collector systems for high turbulent flow applications and thus secondary flow effects on forced-convection heat transfer were not investigated.

As indicated in the studies, the heat flux distributions boundaries were limited to the cases where the uniform heat flux distribution boundaries were symmetrical in terms of direction of the gravitational field. However, the secondary flow circulation patterns in a circular absorber tube could be mirrored on either side of the tube. When the heat flux distribution is asymmetrical in terms of the gravity direction (γ), as is represented in Fig. 1.3 (b) during the morning and afternoon orientation of a parabolic trough solar collector with a sun-tracking system, the buoyancy effects will result in different secondary flow paths. This means that the heat transfer and friction factor characteristics of the collector tube would be affected by the degree of asymmetry. As shown in Fig. 1.3 (a), the symmetrical non-uniform heat flux distribution with the gravity direction occurs when the incident solar radiation is at the zenith angle position. In Fig. 1.3 (b), the asymmetrical non-uniform heat flux distribution with the gravity (g) direction occurs when the incident solar radiation has deviated from the zenith angle position and if the receiver absorber misaligned with the focal line of the solar collector. This could have significant influence on the internal heat transfers and friction factors characteristics of the absorber tubes in the laminar or weak turbulent flow regimes. Stynes and Ihas [29] noted in their study that both the collector frame orientation and the absorber varied with respect to gravity as the parabolic trough solar collector tracks the sun from east to west throughout the day and this could result in misalignment of the absorber with the solar flux distributions on the focal line of the collector. They measured the absorber alignment through photogrammetry for different collector orientation angles to determine the

gravitational effect on the absorber alignment. Stynes and Ihas [30] also measured the reflector slope and absorber misalignment errors with the focal line of a parabolic trough solar collector. Similarly, Christian and Ho [31] used a finite element modelling and ray-tracing to determine the effects of gravitational loading on a parabolic trough solar collector, but the effects of gravity on the absorber alignment was ignored. However, little to no work has been done specifically to investigate the impacts of the asymmetrical non-uniform heat flux distribution boundary on the heat transfer and pressure drop characteristics of a horizontal solar collector tube when the sun is not at its zenith angle.

1.2 Purpose and Motivation of Study

The purpose of this study is to numerically investigate the influence of both the symmetrical and asymmetrical non-uniform heat flux distribution boundaries on the secondary flow, internal convective heat transfer and friction factor characteristics of an absorber tube for a linear focusing solar thermal collector. This study also gives an indication on whether an adapted linear focusing solar collector system (e.g. parabolic trough) could be a viable heating approach for users of high volumes of hot water, and indeed so, what the anticipated heat transfer coefficients could be. It is quite clear from the above assertions that information on the thermal performance for linear focusing solar thermal collector systems due to non-uniform circumferential heat flux distribution boundaries still remains unexplored. There is uncertainty of the extent to which a symmetrical and asymmetrical external wall non-uniform heat flux distribution boundaries, impact on the buoyancy-driven secondary flow and mixed convection heat transfer performance of a horizontal absorber tube and such information are essentially needed by thermal design engineers. The absence of these essential information needed for improving the thermal performance and increase applicability of linear focusing solar thermal collector systems have motivated the present study to fill these gaps conspicuously missing in the literature.

1.3 Scope of the study

This study is focused on the influence of different circumferential heat flux distributions profiles on the thermal performance of an absorber tube for a linear focusing solar thermal collector system such as a parabolic trough or linear Fresnel solar collector. A three-dimensional steady-state numerical investigation conducted for different circumferential spans of heat flux distributions boundaries is implemented in the ANSYS Fluent version 14.0. Three different heat flux distributions boundaries: fully uniform, partial uniform and sinusoidal non-uniform heat flux distributions boundaries are considered. This is to extensively investigate the influence of both the symmetrical and asymmetrical non-uniform heat flux distributions boundaries on the secondary flow, internal heat transfer coefficients and friction factors for laminar and turbulent mixed convections as well as forced-convections. The asymmetrical non-uniform heat flux distribution boundary cases are in terms of the gravitational field directed at offset angles of 20°, 30° and 40°. This study is also limited to a single-phase liquid water flow applicable in the pre-heating phases during direct steam generation, industrial process heat for make-up water pre-heating or in thermal storage systems that do not require phase change, and hot water generations for institutional and domestic uses. Only hydrodynamic and thermally developing flows are considered since fully developed flow rarely occurs in practical applications. The inlet Reynolds number range of 130 and 2200 is used for the laminar flow case. For turbulent flow case, an inlet Reynolds number range of 3030 and 202600 are considered to account for possible turbulent mixed convection and where forced-convection effect could dominate the buoyancy-induced secondary flow. The influence of different fluid inlet temperatures and external heat loss transfer coefficients on the internal heat transfer coefficient and the friction factors of the absorber tube model are also considered in the laminar and turbulent mixed convection regimes. The Nusselt number and thermal efficiency for absorber tube models with different inner diameters and wall thicknesses are considered for non-uniform heat flux distribution boundary for laminar and turbulent flow regimes. It should be noted that since the results of this study are limited to single-phase liquid water heating applications and considering that some of the parameters such as heat transfer coefficient and incident solar heat flux investigated are dimensional, the results are only applicable for cases with the same working fluid considered.

1.4 Outline of the Thesis

The contents of this thesis are organized in nine chapters. Chapter one covers the background information, purpose and scope of the present study. In Chapter two, previous research efforts on the experimental and numerical studies on thermal performance of linear focusing solar thermal concentrators such as parabolic trough and linear Fresnel solar collectors are reviewed. It also contains a review of the experimental and numerical studies on mixed convection heat transfer in horizontal tubes similar to that of a linear solar thermal collector with symmetrical uniform heat flux cases for laminar and turbulent flow conditions. Chapter two also gives a brief review on the mixed convection heat transfer for symmetrical and asymmetrical uniform heat flux distributions boundaries for non-circular tubes. Chapter three gives the description of a linear focusing solar collector lay-out with a parabolic trough reflector field. It also gives a first order heat transfer model, modelling assumptions and an indicative thermal performance comparison for adaption of a linear focusing solar collector as a viable alternative to a traditional flat-plate solar collector for water heating. Chapter four focuses on the model descriptions and numerical heat transfer models for analysing the thermal performance of the absorber tube model. It also presents the governing equations and boundary conditions for the computational domain and the numerical solution procedure. Chapter five presents the grid dependence analysis and model validations to ensure correctness of the simulation results obtained with the tube model. Chapter six analyses the simulation results on the impacts of symmetrical heat flux distributions boundaries on the buoyancy-driven secondary flow, internal heat transfer and friction factors for an absorber tube model of a linear focusing solar collector under laminar flow condition. In Chapter seven, analysis of the simulation results are presented on the impacts of the asymmetrical non-uniform heat flux boundaries in terms gravitational field on buoyancy effect, heat transfer and friction factor characteristics of an absorber tube model for laminar flow regime. In Chapter eight, the analysis of the simulation results are presented for the influence of symmetrical and asymmetrical non-uniform heat flux distributions cases for turbulent flow regime. In Chapter nine, the summary, conclusions on the findings of this study are presented and recommendations for future research study are given.

CHAPTER TWO: LITERATURE SURVEY

2.0 Introduction

This chapter gives a brief review of solar thermal concentrators with emphasis on their basic concepts, types and performance characteristics. Previous research efforts on the experimental and numerical studies on the thermal performance of parabolic trough collectors and linear Fresnel solar collectors are reviewed. Also, previous studies on mixed convection heat transfer in horizontal circular tubes similar to that of absorber tubes of linear focusing solar concentrators with symmetrical uniform heat flux boundary are reviewed. Mixed convection asymmetrical uniform heat flux distributions boundaries in non-circular cross-sections are reviewed.

2.1 Solar Thermal Collector Systems

Solar thermal systems convert the radiant energy from the sun into thermal energy of the heat transfer fluid via solar thermal collector systems of different configurations. The solar thermal collector systems are classified as non-concentrating and concentrating solar collectors [5]. The non-concentrating collectors, which use the same surface for intercepting and absorbing solar radiation, achieve low temperatures due to high thermal losses, which increase with the absorber surface area. Such collectors systems include flat-plate collectors, solar ponds, and solar chimneys and evacuated tube collectors [13]. The concentrating solar collectors work by interposing an optical device between the solar radiation and the energy-absorbing surface [5]. They rely mostly on the beam component of solar radiation, since the diffuse component cannot be concentrated. The concentrators must therefore track the apparent daily motion of the sun across the sky to achieve high concentration of the beam radiation. Two different methods through which the concentrators track the sun's apparent motion were reported in [5, 32]. The first one is the altazimuth method, which requires the tracking device to turn in both altitude and azimuth. This method enables the concentrator to follow the sun exactly. The second one is the one-axis tracking in which the collector tracks the sun in only one direction either from east to west or from north to south. The concentrating collectors can achieve higher temperatures ranging from 200 °C to 1000 °C or even higher, suitable for steam generation for electricity generation via thermodynamic cycles [33]. They can achieve greater thermal efficiency due to small heat loss area relative to the receiver area. Also, for the fact that higher temperatures

permit more thermodynamically efficient energy-conversion cycles, most large-scale solar thermal collectors are of the concentrating type [34].

2.2 Types of Concentrating Solar Thermal Collectors

Different designs of concentrating solar thermal collectors have been developed depending on how they focus sunlight on the receiver [35]. The concentrators can be reflectors or refractors, cylindrical or parabolic and can be continuous or segmented. The receivers can be convex, flat, cylindrical or concave cavities with absorber tubes and can be covered with glazing or be uncovered [36]. The concentrating solar thermal collectors are further classified as imaging and non-imaging depending on whether the image of the sun is focused at the receiver or not [36, 37]. Non-imaging concentrators include Compound Parabolic Collectors (CPCs), which consist of two parabolic mirror segments [13, 36]. As shown in Fig.2.1, they have the capability of reflecting both beam and diffuse radiation within a wide range of acceptance angles.

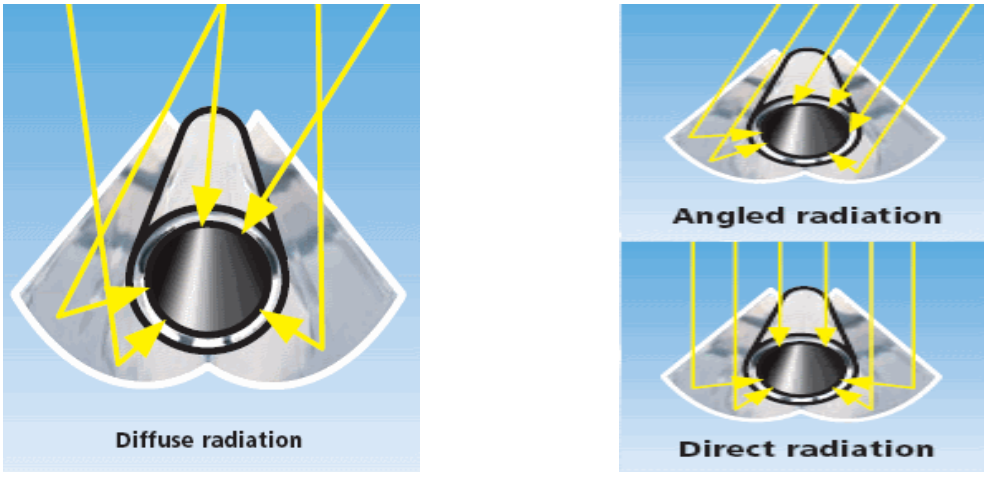

Fig. 2.1 CPC reflecting beam, angled and diffuse radiation of the absorber [34].

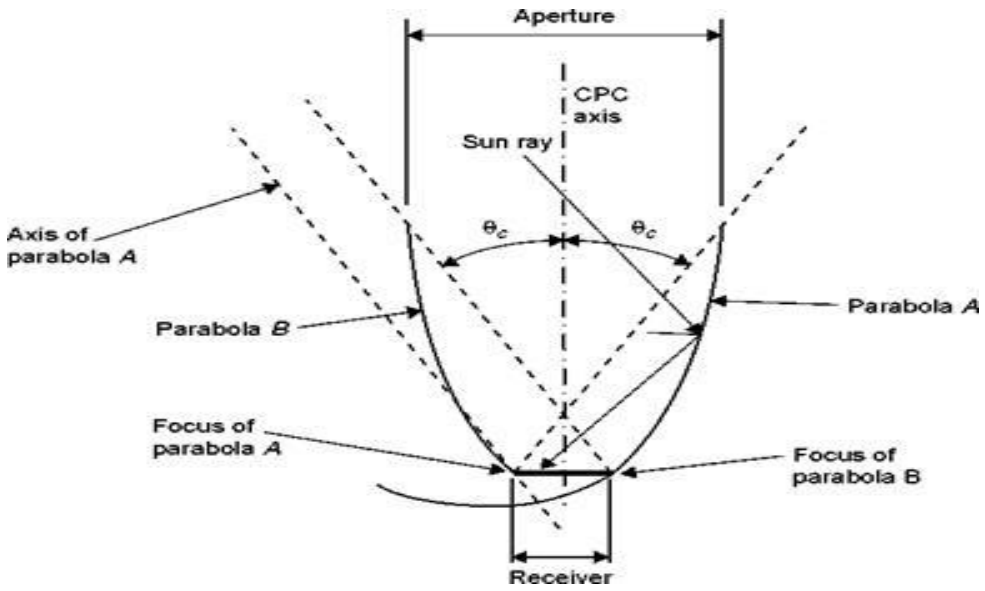

Fig. 2.2 Compound parabolic collector with flat-receiver [13]

Two basic types of compound parabolic collectors have been designed – the symmetric types and asymmetric types. They use two main types of absorbers – the fin type with a pipe and tubular type absorbers. Fig.2.2 shows the construction of a flat-receiver compound parabolic collector. The angle θ_c is the collector half acceptance angle. CPCs can achieve concentration ratios in the range of 3 to 7 [13]. Eames and Norton [38] presented detailed studies on the thermal behavior of the compound parabolic collectors.

The imaging concentrators are classified into two categories [36]: (i) point focusing concentrator with high concentration ratios and (ii) linear or line focusing concentrators with intermediate concentration ratios. The point focusing concentrators include parabolic dish collectors and central receiver collectors shown in Figs 2.3(a) and 2.3(b), while linear focusing concentrators include fixed mirror concentrator, parabolic trough concentrator shown in Fig. 2.4(a) and linear Fresnel concentrator shown in Fig. 2.4(b).

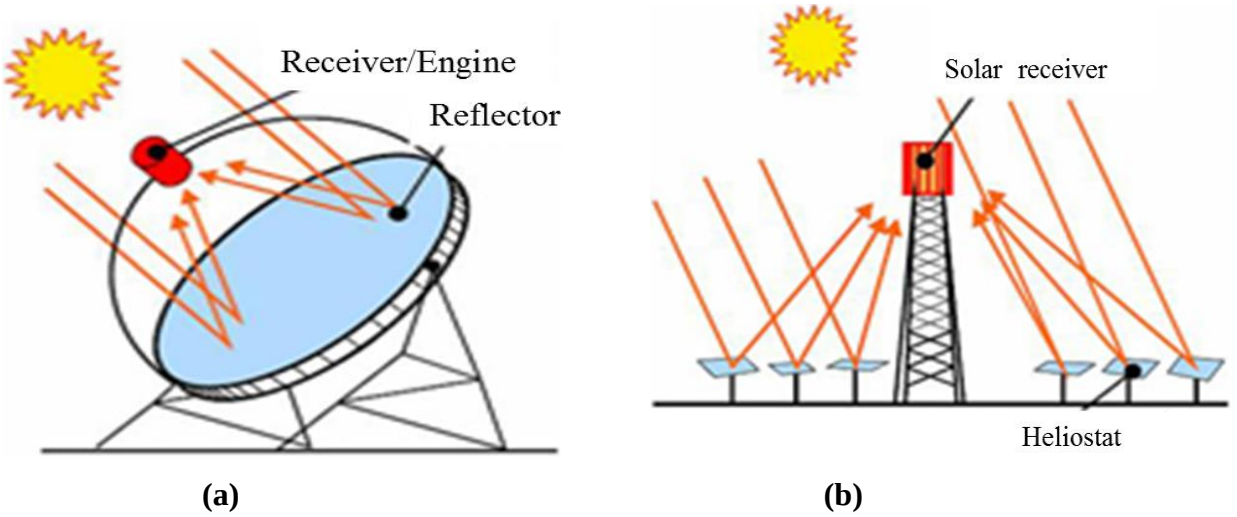

Fig. 2.3(a) Parabolic dish system [39, 40] and **(b)** Central receiver tower with heliostats [39]

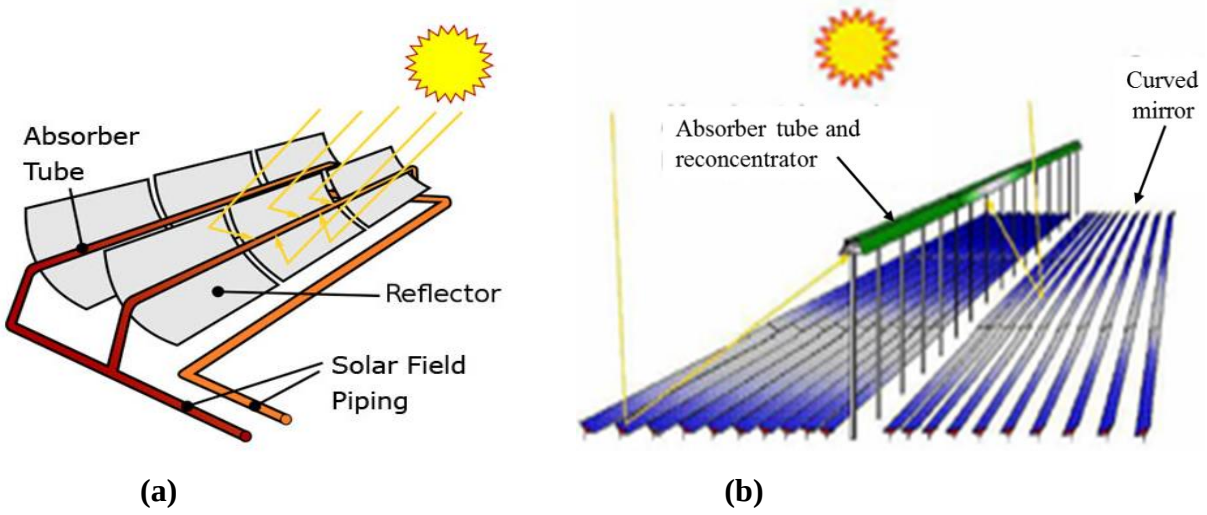

Fig. 2.4 (a) Parabolic trough solar collector [41] and **(b)** Linear Fresnel solar collector [39].

Fig. 2.3(a) shows a parabolic dish which tracks the sun in two axes and concentrates the solar radiation onto a receiver located at the focal point of the dish. The receiver absorbs the radiant solar energy and converts it into thermal energy in a circulating fluid. The thermal energy can then be either converted into electricity using an engine-generator coupled directly to the receiver or transported through pipes to a central power conversion system. Parabolic dish systems can achieve temperatures in excess of 1500 °C and concentration ratios up to 1000 [13].

They are the most efficient of all collector types in terms of their thermal-energy absorption and in power conversion. However, the need to circulate heat transfer fluid throughout the collector field raises design issues such as piping layout, pumping requirements, and thermal losses.

Central receiver towers (as shown in Fig. 2.3(b)) are surrounded by a large array of two-axis tracking heliostats made of slightly concave mirror segments. The heliostats reflect the incident direct solar radiation onto a fixed receiver located on the top of a tower. The receiver, which absorbs the concentrated radiation flux, transfers its energy to a heat transfer fluid. This type of system can achieve concentration ratios of 300 to 1500 and are therefore highly efficient, both in collecting solar energy and in converting it to thermal energy of the heat transfer fluid [5].

Parabolic trough collectors which track the sun in a single-axis consist of a parabolic shaped glass mirrors and a receiver tube covered with a glass tube to reduce heat losses [42]. The parabolic trough collector shown in Fig.2.4 (a) concentrates the direct solar radiation onto a linear receiver tube located along its focal line. The incident energy on the receiver is absorbed by a working fluid that is circulated through the absorber tube [43]. The collector can be oriented in an east-west direction, tracking the sun from north to south, or in a north-south direction, tracking the sun from east to west. The parabolic trough collectors can produce heat at temperatures between 50°C and 400°C and achieve concentration ratios in the range of 10 to 85 [5]. The glass envelope of the receiver has the disadvantage that the reflected rays must pass through glass cover before reaching the tube with transmittance loss of about 0.9, when the glass is clean [5]. However, the glass cover is usually treated with an anti-reflective coating to reduce the transmittance loss, thereby increasing performance of the collector. The optical efficiency of a typical parabolic trough solar concentrator is in the range of 75 – 80% [44].

The linear Fresnel reflector shown in Fig.2.4 (b) consists of an array of linear mirror strips that concentrate the solar radiation onto a linear receiver. The collector field is similar to that of a parabolic trough reflector. However, unlike the parabolic troughs, the individual strips need not be of parabolic shape. The mirror strips could be flat or elastically curved reflectors, which are cheaper than parabolic glass reflectors. The strips mounted close to the ground concentrate solar radiation on a linear fixed receiver mounted on a tower. They can achieve concentration ratios in the range of 10 to 40 and can produce heat at temperatures between 50°C and 250°C [5]. One

substantial difficulty with the linear Fresnel solar concentrator (LFSC) is that of avoiding shading and radiant blocking which leads to increased spacing between reflectors, which in turn leads to large ground utilization relative to collector area [45, 46]. However, Kalogirou [13] stated that the blocking could be reduced by increasing the height of the absorber above the primary mirror, but this can increase cost. Mill *et al.* [47] proposed a compact linear Fresnel concentrator (CLFC) type that can overcome the problem of reflector spacing and shading. Unlike a LFSC which uses only one linear absorber on a single linear tower, a CLFC uses multiple absorbers. The reflector mirrors of CLFCs are closely packed such that the individual reflectors would have the option of directing reflected solar radiation to at least two absorbers. Gharbia *et al.* [48] compared the optical performance of a LFSC and a PTC, and found that the optical efficiency of the LFSC is lower due to its higher incidence angle and the cosine factor. Jannet [49] found that it requires about 33-38% more mirror aperture area for the same solar energy yield compared to the parabolic trough.

2.3 Linear Focusing Solar Thermal Collectors

The most important linear focusing solar thermal concentrating collectors are of the parabolic trough solar collector type and the linear Fresnel solar collector type [50]. These linear solar collectors are applicable for steam production needed for electricity generation [51- 56], for solar cooling systems [57- 63] and for industrial process heating [64-68] and hot water generation [69]. Kalogirou and Lloyd [70] investigated the feasibility of using a parabolic trough solar collector for hot water production at 60°C for two applications – domestic and a hotel, compared with a flat plate solar collector for a low mass flow rate. Ramesh *et al.* [71] and Singh *et al.* [72] designed and carried out performance analyses of parabolic trough solar collectors for water heating applications. Mokhtar *et al.* [73] validated an experimental study on a linear Fresnel solar collector used for water heating application in Blida city, Algeria, in the winter weather condition.

2.3.1 Major Components of the Linear Solar Concentrators

The major components of a linear focusing solar concentrator are the collector support structures, the reflectors and the receiver [74]. The tracking device tracks the sun such that the incident radiations are concentrated on the focal line of the receiver tube. The support structures are the frames for mounting the reflector mirrors and to ensure that the mirrors are optically

aligned with the receivers under wind loading conditions. They are designed to have adequate torsional rigidity to withstand twisting due to wind load, deformations due to collector weight and thermal stresses due to temperature differential and that of the receiver [50]. The reflector mirrors for parabolic trough collectors are made from low-iron float glass of about 4mm with high solar transmittance [74]. The mirrors are made of silvered back plated with selective coatings for a better reflectance of 0.93 and durability than the polished aluminum reflector with a reflectance of 0.87 [75] and metallized acrylic, which are also available in the market [50]. However, the 4 mm glass mirrors are both heavy and expensive than the polished aluminum reflector, which was developed to reduce weight and costs [76].

The key component for efficient thermal performance of a linear focusing solar concentrator is the collector receiver. For a parabolic trough collector, the receiver shown in Fig.2.5 consists of an inner steel absorber tube with a selective coating inside an anti-reflective evacuated glass tube [77]. The selective coating on the steel absorber tube is made of multilayer cermet coating with high solar absorptivity and low thermal emissivity to reduce radiation loss. NREL has developed a receiver coating with high absorptance of 0.96, low emittance of 0.07 and good oxidation resistance at high operating temperatures [74].

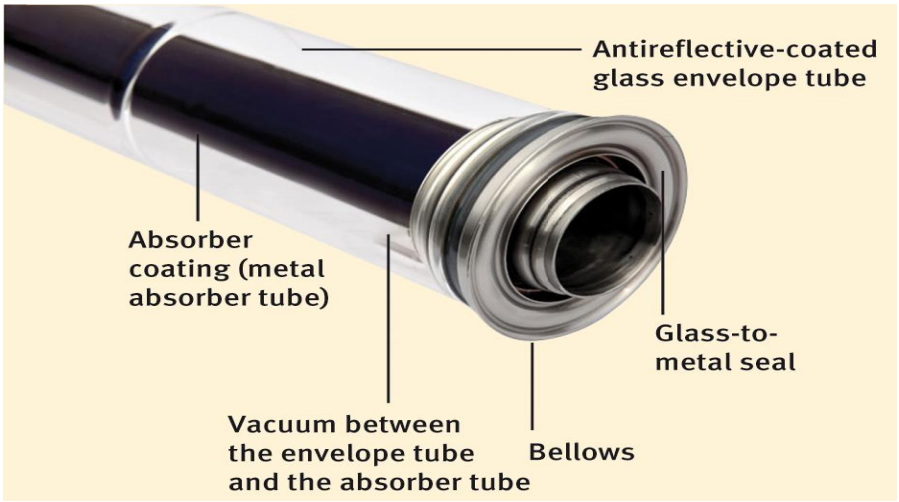

Fig. 2.5 Parabolic trough solar collector receiver [77].

The glass-to-metal seals and metal bellows are used to maintain the vacuum in annular zone and to allow for thermal expansion between the steel and glass tubes. The vacuum within the annulus reduces heat loss by convection. Ratzel *et al* [78] noted that natural convective heat loss in the annulus would be negligible as long as the Rayleigh number is less than 1000. Also, the collector efficiency could be improved by between 5-10%, if the annular pressure of 0.1 Pa could be maintained [79]. However, Thomas and Guven [43] noted that it is usually very difficult to maintain this level of vacuum in the annulus. Roesle *et al*. [80] numerically analyzed the heat loss from the receiver tube and found that the heat losses increase with the receiver length and temperature difference between the heat transfer fluid and the environment. The radiation heat loss rate across the annulus of the receiver was calculated based on radiation exchange equation between two concentric cylinders [81].

For a linear Fresnel collector, the receiver consists of a second stage concentrator as shown in Fig. 2.6 (a) with a single absorber tube mounted inside the cavity and covered with a transparent glass [26].

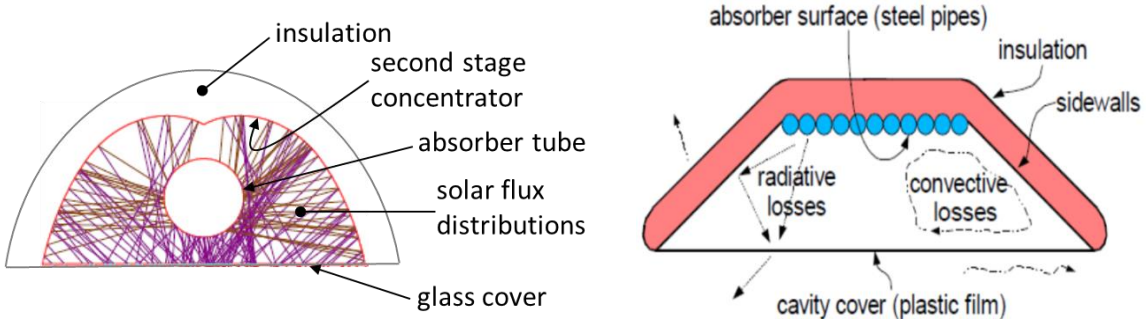

(a) **(b)**

Fig.2. 6 (a) Linear Fresnel collector receiver with second stage concentrator [26] and **(b)** Linear Fresnel trapezoidal cavity receiver multiple absorber tubes [82].

The second stage concentrator enlarges the target for the Fresnel reflectors and also provides insulation to the absorber tube. Another linear Fresnel receiver type shown in Fig. 2.6(b) is a trapezoidal cavity receiver [82]. It consists of multiple absorber tubes covered with a transparent glass cover with air trapped inside the cavity. The backsides of the cavity are covered with opaque insulation to reduce conduction heat losses and the front cover (plastic film) to reduce convective heat losses. The cavity also protects the receiver tubes from wind, rain and dirtiness. Sahoo et al. [83] analyzed the heat losses from the receiver via a laboratory experiment and

computational fluid dynamics model. Facão and Oliveira [85] investigated the natural convection inside the receiver, thermal radiations between surfaces and conduction through the walls and the overall heat loss coefficient was evaluated under steady-state, laminar and uniform temperature distribution on the absorber tubes. Larsen *et al.* [1] noted the heat losses from the receiver are very critical, as this would drastically reduce the thermal efficiency of the collector system and that the losses depend on several factors - geometry of the cavity, materials, insulation thickness, infrared emissivity of the absorber surface and concentration ratio, etc.

2.3.2 Thermal Performance of a Parabolic Trough Receiver Absorber Tube

The receiver absorber tube is of critical importance in solar thermal collector systems, as it absorbs the concentrated solar radiation to increase the temperature of the working fluid [24]. The experimental and numerical studies on thermal performance of absorber tubes of parabolic trough solar collectors are reviewed in this section.

Mohamad *et al.* [85] numerically investigated the receiver tube heat losses for a parabolic trough solar collector for steady-state turbulent flow and uniform solar flux intensity was considered. They found that the heat losses decrease with the mass flow rate and that the rate of heat transfer losses increased with the diameter of absorber tube and thus decreased the thermal efficiency of the collector. They noted that the collector length could reach a maximum point where the heat gain could become equal to the heat losses and any that additional length would be passive.

Eck *et al*. [86] carried out thermal modeling and simulation of parabolic trough receiver tubes. Synthetic oil was used as heat transfer and steady-state turbulent flow was considered. The finite element method model was developed for a receiver tube with non-uniform flux distributions. The study found that a simple analytical model was a helpful tool for the fast prediction of the temperature distribution in the receiver tube. They compared the heat flux losses by the heat collecting element under different conditions for a two-dimensional and a three-dimensional finite element method model and found that there was a good agreement with the measured one.

Jianfeng *et al.* [87] studied the heat transfer and absorption characteristics of an external receiver pipe under unilateral concentrated solar radiation. Hitec heat transfer salt was used as the working fluid and turbulent flow was considered. They found that the local absorption efficiency

increased with the flow velocity, while the wall temperature dropped quickly. The optimal incident energy flux and the average absorption efficiency were found to decrease with an increase in the pipe length. They also found that due to the unilateral concentrated solar radiation and different incident angle, the heat transfer was non-uniform around the pipe circumference.

Heidemann *et al*. [88] studied the steady-state and transient temperature field in the absorber tube of a direct steam generating parabolic trough solar collector using a finite difference method. They developed a universal program for solving the two-dimensional transient temperature field using a modular nodal point library. They found that the temperature field was extremely asymmetric due to the variation of the heat transfer coefficient at the inner surface and the solar irradiation at the outer surface of the absorber tube. The transient behaviour of the absorber tube showed that there was need for steam storage in order to balance not only longer periods without irradiation but also short time shading effects.

Thomas and Guven [89] studied the effect of optical errors on flux distribution around the absorber tube of a trough concentrator. It was found that the total optical error has profound effect on the intercept factor, as well as on the optical efficiency of PTCs. The flux distribution around the absorber was circumferentially non-uniform and symmetrical with respect to the vertical axis.

Reddy *et al.* [90] numerically investigated the heat transfer characteristics of an energy-efficient parabolic trough receiver by introducing longitudinal solid fins in a tubular receiver, longitudinal porous fins, and intermittent porous fins respectively. Therminol VP1 was used as heat transfer and steady-state turbulent flow and uniform heat flux boundary were considered. It was reported that the heat transfer characteristics of the tubular receiver was improved by 17.5%, due to the increase in heat transfer area, thermal conductivity and turbulence, but with a pressure drop of 2 kPa as penalty.

Cheng *et al*. [91] carried out a three-dimensional numerical simulation of coupled heat transfer characteristics of the receiver tube of parabolic trough collector using the Monte Carlo Ray-Trace (MCRT) method and the FLUENT software. The non-uniform solar flux distribution on

the outer wall of the absorber tube was calculated based on the MCRT method and turbulent flow regime was considered. The natural convection due to temperature-dependent properties of the Syltherm 800 liquid oil used as the heat transfer fluid was considered. The simulation results showed that the radiation loss was up to 153.70 Wm^{-2} and so to improve the collector efficiency, the radiation loss should be reduced as much as possible.

Cheng *et al*. [92] also carried out a three-dimensional numerical simulation of the whole parabolic trough solar collector with non-uniform solar flux conditions by coupling finite volume method and MCRT method. Four types of heat transfer fluid were used- the Syltherm 800, the Therminol VP1, the Nitrate Salt and the Hitec XL and turbulent flow regime was considered. It was found that the thermal loss increased, while the efficiency decreased with increase in the inlet temperature of the four heat transfer fluids.

Aldali *et al*. [93] carried out a CFD thermal simulation of a parabolic trough solar absorber pipe to compare three types of pipes with different internal helical fins, and a pipe and aluminum pipe without helical fins. Non-uniform heat flux boundary and turbulent flow of water through the absorber pipe were considered. It was reported that the thermal gradient between the upper and lower temperature for the pipe without a helical fin was higher compared with the pipes with helical fins. It was also reported that the thermal gradient for the aluminum pipe was much lower when compared with the steel pipe.

Yaghoubi and Akbari [94] numerically studied a three-dimensional temperature distribution and its thermal expansion and deformation of a parabolic trough absorber tube of Shiraz solar thermal power plant. Behran-oil and VP1-oil were used as heat transfer fluids, turbulent flow and heat flux boundary was non-uniform. The study noted that the efficiency of a collector depended highly on the location of absorber tube at the focal line. They explained that deformation of the absorber tube due to non-uniform thermal expansion caused by non-uniform solar flux local concentrating ratio over the absorber would cause the tube to misalign with the focal line. They found that decreasing the convection coefficient of the working fluid lead to increase in the deformation of the tube. Thus, to avoid breaking of the glass tube, maximum deformation in the vertical direction should be less than 20 mm and convection coefficient should be more than 350 W/m^2K to avoid the plastic deformation of the absorber tube. They

concluded that to prevent any yielding and glass breakage and to minimize displacement of the absorber tube from its focal point, convection coefficient should not be less than 950 W/m^2K. But there was no validation of these findings.

2.3.3 Thermal Performance of a Linear Fresnel Collector Receiver Absorber Tube

The numerical and experimental studies on thermal performance of absorber tubes of linear Fresnel solar collectors are reviewed in this section. Unlike for parabolic trough solar collectors, only few studies have carried out thermal performance analysis for absorber tubes of linear Fresnel solar collectors and the available studies were based on uniform heat flux distributions boundary. As earlier stated in Chapter one, this is contrary to the optical designs and ray tracing simulation results, which revealed that the solar flux distributions on the receiver tubes are non-uniform.

Abbaa *et al.* [10] carried out a steady state numerical simulations of the thermal performance of the linear Fresnel reflector receiver tubes to determine the optimum tube diameter and length. They assumed a uniform radiation flux impinging onto the receiver tubes. The study presented the model equations for analyzing the thermal behavior and the hydraulic characteristics of the receiver tube. Therminol VP1 was used as heat transfer fluid. They employed the same model previously used by [95, 96] in analyzing the thermal behavior and the hydraulic characteristics of the receiver tube. The study noted that the thermal efficiency was not enough to characterize the receiver performance. Thus, they included the exergetic efficiency in their model output to account for the obvious Carnot cycle efficiency limit and the pumping power losses. The study paid special attention to how the exergetic efficiency was affected by the tubes diameters and the fluid speed, for different radiation intensities and Reynolds number above 10 000. They found that the outlet temperature diminished as the fluid speed increased, but it increased as the tube diameter decreased. The exergetic efficiency was found to increase as the tubes get narrower, until a maximum was achieved. They found that multi-tube receivers have the advantages of allowing more fluid flow through the tubes where radiation intensity is higher and less through the lateral tubes. They suggested fluid flow in series by using different set of tubes such that periphery tubes could be devoted to preheat the fluid when going in one direction, then flowing through the central strip for the final heating up to the maximum temperature. They also

suggested that transient analysis of the receivers be carried out to include effects produced by rapid variations of the concentrated radiation, and by thermal energy storage.

Dey [97] presented the design methodology and thermal modelling of a linear absorber of an inverted air cavity for a north– south oriented compact linear Fresnel reflector based on Mills and Morrison [11] concept. The linear absorber was modelled for turbulent flow direct steam generation. The study proposed model equations for the absorber pipe sizing and spacing, and the possible absorber design configurations. He examined variations of the absorber geometry using a finite element analysis and assumed adiabatic for the absorber surfaces due to the symmetry of the arrangement. Also, a uniform heat flux density and a non-convective air cavity were considered. The conductive losses through the air layer in the cavity from the absorber surface to ambient were modeled with a convective heat transfer coefficient. Steady state temperature distributions and heat flows were obtained using Strand's non-linear heat solver. The dependence of the maximum temperature difference between the fluid in the pipe and the absorbing surface on the pipe size, spacing, and plate thickness of this geometry was examined using a finite element model. It was found that the acceptable temperature difference of less than 20 K could be achieved with a bar thickness of about 6 mm and for pipe spacing which complied with the relevant standards for pressure equipment. However, the variations of temperature difference between an absorbing surface and the heat transfer fluid inside the absorber pipe with Reynolds numbers were not investigated and no specific Reynolds number under which the study was conducted was stated.

Eck *et al.*[26] investigated the thermal load of direct steam-generating tubes with large diameters in the horizontal linear Fresnel collector needed for a 50 MW solar only plant using finite element method. The study showed that the heat flux distribution was highest at the bottom of the outer surface of the absorber tube followed by the sides and abated contribution came from the top. Fig. 2.7(a) shows a linear Fresnel concentrator with compound parabolic cavity secondary stage reflector housing a single larger absorber tube. Fig. 2.7 (b) shows the flux distribution for several zenith angles on the 15 cm diameter absorber tube located at about 13 m above the 52 primary mirrors field. For the collector to be used as a boiler in a Clausius-Rankine cycle, it was subdivided into three sections: the preheater section where water was heated to its saturation temperature, the evaporator section where a two-phase water-steam flow occurred,

and the superheater section where a single-phase steam flow occurred. The investigation showed that the circumferential temperature gradient was the highest at the superheater tube section. This showed that the highest thermal stresses caused by the different thermal strain between the hot and cold side of the tube occurred within the superheating section.

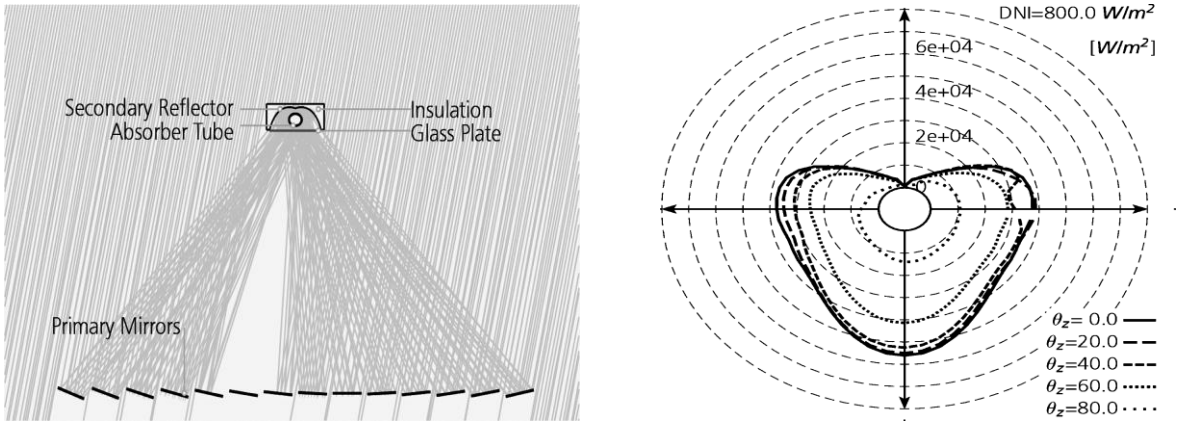

(a) **(b)**

Fig. 2.7(a) Linear Fresnel collector with second stage reflector [26] and **(b)** Heat flux distribution at the outer surface of the absorber Tube [26].

Velázquez *et al.* [24] carried out a numerical simulation of a linear Fresnel reflector concentrator (LFRC) to evaluate its technical feasibility as a direct generator in a Solar-GAX cycle with a cooling capacity of 10.6 kW. The study presented a design methodology for the LFRC based on Mathur *et al*. [27] and one-dimensional numerical models for the fluid flow inside the receptor tube, heat transfer in the receptor tube wall, heat transfer in cover tube wall, and uniform solar flux intensity in the solar concentrator. Their numerical results showed that the LFC used as a direct generator in a Solar-GAX cycle satisfied the quantity and quality of the energy demanded by the advanced cooling system. The reported efficiency was 17.9% higher than that of a single effect water–lithium bromide cycle coupled in an indirect form with a parabolic trough solar collector system. The availability of solar beam radiation had a negligible effect in the COP of the system, but had a significant effect in the capacity of the LFRC and the refrigeration cycle. They also reported that the receptor diameter and glass cover diameter influenced the LFRC thermal performance. The wind speed and ambient temperature did not have a significant influence in the LFRC performance. The LFRC thermal efficiency variation was lower than 2%

with wind speeds from 0 to 6 m/s. The buoyancy-driven secondary flow effect on the heat transfer performance for the absorber tubes was not investigated.

Robledo *et al.* [98] developed a lumped parameter dynamic model for a Fresnel solar collector field for a solar refrigeration plant. The model served as a control model for testing the controller's behavior under simulation. They experimentally validated the model by comparing the model variables with the data obtained from a solar cooling plant at the University of Seville. The model was able to reproduce the plant behavior with a minimum error. Munoz *et al.* [99] investigated the thermal regimes in solar thermal linear Fresnel collector and found that the efficiency curve (thermal and exergetic) indicated two branches referred to as two thermal regimes. As in the case of Munoz *et al.* [94], the first regime gave a rapid increase in efficiency, while the second regime was nearly horizontal indicating that the efficiency had reached the maximum value and that there was no further significant change in the heat transfer processes from the external surface of the absorber to the heat transfer fluid.

Sharma *et al.* [100] numerically investigated the thermal performance of a linear Fresnel solar concentrator with solar intensity of 1000 W/m^2 at different flow regimes- turbulent, transition and laminar flows in an absorber tube of 0.02 m diameter respectively. They used therminol-66 as a heat transfer fluid and assumed the collector aperture diameter of 1.0 m. They explained that the thermal efficiency depends on the collector design parameters, accuracy of the tracking system, mass flow rate of the heat transfer fluid, fluid temperature difference and heat loss coefficients etc. As expected, they found that the convective heat transfer of energy from the absorber tube to the heat transfer fluid was a maximum for the case of turbulent flow regime. Thermal performance of the collector was investigated at a fixed concentration ratio.

Pino *et al.* [101] conducted experimental validation of a thermal model of a linear Fresnel collector system using the solar cooling plant with an absorption chiller located in the School of Engineering at the University of Seville, Spain. The thermal model for receiver pipe was solved using a set of equations programmed into Engineering Equation Solver. The thermal model results were compared with the experimental data. It was observed that the variations between the simulated results and real heat absorbed by water were smaller than 7%. Also, the difference between the model results and the measured output temperature were relatively close due to the

high flow rate through the collector (13m^3/h), but the implication of this on the pumping power was not considered. They attributed the differences between the model results and measured values from the plant to the exclusion of the equations relating to transitory regime in heat transfer in the model.

2.4 Mixed or Combined Convection Heat Transfer in the Absorber Tube

The heat transfer coefficient is very essential to design engineers in determining the heat transfer rate by convection from the inner wall boundary to the heat transfer fluid flowing inside the tube. In a linear focusing solar collector such as a parabolic trough or linear Fresnel solar collector, the concentrated solar flux impinges on the absorber tube from below. This result in non-uniform heat flux distributions over the circumferential surface of the tube-wall and due to buoyancy-effects this could have a significant impact on the internal convective heat transfer coefficient of the collector tube. As earlier stated, a mixed or combined convection heat transfer could arise when the influence of the induced buoyancy-driven flow becomes comparable with the forced convection heat transfer. Studies are lacking for symmetrical or asymmetrical non-uniform heat flux distribution boundary in terms of the gravitational field encountered in linear focusing solar collector systems, where the fluid flow through the receiver absorber tube could be turbulent or laminar, depending on its application.

2.4.1 Mixed Convection Symmetrical Heat Flux Distributions Boundary

A number of experimental and numerical studies have been conducted for mixed convection heat transfer in horizontal circular tubes similar to that of a linear focusing solar collector absorber tube. Unfortunately, these studies considered only symmetrical uniform heat flux distributions or partial uniform heating boundaries in terms of the gravitational field and thus leaving the non-uniform heat flux distribution boundary case untouched. Fand and Keswani [102] noted that in all convective heat transfer processes, forced and natural convection coexist, since the density gradient and the associated buoyancy force field still exist. Ghajar and Tam [103] also noted that the influence of buoyancy forces on the forced convection heat transfer in horizontal tubes is dependent on the Grashof, Prandtl and Reynolds numbers as well as the wall boundary conditions. Other studies on mixed or combined convection heat transfer in horizontal circular include the following experimental and numerical studies.

The experimental results by Mori and Futagami [104] on the buoyancy effect on forced convection heat transfer in uniformly heated horizontal tubes demonstrated the buoyancy-induced secondary flow patterns as show in Fig. 2.8, through flow visualization experiments. They emphasized that the influence of buoyancy forces on forced laminar convection cannot be neglected at large values of $Re \times Ra$

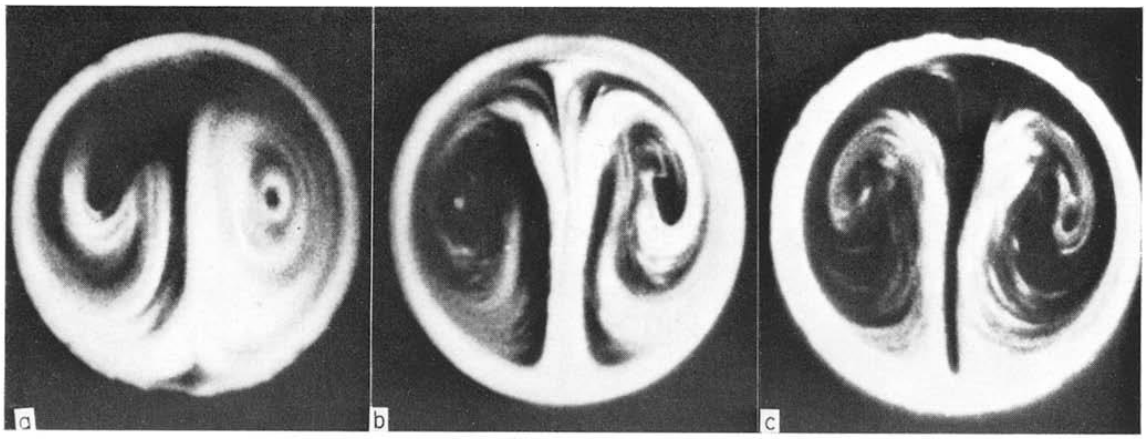

Fig. 2.8 Secondary flow pattern at (a) $\boldsymbol{Re \times Ra = 2 \times 10^4}$, (b) $\boldsymbol{Re \times Ra = 9 \times 10^4}$ and (c) $\boldsymbol{Re \times Ra = 1.6 \times 10^5}$ [104] **.**

Lagana [105] performed an experimental study on mixed convection flow in uniformly heated horizontal, vertical and inclined tubes to envisage the flow patterns. The study was conducted with a thin, semi-transparent electrical conductive gold-film heater attached on the outside surface of a plexiglass pipe. The flow patterns for the mixed-convection were visualized using a dye injection technique. A steady recirculation flow pattern followed by laminar instability was observed for the vertical tube, while steady spiraling flow patterns were observed for the inclined and horizontal tubes similar to the flow pattern obtained by Mori and Futagami [104]. However, the heat transfer characteristics of the tubes were not investigated.

Barozzi *et al.* [106] conducted an experimental investigation of combined forced and free convection in horizontal and inclined tubes. Their study was designed to reproduce the thermal effect of uniform solar irradiation on flat-plate collectors. The heat transfer results were analysed in terms of the local axial Nusselt number (Nu_x) and a non-dimensional downstream distance (x/D_i) of the tubes. For the case shown in Fig. 2.9 for horizontal tubes, the Nusselt

number was found to decrease from very high values near the inlet section and approached an asymptotic level at the downstream portions of the tube. For inclined tubes, it was found that an increase in the angle of inclination of the tube from 0° to 60° resulted in very small reductions in the heat transfer rate.

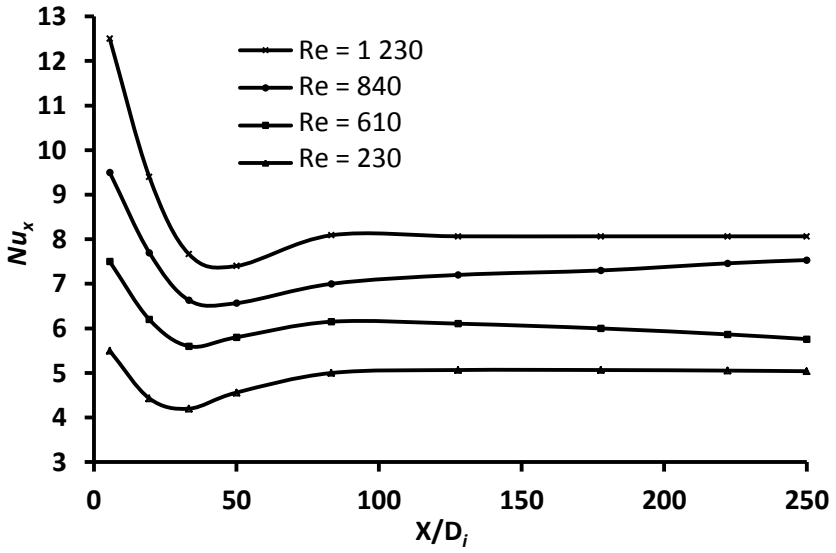

Fig. 2.9 Local Nusselt number as a function of non-dimensional distance (x/D_i) from the inlet [106].

Mohammed and Salman [107] performed an experimental study of laminar mixed convection to investigate the local and average heat transfer in thermally developing and fully developed air flow in a uniformly heated horizontal circular tube. They found that local axial Nusselt numbers (Nu_x) increased with an increase in the heat flux due to secondary flow superimposed on the forced convection flow. They also found that Nu_x decreased from the entrance region and then increased slightly near the exit of tube heated region due to laminarization effect in the near wall region and tube end losses. The average Nusselt number was correlated in terms of Rayleigh number and Reynolds number as: $\overline{Nu} = 3.19(\overline{Ra}/\overline{\mathrm{Re}})^{0.26}$.

Bergles and Simonds [108] experimentally studied the combined forced and free convection for laminar flow in horizontal tubes with uniform heat flux to investigate free convection effects. The study was conducted using electrically heated glass tubing in order to envisage the flow pattern and to obtain quantitative information. It was noted that there was heat conduction around the tube circumference and unintended non-uniform heat generation introduced

experimental uncertainties. For fully developed laminar flow of water, they recommended correlation curves for obtaining heat transfer coefficients in practical situations and concluded that with reasonable heating rates, the heat-transfer coefficients could be three to four times higher than the predicted values at constant fluid property.

Newell and Bergles [109] analytically investigated the effects of free convection on fully developed laminar flow in horizontal circular tubes with uniform heat flux and obtained solutions for heat transfer and pressure drop for both heating and cooling cases of water. The tube exhibited higher Nusselt numbers and friction factors, with the Nusselt numbers being over five times the Poiseuille value at a Grashof number of approximately 106. This is also in line with the findings of Bergles and Simonds [108]. The study found that significant circumferential wall temperature variations exist and a correlation for the difference between the wall temperatures at the top and bottom of the tube was presented. They also presented correlations for the Nusselt number and friction factor from the analytical results.

Piva *et al.* [110] investigated laminar combined convection in horizontal circular ducts both numerically and experimentally under uniform wall heating. Their study accounted for peripheral and axial wall conduction effects in the numerical model and convection with buoyancy effects in horizontal duct flows. In terms of measured mean wall temperature, their results differed from the numerical results by less than ± 0.1°C.

Coutier and Greift [111] investigated mixed laminar convection in a horizontal tube subjected to natural convection around its external boundaries both experimentally and numerically, to analyze the buoyancy effect on the forced flow within the tube. Two flat plate solar collectors with copper absorber tubes and water as the heat transfer fluid were used in the study. The natural convection around the tube resulted from the temperature difference between the tube wall and the fluid medium surrounding it. Fig. 2.10 gives the local and average axial variation of the Nusselt number at 0°, 80° and 280° circumferential angular coordinates, indicating the stronger angular dependence of the secondary flow effect. It was found that the variation in the tube wall temperature had a significant effect on the secondary flow patterns within the tube as well as on the heat transfer.

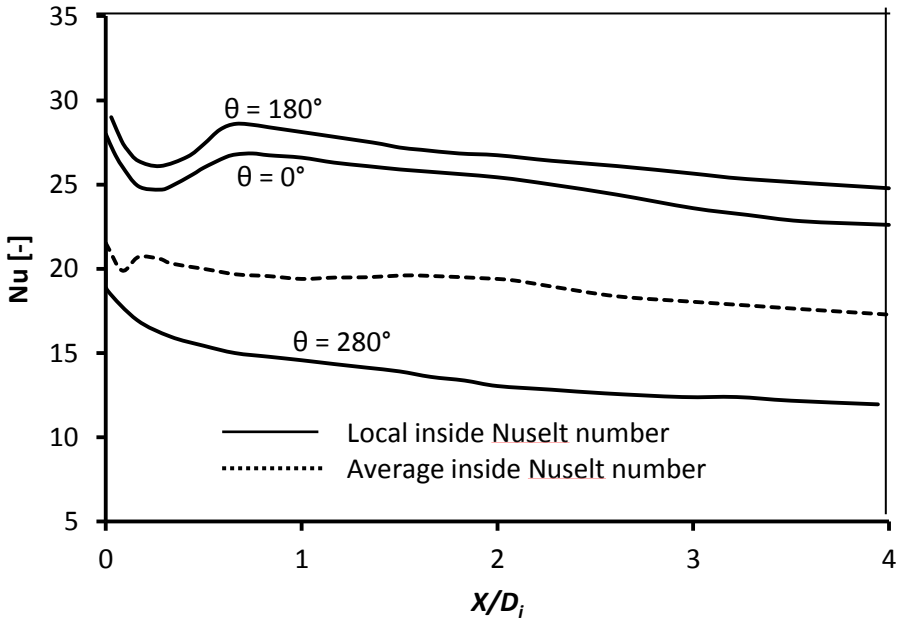

Fig. 2.10 Local and average Nusselt number axial variation at 0°, 80° and 280° angular coordinates [111].

Prayagi and Thombre [112] performed a parametric study on buoyancy induced flow in circular pipes based on uniform heat flux in a solar water heating system. Heat transfer correlations and flow characteristics were established for the buoyancy induced flow through inclined tubes for the case of solar water heating system.

Boufendi and Afrid [113] numerically studied forced and mixed convection heat transfer in a uniformly heated horizontal pipe and noted that mixed convection flow is a three-dimensional heat transfer problem. They found that as the Grashof number increased, the secondary flow developed into two counter-rotating vortices, which lead to improved convective heat transfer.

Zeitoun [114, 115] performed a numerical study for fully laminar forced convection in circumferentially partially heated tubes using the finite volume method. In these studies uniform heat flux and uniform temperature on the heated portion of the tube were investigated while assuming the remaining portion to be adiabatic. It was found that the Nusselt number values increased as the tube wall thickness was increased and also increased with the decrease in the thermal conductivity ratio of the fluid and the tube. However, the influence of buoyancy-induced secondary flow and thermal losses by convection and radiation from the heated surface

were not investigated. Lagana [105] noted that pure forced convective heat transfer rarely occurred in practical applications since buoyancy forces usually exist in any forced convection, even at low temperature differences.

Mori *et al.* [116] also conducted an experimental study to investigate buoyancy effect on the forced-convective heat transfer in a horizontal circular tube with a uniform heat flux. They considered both laminar and turbulent flows and found that buoyancy force has a significant effect on the velocity and temperature fields for the case of laminar flow and less of an effect in the turbulent flow regime. They also found that for a laminar flow case, the Nusselt number was twice as high as those calculated without considering the effects of secondary flow at $Re \times Ra = 4 \times 10^5$. This is similar to the analytical results obtained by Newell and Bergles [109], however, the analytical result over predicted the Nusselt number.

Sadik *et al.* [117] reported on different Nusselt number correlations for hydrodynamically and thermally fully developed flow for combined free and forced convection heat transfer in horizontal circular tubes subjected to uniform wall heat flux conditions as well as uniform wall temperature boundary conditions.

Metais and Eckert [118] experimentally studied the forced, mixed and free convection regimes in laminar and turbulent fluid flow through horizontal and vertical tubes to determine when the heat transfer could be regarded as forced, free or mixed convection regime and to know when anyone could be neglected when compared to the other. They recommended the chart presented in Fig. 2.11, in which the regimes of forced, free and mixed convection for laminar and turbulent fluid flows in tubes for both upward and downward flow could be clearly established in terms of the Grashof, Prandtl and Reynolds numbers. The results in Fig. 2.11 are reported to be valid for both uniform wall temperature (UWT) and uniform heat flux (UHF) boundary conditions.

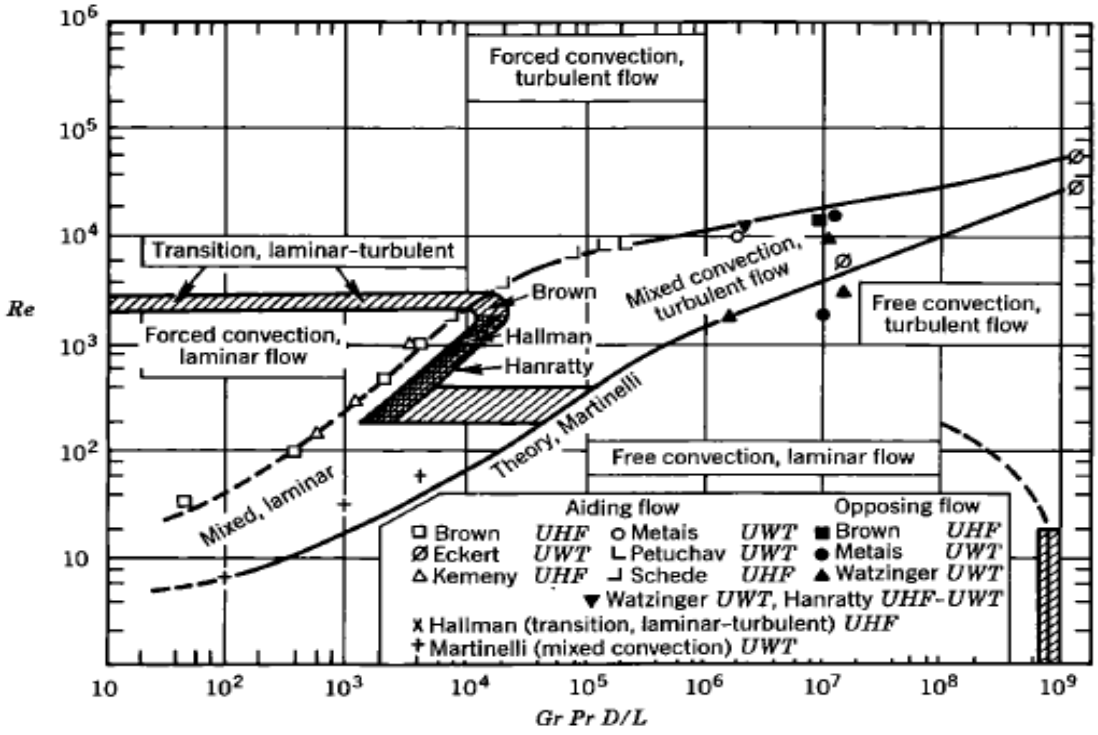

Fig. 2.11 Free, forced and mixed convection regimes for flow inside vertical tubes for $\mathbf{10^{-2} < Pr\frac{D}{L} < 1}$, and also valid for both upward and downward flow [118].

Peyghambarzadeh [119] experimentally investigated the effect of free convection on fully turbulent flow forced convection heat transfer in the thermal entry region of a horizontal tube with a constant heat flux. The study was conducted using air as the heat transfer fluid for Reynolds number ranging from 6500 to 11 000. It was found that the induced secondary flow due to buoyancy forces was significant at higher heat fluxes and low flow rates. Fig. 2.12 indicated that the Nusselt numbers for higher heat fluxes were higher than that of lower heat flux due to higher effect of secondary flow superimposed on the forced convection flow.

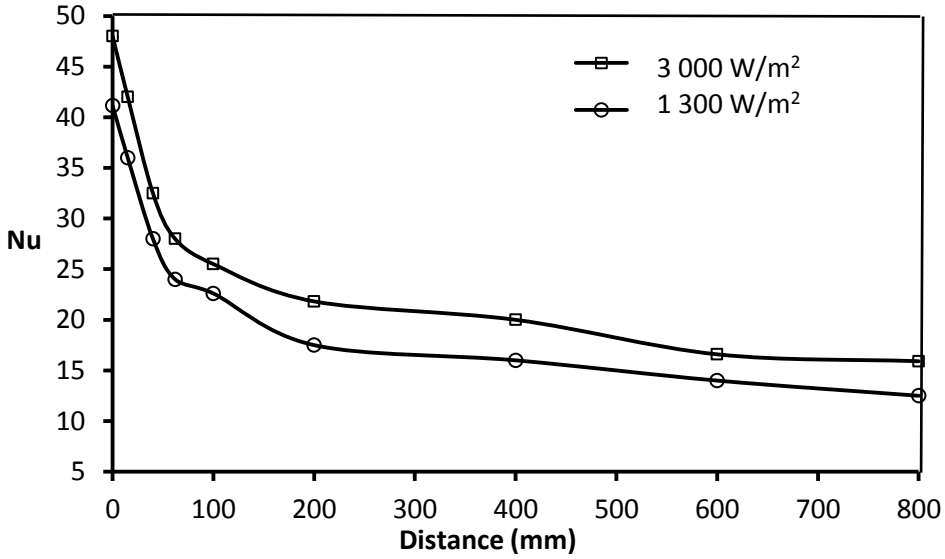

Fig. 2.12 Nusselt number variation along tube length as a function of heat flux at Re = 6500 [119].

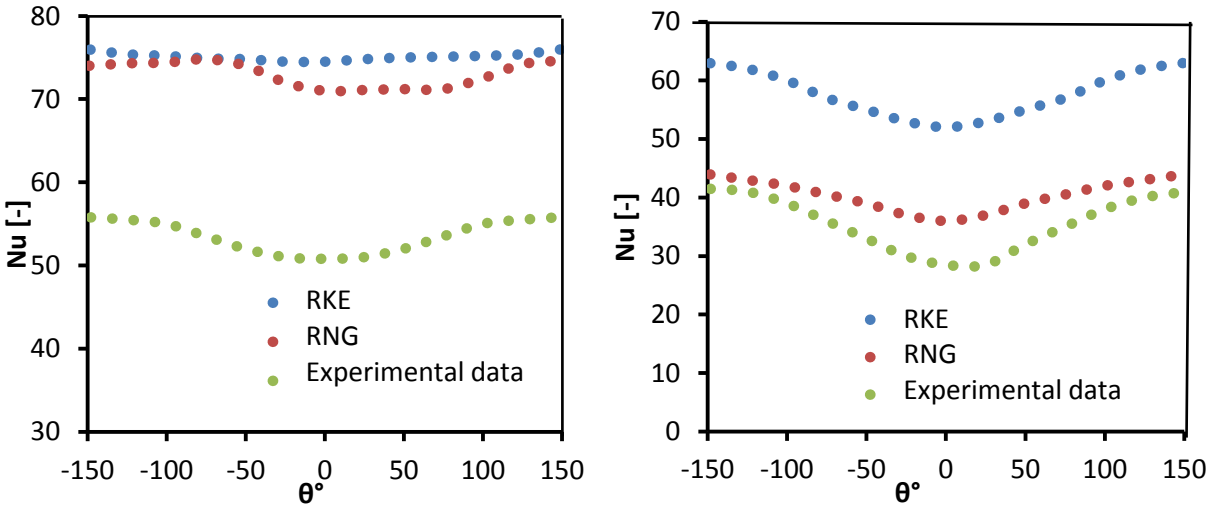

(a) **(b)**

Fig. 2.13 Nu vs. azimuthal coordinate at Re = 5750 and Gr = at 3.00 x 10^8: **(a)** at the entrance section and **(b)** at the exit section [120].

Only a small number of studies have investigated the developing, weakly turbulent mixed convection at moderate and high Rayleigh numbers. Grassi and Testi [120] experimentally investigated the turbulent mixed convection in the entrance region of a uniformly heated horizontal tube and developed heat transfer correlations for developing and fully developed flow

for the turbulent mixed convection. In another study, Grassi and Testi [121] performed numerical analyses of the Reynolds averaged Navier–Stokes equations (RANS) turbulence models for predicting developing mixed convection within a uniformly heated horizontal pipe. Based on Figs. 2.13(a) and 2.13(b) they concluded that the realizable k –ε (RKE) model predicted the heat transfer coefficients much better only in the entrance region, while renormalization-group k–ε (RNG) model performed better only in developed flow. The two models gave a secondary flow motion, with counter-rotating vortices, superimposed on the stream-wise main flow.

2.4.2 Mixed Convection Asymmetrical Heat Flux Distributions Boundary

In all the earlier-mentioned studies, cases were limited only to where the heat flux distribution boundaries (whether uniform or not) were symmetrical in terms of the gravity direction. As earlier indicated in Fig.1.3, the asymmetrical heat flux distributions in terms of the gravity direction occur when the incident solar radiation has deviated from the zenith angle position. The impacts of the asymmetrical non-uniform heat flux boundary condition, which will be present during majority of the day due to the sun-tracking system of the collector, has not yet been investigated. However, only few studies have considered cases of mixed convection asymmetrical uniform heat flux distribution boundaries for non-circular cross-sections, which are not applicable to circular tube-based solar collectors, indicating the need to investigate the asymmetric heating in terms of gravity for a linear focusing solar collector tube. Some of these are briefly mentioned below:

Bazdidi-Tehrani, *et al* [122] numerically investigated the radiation effects on turbulent mixed convection flow between two the asymmetrically heated vertical parallel plates. They reported on the effects of wall emissivity and optical thickness on the fluid flow, thermal fields, Nusselt number, and friction factor. The wall emissivity and optical thickness increased the radiation effects on the centerline velocity, bulk fluid temperature and Nusselt number and friction factor decreased.

Satyamurty and Repaka [123] in their study developed a superposition relation for calculating the local Nusselt number values for forced convective flow through asymmetrically heated parallel-plate channels. The asymmetric thermal boundary condition was in terms of ratio of the

wall temperatures in excess of the entry fluid temperature. They validated their model with numerical results and noted the model is valid as long as the geometric and flow symmetry are maintained.

Kim and Boehm [124] numerically investigated laminar mixed convective flow across a block-mounted plate in a vertical channel with asymmetric heating. In this study, one plate with blocks was heated to a constant temperature and the other was adiabatic. They reported on the buoyancy-induced secondary flow effects and geometry of the channel on the local Nusselt number. This study found that the heat transfer depends on geometric ratios and Reynolds number. They also found that as the Richardson number ($Ri = Gr/Re^2$) values increased, the average Nusselt number value decreased and it also increased with the Richardson number at high Grashof numbers in the recirculation zones in the blocks.

Habchi and Acharya [125] numerically investigated laminar mixed convection in a symmetrically or asymmetrically heated vertical channel. For the symmetric heating both plates were heated and for the asymmetric heating, one plate was heated while the other was adiabatic. They found that as the Gr/Re^2 values increased the velocity of fluid near the hot wall also increased and that the Nusselt number was at its maximum value near the inlet of the channel.

Osborne and Incropera [126] experimentally studied the laminar mixed convection heat transfer for water flow between horizontal parallel plates with uniform asymmetric heating. They reported that buoyancy-driven flow had stronger effects on the bottom plate and low influence on top plate flow conditions, which indicated that forced convection heat transfer dominated at the top plate and mixed convection heat transfer dominated at the bottom plate.

2.5 Conclusion

This chapter presented a brief review of some basic concepts and performance characteristics of linear focusing solar thermal concentrating collectors. It also covered some experimental and numerical studies on thermal performance of linear focusing solar collector receiver tubes. The available literature indicated that some of the previous studies were based on uniform solar heat flux assumptions for convenience and this is contrary to the optical design and ray-tracing

simulation results, which indicated non-uniform heat flux distributions boundaries. In linear focusing solar collectors, concentrated solar flux impinges on the receiver tube from below resulting in non-uniform heat flux distributions boundary and studies are generally lacking on the impacts of this heat flux distributions case on the internal convective heat transfer and friction factors for the collector tubes. The linear focusing solar collectors were generally applied to large-scale applications suitable for steam productions needed for electricity generations and industrial process heats generations. Studies are lacking for applications for large volume hot water generation for institutions and where there could be space restrictions, and for flow regimes where buoyancy-effects in the laminar and weak turbulent flow regimes could be employed in enhancing the harnessing the radiant solar energy. Also, in a number of experimental and numerical studies mixed convection heat transfer were investigated in horizontal circular tubes similar to that of linear focusing solar collector tube under uniform thermal boundary conditions and non-uniform heat flux cases have not been investigated. The uniform heat flux cases indicated that due to buoyancy-driven secondary flow, the temperature and axial velocity profiles, internal heat transfer coefficients and friction factors differed significantly from the cases where buoyancy effects were neglected (pure forced convection), especially in the laminar flow regime, and to a lesser extent in the low turbulent flow regimes. Studies are lacking for the developing, weakly turbulent mixed convection heat transfer in collector absorber tubes for uniform and non-uniform heat flux boundary conditions. Mixed convection heat transfers for asymmetrical heat flux distributions boundary on non-circular cross-sections, which are not applicable to circular tube-based solar collectors were reviewed. No information could be found in the literature on the influence of asymmetrical non-uniform heat flux boundary in terms of gravity direction on mixed convection heat transfer and friction factors for linear focusing solar collector tubes. The asymmetrical non-uniform heat flux distributions boundary usually occurs in linear focusing solar thermal collectors when the incident radiation from the sun has deviated from the zenith angle position and this could significantly influence the thermal performance of the absorber tubes.

CHAPTER THREE: FIRST ORDER THERMAL PERFORMANCE MODEL

3.0 Introduction

This chapter gives description of a linear solar collector lay-out with a parabolic trough reflector field for adaption as an alternative to a traditional flat-plate solar collector for water heating applications. It presents a first order heat transfer model, modeling assumptions and an indicative thermal performance comparison for the two collectors. The intension is to demonstrate the possible first order advantage of a parabolic trough collector type compared to a flat plate collector type for hot water production. Several efficiency performance strategies exist for both collector types, but those fall beyond the scope of this chapter.

Data reduction for the fluid flow through the collector tube model and some important dimensionless parameters for mixed and forced-convection heat transfer are also presented.

3.1 Physical Model Description

Fig. 3.1(a) shows a schematic representation of a linear solar collector lay-out with a parabolic trough reflector field, which concentrates the solar radiation onto the bottom portion of a tube. The absorber tube has an outer diameter of D_o, an inner diameter of D_i and a length of L. For comparison purposes, Fig. 3.1(b) shows a traditional flat-plate collector lay-out type which consists of a number of parallel tubes bonded onto a metal plate, each with an outer diameter of D_o, an inner diameter of D_i, and a length of L, spaced at a centre-to-centre distance of p. Thermal insulation is present at the bottom of the metal plate. Solar radiation hits the upper part of the tubes with additional heat being conducted via the collector plate to bonded joints. Both collectors have the same projected surface area and are exposed to the same incident heat flux intensity, q_s'' from the sun as could be the case when the sun is at its zenith position.

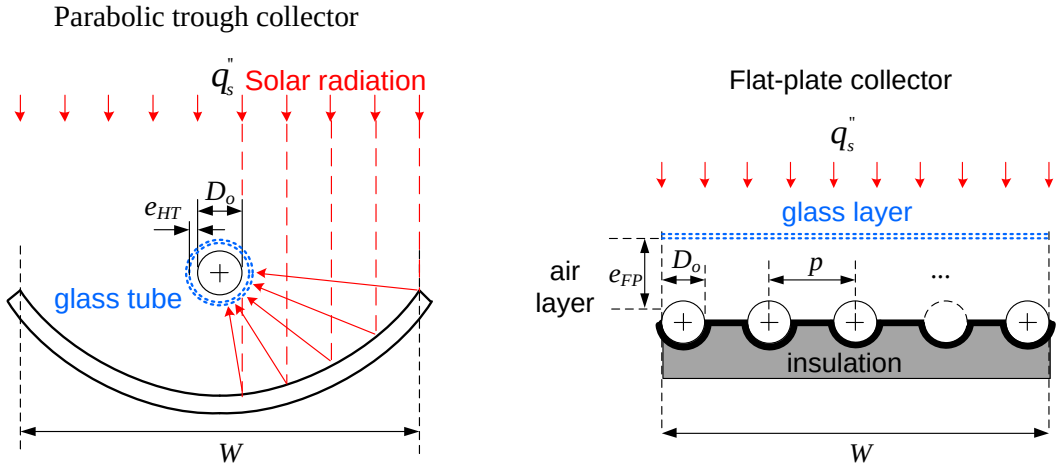

(a) (b)

Fig. 3.1(a) Parabolic trough solar collector lay-out and **(b)** Flat plate collector lay-out.

Both collectors can be additionally insulated by the inclusion of a glass cover at a distance of *e* from the metal plate for the flat plate collector and a glass cover at a distance *e* from the outer diameter of the collector tube for the parabolic trough collector**.**

3.2 Modelling Assumptions

In order to simplify the calculations, the following assumptions were made:

(i) Thermal properties of the heat transfer fluid (liquid water) and the collector materials are assumed constant and independent of temperature except for the fluid density and viscosity of the fluid varied for the inlet temperature range of 20 ^{0}C to 87 ^{0}C considered in the present study (as is discussed in Chapters 6 to 8).

(ii) The energy absorbed and the reflection loss for the glass cover are neglected and the incident angle of 0^o was considered. The anti-reflectance of the glass is assumed of having no effects on the relative comparison of the thermal efficiency.

(iii) The thermal resistance in the metal components are neglected compared to the thermal resistance of the other components due to their relatively high thermal conductivities.

(iv) Heat losses through insulation of the collectors and from the edges and supports of the collector are neglected to focus the comparison only on the heat flux distributions on the tubes.

(v) The heat flux losses via convection and radiation are the dominant thermal losses in the solar thermal collectors and are modelled using first-order approximations.

(vi) The fluid flow through systems is assumed incompressible (constant pressure at all points in the collector tube) and the systems operate under steady-state conditions (constant solar heat flux incident on the collector tube with a uniform cross-sectional area and no flow across the tube-wall boundary).

The listed assumptions will have the same impact on both collector types and would thus on a first order not influence the relative comparison made in this chapter.

3.3 First Order Heat Transfer Model

As shown in Figs 3.1 (a) and (b), the effective collector area for both the parabolic trough and traditional flat-plate collector lay-outs intercepting the incident solar radiation is:

$$A_{col} = LW \tag{3.1}$$

The heat received by the parabolic trough collector tube surface is presented as:.

$$q_{col,PT} = \alpha_w \eta \tau_g q_s'' A_{col} = \alpha_w \eta \tau_g q_s'' LW \tag{3.2}$$

Here the reflector efficiency is η, the absorptivity of the tube surface is α_w and the transmittance of the glass cover is τ_g. L is the effective length of the collector.

Similarly, for the heat received by the absorber plate for the flat-plate collector lay-out is given (without reflector efficiency) as:

$$q_{col,FP} = \alpha_w \tau_g q_s'' \ A_{col} = \alpha_w \tau_g q_s'' LW \tag{3.3}$$

In order to express the heat transfer rate absorbed into the heat transfer fluid, the energy balance principle is utilized. Fig.3.2 shows a first order thermal resistance network linking the metal collector tube surface at temperature T_w, with the fluid within at temperature T_b, and the ambient at a temperature T_∞. The heat received, q_{col}, is incident only on the outer surface of the metal collector since heat absorption in the glass and air layers are ignored, since it would

have the same impact on both the collector types. For the flat-plate collector the entire absorption plate is approximated to be at a temperature of T_w. In reality a temperature difference will be present which reduces the efficiency of such a collector system. This conservative approach does not alter the outcome of this comparison as will be shown later.

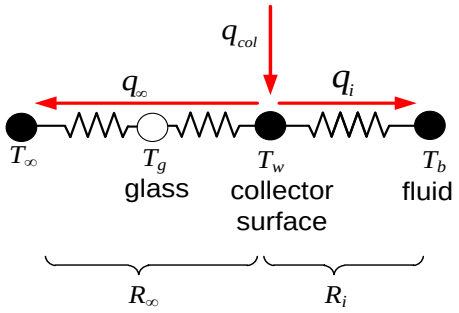

Fig. 3.2 First order thermal resistance network.

For steady state conditions the heat flow to the fluid, $\dot{q}_i$, and to the ambient, $\dot{q}_\infty$, can be expressed as:

$$q_{col} = q_i + q_\infty = \frac{(T_w - T_b)}{R_i} + \frac{(T_w - T_\infty)}{R_\infty} \tag{3.4}$$

Here R_i and R_o are the effective overall average thermal resistance to the heat transfer fluid and the thermal resistance to the ambient via the glass layer (if present).

The thermal resistance to the fluid for the flat-plate collector is determined by employing the average inner tube heat transfer coefficient, $\bar{h}_i$, the total inner heat transfer surface, $\pi D_i LW/p$, the thermal conductance over the metal bond between the collector plate the tube wall, C_{bond}, and the total length of the bonds for all the tubes, LW/p:

$$R_{i,FP} = \frac{p}{\pi D_i LW \bar{h}_i} + \frac{p}{C_{bond} LW} \tag{3.5}$$

The thermal conduction in the tube wall is ignored for now due to the low significance that it has on the performance of the collector system in this comparison. It is, however, included in

later sections of this study when more detailed analyses are conducted. The value of C_{bond} based on experiments of commercial solar collectors has been reported to range from 2 W/mK to 6 W/mK [127]. A value of 4 W/mK is adopted here.

For the linear trough solar collector, which only has one collector absorber tube, the thermal resistance to the fluid is given as:

$$R_{i,PT} = \frac{1}{\pi D_i L \bar{h}_i} \tag{3.6}$$

For the thermal resistance to the ambient, the following are taken into consideration: the air gap thermal conduction resistance acting as an insulation layer, first order radiation heat transfer between the glass and the collector surface over the air gap, external convection heat transfer from the glass surfaces, and radiation heat emitted from the glass surface.

For the flat-plate collector the thermal resistance to the ambient is given as, based on the full collector surface area, LW:

$$R_{\infty,FP} = \frac{1}{LW}\left[\left(\frac{k_a}{e_{FP}} + \frac{\sigma(T_w^4 - T_g^4)}{(1/\varepsilon_{tu} + 1/\varepsilon_g - 1)(T_w - T_g)}\right)^{-1} + \left(\bar{h}_o + \frac{\sigma\varepsilon_g(T_g^4 - T_\infty^4)}{T_g - T_\infty}\right)^{-1}\right] \tag{3.7}$$

Here k_a is the thermal conductivity of the air-gap having a width of e_{FP} and was evaluated at the average steady state temperature between T_w and T_g. The radiative heat balance between the collector plate and the glass was evaluated as that of two infinite parallel plates given by:

$$q = \sigma LW\left(T_w^4 - T_g^4\right)\Big/\left(1/\varepsilon_{tu} + 1/\varepsilon_g - 1\right). \tag{3.8}$$

Here ε_{tu} and ε_g are the emissivities from the collector and glass surfaces with:

$$\varepsilon_{tu} = 0.0003T_w + 0.3171 \text{ [128]} \tag{3.9}$$

and ε_g = 0.91 is the emissivity of the glass cover of the collector considered, which represents that of Pyrex glass [129] also used in the Schott's heat collector element (HCE) [130]. The

external convection heat transfer coefficient, $\bar{h}_0$, is based on the following Nusselt number relationship for flow over a flat plate in terms of the Reynolds number and Prandtl number:

$$\overline{\mathrm{Nu}}_W = 0.664 \mathrm{Re}_W^{\frac{1}{2}} \mathrm{Pr}^{\frac{1}{3}} \tag{3.10}$$

with an air-speed of 15 km/hr (arbitrary value) and all air properties evaluated at 300 K. The radiation heat loss is expressed as:

$$q = \sigma \varepsilon_g L W \left(T_g^4 - T_\infty^4 \right). \tag{3.11}$$

For simplicity, convection and radiation temperature sink values are taken to be the same at T_∞. In reality, different heat sink temperatures should be used, but this will only complicate the comparison and will not alter the key outcomes.

Similarly, for the parabolic trough collector, the thermal resistance to the ambient is given as:

$$R_{\infty,PT} = \frac{1}{\pi (D_o + 2e_{PT}) L} \left[\left(\frac{k_a}{e_{PT}} + \frac{\sigma (T_w^4 - T_g^4)}{(1/\varepsilon_{tu} + 1/\varepsilon_g - 1)(T_w - T_g)} \right)^{-1} + \left(\bar{h}_0 + \frac{\sigma \varepsilon_g (T_g^4 - T_\infty^4)}{T_g - T_\infty} \right)^{-1} \right] \tag{3.12}$$

Here, for simplicity the thermal resistance relationship over the cylindrical gap is approximated as linear (valid if the air gap is relatively small), and applied over the outer surface of the glass tube, $\pi (D_o + 2e_{PT}) L$, by ignoring the thickness of the glass itself. The convection heat transfer coefficient on the outer surface, $\bar{h}_o$, is expressed as $\bar{h}_o = 5.7 + 3.8v$ [15] and is related to the same air speed, *v*, used for the flat plate collector. The radiation heat loss is dealt with in the same manner as in the flat plat collector, but only applied to the outer surface of the single glass tube and the radiation exchange with the solar concentrator was omitted. If these were to be included, the calculated performance of the collector will increase and this conservative approach will not alter the key outcomes of this comparison. It will either reduce the flat plate collector efficiency compared to the parabolic trough collector type, or influence both of the collectors' efficiencies in a similar manner.

3.4 Indicative Thermal Performance Comparison

The intention here is an initial first order comparison of the efficiency of the two collectors under laminar flow conditions in order to determine the proportion of the intercepted solar radiation absorbed into the heat transfer fluid. (The difference of thermal behaviour on the inside of the tube between laminar and turbulent flow regime conditions is covered later in this thesis.) The thermal performance (or efficiency) for the collectors is expressed as the proportion of the intercepted solar radiation over the entire collector surface, that is taken up by the heat transfer fluid, q_i:

$$\eta_{col} = \frac{q_i}{q_s'' LW} \tag{3.13}$$

The parameters for the initial comparison are: D_o = 40 mm, D_i = 35 mm, p = 80 mm, W = 1 m, L = 2 m, $e_{FP} = e_{PT}$ = 25 mm, η = 0.9, $T_{atm} = T_\infty$ = 27 °C and α_w = 0.85 is the absorptivity of the absorber tube, which represents an absorber tube with iron oxide coating [131]. These inputs are used for demonstration purposes in order to identify the conditions that favour an adaption of the considered linear trough collector system for a flat-plate system, with specific focus on the internal heat transfer coefficient. Other dimensions and parameters could also be selected, but a full analysis of this falls beyond the scope of this chapter.

The overall collector efficiencies are determined in terms of the difference between the local bulk fluid temperature and the ambient temperature for a symmetrical solar flux, q_s'' = 1000 W/m^2. This heat flux value is chosen to represent a clear sunny day in a region with relatively high levels of solar irradiance. It should be noted that the radiation heat flux used for the traditional flat-plate collector is global radiation and the same radiation heat flux value is used for the parabolic trough solar collector and was considered as beam radiation.

Also, for this comparison, the inner tube-wall heat transfer coefficients based on the Nusselt number are determined from:

$$Nu = \frac{hD_i}{k} \tag{3.14}$$

Here k is the thermal conductivity of the heat transfer fluid evaluated at the bulk fluid temperature and D_i is the inner diameter of the collector absorber tube.

As reference datum, a Nusselt number of 4.36 for both the flat plate and parabolic trough collectors are used. This value is generally associated with the fully developed flow under uniform wall heat flux conditions (without secondary flow effects). For developing flow, close to the inlet to the collector tube, higher Nusselt number can be expected. However, for demonstration purposes, the more conservative fully developed flow Nusselt number is used in the datum case. In a linear trough collector, however, since concentrated heating occurs from below and there is a circumferential non-uniform heat flux distribution, a significant amount of buoyancy driven secondary flow is present within the tube which results in a higher enhancement of the internal convective heat transfer. For that reason Nusselt numbers of 10 and 15 for the linear trough collector are also considered. The higher Nusselt numbers are not considered for the flat plate collector because of the uniform heating which occurs from the top surface of the absorber tubes and thus, little to no heat transfer enhancement will be present. A detailed numerical investigation that better estimates the internal convective heat transfer enhancement due to the buoyancy-induced secondary flow phenomenon for symmetrical and asymmetrical different circumferential spans of a non-uniform concentrated heat flux distributions are presented in the subsequent Chapters.

Fig 3.3 indicates the steady state overall efficiencies for a parabolic trough collector and a flat-plate solar collector in terms of the difference in temperature between the average internal bulk water temperature and the surrounding temperature for a symmetrical applied heat flux of q_s'' = 1000 W/m^2. As expected, as the fluid temperatures increase (resulting in higher temperature differences), the thermal efficiencies of the collectors decrease. From Fig. 3.3, it can be seen that for the parabolic trough collector, an indicative maximum efficiency of up to 74% is obtained when an inner Nusselt number of 15 is considered. As

the Nusselt number decreases, so does the collector efficiency decreased. For the flat-plate collector a highest efficiency of approximately 74% is also achieved at low fluid temperature differences. The rate of decrease in the efficiency in terms of the temperature difference is, however, the highest with the flat plate collector. This result in line with the collector thermal efficiency obtained with a three dimensional numerical model for flat-plate liquid solar collectors developed by Cerón *et al.* [132] for a uniform tube-wall heating condition. The model considered the incident solar radiation absorption, transmission and reflection, mixed convection flow in the absorber tubes, heat losses by convection and radiation to the ambient. The model was successfully validated with their own experimental data with uncertainty of 1.5%. At 0° fluid temperature difference, the collector thermal efficiency obtained with the model was approximately 70% for the same q_s'' = 1000 W/m^2.

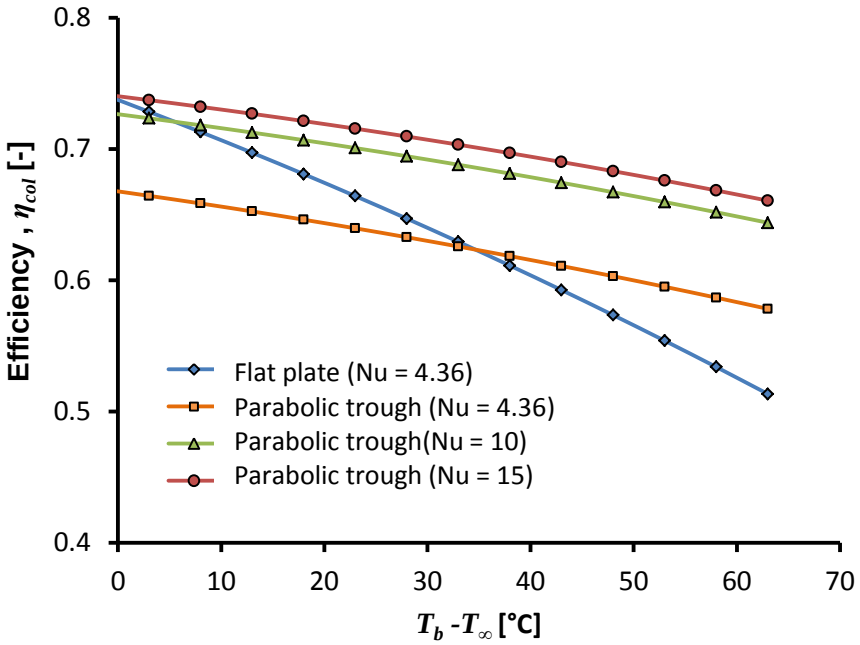

Fig. 3.3 Overall efficiency of both collector lay-outs for Nu = 4.36, as well as for Nu = 10 and Nu = 15 for the parabolic trough collector for q_s'' = 1000 W/m^2.

For the current set of inputs, the parabolic trough collector case has a higher efficiency than the flat-plate collector for temperature differences above approximately 35°C. Also, at high temperature differences the parabolic trough collector type significantly outperform the flat-plate collector in both efficiency and heat input rate (not shown).

Based on this first order comparison it is seen that even though the heat transfer fluid flow is laminar, a relatively small increase in the convection heat transfer coefficient can result in a significant thermal advantage when a solar concentrating system, such as a parabolic trough or linear Fresnel collector set-up is employed. Also, based on the indicative trend in Figs 3.3, it appears as though a linear solar collector system might technically be a viable alternative for flat plate collector system for water heating, if adapted and if a Nusselt number of 10 and more are achieved. Also, Cerón *et al.* [132] noted that the Nusselt number for the absorber tubes of the flat-plat solar collector was higher in fully developed region due to secondary flow that increased the heat transfer rate compared with that of a horizontal tube with uniformly heated tube-wall. The Nusselt number for the absorber tubes of the flat-plat solar collectors is however less than the case of linear focusing solar collectors due to circumferential non-uniform heating of their absorber tubes. Thus, the increased thermal performance could therefore be an acceptable trade-off for the increased complexity of this solar collector system (in terms of possible sun-follower systems) when compared to a flat-plate collector. This could be applicable to high volume hot water users for where the space for solar energy collection is limited.

For the remaining Chapters of this study, no outer glass covering is considered except for the model validation purposes, in order to place focus mainly on the influence of the circumferential angle span of the impinging heat flux. The inclusion of glass cover might impact the heat flux distribution on the collector tube wall due to optical refraction, reflection and absorption. In addition, if the void between the glass cover and the tube is not evacuated, the thermal mass of air in the annular space could result in heat fluxes on the tube surface that are more uniform. These influences fall beyond the scope of this study.

3.5 Conclusion

In this chapter, a first order thermal performance model for a linear solar collector with a parabolic trough reflector field for adaption as an alternative to a traditional flat-plate solar collector for water heating applications is presented. A significant amount of buoyancy-driven secondary flow is expected to be present in a linear trough collector due to circumferential non-uniform heating of the collector absorber tube from below, which results in a higher internal heat transfer enhancement than in the flat-plate collector with uniform heating from the top surface. It is found that for a linear solar collector with a parabolic reflector field if adapted could be an alternative to traditional flat-plate solar collector for water heating applications. The improved thermal efficiency associated with the higher internal heat transfer coefficient due to buoyancy-induced secondary flow could be an acceptable trade-off for a linear trough solar collector system which uses a sun-tracking system when compared to a flat-plate collector.

CHAPTER FOUR: NUMERICAL MODEL, OUTPUT DEFINITION AND SOLUTION PROCEDURE

4.0 Introduction

This chapter focuses on the model description and numerical heat transfer models for analyzing the thermal performance the absorber tube in the parabolic trough collector type. As indicated in the previous chapter, the magnitude of the heat transfer coefficient is an important performance parameter. The intension is to determine the heat transfer coefficient, along with other quantities for different geometric and operating conditions. The following are covered in the chapter: a description of the domain, a heat transfer modeling methodology and data analysis section, the governing equations, the boundary conditions and material properties and the numerical solution procedure.

4.1 Tube Model Description

Refer to Fig. 4.1 giving a representation of the computation domain consisting of a horizontal absorber tube model containing the heat transfer fluid. In order to define the thermal boundary condition and to describe the data analysis method, the tube wall is divided into $M \times N$ number of sections (in the axial and circumferential directions respectively). The $M \times N$ sections do not necessarily match-up with the computation grid and are only used for the boundary condition definition and reference system for discussion purposes. The tube has a wall thickness of t, inner diameter D_i, outer diameter of D_o, and a total length of L_{TOT}. Different dimensional cases (case 1 to 4) were considered as is described in Table 4.1. The tube model dimensions were selected based on the available commercial sizes. The tube model length is based on the LS-2 collector module which normally has absorber tube lengths of 4 m or more [133]. A 10 m length is considered for the present study, which represents the absorber tube length for two LS-2 collector modules, which could be suitable for direct water heating. Unless stated otherwise, most result presented will be for case 1.

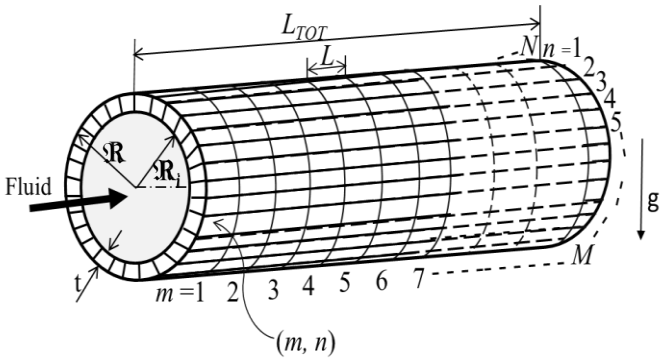

Fig. 4.1 Tube model for symmetrical heat flux boundary divided into $M \times N$ number of sections.

Table 4. 1 Dimensional cases

Case	Outer diameter, D_o (m)	Inner diameter, D_i (m)	Thickness, t (m)	Length, L_{TOT} (m)	Length to diameter ratio L_{TOT}/D_i
1	0.0730	0.0627	0.00516	10	160
2	0.0603	0.0525	0.00391	10	190
3	0.0483	0.0409	0.00368	10	244
4	0.0422	0.0351	0.00356	10	281

Figs 4.2 (a) and (b) show the cross-section of the tube model in Fig. 4.1 with a symmetrical partial uniform and sinusoidal non-uniform heat flux distributions over the outer-wall surface of the tube model for an effective incident heat flux angle span of α = 140°. This angle span is a function of the reflector system width, rim angle and the focal position of the parabolic trough for instance (other angle spans are considered later in the thesis also). The numbering system employed in simulating different circumferential heat flux distributions on the tube model is also shown. As will be described later, the heat flux distributions are selected arbitrarily in order to demonstrate what impact a non-uniform heat flux condition has, on the thermal performance of a collector tube. True heat flux distributions are highly dependent on the actual geometrical lay-out of a solar collector and falls beyond the scope of this study.

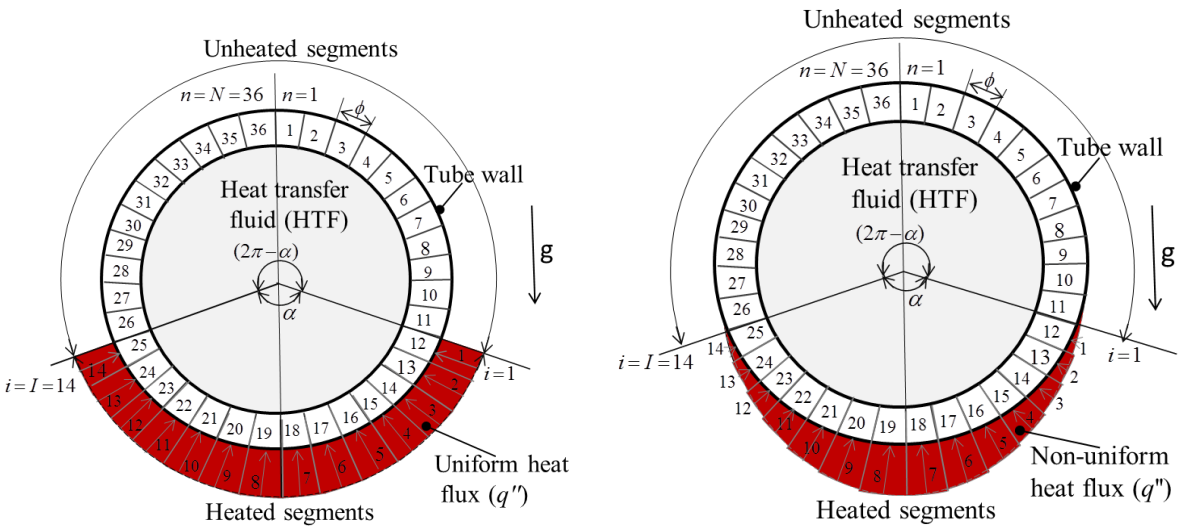

(a) (b)

Fig. 4.2 Cross-section of the tube model in Fig. 4.1with (a) symmetrical partial uniform and (b) non-uniform heat flux distributions boundaries**.**

The symmetrical heat flux distribution boundary occurs when the radiation heat flux from the sun is at the zenith angle position for a collector tube that is oriented in the north-south direction as shown in Fig. 1.3 (a). For the symmetrical partial uniform heat flux case in Fig.4.2 (a), the directly heated portion of the tube model receives uniform heat flux intensity, while the remaining upper portion of the tube receives no incident heat flux. In Fig.4.2 (b), the symmetrical non-uniform heat flux distributions case is such that the lower central portion of the tube model receives maximum amount of heat flux, which decreases upward on both sides of the tube towards the top portion, depending on the collector reflector geometry and the solar position.

Fig. 4.3 shows a cross-sectional view of the tube under the influence of the gravitational field at an alignment angle of γ (°) with respect to the symmetry plane of the heat flux distribution (note the direction of gravity). It represents the asymmetrical non-uniform heat flux distribution case and the numbering system employed for simulating the heat flux distributions around on the tube model. As the sun position changes from east to west during the day, the alignment angle would change. This situation could significantly influence the

heat transfer and friction factor characteristics of the tube due the interactions of the gravity body force with the thermal properties of the heat transfer fluid such as the fluid density.

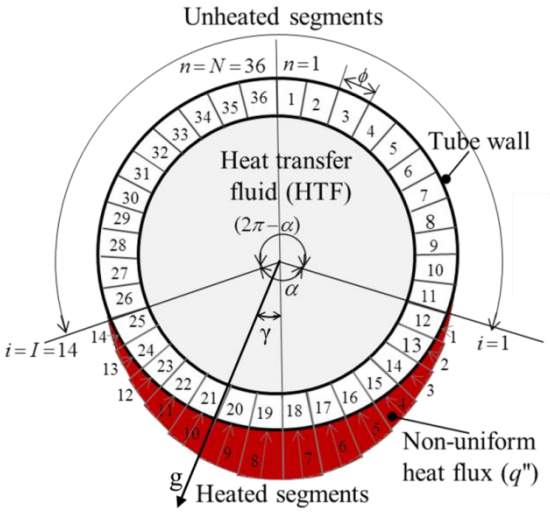

Fig. 4.3 Tube model for asymmetrical non-uniform heat flux boundary with gravity force (g) directed at γ° .

N = 36 is used to piecewise uniformly describe the circumferential heat flux distributions, for the purpose of this study. Each segment subtended an angle span of ϕ defined as:

$$\phi = \frac{2\pi}{N} \tag{4.1}$$

The angle span of the heated (incident) and unirradiated portions of the absorber tube model are α and $2\pi - \alpha$ respectively. Also $n_{i=1}$ is the segment (in a clockwise fashion) where the heat flux distribution starts and can be expressed in terms of α in Eq. (4.2).

$$n_{i=1} = \frac{[N-I]}{2} + 1 \tag{4.2}$$

where $n = 1, 2, 3 \ldots N = 36,$ and $i = 1, 2, 3 \ldots I.$ I is the number of segments of the tube model that are directly heated with the external heat flux (with α being multiples of 20° for this study), expressed in Eq. (4.3).

$$I = \frac{\alpha}{2\pi} N \tag{4.3}$$

4.2 Modeling Methodology and Data Analysis Requirements

This section describes the thermal modelling methodology and the required data analysis needed in this study. Important parameters, non-dimensional numbers and output quantities are defined. First the heat transfer considerations are discussed, followed by the pressure drop considerations and lastly the relevant dimensional numbers.

A generic control volume is needed to assist in the heat transfer data analysis for the inner and outer wall thermal boundary conditions for the absorber tube model as well as the results that are given in the subsequent sections of this study. Fig. 4.4 shows a generic control volume of an element at location (*m, n*) on the tube model in Figs 4.1 and 4.3(a), indicating the heat transfer components and dimensions: L, t and ϕ, in the (x, r, ϕ) coordinate system. A_o and A_i are the external wall surface and the wetted internal wall surface areas of the element.

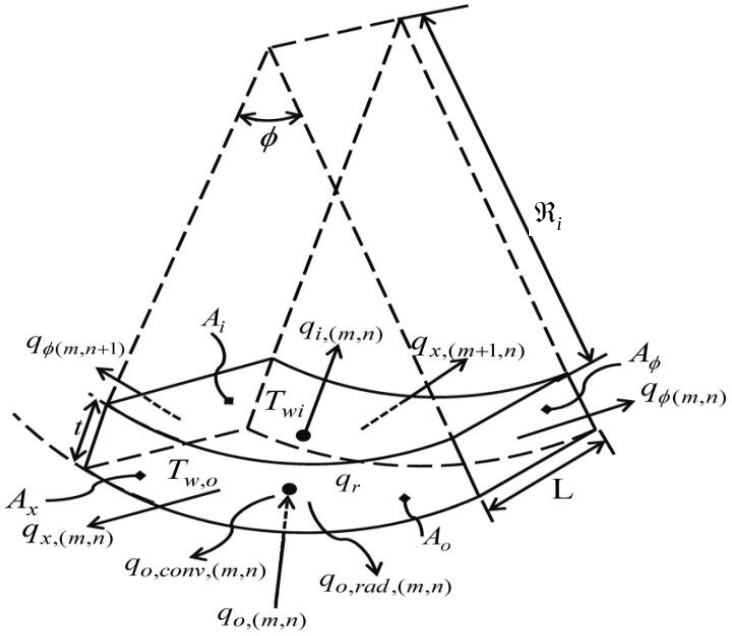

Fig. 4.4 Control volume of the element at location (*m, n*) in Figs 4.1 and 4.3.

By applying the energy balance principle to the element in Fig.4.4, the following can be obtained for steady-state conditions:

$$q_{o,(m,n)} = q_{i,(m,n)} + q_{x,(m,n)} + q_{x,(m+1,n)} + q_{\phi,(m,n)} + q_{\phi,(m,n+1)} + q_{o,conv,(m,n)} + q_{o,rad,(m,n)} \tag{4.4}$$

A brief description of each term (measured in watts) from left to right are given in the paragraphs that follow.

$q_{o,(m,n)}$ is the incident heat transfer rate on the outer wall surface at location (m, n) expressed in Eq. (4.5) as follows:

$$q_{o,(m,n)} = q''_{o,(m,n)} A_{o,(m,n)} \tag{4.5}$$

While $q_{i,(m,n)}$ is the heat transfer rate to the working fluid at location (m, n) which can be expressed as follows:

$$q_{i,(m,n)} = h_{i,(m,n)}.A_{i,(m,n)}(T_{w,i,(m,n)} - T_{b,m}) \tag{4.6}$$

where $h_{i(m,n)}$ is the hypothetical local internal heat transfer coefficient, $A_{i,(m,n)}$ is the inner wall surface area, $T_{wi,(m,n)}$ is the inner wall temperature and $T_{b,m}$ is the fluid bulk temperature at the axial position m defined as:

$$T_{b,m} = T_{b,m-1} + \frac{\sum_{n=1}^{N} q_{i,(m,n)}}{\dot{m} c_P} \tag{4.7}$$

where $\dot{m}$ is the mass flow rate of the heat transfer fluid, c_P is the specific heat of the heat transfer fluid and $T_{b,m\text{-}1}$ is the upstream local bulk fluid temperature. The average internal heat transfer coefficient $\bar{h}_{i,m}$ is related to the average Nusselt number as follows:

$$\overline{Nu}_{i,m} = \frac{\bar{h}_{i,m} D_i}{k_f} \tag{4.8}$$

where $\bar{h}_{i,m}$ is the circumferential average internal heat transfer coefficient at location m:

$$\bar{h}_{i,m} = \frac{\sum_{n=1}^{N} q_{i,(m,n)}}{\pi D_i L(\bar{T}_{w,i,m} - T_{b,m})} \tag{4.9}$$

and where $\bar{T}_{w,i,m}$ is the circumferential average local inner-wall temperature at location m:

$$\overline{T}_{w,i,m} = \frac{1}{N}\sum_{n=1}^{N} T_{w,i,(m,n)} \tag{4.10}$$

The average internal heat transfer coefficient, $\overline{h}_i$ over the full length of the tube model in terms of the overall inner-wall surface temperature, $\overline{T}_{w,i}$ can be expressed as follows:

$$\overline{h}_i = \frac{\sum_{m=1}^{M}\sum_{n=1}^{N} q_{i,(m,n)}}{\pi D_i L_{TOT}\left(\overline{T}_{w,i} - \overline{T}_b\right)} \tag{4.11}$$

Returning to Eq. (4.4), $q_{x,(m,n)}$ and $q_{x,(m+1,n)}$ are the conductive heat transfers in the axial direction, modelled from Fourier's law of heat conduction [134]. Also, in Eq. (4.4) the conductive heat transfers in the tangential direction, $q_{\phi,(m,n)}$ and $q_{\phi,(m,n+1)}$ are also modelled with the Fourier law. $q_{o,conv,(m,n)}$ is the forced-convective heat transfer loss from the outer-wall surface at (m, n) to the surrounding of the tube modeled from Newton's law of cooling [135] as:

$$q_{o,conv,(m,n)} = h_{o,(m,n)} A_o (T_{w,o,(m,n)} - T_{atm}) \tag{4.12}$$

where $T_{w,o,(m,n)}$ is the outer-wall temperature at (m,n), T_{atm} is the ambient free-stream air temperature and $h_{o(m,n)}$ is the external convective heat transfer coefficient.

The last term in Eq. (4.4), $q_{o,rad,(m,n)}$, represents the first order radiative heat transfer loss to the surrounding modelled from the Stefan-Boltzmann law of the emissive power of a surface at a thermodynamic temperature as follows:

$$q_{o,rad,(m,n)} = \varepsilon_{tu}\sigma A_o (T^4_{w,o,(m,n)} - T^4_{\infty}) \tag{4.13}$$

where ε_{tu} is emissivity of the tube model expressed in using the relation mentioned earlier in terms of the tube outer-wall temperature [128] and σ is the Stefan-Boltzmann constant being $5.67\text{x}10^{-8}$ W/m^{2}K^4 [134].

The average overall heat transfer coefficient, U from the surrounding of the collector tube model to the heat transfer fluid in the tube can be expressed as [14]:

$$U = \left[\frac{1}{U_o} + \frac{\Re_o}{\bar{h}_f \Re_i} + \frac{\Re_o}{k_w} \ln\left(\frac{\Re_o}{\Re_i}\right) \right]^{-1} \tag{4.14}$$

where R_i and R_o are the inner and outer radii of the tube, U_o is the external heat loss coefficient due to convective and radiative heat flux losses of the tube. When $T_a = T_\infty$ (as assumed in this study to be 303 K for simplicity reasons), this can be written as:

$$U_o = \bar{h}_{rad} + \bar{h}_o \tag{4.15}$$

where $\bar{h}_o$ is the forced convective heat transfer coefficient due to wind defined in Chapter 3 and $\bar{h}_{rad}$ is the average equivalent radiation heat transfer coefficient from the outer-wall surface of the tube to the surrounding expressed as:

$$\bar{h}_{rad} = \varepsilon_{tu} \sigma_{SB} (\bar{T}_{w,o} + T_\infty)(\bar{T}_{w,o}^2 + T_\infty^2) \tag{4.16}$$

$\bar{T}_{w,o}$ is the average outer-wall temperature of the tube model.

Also, the thermal efficiency (η_{th}) of the tube model can be expressed as follows:

$$\eta_{th} = \frac{\dot{m} c_p (T_{b,M} - T_{b,0})}{\sum_{m=1}^{M} \sum_{n=1}^{N} q_{w,(m,n)}} \tag{4.17}$$

where $T_{b,M}$ is the approximate bulk (averaged) outlet fluid temperature at position $m = M$, and $T_{b,0}$ is the bulk inlet fluid temperature at $x = 0$.

The dimensionless non-uniform tube-wall temperature factor, θ_f for different circumferential position of the tube model is expressed in Eq. (4.18). θ_f is essential for determining the non-uniformity of the tube-wall temperature distributions due to non-uniform circumferential heat flux distributions over the circumferential outer surface of the tube model.

$$\theta_f = \frac{T_{w,o,(n)} - T_b}{\overline{T}_{w,i,(n)} - T_b} \tag{4.18}$$

$$\overline{T}_{w,i,(n)} = \frac{1}{N}\sum_{n=1}^{N} T_{w,i,(m,n)} \tag{4.19}$$

Here $\overline{T}_{w,i,(n)}$ is the local average circumferential inner-wall temperature, $T_{w,o,(n)}$ is the local outer-wall temperature of the tube for segment *n* and T_b is the local bulk fluid temperature of the tube.

The fluid flow through the collector tube model encounters pressure drop due to friction loss at the internal wall boundary of the tube. Thus, forced-convective flow is required through pumping of the fluid to sustain the fluid flow and enhance heat transfer to the fluid. The pumping power, $\dot{P}$, required for overcoming the pressure drop in the tube and turbulent dissipation is expressed as:

$$\dot{P} = \frac{\dot{m}}{\rho_o}\Delta p \tag{4.20}$$

where ρ_o is the constant density of the fluid, ṁ is the mass flow rate and Δp is the pressure drop along the tube length (L_{TOT}) is expressed [134] as:

$$\Delta p = f\frac{L_{TOT}}{D_i}\frac{\rho_o \bar{v}^2}{2} \tag{4.21}$$

where $\bar{v}$ is the mean fluid velocity and *f* is the friction factor. For laminar flow case in a circular tube, the friction factor of the Poiseuille law for laminar flow is expressed [134]as:

$$f = \frac{64}{\mathrm{Re}} \tag{4.22}$$

The temperature dependent density, ρ, of the heat transfer fluid is defined based on Boussinesq approximation [134] expressed as:

$$\rho = \rho_o(1 - \beta\Delta T) \tag{4.23}$$

where ρ_o is the constant density, β is the thermal expansion coefficient of the heat transfer fluid at constant pressure, ρ_o is the base density at the reference temperature of 300 K and ΔT is the temperature difference between the average inner wall temperature and the bulk fluid temperature.

The important dimensionless parameters for investigating the mixed natural and forced-convection heat transfer for the tube model considered in this study are the Grashof number, *Gr*, Reynolds number, Re, Prandlt number, Pr, and Richardson number, Ri, [134, 136]:

$$Gr_{q''} = g\beta(2\Re_i)^3 \Delta T V^{-2} \tag{4.24}$$

$$\mathrm{Re} = 2\Re_i \rho v / \mu \tag{4.25}$$

$$\mathrm{Pr} = c_p \mu / k \tag{4.26}$$

Here ΔT is the temperature difference between the average values of the inner tube-wall temperature and the bulk fluid temperature over the tube length and V represents the kinematic viscosity evaluated at the bulk fluid temperature and μ is the dynamic viscosity of the heat transfer fluid.

The Richardson number (*Ri*)) indicates the relative strength of the natural convection due to buoyancy-induced secondary flow resulting from the circumferential non-uniform heating to forced- convection heat transfer in the absorber tube model.

$$\mathrm{Ri} = \frac{\mathrm{Gr}}{\mathrm{Re}^2} \tag{4.27}$$

If R*i* *>10,* forced-convection is considered negligible and if Ri < *0.1*, natural convection is negligible. If *0.1*< Ri *<10*, the heat transfer is considered as mixed convection [136].

The values for $\bar{h}_{i,m}$, $\bar{h}_i$ and $\bar{T}_{wo}$ in eqns. (4.9), (4.11) and (4.16) along with the friction factors and the dimensionless numbers were determined from the results of numerical simulations implemented in ANSYS Fluent version 14.0 [137], for fully uniform heat flux boundary and for different circumferential spans of symmetrical (gravity directed at $\gamma = 0°$) non-uniform heat flux distribution boundary conditions. The values are also determined for different

circumferential spans of asymmetrical (gravity directed at γ = 20°, 30° and 40°) non-uniform heat flux distributions boundaries.

4.3 Governing Equations

The fluid flow is assumed incompressible, steady-state and laminar or turbulent flow. The equations governing for the fluid flow through the tube are the continuity, momentum and energy equations and the *k-ε* two-equation turbulent model equations [138, 139]. These equations in cylindrical coordinates (r, ϕ, x) are expressed as follows:

Continuity equation:

$$\frac{1}{r}\frac{\partial(rv_r)}{\partial r}+\frac{1}{r}\frac{\partial v_\phi}{\partial \phi}+\frac{\partial v_x}{\partial x}=0 \tag{4.28}$$

where v_r, v_ϕ and v_x are the radial, polar and axial velocity components respectively.

Momentum equations:

r-momentum:

$$\rho\left(v_r\frac{\partial v_r}{\partial r}+\frac{v_\phi}{r}\frac{\partial v_r}{\partial \phi}+v_x\frac{\partial v_x}{\partial x}-\frac{v_\phi^2}{r}\right)=-\frac{\partial p}{\partial r}+\mu_{ef}\left[\nabla^2 v_r-\frac{v_r}{r^2}-\frac{2}{r^2}\frac{\partial v_\phi}{\partial \phi}\right]+\rho g_r \tag{4.29}$$

ϕ-momentum:

$$\rho\left(v_r\frac{\partial v_\phi}{\partial r}+\frac{v_\phi}{r}\frac{\partial v_\phi}{\partial \phi}+v_x\frac{\partial v_\phi}{\partial x}-\frac{v_r v_\phi}{r}\right)=-\frac{1}{r}\frac{\partial p}{\partial \phi}+\mu_{ef}\left[\nabla^2 v_\phi-\frac{v_\phi}{r^2}+\frac{2}{r^2}\frac{\partial v_r}{\partial \phi}\right]+\rho g_\phi \tag{4.30}$$

x-momentum:

$$\rho\left(v_r\frac{\partial v_x}{\partial r}+\frac{v_\phi}{r}\frac{\partial v_x}{\partial \phi}+v_x\frac{\partial v_x}{\partial x}\right)=-\frac{\partial p}{\partial x}+\mu_{ef}\nabla^2 v_x+\rho g_x \tag{4.31}$$

where $\nabla^2 \equiv \frac{1}{r}\frac{\partial}{\partial r}\left(r\frac{\partial}{\partial r}\right)+\frac{1}{r^2}\frac{\partial^2}{\partial \phi^2}+\frac{\partial^2}{\partial x^2}$ and μ_{ef} is the total effective viscosity of the flow defined as:

$$\mu_{ef} = \mu_l + \mu_{ed} \tag{4.32}$$

μ_l is the laminar viscosity and μ_{ed} is the turbulent eddy viscosity defined as:

$$\mu_{ef} = \rho C_\mu \frac{k^2}{\varepsilon} \tag{4.33}$$

Here C_μ is an empirical turbulent constant, ε is the turbulent energy dissipation, and $\vec{g}$ is acceleration due gravity vector. The density term in the computational domain was assumed constant except in the body force term of the momentum equation. As mentioned earlier, the Boussinesq approximation was employed to account for the density variation as a function of temperature.

Energy Equation:

$$\frac{1}{r}\frac{\partial}{\partial r}(\rho r v_r T) + \frac{1}{r}\frac{\partial}{\partial \phi}(\rho v_\phi T) + \frac{\partial}{\partial x}(\rho v_x T) = \frac{1}{r}\frac{\partial}{\partial r}\left(r(\mu_l + \frac{\mu_{ed}}{\sigma_{ed}})\frac{\partial T}{\partial r}\right) + \frac{1}{r}\frac{\partial}{\partial \phi}\left(\frac{1}{r}(\mu_l + \frac{\mu_{ed}}{\sigma_{ed}})\frac{\partial T}{\partial \phi}\right) + \frac{\partial}{\partial x}\left((\mu_l + \frac{\mu_{ed}}{\sigma_{ed}})\frac{\partial T}{\partial x}\right) \tag{4.34}$$

Turbulence model equation:

For laminar flow computation, the turbulent eddy viscosity is zero. For turbulent flow the *k*-ε two-equation turbulence model obtained from the Navier-Stokes equation [139] was used. The *k*-ε two-equation turbulence model is expressed as follows:

***k*-equation turbulence model**

$$\frac{1}{r}\frac{\partial}{\partial r}(\rho r v_r \kappa) + \frac{1}{r}\frac{\partial}{\partial \phi}(\rho v_\phi \kappa) + \frac{\partial}{\partial x}(\rho v_x \kappa) = \frac{1}{r}\frac{\partial}{\partial r}\left(r(\mu_l + \frac{\mu_{ed}}{\sigma_\kappa})\frac{\partial \kappa}{\partial r}\right) + \frac{1}{r}\frac{\partial}{\partial \phi}\left(\frac{1}{r}(\mu_l + \frac{\mu_{ed}}{\sigma_\kappa})\frac{\partial \kappa}{\partial \phi}\right) + \frac{\partial}{\partial x}\left((\mu_l + \frac{\mu_{ed}}{\sigma_\kappa})\frac{\partial \kappa}{\partial x}\right) - \rho\varepsilon + G_k + G_B \tag{4.35}$$

ε -equation turbulence model

$$\frac{1}{r}\frac{\partial}{\partial r}(\rho r v_r \varepsilon)+\frac{1}{r}\frac{\partial}{\partial \phi}(\rho v_\phi \varepsilon)+\frac{\partial}{\partial x}(\rho v_x \varepsilon)=\frac{1}{r}\frac{\partial}{\partial r}\left(r(\mu_l+\frac{\mu_{ed}}{\sigma_\varepsilon})\frac{\partial \varepsilon}{\partial r}\right)+$$
$$\frac{1}{r}\frac{\partial}{\partial \phi}\left(\frac{1}{r}(\mu_l+\frac{\mu_{ed}}{\sigma_\varepsilon})\frac{\partial \varepsilon}{\partial \phi}\right)+\frac{\partial}{\partial x}\left((\mu_l+\frac{\mu_{ed}}{\sigma_\varepsilon})\frac{\partial \varepsilon}{\partial x}\right)-C_2\rho\frac{\varepsilon^2}{k}+C_1\frac{\varepsilon}{k}(G_k+C_3G_B) \quad (4.36)$$

where C_μ, C_1, C_2, σ_k, σ_ε and σ_{ed} are the empirical turbulent constant [138 140] given as C_μ = 0.09, C_1 = 1.43, C_2 =1.92, σ_k =1.0, σ_ε =1.3 and σ_{ed} = 0.9. G_B is the turbulent kinetic energy generation due to buoyancy [138, 141].

The production term, G_k which represents the kinetic energy transfer from the mean flow to the turbulent motion through the interaction between the turbulent fluctuations and the mean flow velocity gradients is given by [139] as:

$$G_k=\mu_{ed}\left\{\left(\frac{\partial v_x}{\partial r}+\frac{\partial v_r}{\partial x}\right)^2+\left(\frac{\partial v_\phi}{\partial x}+\frac{1}{r}\frac{\partial v_x}{\partial \phi}\right)^2+\left(\frac{1}{r}\frac{\partial v_r}{\partial \phi}+\frac{\partial v_\phi}{\partial x}-\frac{v_\phi}{r}\right)^2+\right.$$
$$\left.2\left[\left(\frac{\partial v_r}{\partial r}\right)^2+\left(\frac{1}{r}\frac{\partial v_\phi}{\partial \phi}+\frac{v_r}{r}\right)^2+\left(\frac{\partial v_x}{\partial x}\right)^2\right]\right\} \quad (4.37)$$

By reduction to a general convection-diffusion equation in cylindrical coordinates is obtained and then solved numerically.

$$\frac{1}{r}\frac{\partial(\rho r v_r \varphi)}{\partial r}+\frac{1}{r}\frac{\partial(\rho v_\phi \varphi)}{\partial \phi}+\frac{\partial(\rho v_x \varphi)}{\partial x}=\Gamma_\varphi\nabla^2\varphi+S_\varphi$$
$$=\Gamma_\varphi\left[\frac{1}{r}\frac{\partial}{\partial r}\left(r\frac{\partial \varphi}{\partial r}\right)+\frac{1}{r^2}\frac{\partial^2\varphi}{\partial \phi^2}+\frac{\partial^2\varphi}{\partial x^2}\right]+S_\varphi \quad (4.38)$$

The diffusion coefficient, Γ_φ corresponding to the conservation variable φ (i.e. mass, momentum and energy conservations) and S_φ is the source term are given in Table 4.2.

Table 4. 2 Convection-diffusion equation variables

Equation	φ	Γ_φ	S_φ
Continuity	1	0	0
r-momentum	v_r	μ_{ef}	$-\frac{\partial p}{\partial r}+\mu_{ef}\left[-\frac{v_r}{r^2}-\frac{2}{r^2}\frac{\partial v_\phi}{\partial \phi}\right]+\frac{v_\phi}{r}+g_r\beta$
ϕ-momentum	v_ϕ	μ_{ef}	$-\frac{1}{r}\frac{\partial p}{\partial \phi}+\mu_{ef}\left[-\frac{v_\phi}{r^2}+\frac{2}{r^2}\frac{\partial v_r}{\partial \phi}\right]-\frac{v_\phi v_r}{r}+g_\phi\beta$
z-momentum	v_x	μ_{ef}	$-\frac{\partial p}{\partial r}+g_z\beta$
Energy	T_{iw}	$\mu_l+\frac{\mu_{ed}}{\sigma_{ed}}$	0
k - turbulence	k	$\mu_l+\frac{\mu_{ed}}{\sigma_k}$	$-\rho\varepsilon+G_k+G_B$
ε - turbulence	ε	$\mu_l+\frac{\mu_{ed}}{\sigma_\varepsilon}$	$-C_2\rho\frac{\varepsilon^2}{k}+C_1\frac{\varepsilon}{k}(G_k+C_3G_B)$

4.4 Boundary Conditions and Material Properties

4.4.1 Boundary Conditions

The boundary conditions applied for the domain model are as follows:

- *Inlet boundary conditions* (x = 0):

A uniform inlet velocity was used (uniform mass flux because the fluid is incompressible), since in practice the flows in pipes rarely have fully developed velocity distributions at the inlet. Unless stated otherwise, all variables were initiated with uniform values. The uniform values are based on the case under consideration:

$$\dot{m}_r = \dot{m}_\phi = 0.006 \text{ kg/s} - 10 \text{ kg/s and } \dot{m}_x = \text{uniform} \tag{4.39}$$

The inlet Reynolds number ranges of 130 to 2200 and 3030 to 220600 are considered in order to account for the impacts of buoyancy effects and mixed convective heat transfer in the laminar and weak turbulent flow regimes for the heat flux boundary conditions considered.

Fluid inlet temperature range:

$$T_f(\phi, r) = T_{b,0} = 300 \text{ K to } 360 \text{ K} \tag{4.40}$$

This inlet fluid temperature range accounts for the impact the inlet fluid temperature rise has on the thermal performance of a solar collector tube for the heat flux boundary conditions considered.

The turbulence variables at the inlet and outlet of the tube model are applied using an empirical relation for the turbulence intensity, *I* [137] expressed in Eq. (4.41):

$$I \equiv \frac{\sqrt{\frac{2}{3}k}}{\bar{v}_{avg}} \cong \frac{0.16}{\text{Re}^{\frac{1}{8}}} \tag{4.41}$$

- *Outlet boundary conditions* ($x = L_{TOT}$):

A zero pressure gradient condition was applied across the outlet boundary, and the outlet pressure was set as follows:

$$P(\phi, r) = P_o \tag{4.42}$$

- *Tube model inner-wall surface boundary condition*($r = \Re_i$):

No-slip conditions are applied at inside wall surface of the tube:

$$v_r = v_\phi = v_x = 0 \tag{4.43}$$

- *Near-wall flow boundary condition*:

The k-ε two-equation turbulence model cannot be applied in the regions close to the solid boundary where viscous effects are dominant over turbulence [140]. The two methods usually employed in solving the near-wall region flow problems are the low Reynolds number modelling and wall function method. The standard wall function in ANSYS Fluent [137] was adopted for solving the near-wall region flow in the tube inner-wall.

- *External wall surface boundary conditions* ($r = \Re_o$):

The external wall surface incident boundary heat flux cases considered are expressed in terms of the concentrated base-level heat flux, q'' in Table 4.3.

Table 4.3 External surface heat transfer distribution types.

Heat flux distribution type		**Outer wall incident heat flux**	**Wall element range**
Sinusoidal non uniform heat flux cases:	Heated segment:	$q''_{o,(m,n)} = q'' \sin\left[\frac{\pi}{\alpha}\phi(n - n_{i=1} + \frac{1}{2})\right]$	$m \in [1, M]$ and $n \in [n_{i=1}, n_{i=1} + I)$
	Unheated segment:	$q''_{o,(m,n)} = 0$	$m \in [1, M]$ and $n \notin [n_{i=1}, n_{i=1} + I)$
Partial uniform heat flux cases:	Heated segment:	$q''_{o,(m,n)} = q'' \frac{2}{\pi}$	$m \in [1, M]$ and $n \in [n_{i=1}, n_{i=1} + I)$
	Unheated segment:	$q''_{o,(m,n)} = 0$	$m \in [1, M]$ and $n \notin [n_{i=1}, n_{i=1} + I)$
Associated fully uniform heat flux cases:	All segments:	$q''_{o.(m,n)} = q'' \frac{\alpha}{\pi^2}$	$m \in [1, M]$ and $n \in [1, N]$

q'' represents the irradiation heat flux intensity incident on an absorber tube model from a linear focusing solar collector reflector field. For a uniform heat flux boundary in Fig. 4.5 (a), uniform incident heat flux intensity is applied on all the segments of the tube model. In Fig. 4.6, by contrast, the non-uniform heat flux distribution boundary on the tube model is such that the lower central portion of the tube receives the maximum heat flux, which decreases upward on both sides of the tube to the top portion. Fig 4.6 (b) indicates the asymmetrical case for the non-uniform heat flux distributions boundary in terms of gravitational field, which occurs where the solar radiation has deviated from the zenith angle position as represented in Fig. 1.3. Heat flux base-level intensities of q'' = 7.1 kW/m^2, 14.2 kW/m^2 and 21.3 kW/m^2 were used in this study for indicative purposes. This base-level intensity would depend on the concentration factor of the linear solar collector and the applicable solar radiation level. Unless stated otherwise, the results shown are for 7.1 kW/m^2.

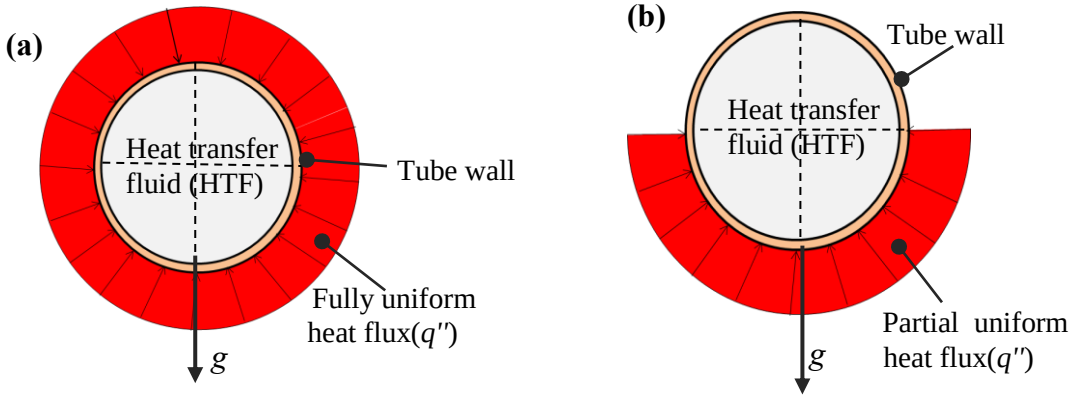

Fig. 4.5 (a) Fully uniform and (b) partial uniform heat flux distributions boundaries.

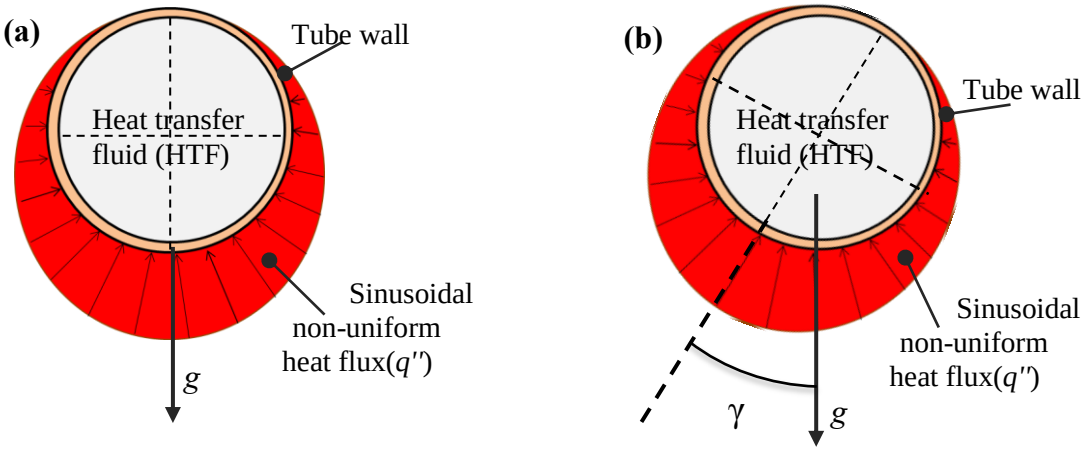

Fig. 4.6 (a) Symmetrical and (b) asymmetrical non-uniform heat flux distributions boundaries.

The choice of using a sinusoidal distribution is loosely based on the ray-tracing results by Wirz et al. [142] which indicated higher heat flux intensity distributions on the lower portion and very low in the upper portion of the collector absorber tube. In a ray-tracing investigation conducted by He *et al*. [17] it was shown that the heat flux distribution is dependent on a number of parameters including the reflector rim angle and that in some cases there is a shadow effect due to the presence of the collector tube itself while in other cases there is no shadow effect. Those cases without the shadow effect are represented here by a sinusoidal

distribution. Specific heat flux distributions can be obtained from direct ray-tracing of heat flux distribution, but are not incorporated into this study and this could be investigated separately.

The external wall heat flux distribution boundaries in Table 4.3 and the convective and radiative heat losses in Eqs (4.12) and (4.13) were implemented according to the angular position of the boundary cell via user-defined functions of the ANSYS Fluent code. Unless indicated otherwise, an ambient and surrounding temperature of $T_{atm} = T_{\infty} = 303$ K were used.

4.4.2 Fluid and Tube Material Properties

General material properties for the fluid and tube are supplied in Table 4.4. The thermal properties of the tube material were considered independent of temperature and fluid density (ρ) and viscosity (μ) vary with temperature.

Table 4.4 Properties of the heat transfer fluid and tube material

Property	Heat transfer fluid (HTF) (water)	Stainless steel tube wall
Density (ρ_o)[kg/m^3]	998.2	8030
Specific heat capacity[J/kgK]	4182	502.48
Thermal conductivity [W/mK]	0.61	16.27
HTF temperature [°C]	27	-
Dynamic viscosity (μ) [kg/ms]	0.000844	-
Coefficient of cubic expansion (β)[K^{-1}]	0.0002705	-
Prandtl number (Pr) [-]	5.8	-

4.5. Numerical Solution Procedure

A three dimensional steady-state numerical simulation for the present study is implemented in ANSYS Fluent version 14.0 [137], for laminar and turbulent flow regimes. ANSYS Fluent CFD package is based on finite volume method. ANSYS Fluent is capable of handling a wide range of fluid flow and heat transfer problems, including incompressible and compressible flows, laminar and turbulent flows, single-phase and multi-phase flows etc. and also performs both steady-state and transient analyses. It uses two kinds of solvers –

pressure–based and density–based solvers. The pressure–based solver is employed in this study. This solver is applicable for a wide range of fluid flow regimes and it allows flexibility in the solution procedure. The governing equations were solved numerically as implemented in ANSYS Fluent based on the finite volume method described by Patankar [143], Ferziger and Perifi [144] and Versteeg and Malalasekera [145]. The computational domain, which consists of the tube model and the heat transfer fluid inside the tube, was meshed with Hex8 cells and Wed6 cells structures by using the grid generation tool of the ANSYS Workbench. Hexahedral mesh structures give the highest solution accuracy, while triangular prism mesh structures resolve the boundary layers very efficiently [137]. The convective terms in the momentum and energy equations are discretised and solved using a second-order upwind scheme to obtain more accurate results and the standard SIMPLEC algorithm was used for the pressure-velocity coupling. The k-ε model is employed for the turbulent flow and standard wall function was adopted in resolving the near-wall regions flow problem. The boundary conditions and material properties in ANSYS Fluent were modified to suit the case for the present study. The heat flux boundary conditions in Table 4.3 were applied according to the angular position of the boundary cell via user defined functions. For the pressure-based solver employed in this study, the decrease in the residual values to 10^{-3} for continuity and momentum equations and to 10^{-6} for energy equation is generally the least qualitative convergence. The convergence criteria for the continuity, momentum and energy equations were set such that the maximum residual values had to be less than 10^{-7} and 10^{-8} respectively.

4.6 Conclusion

In this chapter, the domain description, modeling methodology and the numerical procedures were presented. The heat transfer model considered circumferential heat flux distributions boundary, heat conduction through the tube wall, heat transferred to the working fluid and the thermal losses via convection and radiation. Uniform heat flux distribution, symmetrical and asymmetrical non-uniform heat flux distributions boundaries were described. In the next chapters the thermal and pressure drop performance of different tubes under different flow scenarios and thermal boundary conditions will be presented.

CHAPTER FIVE: NUMERICAL MODEL VALIDATIONS

5.0 Introduction

This chapter focuses on the grid analysis and model validations to ensure correctness of the simulation results obtained with the tube model. The model validations are conducted by comparing the numerical simulation results with some analytical expressions, empirical correlations for laminar and turbulent flow conditions, and experimental tests results published by other researchers.

5.1 Grid Analysis of the Domain Model

A series of grid independence studies was conducted in terms of the outlet temperature rise of the heat transfer fluid for the laminar flow regime at an inlet Reynolds number range of 130 to 2200 and turbulent flow regime at an inlet Reynolds number range of 3030 to 202600. Fig. 5.1 shows an example of the computational domain used for the grid analysis, meshed with Hex8 and Wed6 grid structures, created with the advance size function grid generation tool of the ANSYS Workbench [137]. The Hex8 cells consist of hexahedron element with 8 vertices, 12 edges and bounded by 6 quadrilateral faces and Wed6 cells consist of triangular prism element with 6 vertices, 9 edges, bounded by 2 triangular and 3 quadrilateral face structures. The number of nodes generated is 163423.

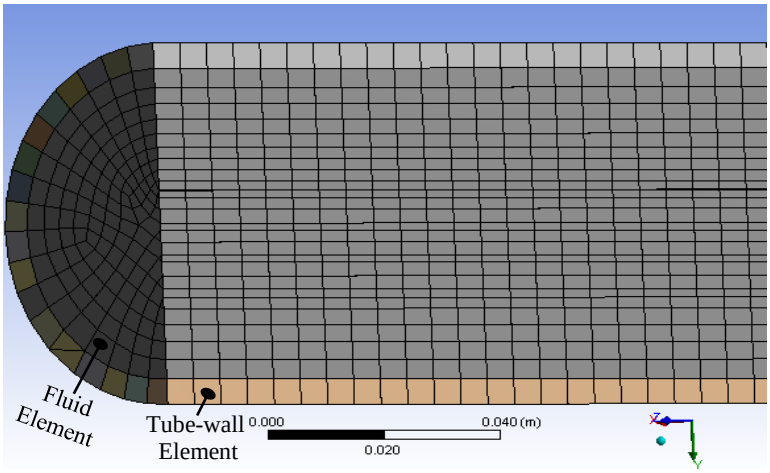

Fig. 5.1Cross section of the computational domain meshed with Hex8 and Wed6 grid structures.

The grid refinement close the wall boundary was handled by addition of inflation layer at the inner tube-wall boundary and this was program controlled during the simulations. It was ensured that the grid is sufficiently fine in order not to have a significant effect on the numerical simulation results. As earlier stated, the hexahedral mesh structures give the highest solution accuracy and triangular prism mesh structures resolve the boundary layers very efficiently [137]. The y^+ produced for the turbulent flow case is 39 and the k-epsilon standard wall function employed in this study requires y^+ between 30 and 60. The y^+ is expressed in Eq. 5.1 as follows:

$$y^+ = \frac{y}{\mu}\sqrt{\rho\tau_w} \tag{5.1}$$

Where y is the distance from the wall to the cell centre, μ is the fluid viscosity, ρ is the fluid density and τ_w is the wall shear stress [137].

For demonstration purposes, the grid refinement test results conducted at an inlet Reynolds number of 202 for laminar flow case and a Reynolds number of 12000 for the case of turbulent flow, for α = 360° uniform heat flux distribution are presented in Tables 5.1 and 5.2. Also, energy balance checks of the heat transfer model were performed of the resultant heat flux distributions on the tube model, which gave an average percentage error of < 1% of the resultant heat flux distributions.

Table 5.1 Grid refinement test results for a laminar flow condition

Number of numerical cells	Bulk fluid outlet temperature (K)	Change in outlet temperature due to refinement
145688	397.4844	-
465854	397.3815	0.102
481327	397.3763	0.005
508028	397.3747	0.002
525147	397.3648	0.009
540108	397.3563	0.008

Table 5.2 Grid refinement test results for a turbulent flow condition

Number of numerical cells	Bulk fluid outlet temperature (K)	Change in outlet temperature due to refinement
145688	306.1629	-
327000	306.1656	0.0027
436218	306.1666	0.001
585117	306.1657	0.0009
652000	306.1653	0.0004

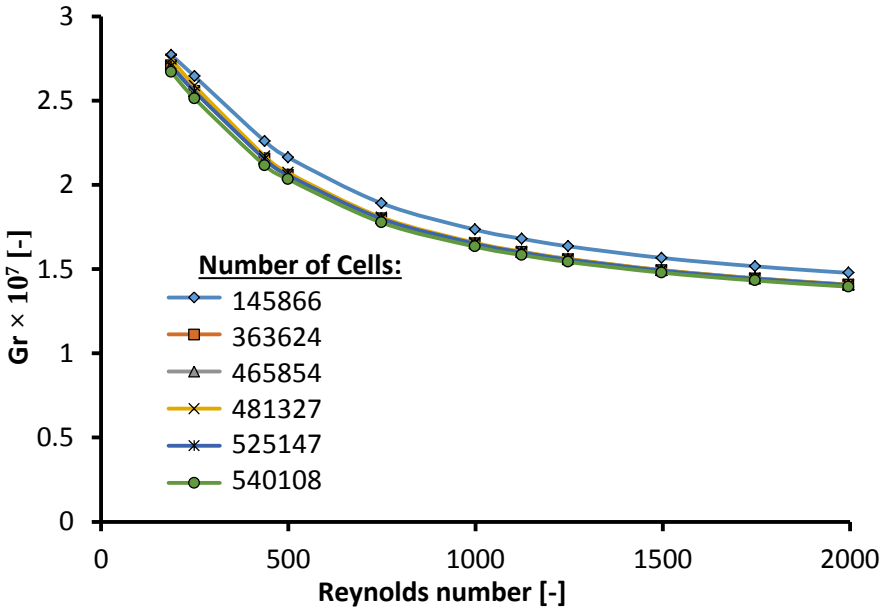

Fig. 5.2 Grid independence study in terms of Grashof (Gr) number

Grashof number (Gr) is an important governing parameter in mixed convection flows. Thus, a grid dependence study in terms of the Grashof number is presented in Fig.5.2 for inlet Reynolds number range of 130 to 2000, indicating insignificant effect of the grid cells on the buoyancy driven flow as the grid cells were refined by increasing the number of cells from 145 866 to 540 108 cells.

5.2 Model Validation with Analytical Expressions

In this section, the axial local Nusselt number determined from the simulation results for α = 360° span of uniform heat flux at the inlet Reynolds number of 202, when the fluid density is independent of temperature is compared with the analytical expression, $Nu_D = 4.36$. Fig. 5.3 shows the results for the axial local Nusselt number obtained for the numerical simulation for α = 360° span of circumferential uniform heat flux distribution base-level intensity of 7.1 kW/m^2, compared with that of the analytical expressions. The axial local Nusselt number values for the numerical model are in good agreement with the analytical expressions and has a deviation of 7% in terms of Nu = 4.36, at $Gz^{-1} \approx 0.0828$, as the flow becomes more fully developed towards the exit of the tube and decreased to 4% at $Gz^{-1} \approx 0.128$.

The model is also validated by comparing the friction factor obtained from the numerical results for α = 360° span of uniform heat flux case and that of the Poiseuille law for laminar flow in Eq. (3.17) for an inlet Reynolds number range of 130 to 2000. Fig.5.4 shows the results for the friction factor determined from the numerical model, compared with the friction factor for the analytical expression, $f = 64/\mathrm{Re}$.

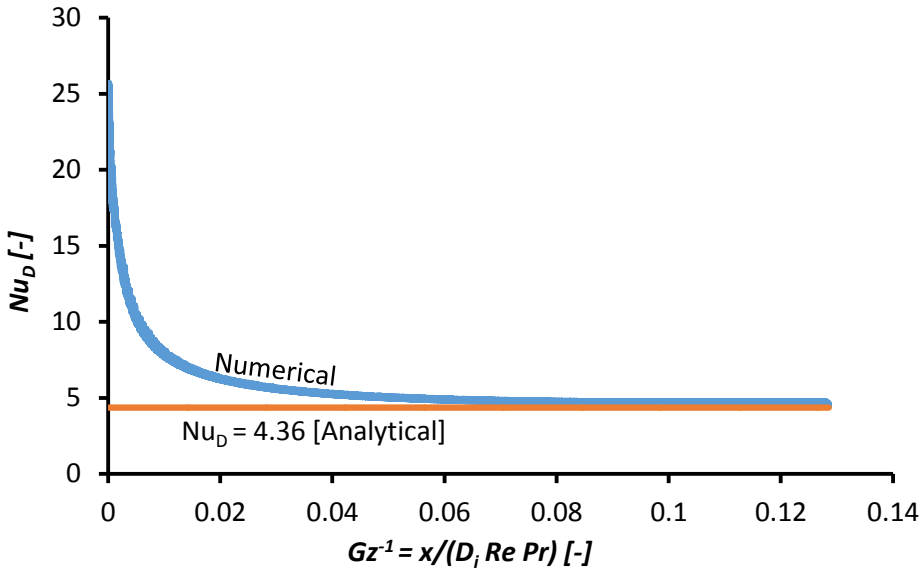

Fig. 5.3 Axial local Nusselt number for numerical and analytical expression an inlet Reynolds number of 202

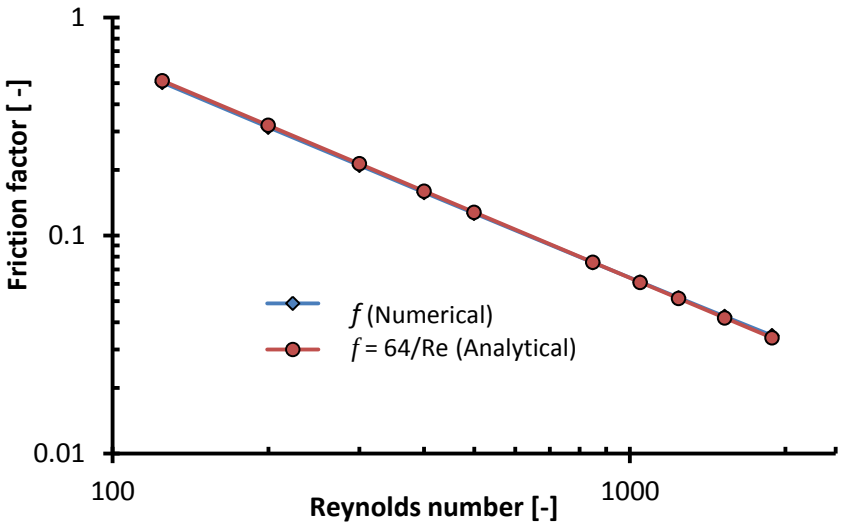

Fig. 5.4 Friction factors for analytical and numerical results

The friction factor for the numerical model gave an average deviation of 2% in terms of $f = 64/\mathrm{Re}$. Fig 5.4 shows that the friction factor obtained from the numerical model is in good agreement with the analytical expressions.

5.3 Model Validation with Experimental Correlations

The model is further validated for verifying the case of an absorber tube with buoyancy driven secondary flow by comparing the calculated axial local Nusselt number with results and correlations published by other researchers. These include the Shah correlation [146] in Eq. (5.2) and an experimental correlation [147] in Eq. (5.3) developed for the laminar flow heat transfer under uniform heat flux boundary conditions, although not basically for mixed convection laminar flow. Eqs. (5.2) and (5.3) are also limited to thermally developing condition (for uniform wall heat flux boundary conditions) and fully developed flow rarely occurs in practical applications.

$$Nu(x) = 1.953\left(\mathrm{Re}_{D_i}\,\mathrm{Pr}\frac{D_i}{x}\right)^{1/3} \quad \text{for} \quad \mathrm{Re}_{D_i}\,\mathrm{Pr}\frac{D_i}{x} \geq 33.3 \tag{5.2}$$

$$Nu(x) = \left[4.364^3 + 1 + \left(2.117\left(\mathrm{Re}_{D_i}\,\mathrm{Pr}\frac{D_i}{x}\right)^{1/3} - 0.6\right)^3\right]^{1/3} \tag{5.3}$$

Here Re_{Di} is based on the inner diameter of the tube: $\mathrm{Re}_{D_i} = \rho \bar{v} D_i / \mu$. The governing parameters include Nusselt number ($Nu_{(x)}$), Reynolds number (*Re*), Prandtl number (*Pr*), tube inner diameter of D_i is 62.7 mm, wall thickness of *t* is 5.1 mm, length-to-inner diameter ratio (L_{TOT} /D_i) of approximately 160 and a base-level uniform heat flux intensity of 7.1 kW/m^2. However, a perfect reproduction of the actual experimental thermal boundary conditions is difficult since detailed information about the actual experimental conditis not readily available. Fig. 5.5 shows the calculated axial local Nusselt numbers with buoyancy driven secondary flow compared with the Nusselt number correlations in Eqs (5.1) and (5.2) for an inlet Reynolds number of 800. It shows that the axial local Nusselt number results obtained from the numerical are in good agreement with the correlations and that the same trends were obtained.

For the mass flow rate shown at $Gz^{-1} \approx 0.00625$ for instance, the numerical results have a deviation of 15% in terms of Eq. (5.1) and 18% in terms of Eq. (5.2), while at $Gz^{-1} \approx 0.0472$ these deviations are 3% and 10% respectively as the flow, became more developed down the tube length.

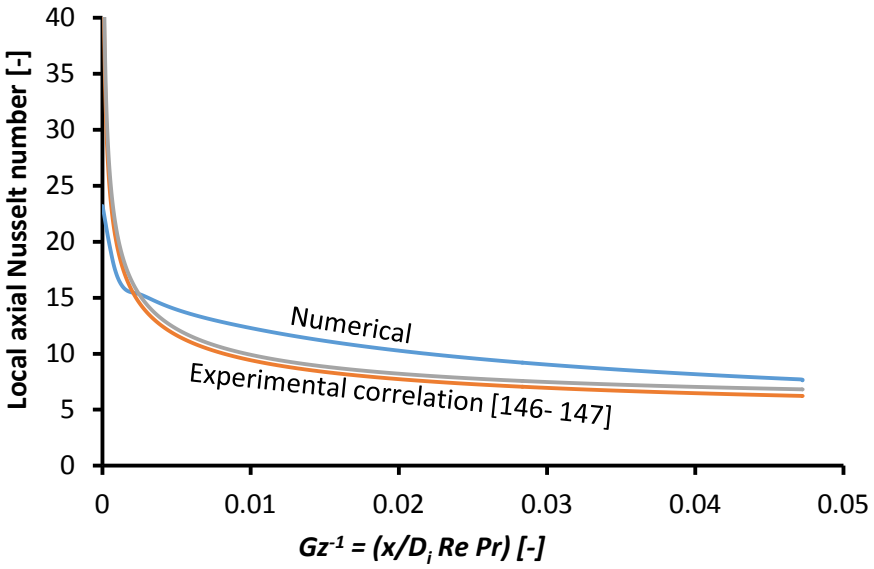

Fig. 5.5 Axial local Nusselt number for numerical and experimental correlations an inlet Reynolds number of 800

These differences could be due to mismatched thermal boundary conditions used for the correlations and this study, and also due to the buoyancy effects which we will show in this study is dependent on the wall thermal boundary conditions, as is also allured to by Ghajar and Tam [103]. Note that these correlations do not yet take into consideration the impact of asymmetric non-uniform heat flux conditions.

Fig. 5.6 compares the friction factor obtained from the numerical results for a α = 360° span of uniform heat flux distribution; when density of the fluid is temperature dependent with the friction factor correlation for laminar flow mixed convection [147]. The friction factor values for the model is also in good agreement with that of the friction factor correlation and has an average deviation of 3.7% in terms of the correlation.

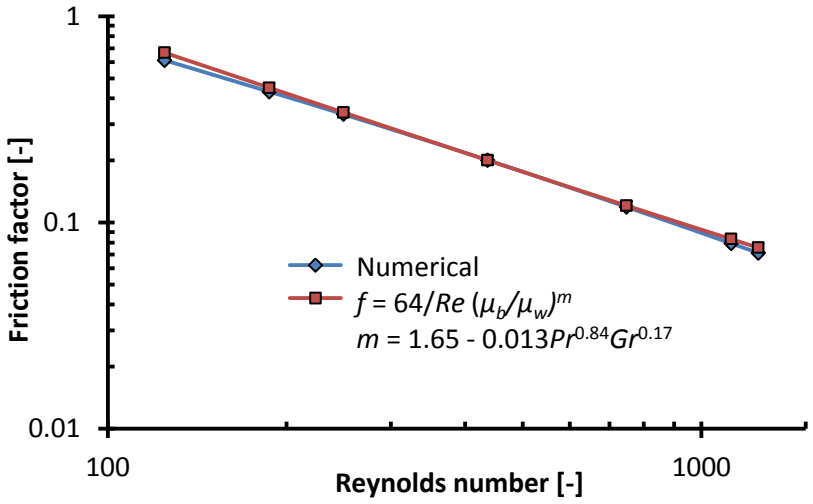

Fig. 5.6 Friction factors for numerical results and experimental correlation with secondary flow effects

The model is further validated by comparing the Nusselt number determined from the simulation results for α = 360° span of uniform heat flux and the Nusselt number correlations presented in Table 5.3 in terms of the friction factor, *f*, Reynolds number, *Re*, and Prandtl number, *Pr*, for turbulent flow in circular tubes, when density of the fluid is considered independent of temperature.

Fig. 5.7 shows the Nusselt number values obtained from the numerical simulation for a 360° span of uniform heat flux distribution, compared with the Nusselt number correlations presented in Table 5.3. The Nusselt number correlation by Dittus-Boeter and Sieder-Tate has the maximum relative errors of + 25% and – 40% (where + means over predicted errors and - means under predicted errors) in the range of $0.67 \leq Pr < 100$. However, the more accurate ones are the Petukhov and Gneilinski correlations with 6% in the range of $0.5 \leq Pr < 200$ and 10% accuracy in the range of $200 \leq Pr < 2000$ [148].

Table 5.3 Standard empirical correlations of Nusselt numbers and friction factors [134]

Gnielinski correlation	$\overline{Nu}_i = \dfrac{\left(\frac{f}{8}\right)(\mathrm{Re}-1000)\mathrm{Pr}}{1+12.7\left(f/8\right)^{0.5}\left(\mathrm{Pr}^{2/3}-1\right)}$ $f = (0.790\ln\mathrm{Re}-1.64)^{-2}$	$\begin{pmatrix} 0.5 \leq \mathrm{Pr} \leq 2000 \\ 3\times10^3 < \mathrm{Re} < 5\times10^6 \end{pmatrix}$ $(10^4 < \mathrm{Re} < 10^6)$
Sieder-Tate correlation	$\overline{Nu}_i = 0.027\mathrm{Re}^{4/5}\,\mathrm{Pr}^{1/3}\left(\dfrac{\mu_b}{\mu_w}\right)^{0.14}$	$\begin{pmatrix} 0.7 \leq \mathrm{Pr} \leq 16{,}700 \\ \mathrm{Re} \geq 10{,}000 \end{pmatrix}$
Petukhov correlation	$\overline{Nu}_i = \dfrac{\left(\frac{f}{8}\right)\mathrm{Re}\,\mathrm{Pr}}{1.07+12.7\left(f/8\right)^{0.5}\left(\mathrm{Pr}^{2/3}-1\right)}\left(\dfrac{\mu_b}{\mu_w}\right)^{n}$ $n = 0.11$ for heating and 0.25 for cooling.	$\begin{pmatrix} 0.7 \leq \mathrm{Pr} \leq 16{,}700 \\ \mathrm{Re} \geq 10{,}000 \end{pmatrix}$
Dittus- Boelter correlation	$\overline{Nu}_i = 0.023\mathrm{Re}^{0.8}\,\mathrm{Pr}^{0.4}$	$\begin{pmatrix} 0.7 \leq \mathrm{Pr} \leq 160 \\ \mathrm{Re} \geq 10{,}000 \end{pmatrix}$
Blasius equation[148]	$f = 0.361\mathrm{Re}^{-0.25}\left(\dfrac{\mu_b}{\mu_w}\right)^{-0.25}$	

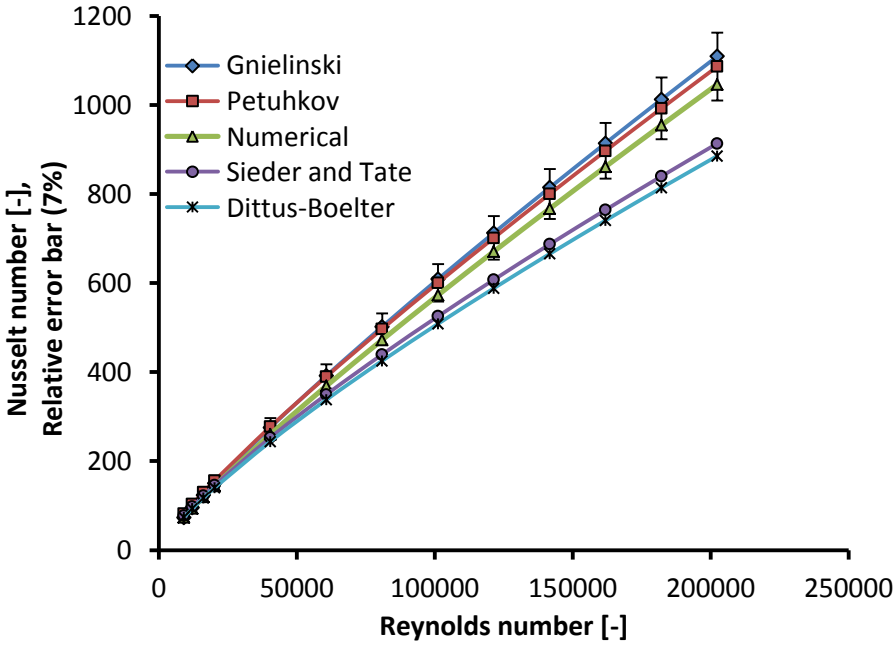

Fig. 5.7 Nusselt numbers for $\alpha = 360^{o}$ uniform heat flux and that of experimental correlations in Table 5.3

Fig. 5.7 indicates that the Nusselt number values obtained from the numerical results are generally in good agreement with the Nusselt number correlations in Table 5.3. The Nusselt number values for the model and that of the Petukhov and Gneilinski correlations are within the error bars of 7%. However, it under-predicted the Nusselt number values for the Dittus-Boeter and Sieder-Tate correlations. The discrepancies could be due to the experimental uncertainties associated with these correlations (+ 25% and – 40% errors). The Nusselt number values for the model have the lowest deviation with that of Gneilinski correlation, which has been regarded as the most accurate correlation for the Nusselt number turbulent flow in circular tubes [134].

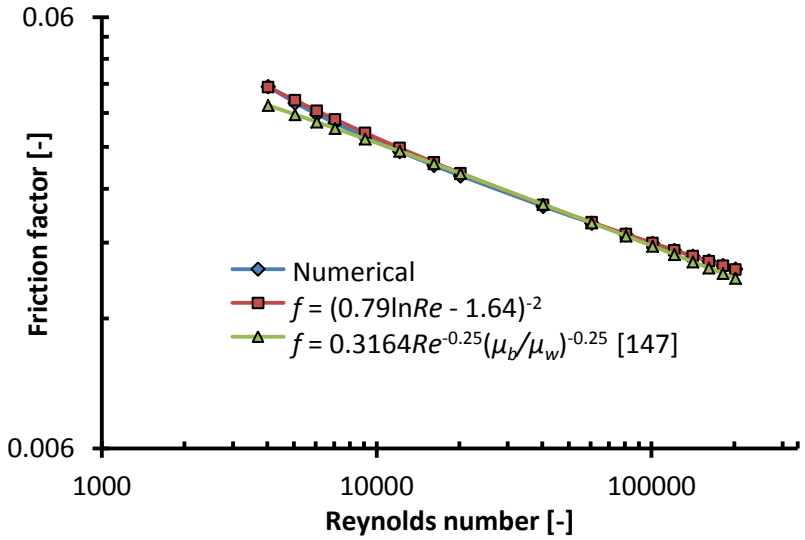

Fig. 5.8 Friction factor for α = 360° uniform heat flux distribution and friction factor correlation in Table 5.3.

Also, further validation is carried out by comparing the friction factor determined from the numerical results for α = 360° span of uniform heat flux at the inlet Reynolds number range of 4040 and 202 400 with the friction factor correlations, $f = (0.79\ln \mathrm{Re} - 1.64)^{-2}$ and $f = 0.361\mathrm{Re}^{-0.25}(\mu_b/\mu_w)^{-0.25}$ [147], when density of the fluid was also independent of temperature (β = 0). Fig. 5.8 shows that the friction factors results for the model are in good agreement with the friction factor correlations. It has an average deviation of 0.8% in terms of $f = (0.79\ln \mathrm{Re} - 1.64)^{-2}$ and $f = 0.361\mathrm{Re}^{-0.25}(\mu_b/\mu_w)^{-0.25}$.

5.4 Model Validation with Experimental Tests Results

The tube model is also validated with some experimental tests results to further check its correctness. The first check was done by comparing the heat loss (Fig.5.9) as a function of the absorber tube temperature from the simulation results and that of the experimental results for the heat loss tests of the Schott's 2008 PTR70 parabolic trough receiver performed by Burkholder and Kutscher [149] at the NREL Heat Collecting Element (HCE) Heat loss test Stand. In this test, electric resistance heaters on the inside of the HCE were used to bring the absorber tube surface up to desired test temperatures. The thermal emittance of the absorber was determined from the measured heat losses and temperatures. The heat loss results were validated from the HCE in a solar field estimated from the Forristall's parabolic trough

collector model [18]. Therminol VP-1 was used as the heat transfer fluid. The tested Schott's receiver had a length of 4.06 m, with inner and outer diameters of 0.066 m and 0.07 m, and a glass envelope of inner and outer diameters of 0.115 m and 0.12 m. The data used for the model validation of this study are also given in Table 5.4.

Table 5.4 Parameters for the Schott PTR70 Lab test [150] used for the model validation

Parameter	Value
Heat collector Element length	4.06 m
Absorber inner diameter (D_i)	0.066 m
Absorber outer diameter (D_o)	0.070 m
Glass inner diameter ($D_{i,g}$)	0.115 m
Glass cover external diameter ($D_{o,g}$)	0.120 m
Glass transmittance (τ_g)	0.00
Glass reflectance (ρ_g)	0.11
Incident angle (ϕ_{in})	0^o
Ambient temperature	23 ^{o}C
Selective coating emissivity	$\varepsilon = 0.062+2x10^{-7}T$

Figs 5.9 and 5.10 show that the numerical model results and that of the experimental tests results are in good agreements and almost all the values are within the experimental error bars of 7%. In Fig.5.10, the model results indicate better prediction of the glass temperature at lower absorber temperature. However, at higher absorber temperature, it over- predicted the glass temperature and this could be attributed to the inaccurate emittance values of the glass determined form the experimental heat loss measurements under steady-state condition. The emittance determined through the heat loss measurements cannot guarantee accurate glass temperature due to the variation of the optical properties of the HCE with temperature and the effects of anti-reflection coating on the glass which were not considered in the present model.

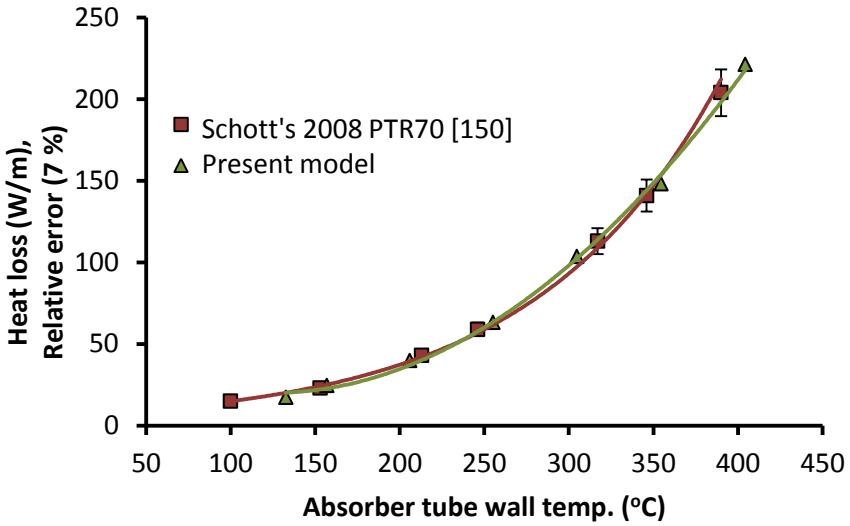

Fig. 5.9 Variation of the collector heat loss with the absorber tube temperature

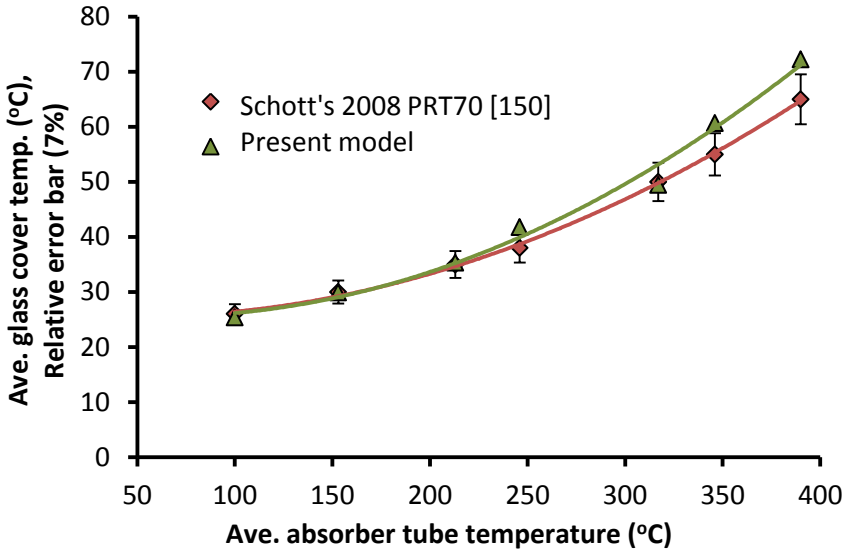

Fig. 5.10 Variation of the average glass cover temperature with the absorber tube temperature

The second check is performed by comparing the model results for the collector efficiency and heat loss as functions of the collector operating temperature respectively and that of the SANDIA final test results for the Schott's HCE on a LS-2 collector module [150]. The Schott HCE consists of an absorber tube with outer diameter of 0.07 m coated with a high

absorptance cermet selective coating and a Pyrex glass tube with outer diameter of 0.125 m and vacuum in the annulus to minimize convection heat loss. The data used for the model validation are given in Table 5.5. Syltherm 800 liquid oil is used as the heat transfer fluid and the thermal properties were obtained from [151]. As it could be expected, the collector efficiency decreased and the heat losses increased with an increase in the fluid temperature due to increase in convection, conduction and radiation heat losses.

Table 5.5 Parameters for the Schott HCE on the LS-2 Collector [148] used for the model validation.

Parameter	**Value**
Ave. Normal incidence pyrheliometer reading	934.30 – 1051.08 W/m^2
Ave. Wind speed	3.1 – 13.8 MPH
Concentrator length (L)	7.8 m
Collector aperture (W)	5.0 m
HCE length	4.0 m
Ave. ambient temperature	3.52 – 14.67 ^{o}C
Average flow rate	9.95 -14.68 gal/min
Absorber inner diameter (D_i)	0.066 m
Absorber outer diameter (D_o)	0.070 m
Glass inner diameter ($D_{i,g}$)	0.109 m
Glass outer diameter ($D_{o,g}$)	0.12 m
Receiver absorptance (α_a)	0.96
Glass transmittance (τ_g)	0.935
Selective coating emissivity	ε = 0.000327 T - 0.065971
Incident angle (ϕ_{in})	0^o

Figs 5.11 and 5.12 show that the model results of the current study, the experimental tests results and that of the curve fit for LS-2/ UVAC2 HCE respectively are in good agreements and most of the values for the case of the collector efficiency are within the experimental error bars of 3%.

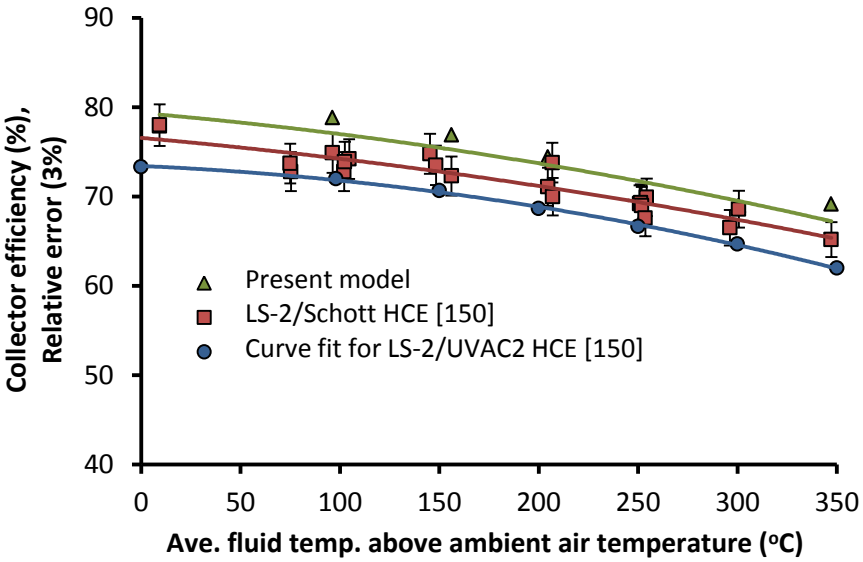

Fig. 5.11 Variations of the collector efficiency with the average fluid temperature above ambient air temperature

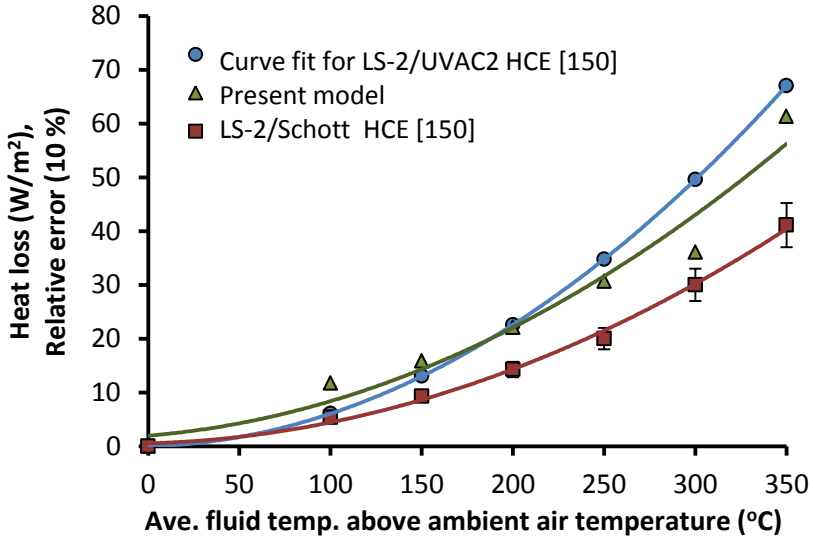

Fig. 5.12 Variations of the collector heat loss with the average fluid temperature above ambient air temperature

However, the model results over-predicted the collector efficiency. In Fig. 5.12, the model results for the heat loss and that of the curve fit for LS-2/UVAC2 HCE indicated some discrepancies with the experimental results (shown with error bars of 10%), especially at higher operating temperatures. The discrepancies could be due to variation of the optical properties of the HCE with temperature, the uncertainty in measuring small temperature change across the HCE, the assumptions of negligible heat conduction at the ends of HCE, possible misalignment between HCE and the collector [18] and the uncertainties due to the thermal properties of the heat transfer fluid and the empirical correlations used in determining the heat transfer coefficients.

The model is also validated by comparing the simulation results with the NREL model developed by Forristall [18] and the experimental tests results for a LS-2 solar collector module placed on the AZTRAK rotating platform at the Sandia National Laboratory (SNL). Detailed information on the AZTRAK testing and the tests results can be found in Dudley *et al.* [152]. The Sandia test and NREL model considered both on-sun and off-sun conditions and the HCE with vacuum intact (pressure in the annulus: $\simeq$ 0.013Pa) and vacuum lost (annulus filled with ambient air) and the absorber tube with no glass cover. The absorber tubes are coated with black chrome and cermet selective coatings and buoyancy effects were not considered in these tests. The present model is validated for the case of on-sun, vacuum and no vacuum conditions and the cermet selective coatings on the absorber tube. The experimental data for the LS-2 solar collector module used for the model validation are shown in Table 5.6 Syltherm 800 liquid oil is used as the heat transfer fluid and the thermal properties for the fluid are obtained from [151]. The cermet coating had better thermal performance than the black chrome at high temperatures and does not oxidize in the event of vacuum lost [152].

Table 5.6 Parameters for the SEGS LS-2 Solar Collector tests by Dudley *et al.* [152] and Forristall [18] used for the model validations.

Parameter	**Value**
Direct solar irradiation	880.6 – 982.3 W/m^2
Wind speed	0.1 – 4.2 m/s
Concentrator length (L)	7.8 m
Collector aperture (W)	5.0 m
Concentrator rim angle	70^o
HCE length	4.0 m
Ambient temperature	21.2 – 31.1 ^{o}C
HTF volumetric flow rate	47.7 -56.3 l/min
Absorber inner diameter (D_i)	0.066 m
Absorber outer diameter (D_o)	0.070 m
Glass inner diameter ($D_{i,g}$)	0.109 m
Glass outer diameter ($D_{o,g}$)	0.115 m
Receiver absorptance (α)	0.96
Glass transmittance (τ_g)	0.935
Glass envelope reflectance (ρ)	0.045
Selective coating emissivity	ε = 0.000327 T - 0.065971
Selective coating solar absorptivity	0.92
Concentrator emissivity	0.97
Incident angle (ϕ_{in})	0^o

Figs 5.13 and 5.14 indicate an increase in heat losses and a decrease in the collector efficiency respectively, with an increase in the fluid temperature due to the increase in convection, conduction and radiation heat losses for both cases of vacuum and air in the annulus. Also, the increase in heat losses and decrease in efficiency are more pronounced for the case with ambient air in the annulus. Figs 5.13 and 5.14 show that the model results are in good agreements with the experimental tests results and that of the NREL model and most of the values for the collector efficiency are within the experimental error bars of 3%.

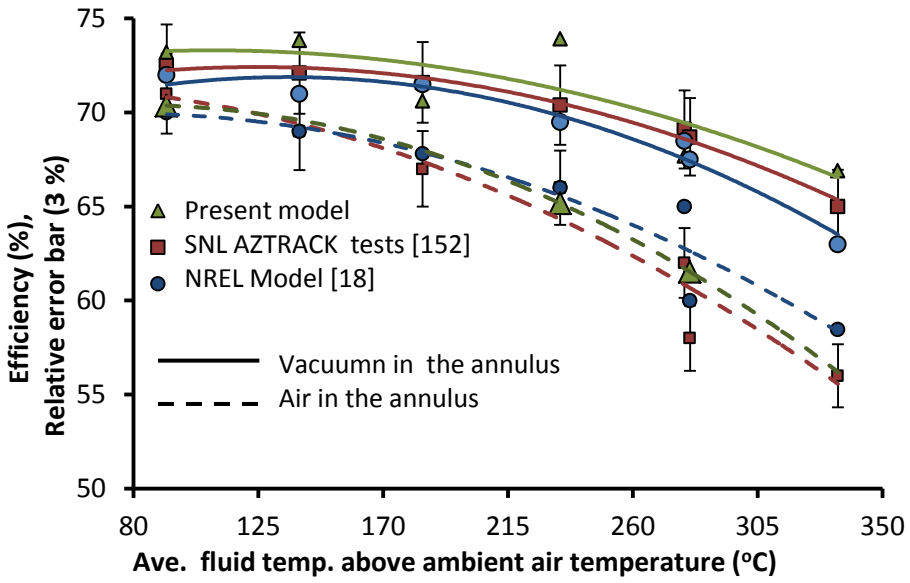

Fig. 5.13 Variations of the collector efficiency with the average fluid temperature above ambient air temperature

In Fig. 5.14, the model results and that of the NREL model indicated some discrepancies with the experimental results (shown with error bars of 10%), especially for the case with air in the annulus. The discrepancy could be due to the uncertainties from empirical correlations used for the heat transfer coefficients and the assumption that the glass cover is opaque to infrared radiation with gray and diffuse surfaces [153]. The errors could also be due to the thermal loss through the steel support bracket and optical effects such as the mirror alignment, aberration in mirrors and tracking system errors [18], which were not considered in the present model.

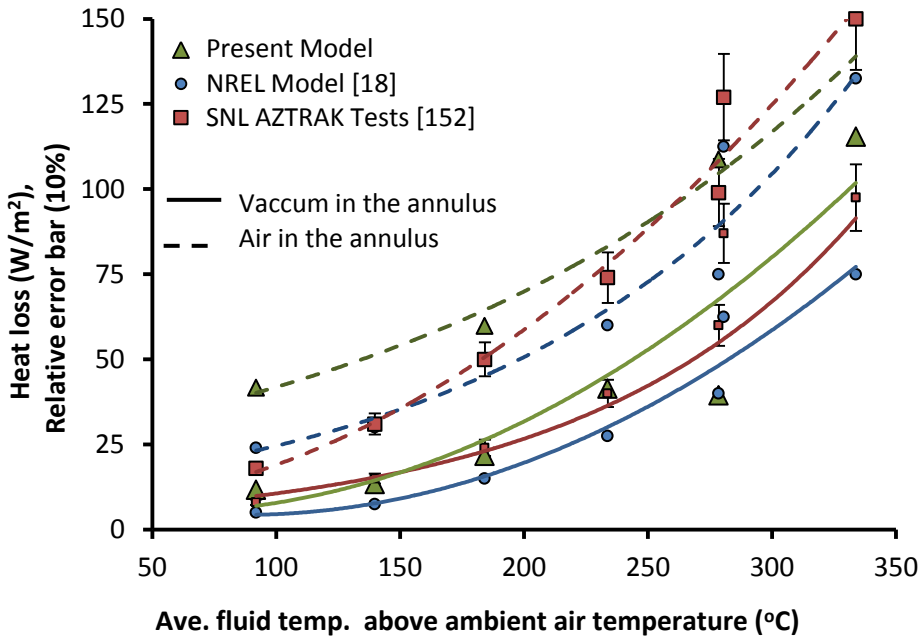

Fig. 5.14 Variation of the collector heat loss with the average fluid temperature above ambient air temperature

5.5 Conclusion

In this chapter, grid refinement tests are conducted in terms of outlet temperature rise of the heat transfer fluid. It was found that the grid is sufficiently fine and has insignificant effect on the numerical results. The model validations were also conducted to check the correctness of the numerical results obtained with the tube model. The Nusselt number and friction factor values determined from the numerical results are in good agreement with both the analytical expressions and empirical correlations for laminar and turbulent flow conditions. The model is further validated with some experimental tests results published by other researchers. The heat losses and the collector efficiency for the model are in good agreement with that of the experimental results. In the next chapter symmetrical heating configurations with different angle spans will be considered for laminar flow conditions.

CHAPTER SIX: NUMERICAL RESULTS AND ANALYSIS FOR SYMMETRICAL HEAT FLUX DISTRIBUTIONS FOR LAMINAR FLOW HEAT TRANSFER

6.0 Introduction

This chapter presents analysis of the numerical simulation results on the impacts of symmetrical heat flux distributions boundaries on the buoyancy-driven secondary flow phenomenon, internal heat transfer enhancement and friction factor characteristics for improving the thermal performance of an absorber tube model for a linear focusing solar collector (e.g. parabolic trough solar collector) under laminar flow condition. The results presented in this chapter and other chapters are limited to single-phase liquid water heating application as in the case of linear focusing solar thermal collector system and considering that some of the parameters investigated are dimensional and as such, the results are only applicable for cases with the same working fluid.

6.1 Temperature Contours for Symmetrical Heat Flux Distributions Boundary

Figs 6.1 and 6.2 give visual representations of some of the simulation results under steady state conditions at ambient temperature of 30°C and atmospheric pressure, for partial uniform, fully uniform and sinusoidal non-uniform heat flux distributions boundaries. The figures differentiate the tube-wall temperature contours for different heat flux boundaries, from the usual assumption of uniform wall heat flux or temperature, where a horizontal tube is heated from below. The sinusoidal non-uniform heat flux case in Fig 6.1 represents a case for a linear focusing solar collector, where the solar heat flux reflected from a parabolic surface impinges on the absorber tube from below, resulting in non-uniform heat flux boundary as represented in Fig. 4.2 (b). The figures indicate the secondary flow effects on the tube-wall temperature profiles at the inlet Reynolds number of 800. The inlet temperature of the heat transfer fluid is 27°C. The absorber tube is that of geometry case 1 with an outer diameter, D_o of 73 mm and wall thickness, t is 5.2 mm. As expected, it can be observed that the outer-wall surface temperatures increase in the flow direction. The tube-wall temperature contours are quite different from each other.

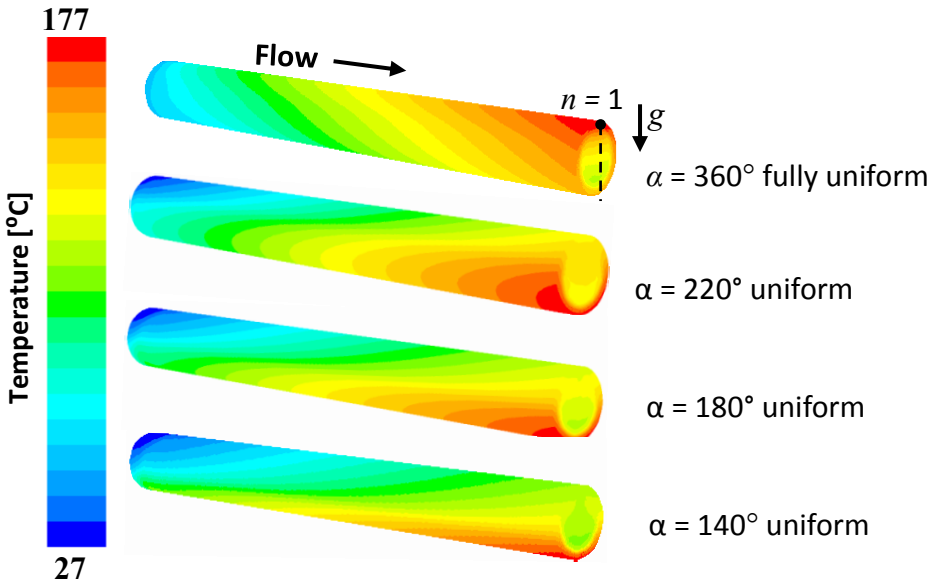

Fig. 6.1 Tube-wall temperature contours for the fully uniform and partial uniform heat flux distributions for Re = 800, q'' = 7.1 kW/m^2 and temperature range of 27 ºC to 177 ºC

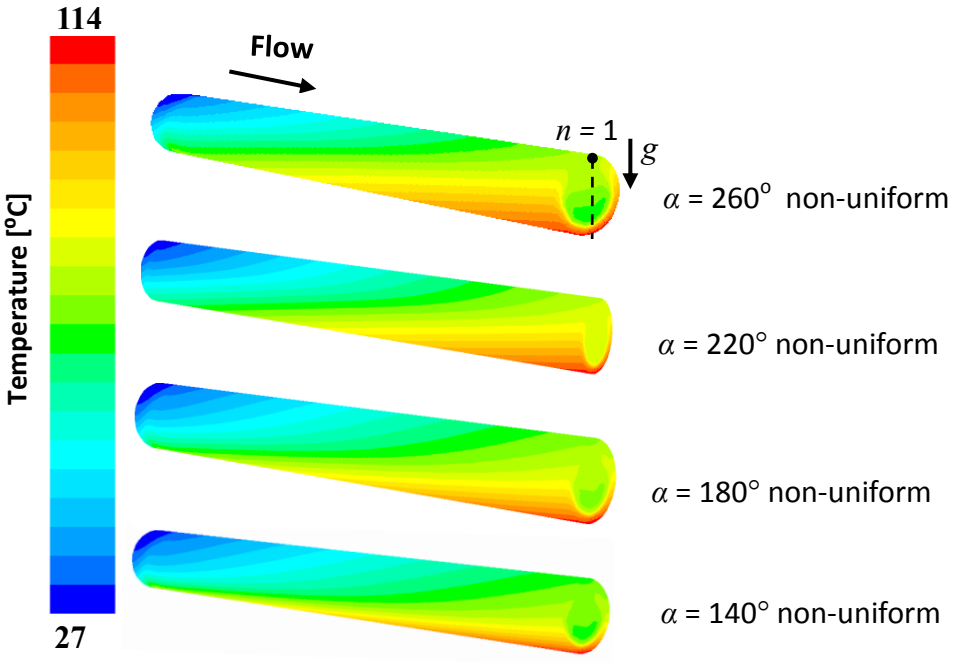

Fig. 6.2 Tube-wall temperature contours for sinusoidal non-uniform heat flux distributions for Re = 800, q''_s = 7.1 kW/m^2 and temperature range of 27 ºC to 114 ºC

For α = 360° span of fully uniform heat flux (Fig.6.1), it can be seen that the upper region at the outlet is the warmest, as shown by the red shade increases, a larger portion of the tube's outer surface is at temperatures close to the peak temperature. This is due to buoyancy effects which brings warm fluid into contact with the upper region of the tube, thereby increasing the thermal mixing of heat transfer fluid and hence heat transfer rate. For the α = 220°, 180° and 140° spans (excluding α = 360°) of the partial uniform (Fig.6.1) and the sinusoidal non-uniform (Fig. 6.2) heat flux distribution cases for a 10 m length tube considered, it can be observed that as the angle span increases, a larger portion of the tube's outer surface is at temperatures close to the peak temperature. This could vary depending on the tube length considered. The temperatures in the upper regions are lower because of little (or no significant) incident heat flux in those locations. In general, the upper regions of the tubes towards the inlet portion are cooler, as shown by the blue shade for the sinusoidal distributions compared to the partial uniform cases.

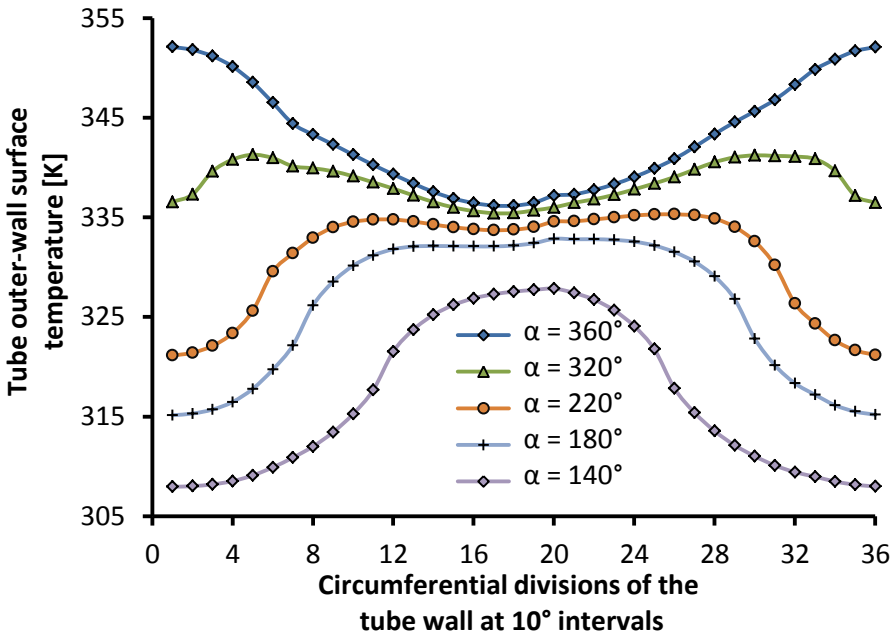

Fig. 6.3 Tube outer-wall surface temperature profiles for fully and partial uniform heat flux distributions for Re = 1100 and q'' = 7.1 kW/m^2.

The non-uniform tube-wall temperature variations over the circumferential surface of some of the tubes in Figs 6.1 and 6.2 are plotted in Figs 6.3 and 6.4, indicating secondary flow effects at different spans of the heat flux distributions boundaries. In these figures, the two ends of the plots represent top potions (n = 1 and 36), while the centre potions represents the bottom potions (18 and 19) of the tube as shown in Fig.4.2.

Fig. 6.3 shows the length-wise averaged outer surface temperature profiles according to section numbers n = 1 to n = 36, as represented in Fig. 4.2 (a), for the α = 140°, 180°, 220°, 320° spans of partial uniform heat flux and α = 360° span of fully uniform heat flux for an inlet Reynolds number of 1100. It can be seen that the temperature profiles for α = 140°, 180° and 220° are quite different from that of α = 320° and 360°, as it is also revealed for the case of α = 360° in Fig. 6.2. For α = 140°, 180° and 220°, the temperature reaches a maximum in the lower region ($n \approx 18$) of the tube. By contrast, for α = 320° and 360°, the temperature reaches a maximum at the upper region of the tube ($n \approx 1$ or $n \approx 36$). This is in line with the findings reported by Coutier and Greif [111] who only considered uniform heat flux conditions and who noted that the maximum temperature occurred at the upper part of the tube. These variations in the temperature profiles can be attributed to the influence of buoyancy forces resulting from the density difference in the fluid. Similar trends were also observed for other Reynolds numbers.

Fig. 6.4 also shows the length-wise averaged outer surface temperature profiles of the tube for the section numbers, n = 1 to n = 36, as represented in Fig. 4.2 (b), for α = 140°, 180°, 220°, 260° and 360° spans of sinusoidal non-uniform heat flux distributions shown in Fig. 6.2 at the inlet Reynolds number of 1100. It indicates that the outer-wall temperature increases with an increase in the heat flux span due to an increase in the circumferential surface of the tube exposed to the incident heat flux. It was found that, unlike the case of the heat flux distributions in Fig. 6.3, the maximum outer-wall temperature only occurs at the lower region of the tube (n ≈ 18 and 19), which corresponds to the position where the heat flux distributions reach its peak and decreases towards the upper region of the tube with a little incident heat flux.

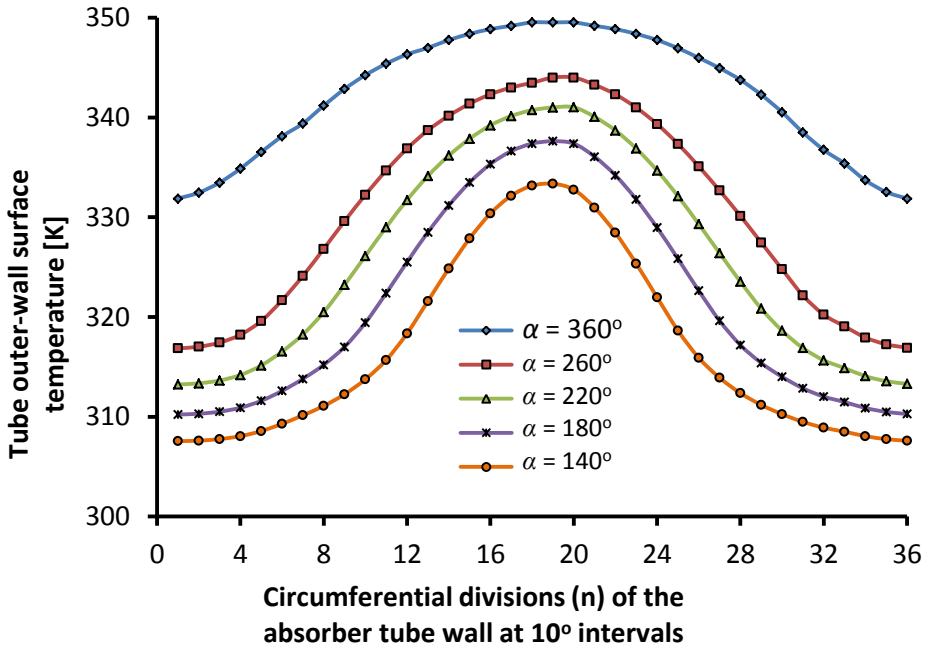

Fig. 6.4 Tube outer-wall surface temperature profiles for sinusoidal non-uniform heat flux distributions for Re = 1 100 and q'' = 7.1 kW/m^2

6.2 Fluid flow velocity and temperature distributions

Fig. 6.5 shows the in-plane fluid velocity vectors (a) as well as the fluid and wall temperature distributions (b) at the outlet of the absorber tube for α = 360° with uniform heat flux at inlet Reynolds numbers of 130, 200 and 500. It can be seen from Fig. 6.5 (a) that the velocity distributions varied from one Reynolds number to the next, indicating different mixing intensities within the heat transfer fluid. The velocity vector arrows indicate the upward moving buoyancy-driven flow of the less dense fluid and the downward moving momentum-driven flow of the denser fluid due to influence of the gravity field. It can be seen that the denser fluid descends to the lower region of the tube along the vertical centre of the tube, while the less dense fluid ascends along the tube inner-wall. Due to this, counter-rotating transverse vortices are produced that are superimposed on the forced-convection flow, as also noted by Ghajar and Tam [103] and by Sadik *et al*. [117]. The overall result of this phenomenon is an improved thermal mixing of the heat transfer fluid, thereby increasing the heat transfer coefficients compared to when buoyancy effects are not present. Flow without buoyancy driven secondary flow is normally characterised by a lower heat transfer

coefficients [154]. It can also be seen that as the Reynolds number increases the temperature gradients decrease. Fig. 6.5 (a) also shows that the relative intensity of the upward and downward circulations of the fluid decrease with an increase in the Reynolds number. This indicates that the influence of the buoyancy-induced secondary flow on the laminar mixed convection decreases with an increase in the Reynolds number because of the increase in forced-convection effects.

Fig. 6.5 (b) shows that the temperature distributions in the fluid vary between the Reynolds number cases. It shows the stratified layers of fluid with higher temperatures towards the upper regions of the tube and the fluid layers with lower temperature towards the bottom region, despite the tube being heated uniformly.

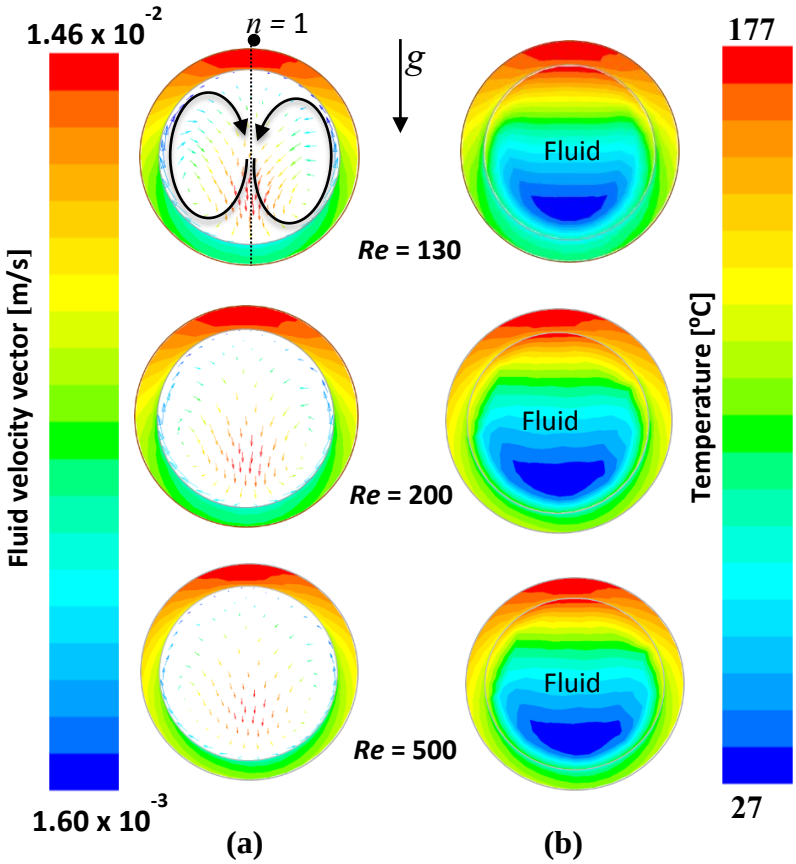

Fig. 6.5 (a) Fluid flow velocity and (b) temperature distribution in the fluid for symmetrical uniform heat flux distribution, q'' = 7.1 kW/m^2 at different Reynolds numbers

It can also be observed that the temperatures in the stratified layers of the fluid are lower as the Reynolds number increases, which may be due to the increase in forced-convection effects and decrease in buoyancy effects. The blue shade in the fluid shows the portion of the fluid with the lowest temperature, which occurred slightly above the heated tube-wall.

Fig 6.6 also shows the in-plane fluid velocity vectors (Fig. 6.6 (a)) as well as the temperature distributions in the fluid and wall at the outlet of the tube for α = 360° with a sinusoidal non-uniform heat flux distributions (Fig. 6.5 (b)) at the inlet Reynolds numbers of 130, 200 and 500. As in the case of Fig. 6.5 (a), it can be observed in Fig. 6.6 (a) that the velocity distributions in the fluid also varied due to buoyancy effects. Figs 6.5 and 6.6 represent cases with the same amount of heat input rate (watts) defined in Eq.4.5. Fig. 6.6 (a) also shows that the intensity of the buoyancy-driven secondary flow effects decrease as the Reynolds number increases.

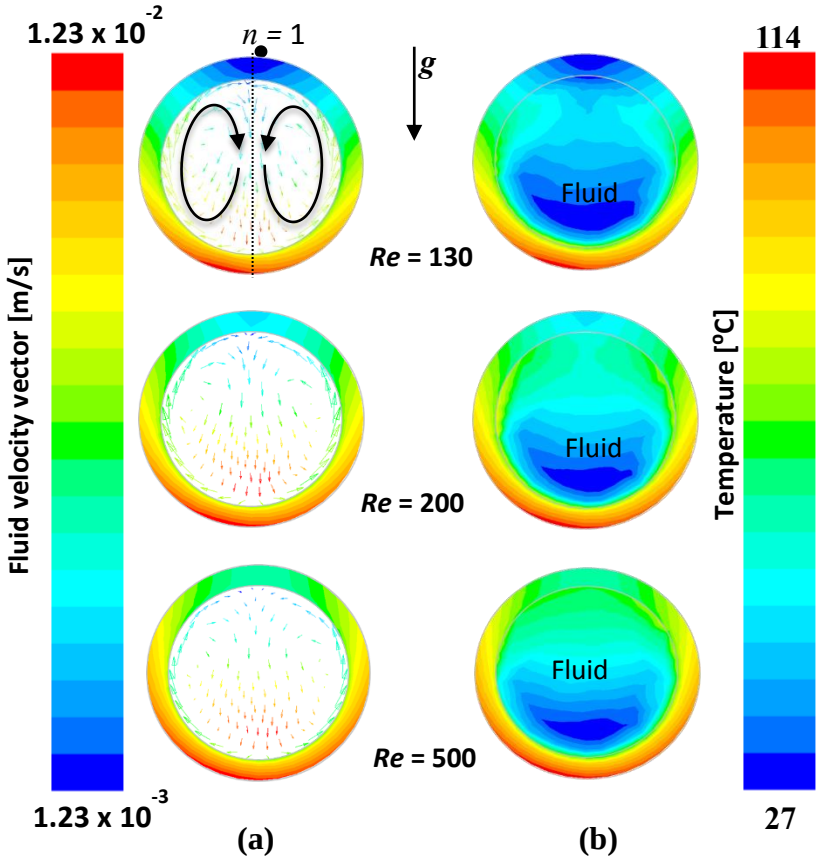

Fig. 6.6 (a) Fluid flow velocity, (b) temperature distribution in the fluid for a symmetrical non-uniform heat flux distribution intensity, q'' = 7.1 kW/m^2 at different Reynolds numbers.

Fig. 6.6 (b) indicates that the temperature distributions in the fluid vary owing to buoyancy effects. The temperature of the tube-wall and that of the fluid near the heated wall are higher than the fluid temperature towards the inner region of the tubes. It can be seen that the temperature distributions in the fluid appear in different layers for the inlet Reynolds number cases considered. The temperature gradient in the fluid also decreases as the Reynolds number increases. The fluid with a higher temperature circulates to the upper regions of the tube. The blue shade in the fluid near the lower region of the tube indicates the lowest temperature region of the fluid.

6.3 Richardson Number for Circumferential Spans of Symmetrical Heat Flux Distributions Boundary

It was found that the Richardson number behaviour for the partial uniform and sinusoidal non-uniform heat flux distributions only differed very slightly. As earlier stated, if $Ri > 10$, natural convection dominates and if $0.1 < Ri < 10$, mixed convection dominates the heat transfer process. Fig. 6.7 only presents the variation of *Ri* with the circumferential span of the non-uniform heat flux distribution boundary, indicating the relative impacts of buoyancy effects on the forced convection flow for Reynolds number range of 500 to 1100. It is found that *Ri* increases with an increase in the circumferential span of the heat flux distribution boundary due to an increase in the effective heat input rate (W) into the absorber tube as a result of an increase in the circumferential surface of the tube exposed to the incident heat flux. Also, Fig. 6.8 indicates that *Ri* increases with an increase in heat flux intensity due to an increase in the heat transfer rate and the increase in the circumferential surface of the absorber tube exposed to the incident heat flux. The *Ri* for the higher heat flux intensity is represented with broken lines. It was found that *Ri* decreases with an increase in Reynolds number, which shows the stronger influence of buoyancy effects at lower Reynolds numbers and the weaker influence of buoyancy effects at higher Reynolds numbers. In Fig. 6.7, for $\alpha = 320°$ to $360°$, *Ri* is greater than 10 for all the Reynolds number cases considered, indicating that the heat transfer is dominated by the natural convection effect due to the induced secondary flow effects and that the forced-convection effect is negligible at the higher spans of the heat flux distributions. For $\alpha = 140°$ to $260°$, Ri is found to be less than 10 for the Reynolds number of 1100 and for $\alpha = 140°$ to $160°$ for the Reynolds number of

800. This shows that mixed convection was present. In both Figs 6.7 and 6.8, $Ri < 0.1$ is not observed, indicating that the influence of pure forced-convective heat transfer is negligible.

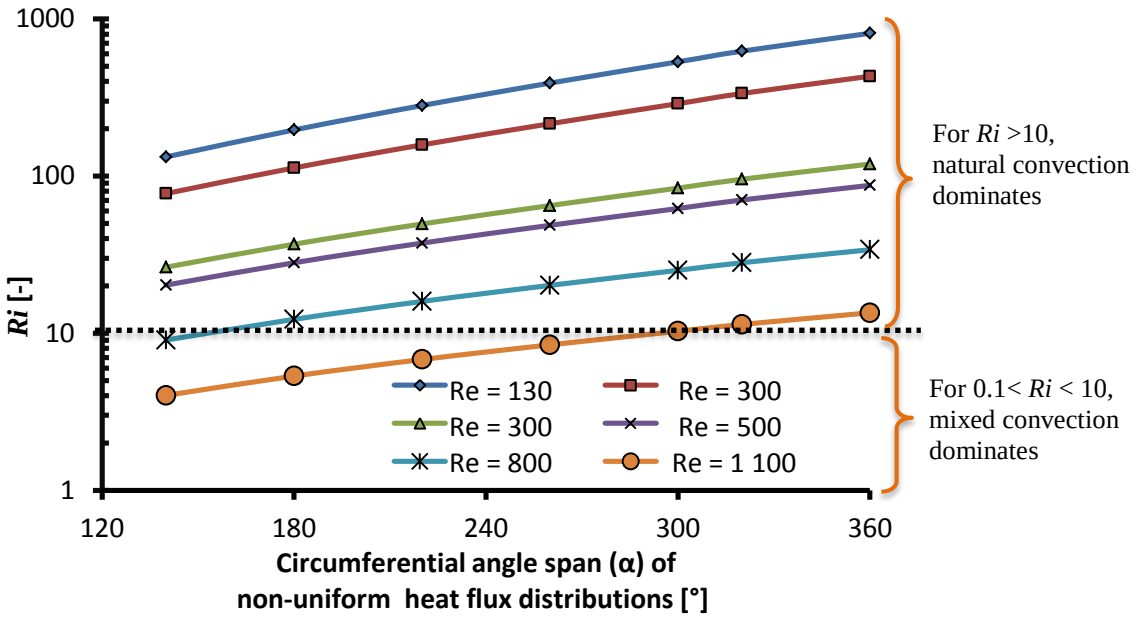

Fig. 6.7 Variation of *Ri* with circumferential spans (α) of the sinusoidal non-uniform heat flux distributions for q'' = 7.1 kW/m^2

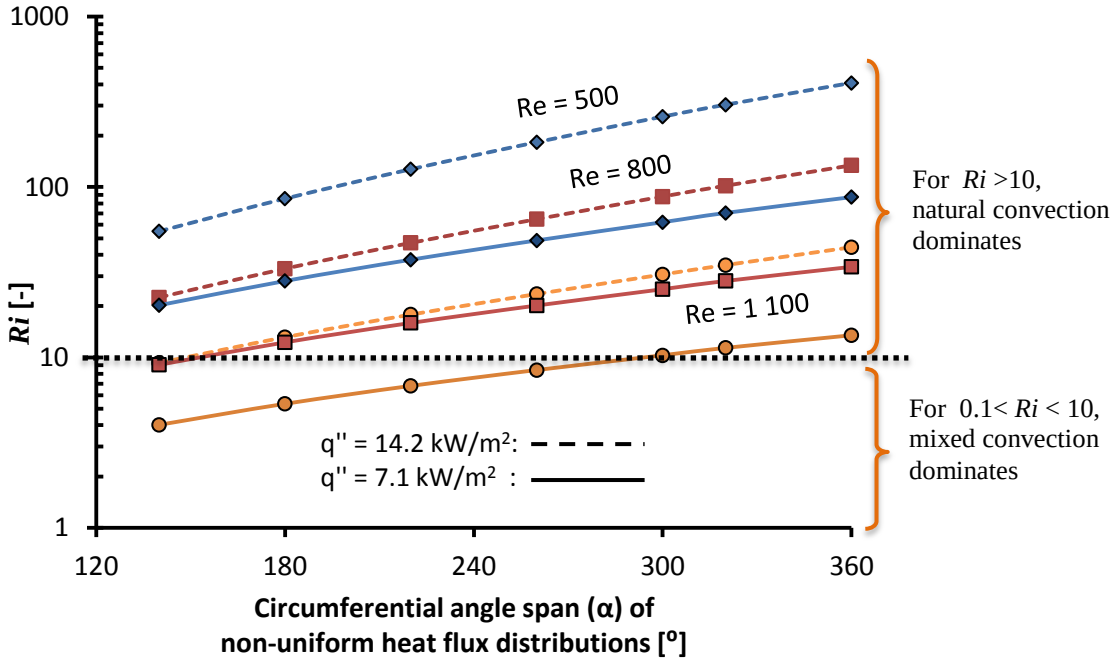

Fig. 6.8 Variation of *Ri* with circumferential spans (α) of the sinusoidal non-uniform heat flux distributions boundary for two heat flux intensities.

6.4 Heat Transfer Coefficients for Different Base-Levels Heat Flux Intensities

In order to demonstrate the heat transfer enhancement due to buoyancy effects, two scenarios will now be considered at different inlet Reynolds numbers (Re_{Di}) for three different base-level heat flux intensities for $\alpha = 260^{o}$. In the first scenario, buoyancy-driven flow is ignored (presented in Fig. 6.9), while in the second scenario it is included (presented in Fig. 6.10). It should be noted that the results presented in Figs. 6.9 and 6.10 and other figures in this study are limited to single-phase liquid water heating applications. Also, considering that some parameters such as heat transfer coefficient and the incident solar heat flux considered are dimensional and as such, the results are only applicable for cases with the same working fluid as considered in this study. In Fig. 6.9 as expected, the internal heat transfer coefficient increases with the Reynolds number since the flow is not yet fully developed. For the first case, it was found that there is no significant difference in the average internal heat transfer coefficients for uniform and non-uniform heat flux intensities. This implies that for this scenario, the average internal heat transfer coefficient is also independent of the heat flux distribution profiles (for instance uniform versus non-uniform).

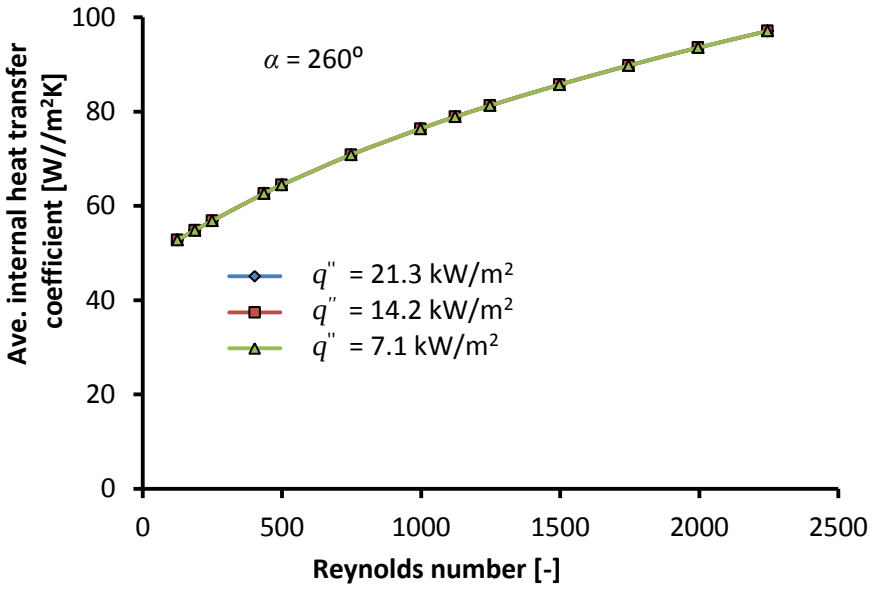

Fig. 6.9 Average internal heat transfer coefficients for a sinusoidal non-uniform heat flux distributions for different base-level intensities with no secondary flow

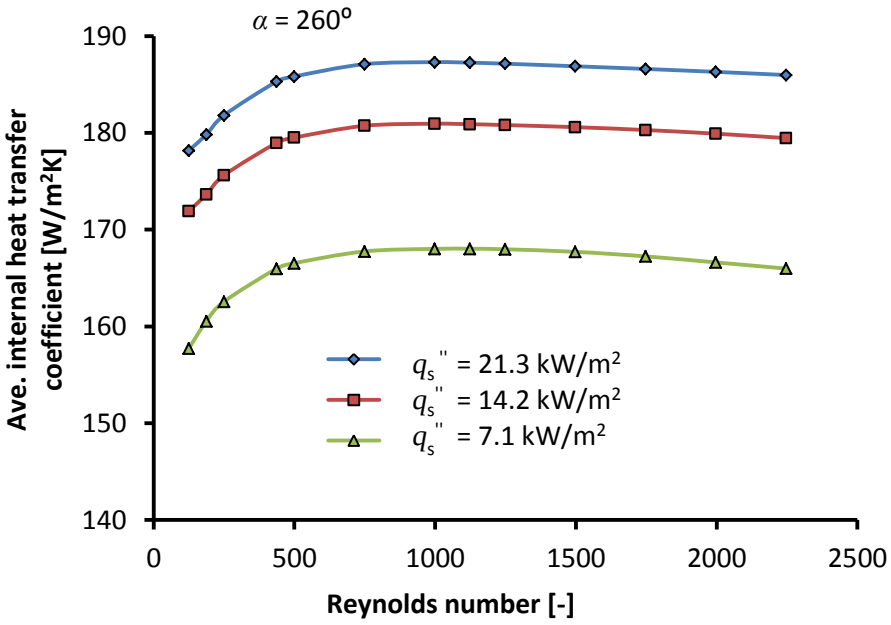

Fig. 6.10 Average internal heat transfer coefficients for a sinusoidal non-uniform heat flux distributions for different base-level intensities with secondary flow present.

For the second case (see Fig. 6.10), it can be seen that there is a significant enhancement in the average internal heat transfer coefficients with an increase in the heat flux intensities. This is attributed to the increase in buoyancy-induced secondary flow due to high fluid density gradient resulting from the temperature gradient between the fluid and the heated tube-wall surface, as a result of the increase in the intensity of the heat flux boundary conditions. This is in line with the experimental results by Mohammed and Salman [107] and Mori *et al*. [116] who only investigated the case of uniform heat flux condition. Figs 6.9 and 6.10 underscore the importance of heat transfer enhancement due to buoyancy-induced secondary flow effects on the internal heat transfer coefficients of a horizontal circular absorber tube, due to heat flux intensity and heat flux distribution boundary. For the heat flux intensities considered, the average internal heat transfer coefficients are 163%, 154% and 135% respectively higher than where the buoyancy-effect is neglected in Fig 6.8. Thus, the influence of buoyancy effects on the internal forced-convective heat transfer is dependent on both the heat flux intensity and the heat flux distribution boundary in the laminar flow regime.

6.5 Heat Transfer Coefficients for Different Circumferential Spans of Non-Uniform Heat Flux Boundaries

The impact of different circumferential heat flux spans of α = 140°, 180°, 220° and 260° on heat transfer coefficients for different inlet Reynolds numbers are shown in Figs 6.11 and 6.12 for a scenario without and with buoyancy effects respectively. As expected the average internal heat transfer coefficients increases with the Reynolds number, irrespective of whether buoyancy effect is considered. Without buoyancy effects there is no significant increase in the internal heat transfer coefficients for different angle spans (see Fig 6.11).

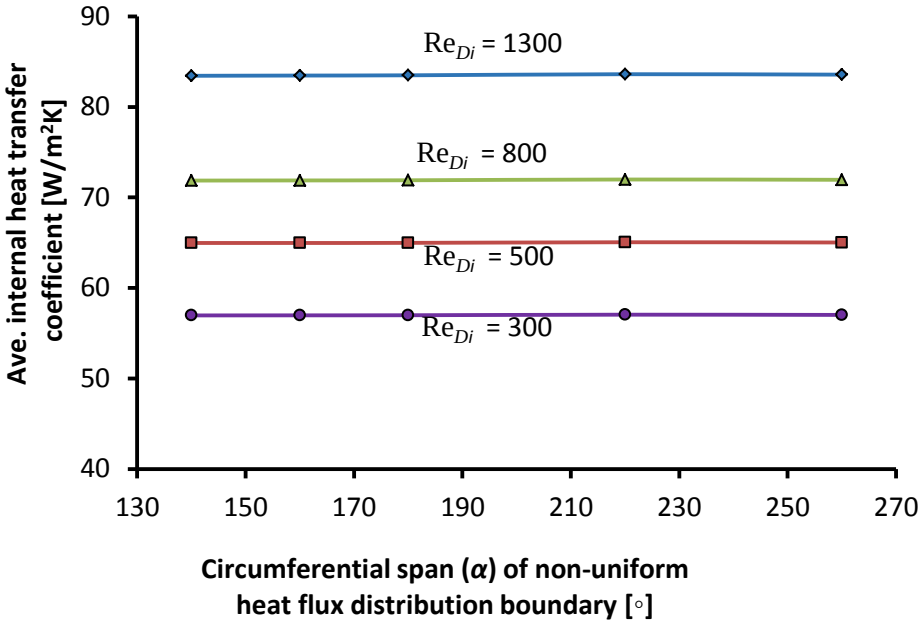

Fig. 6.11 Average internal heat transfer coefficient for different circumferential spans of sinusoidal non-uniform heat flux boundaries with no secondary flow

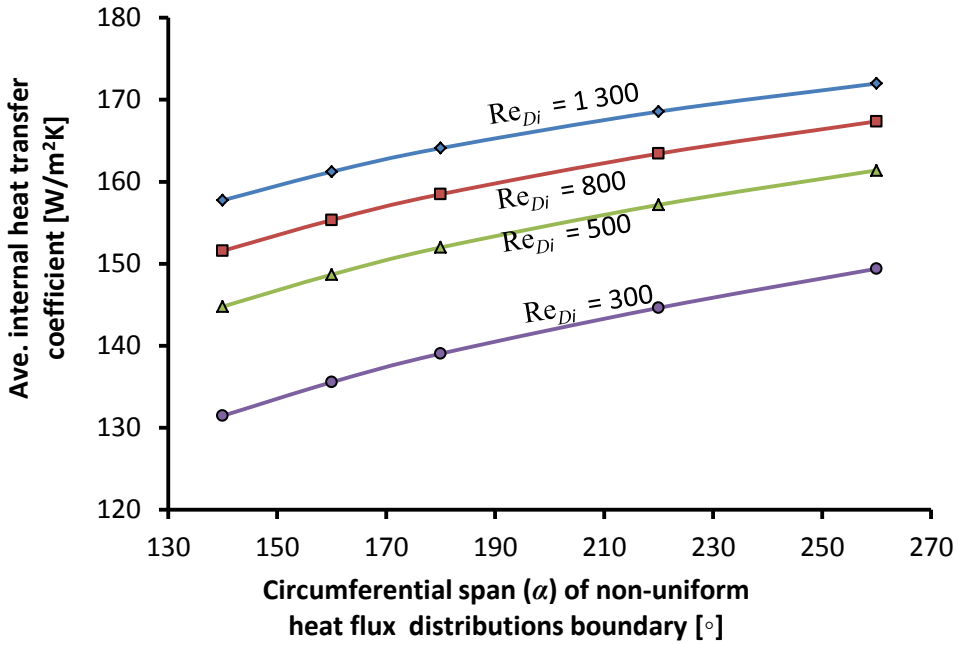

Fig. 6.12 Average internal heat transfer coefficient for different circumferential spans of sinusoidal non-uniform heat flux boundaries with secondary flow.

As before when, however, buoyancy effects are present (see Fig. 6.12), there is a significant increase in the average internal heat transfer coefficient as the heat flux circumferential span is increased. This mirrors the findings from Fig. 6.11, and is mainly due to an increase in the effective heat input rate (W) into the tube as a result of an increase in the circumferential surface of the tube exposed to the incident heat flux. It is found that between Re_{Di} = 300 and 1300, the average internal heat transfer coefficients increases by 20% and 15% respectively, between $\alpha = 140^{o}$ and 260^{o}.

The impact of the buoyancy effect and the heat flux intensity on the axial local internal heat transfer coefficients (based on Eq. 4.11) are shown in Fig. 6.13 for α = 260° span of non-uniform heat flux distributions boundary for an inlet Reynolds number of 1100. In this figure a comparison is made between the axial local heat transfer coefficients where buoyancy effects are considered (shown with the broken lines) and where it is neglected (solid lines).

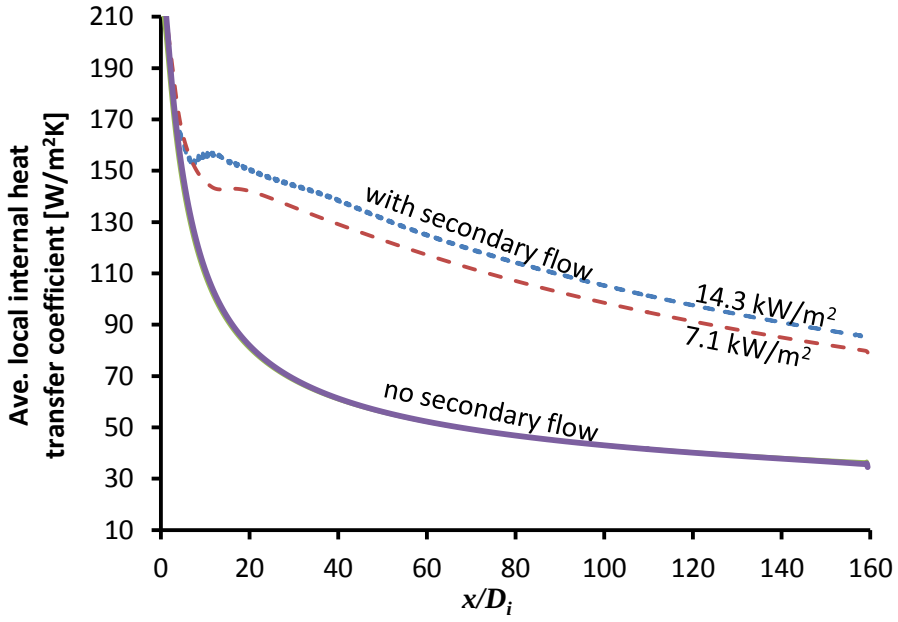

Fig. 6.13 Average axial local internal heat transfer coefficients for a sinusoidal non-uniform heat flux distributions at an inlet Reynolds number of 1100 with α = 260°.

With buoyancy effects, the axial local heat transfer coefficients are greater by up to 128% and 144% (for the two heat flux intensities respectively) between x/D_i ≈1.0 and 98, compared to the scenario without buoyancy effects. For both scenarios the highest heat transfer coefficients are present at the tube inlet where the thermal boundary layer is at its thinnest. It can be observed that at the hydrodynamic and thermal inlet region of the tube, the heat transfer coefficient coincided, indicating no significant influence of buoyancy effect, due to low temperature gradient. Also, the results of T_{TOT}/D_i given in Table 4.1 indicate that the thermal entry region could be only about 1/3 of the total length of the tube for the lowest Reynolds number case considered. As the flow continued downstream, the buoyancy effect dominated that of forced-convection and the heat transfer coefficient became higher. As the flow becomes more developed and the thermal boundary layer becomes thicker, the heat transfer coefficient decreases, which could be due to decrease in buoyancy effect. At $x/D_i \approx 7$, the change in the heat transfer coefficients gradient could be due to the slight increase in the heat transfer coefficient due to buoyancy effects at the point where the flow tends to depart from the region, where the influence of the hydrodynamic and thermal boundary layer effect

could be insignificant. Fig. 6.13 also indicates that the flow the flow is not fully developed and fully developed flow rarely occurs in real flow application.

Fig.6.14 shows the variations of the average overall heat transfer coefficients, *U*, with the circumferential span of sinusoidal non-uniform heat flux distributions at different Reynolds numbers. The average overall heat transfer coefficient is determined based on Eq. (4.14) with the external heat loss coefficient of 25.3 W/m^{2}K determined from Eq. (4.15). It was found that the overall heat transfer coefficients increases with an increase in the circumferential span of non-uniform heat flux distributions. This is due to the influence of buoyancy effects as result of an increase in the heat input rate (W) associated with an increase in the circumferential surface of the tube with incident heat flux. It can also be observed that the difference in the overall heat transfer coefficients decreases as the Reynolds number increases at higher angle spans, but the differences are higher at lower angle spans due to higher buoyancy effects at lower Reynolds numbers.

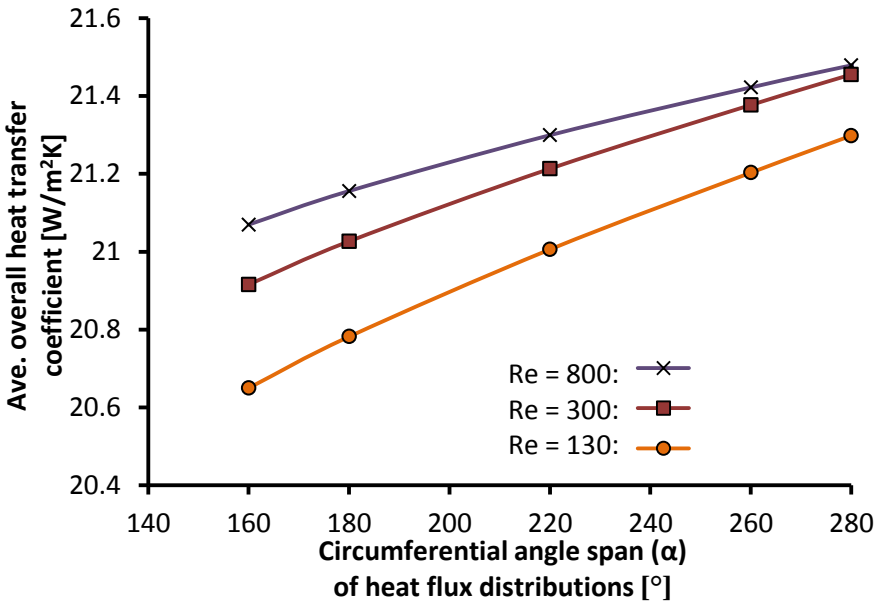

Fig.6.14 Variation of the average overall heat transfer coefficient for sinusoidal non-uniform heat flux distributions for external loss heat transfer coefficient of 25.3 W/m^{2}K.

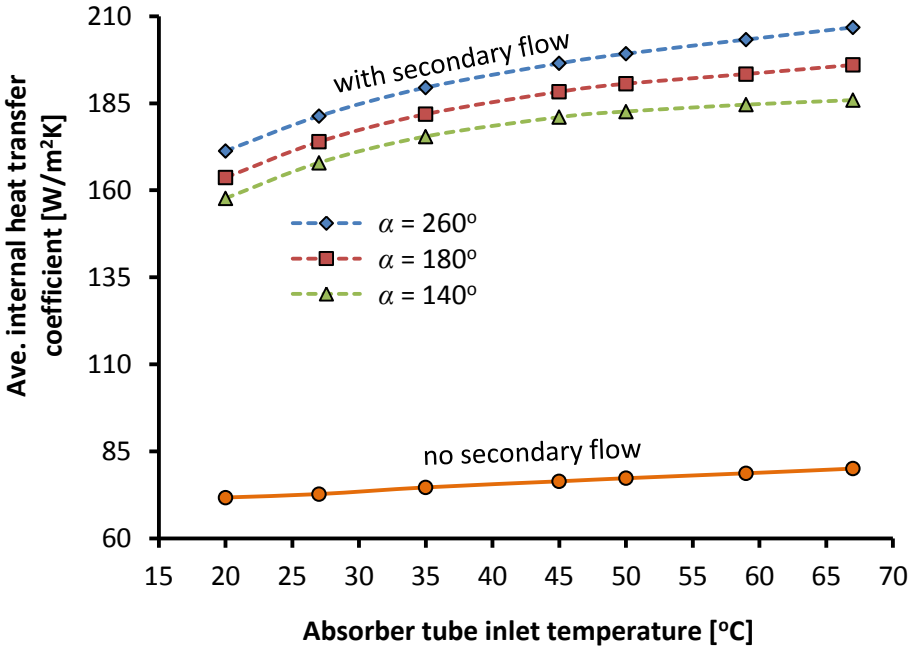

Fig. 6.15 Variation of average internal heat transfer coefficient for an absorber tube at different heat transfer fluid inlet temperature.

Fig. 6.15 indicates the impact of the inlet fluid temperature on the average internal heat transfer coefficient with the absorber tube for the heat flux spans of α = 140°, 180° and 260°. For these heat flux span cases considered, where buoyancy effect is present, the average internal heat transfer coefficients are up to 132%, 144% and 158% higher respectively than where it is neglected (pure forced convection). This indicates a very high significant internal heat transfer enhancement due to buoyancy-driven secondary flow effect for the non-uniform heat flux distributions boundary. Also, for the case of α = 260°, the average internal heat transfer coefficient increases up to 21% and 12% respectively, where the buoyancy effect is present compared to when it is neglected, when the inlet fluid temperature is increased from 20°C to 67°C, at the same ambient temperature. This could be due to an increase in the intensity of the buoyancy-induced flow due to a decrease in the fluid viscosity with an increase in fluid temperature. This indicates the influence of pre-heating the inlet heat transfer fluid on the internal heat transfer coefficient of the absorber tube.

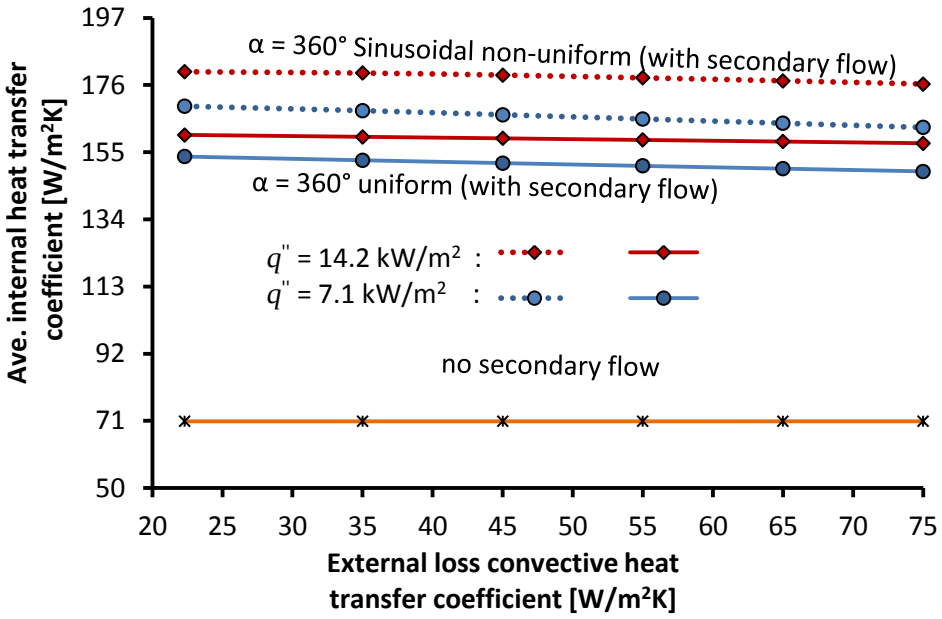

Fig. 6.16 Influence of external convective heat loss transfer coefficient on internal heat transfer coefficient for α = 360° spans of uniform and sinusoidal non-uniform heat flux distributions for inlet Reynolds number of 800.

Fig.6.16 shows the influence of the external convective heat loss transfer coefficient due to variations of wind effects around the solar collector on the average internal heat transfer coefficient for the tube model with uniform and non-uniform heat flux boundaries, where buoyancy effect is present and where it is neglected. The figure indicates that the average internal heat transfer coefficients for uniform and non-uniform heat flux boundaries are different due to their different impacts on buoyancy effects. The average internal heat transfer coefficients for the uniform and non-uniform heat flux boundaries are 110% and 122% higher than where buoyancy effects are neglected. It is found that the average internal heat transfer coefficient decreases with an increase in the external convective heat loss transfer coefficient. This could be due to the impact of conjugate heat transfer in the tube-wall on the secondary flow patterns within the tube. The external convective heat loss transfer coefficient increases with an increase in the air velocity around the collector receiver outer surface. This results in an increase in the external convective heat loss and a decrease in the heat transfer rate from the external tube-wall surface to the heat transfer fluid in the tube.

6.6 Nusselt numbers and thermal efficiency for absorber tubes with different diameters and wall thicknesses for non-uniform heat flux distributions

Fig. 6.17 shows the variation of the average Nusselt number trends for absorber tubes with different inner diameters and wall thicknesses for the different geometric cases mentioned in a previous chapter with α = 140°, 180°, 220° and 260° and with an inlet Reynolds number of 800. The three inner diameters of 62.7 mm, 52.5 mm, and 40.9 mm, result in length-to-inner diameter ratios of 160, 191 and 245 respectively. Fig. 6.17 indicates that Nusselt number increases with an increase in the circumferential span (α) of the heat flux distributions around the absorber tube surface, which could be due to an increase in the effective heat input rate into the tube as result of an increase in the circumferential surface of the tube exposed to incident solar heat flux. It is also found that the average Nusselt number increases with an increase in the tube inner diameter and wall thickness for the conditions considered in this study. These variations could be due to several factors, such as the length-to-diameter ratio, the internal fluid volume available for secondary flow development, and the tube-wall conduction around the circumference which can alter the conjugate heat transfer arrangement. It could be noted that the average Nusselt numbers are well above a value of 10. Based on this and the analysis comparison earlier conducted in Chapter three, the parabolic trough collector adaption will have favorable thermal efficiencies compared to the flat-plate collector type considered here.

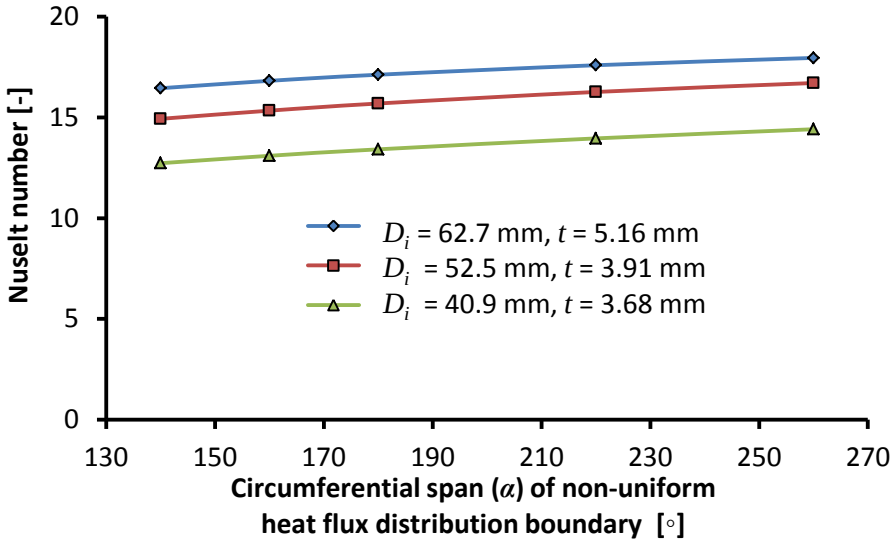

Fig. 6.17 Average Nusselt number of absorber tubes with different inner diameters and wall thicknesses for Re = 800 and q'' = 7.1 kW/m^2

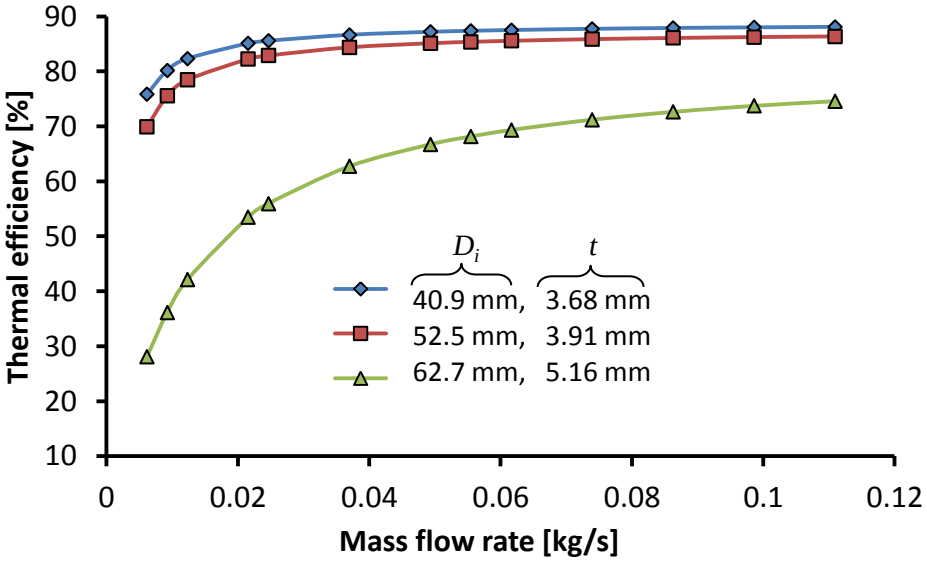

Fig. 6.18 Thermal efficiency of tubes with different inner diameters and wall thicknesses for q'' = 7.1 kW/m^2

Fig. 6.18 shows the thermal efficiency of the absorber tubes with different inner diameters and wall thicknesses, determined from Eq. (4.17) at different mass flow rate. The figure shows for instance, the thermal efficiency of the tubes for a symmetrical 260° span of non-uniform heat flux distributions. It is found that the thermal efficiency increased with the decrease in the inner diameter and wall thickness of the tube. Similar trends were also obtained for other angle spans of the sinusoidal non-uniform heat flux distribution boundary. Also, increasing the circumferential surface of the tubes exposed to the incident heat flux by increasing the angle span of heat flux distribution boundary would result in an increase in the effective heat transfer rate into the tubes. The lower thermal efficiency of the tube with higher inner diameter and wall thickness could be due to its higher thermal resistance as a result of its larger wall thickness. The decrease in the inner diameter of the tube and wall thickness in order to increase the thermal efficiency could result in an increase in pressure drop and the consequent increase in pumping power to overcome the pressure drop and to sustain the fluid flow and heat transfer, since pressure is inversely related to the tube diameter and directly to the square of the velocity of the heat transfer fluid [134].

6.7 Friction factors for symmetrical non-uniform heat flux boundaries

The impact of buoyancy-driven secondary flow and the non-uniform heat flux intensity on the friction factors characteristics are shown in Fig. 6.19 for an absorber tube with inner diameter of 62.7 mm and wall thickness of 5.7 mm. The pressure drops for the absorber tube were obtained from the numerical results and subsequently the friction factors are determined from Eq. (3.16). As expected, the friction factors decrease with an increase in Reynolds number due to the increase in the velocity of the fluid. It is found that where buoyancy effect is present (indicated with the broken lines), the friction factor values for the two heat flux intensities are up to 77% and 46% respectively higher than when it is neglected, for the inlet Reynolds number range of 130 to 2 200.

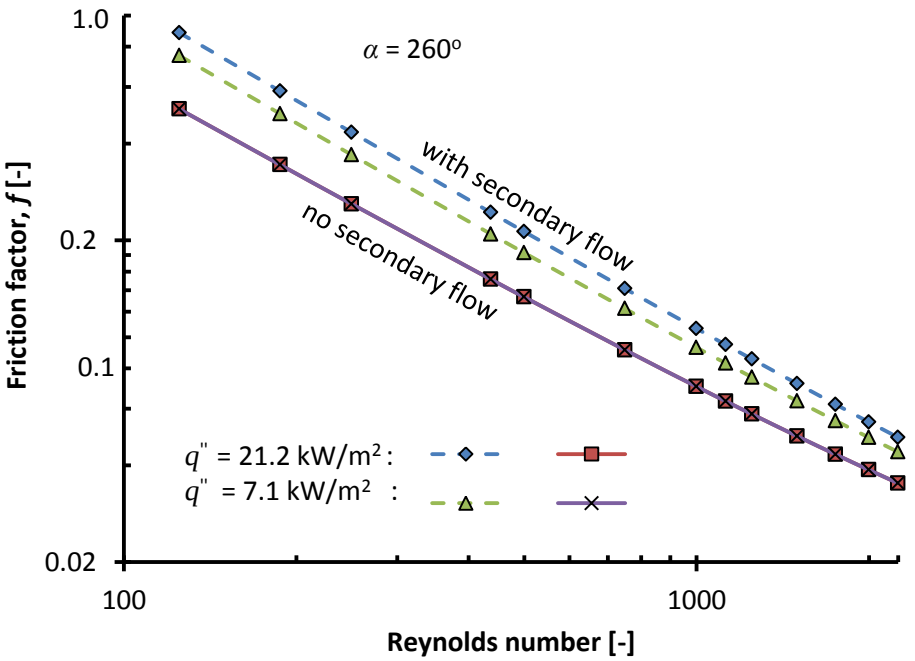

Fig. 6.19 Variation of the friction factors with Reynolds numbers for a sinusoidal non-uniform heat flux distributions, q'' = 21.2 kW/m^2 and 7.1 kW/m^2

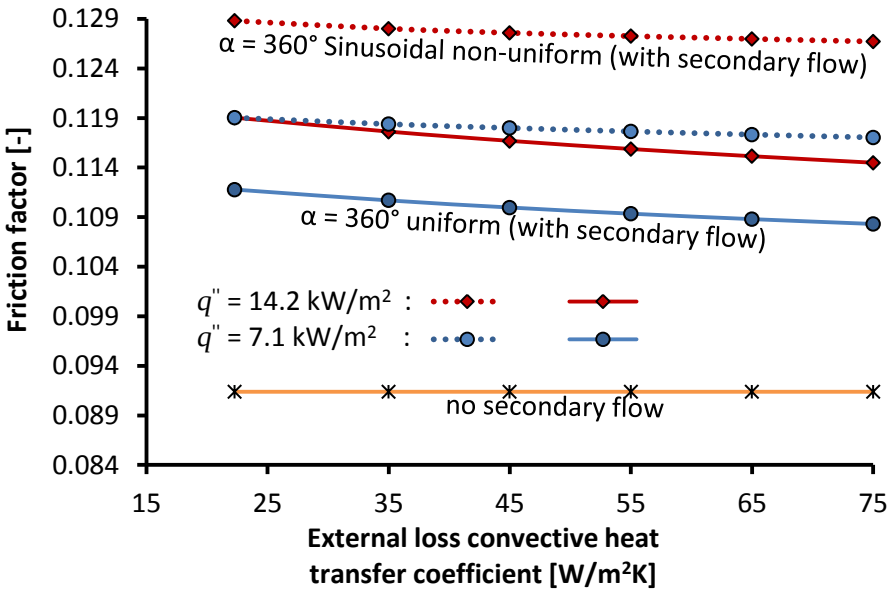

Fig. 6.20 Influence of external convective heat loss transfer coefficient on the friction factor for uniform and non-uniform heat flux distributions boundaries.

Fig. 6.20 shows the influence of external convective heat loss transfer coefficient on the friction factor for α = 360° with uniform and sinusoidal non-uniform symmetrical heat flux distributions boundaries. The non-uniform heat flux distribution case is shown with the broken lines. The friction factors for the uniform and non-uniform cases decrease with an increase in the external convective heat loss transfer coefficient, where buoyancy-effect is present and constant where it is neglected. With the buoyancy effect present, the friction factors for uniform and non-uniform heat flux are is approximately 19% and 39% higher than where it is neglected for heat loss transfer coefficient of 75 W/m^{2}K. The friction factor for the non-uniform heat flux case is higher than that of the uniform heat flux case due to their different impacts on buoyancy effects.

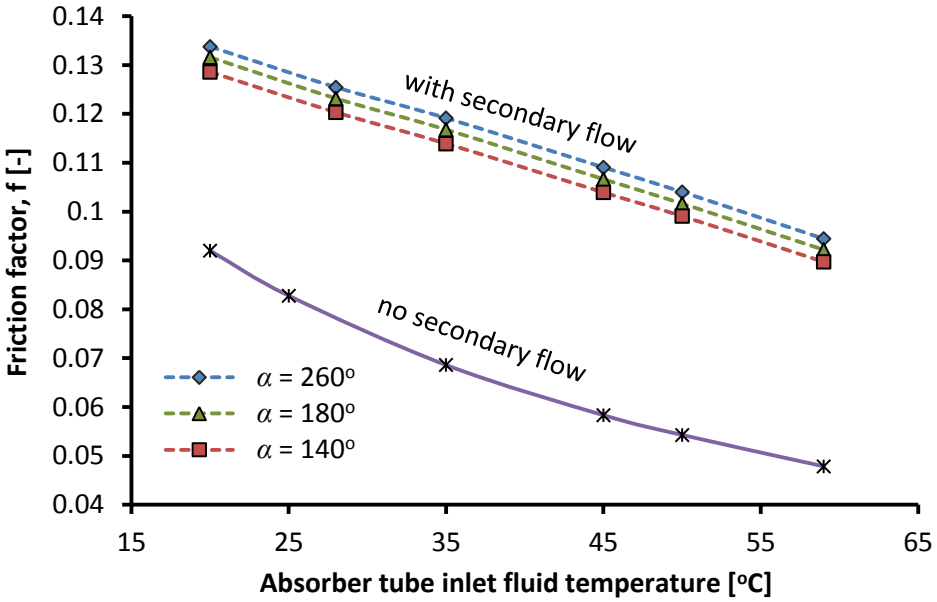

Fig. 6.21 Variation of the friction factors for an absorber tube at different heat transfer fluid inlet temperature and q'' = 7.1 kW/m^2

Fig.6.21 indicates the variations of friction factor values in terms of the inlet fluid temperature for α = 140°, 180° and 260° span of non-uniform heat flux distributions boundaries. For the heat flux distributions spans considered, the friction factor values are up to 88%, 93% and 98% respectively higher when buoyancy effects are present compared to when they are neglected. Fig. 6.21 also indicates that the friction factor decreases with an increase in the inlet temperature of the heat transfer fluid. The influence of the fluid inlet temperature on the friction factor is higher than that of the external convective heat loss transfer coefficient on the friction factor as shown in Fig. 6.20.

6.8. Conclusion

The influence of different circumferential spans of symmetrical partial uniform, sinusoidal non-uniform and fully uniform heat flux boundaries on the buoyancy effect, internal heat transfer and friction factor characteristics were analysed at the inlet Reynolds number range of 130 to 2 200. As expected, the average internal heat transfer coefficient for the absorber tube model considered increases with an increase in the inlet Reynolds number. It is found that with buoyancy-driven secondary flow present, the internal heat transfer coefficients of

the absorber tube increases with the heat flux intensity and spans of the uniform and non-uniform heat flux distributions boundary. Also, with the secondary flow effect present, the average internal heat transfer coefficient is up to three times higher than the case of pure forced-convection (no secondary flow effect), indicating higher internal heat transfer enhancement and thus, improved thermal performance. It is also found that with the buoyancy effect present, the friction factor value is approximately twice higher than where it is neglected and that it increases with the heat flux intensity. However, at the same ambient temperature condition, the friction factor value decreases with an increase in the absorber tube inlet fluid temperature, while the internal heat transfer coefficient increased with an increase in the absorber tube inlet fluid temperature. In the next chapter asymmetric heat flux distributions in terms of the gravitational direction will be considered.

CHAPTER SEVEN: NUMERICAL RESULTS AND ANALYSIS FOR ASYMMETRICAL HEAT FLUX DISTRIBUTIONS FOR LAMINAR FLOW HEAT TRANSFER

7.0 Introduction

In this chapter, the numerical simulation results are presented and discussed for the influence of circumferential spans of asymmetrical non-uniform heat flux boundaries in terms gravitational field on buoyancy effect, internal heat transfer and friction factor characteristics of an absorber tube model considered. The results for the asymmetrical non-uniform heat flux cases are compared with that of symmetrical non-uniform heat flux cases. An absorber tube model (dimensional case 1) is used with a length of 10 m, outer diameter of 73 mm and wall thickness of 5.2 mm.

7.1 Temperature Contour for Asymmetrical Non-Uniform Heat Flux Distributions

Fig. 7.1 shows the converged tube-wall temperature contours for different angle spans for an asymmetry angle of $\gamma = 30°$. The temperature contours show the asymmetrical non-uniform temperature profiles over the circumferential outer wall surface of the tube linked to the asymmetric nature of the heat flux distribution. It was found that the outer-wall surface temperatures increase in the flow direction as expected, and is the highest with the larger angle spans. Highest temperatures are obtained on the lower portions of the tube which coincided with the peak heat flux levels.

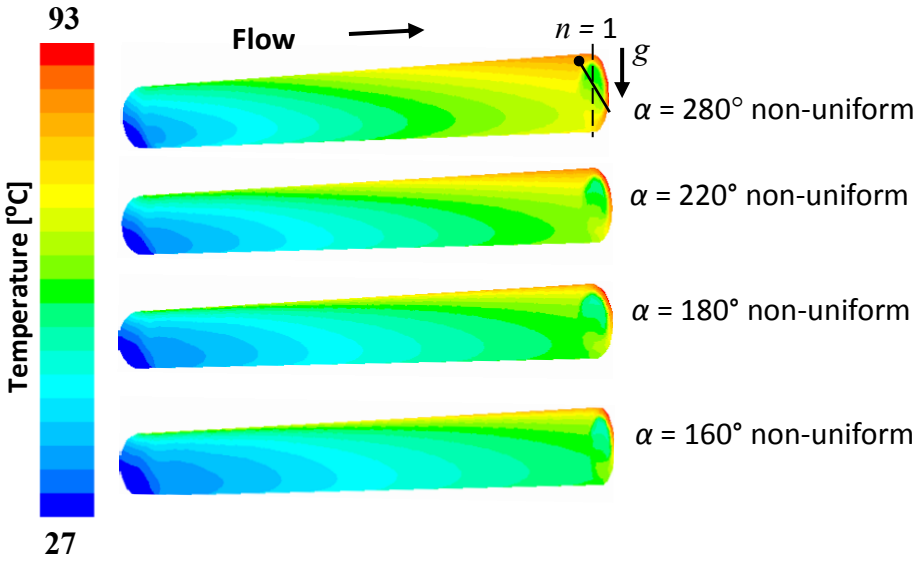

Fig. 7.1 Temperature contours for different angle spans of asymmetrical (γ = 30°) non-uniform heat flux distributions intensity of 7.1 kW/m^2.

7.2 Non-uniform Tube-Wall Temperature Factor

The non-uniformity of the tube-wall temperatures for the asymmetrical heat flux case in Fig. 7.1 are demonstrated in Fig. 7.2. The non-uniform temperature factor, θ_f, expressed in Eq. (4.18) is plotted against the circumferential position (n) for different α values. Fig.7.2 is based on the average outer surface temperature of the full axial length-wise of the tube model. θ_f is essential in determining the non-uniform tube-wall temperature distributions due to non-uniform heat flux distributions over the circumferential outer surface of the tube model. It can be seen that peak θ_f values decrease with an increase in the angle span of the heat flux distributions. The regions with low θ_f values correspond to the region of tube with little or insignificant incident heat flux, while those regions with high θ_f values correspond to the region of higher heat flux. Each angle span profile should be viewed as a whole.

The larger the range of θ_f, the more non-uniform the circumferential wall temperatures are. Thus, it can be seen that the larger angle span cases had lower degrees of non-uniformity in the tube wall temperature. When θ_f = 0, it indicates that either the inner-wall or outer-wall had the same temperature, or that the outer wall temperature is equal to the bulk fluid temperature. This is an indication that little to no overall radial heat transfer occurred at that location. For θ_f > 0, it indicates that there is significant heat transfer from the outer-wall to the fluid. It can also be observed in Fig. 7.2 that towards the ends of the profiles ($n \approx 1$ and $n \approx 36$), θ_f is smaller for smaller heat flux angle spans. This indicates less heat transfer from the outer-wall to the fluid at such locations and this occurs towards the upper region of the tube, which receives very little amount of heat flux.

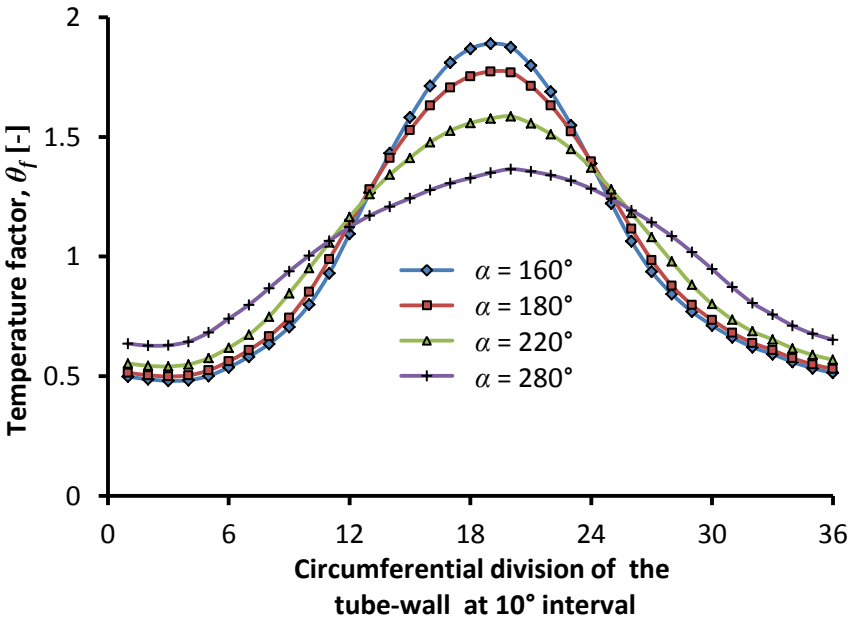

Fig. 7.2 Non-uniform tube wall temperature factor for different spans (α) of asymmetrical non-uniform heat flux boundaries for γ = 30°.

Fig.7.3 shows the non-uniform wall temperature factor profiles for α = 220°. It can be seen that the temperature factor slightly deviated from that of the symmetrically heated case (gravity directed at $\gamma = 0°$). When $\gamma = 40°$, the maximum non-uniform temperature factor shifted away from $n \approx 18$ to 19, *to* $n \approx 20$ to 21. This deviation indicates a significant influence on the internal heat transfer characteristics of the tube model as shown later.

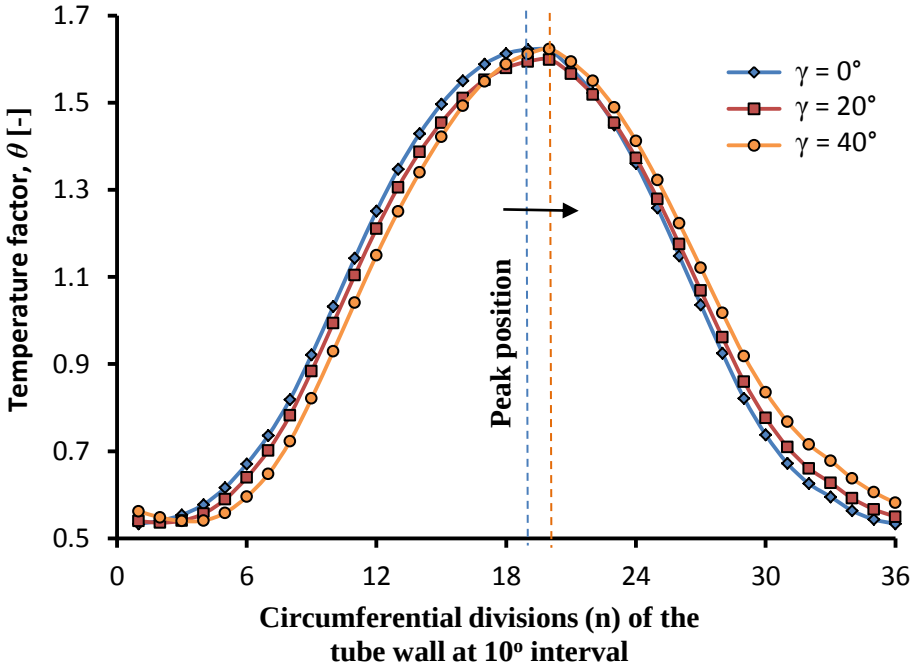

Fig. 7.3 Non-uniform tube wall temperature factor for α = 220° span of symmetrical and asymmetrical sinusoidal non-uniform heat flux distributions boundary

7.3 Fluid Flow Velocity Field and Temperature Distributions

Figs 7.4 (a) and 7.5 (a) show the in-plane velocity vector distributions in the heat transfer fluid at the outlet of the tube model for symmetrical (γ = 0°) and asymmetrical (γ = 30°) for 220° span of sinusoidal non-uniform heat flux distributions.

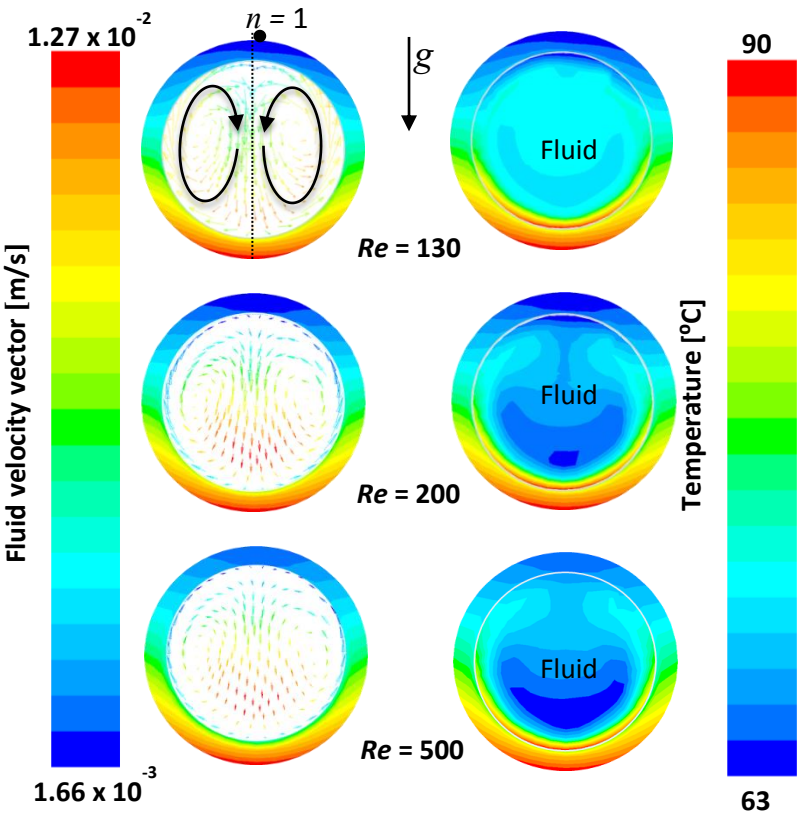

Fig. 7.4 (a) Fluid flow velocity and (b) temperature distribution in the fluid for α = 220° span of symmetrical (γ = 0°) non-uniform heat flux distribution, q'' = 7.1 kW/m^2

The figures give comparisons of the influence of symmetrical and asymmetrical sinusoidal non-uniform heat flux distribution boundaries on the in-plane velocity vector distributions in the heat transfer fluid at the outlet of the tube model at different inlet Reynolds numbers. The velocity vector arrows indicate the upward moving buoyancy-driven flow of the less dense fluid and the downward moving momentum-driven flow of the denser fluid due to influence of the gravity field. It can be seen in Fig. 7.4 (a) that the denser fluid descends to the lower region of the tube along the vertical center of the tube, while the less dense fluid ascends along the tube inner-wall. As before, this is due to the temperature gradient in the fluid and this creates counter-rotating vortices that are superimposed on the forced convection flow as also reported in [103, 116 and 155] for uniform heat flux cases. As also noted in Chapter six,

this phenomenon improves the mixing of the heat transfer fluid and hence increases the heat transfer rate in laminar flow which are generally characterised by low heat transfer coefficient compared with turbulent flow.

In Fig. 7.5 (a), it can be seen that the fluid descending to the lower region of the absorber tube model had shifted away from the heat flux symmetry plane due to the misalignment of the non-uniform heat flux distributions boundary with the gravity field.

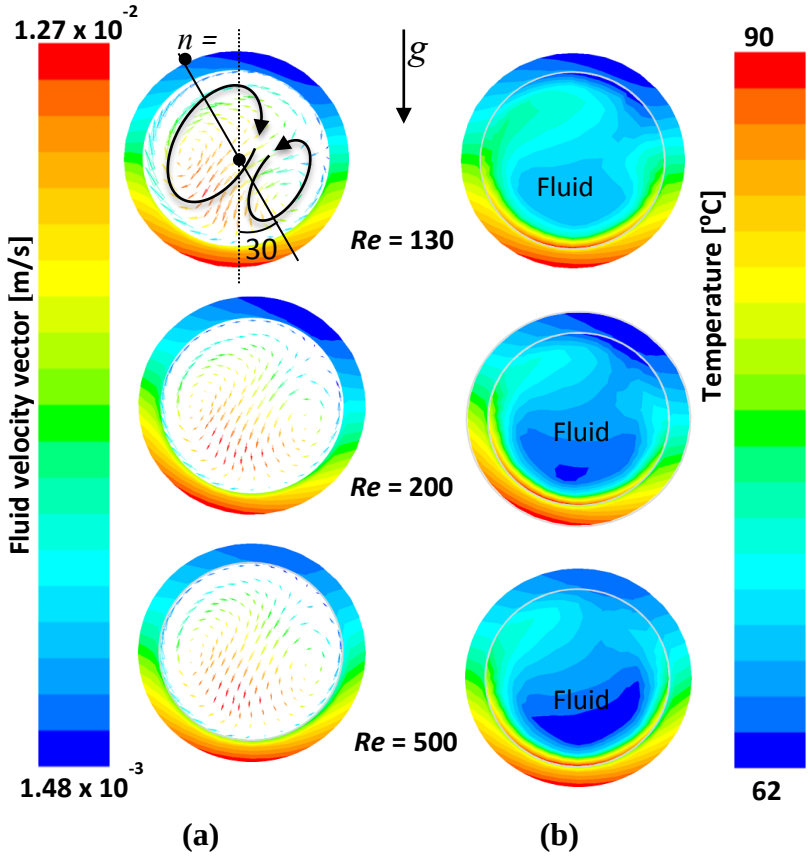

Fig. 7.5 (a) Fluid flow velocity and (b) temperature distribution in the fluid for α = 220° span of asymmetrical non-uniform heat flux distribution, *q"* = 7.1 kW/m^2

This situation could retard the upward and downward fluid circulations and could impede the effective thermal mixing of the fluid and thus a decrease in the internal heat transfer rate. Fig.7.5 (a) demonstrates the influence of misalignment of the heat flux boundary with the symmetrical axis on the velocity distribution profile of laminar mixed convection for an absorber tube in a horizontal orientation. It can also be seen that the intensity decreases with the increase in Reynolds number. As before the influence of the buoyancy effects in laminar mixed convection decrease with an increase Reynolds number due to an increase in forced convection effects.

Figs 7.4 (b) and 7.5 (b) show the temperature distributions in the fluid at the outlet of the tube and around the tube-wall, for the symmetrical and asymmetrical non-uniform heat flux cases in Figs 7.4 (a) and 7.5 (a). The figures indicate that the temperature distributions in the fluid vary due to the non-uniform heat flux distribution boundary and that the temperature of the fluid near the heated wall is higher than the temperature fluid towards the inner region of the tube. Unlike in Fig. 7.4 (b), it can be seen in Fig. 7.5 (b) that the fluid layers are slanted due to the misalignment of the non-uniform heat flux boundary with the gravity field. The temperature gradient in the fluid decreases with the increase in Reynolds number. The red shade in the lower region of the tube shows the most heated region of the fluid. While the blue shade on upper region of the tube indicates the cooler region of the tube simply because there is little or insignificant incident heat flux in those regions. Also, the blue shade indicates the fluid layers at different temperatures, with the lowest temperature region occurs slightly above the heated tube wall.

7.4 Richardson Number for Non-uniform Heat Flux Distributions Boundary

Fig.7.6 shows the variation of Richardson number at different circumferential angle spans of symmetrical (γ = 0°) compared with the asymmetrical (γ = 30°) sinusoidal non-uniform heat flux distributions boundaries at different inlet Reynolds numbers. It indicates the relative strength of buoyancy effects due to non-uniform heat flux boundary to the forced convection heat transfer. In Fig.7.6, the symmetrical case types are shown in solid lines, while asymmetrical case types are shown with broken lines. For both case types, *Ri* increases with

an increase in the circumferential surface of the tube exposed to the incident heat flux and thus an increase in the effective heat input rate into the absorber tube. It is found that *Ri* for the symmetrical case is approximately 7.1% higher than that of asymmetrical case for the Reynolds number cases considered. This reveals that the influence of buoyancy-induced secondary flow decreases when there is misalignment between the gravity field and the heat flux symmetry plane. It is further found that *Ri* decreases with an increase in Reynolds number, indicating that the buoyancy effects also decrease with an increase in Reynolds number. This could be due to the increase in the forced convection effects. For all the cases considered at *Re* = 400 and *Re* = 500, *Ri* is greater than 10, which indicates that the heat transfer is dominated by natural convention due to buoyancy effect and that forced convection effect is negligible. For some *Re* = 800 cases (α = 140° to 260°) and all Re = 1300 cases, *Ri* is found to be between 0.1 and 10, which indicates mixed convection states.

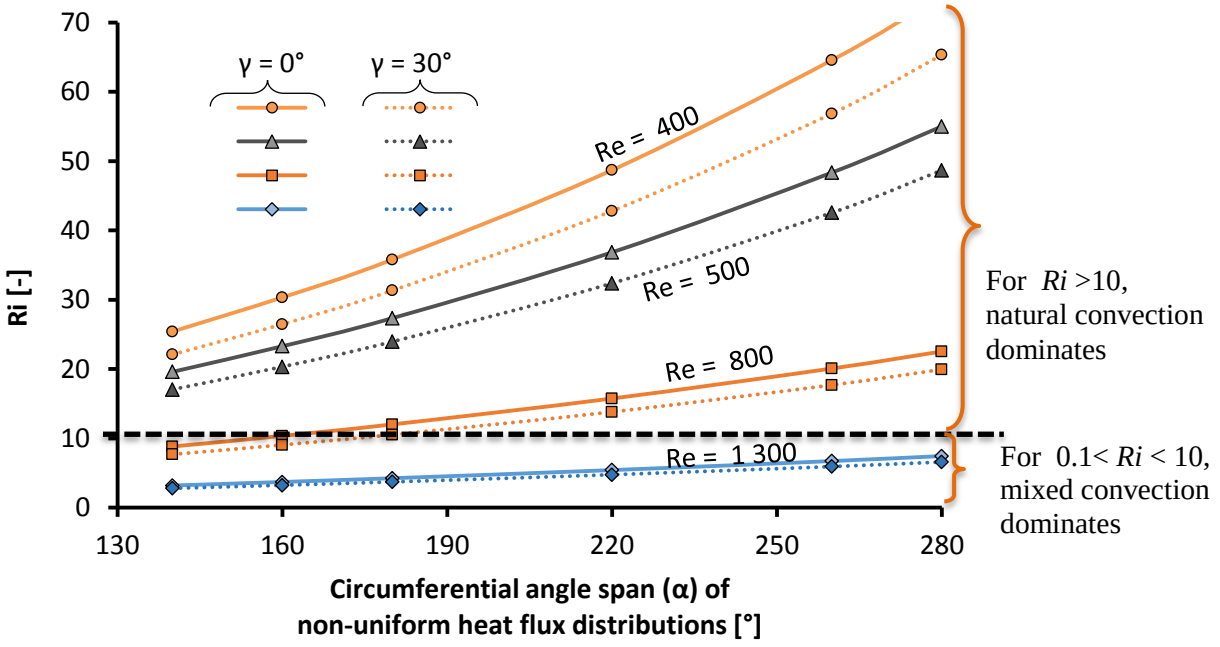

Fig. 7.6 Variation of ***Ri*** with different angle spans of symmetrical and asymmetrical non-uniform heat flux distributions, q'' = 7.1 kW/m^2

7.5 Internal Heat Transfer Coefficients for Non-Uniform Heat Flux Boundary

Fig. 7.7 shows the variation of the average internal heat transfer coefficient for α = 220° at γ = 0°, 20°, 30° and 40° for the non-uniform heat flux distributions at various inlet Reynolds numbers, for q'' = 7.1 kW/m^2. Also included in this figure, for comparative purposes, are the heat transfer coefficients for the associated fully uniform heat flux case (see Table 4.2). All results in this figure are thus for absorber tube cases having the same incident heat transfer rate [W] on the outer tube wall. The fully uniform heat flux case distributes the heat evenly as shown in Fig.4.5 (a), while the non-uniform sinusoidal heat flux distributions result in higher heat flux concentrations over a smaller outer tube surface.

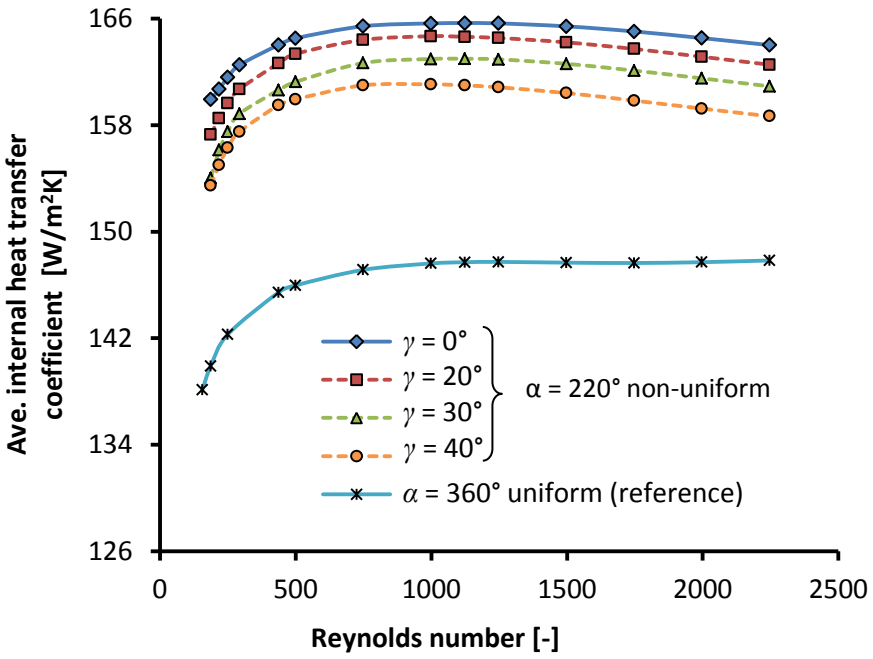

Fig. 7.7 Variation of the average internal heat transfer coefficient for α = 220° span of symmetrical and asymmetrical non-uniform heat flux, q'' = 7.1 kW/m^2

Symmetrical (γ = 0°) heat flux cases are represented with solid lines while asymmetrical cases are represented with the broken lines. Fig.7.7 demonstrates that the misalignment between the heat flux symmetry plane and the gravity field has an influence on the average heat transfer coefficient. The heat transfer coefficient decreases as γ increases. This could be due to differences in buoyancy-induced secondary flow and the relative sizes of the

circulation vortices. For all the cases contained in Fig. 7.7 it was, however, found that concentrated heat flux cases described by the sinusoidal type function have higher effective heat transfer coefficients than the associated uniform heat flux case, even though the same incident heat transfer rate was applied. It was found that the average internal heat transfer coefficient decreases as the non-uniform heat flux distributions deviated from the symmetrical axis of the tube model. This could be due to decrease in the influence of buoyancy-induced secondary flow. The average internal heat transfer coefficient for the symmetrical case (γ = 0°), is 1.7%, 3.8% and 4.3% higher than that of the asymmetrical cases of γ = 20°, 30° and 40°, and 14% higher than the associated uniform heat flux case, all at a Reynolds number of 187. It can also be observed in Fig. 7.7 that the heat transfer coefficient decreased slightly at higher Reynolds numbers. This could be due to decrease in the effective buoyancy-effect with an increase in Reynolds numbers. In Fig. 7.6, buoyancy-effects also decrease with an increase in Reynolds number and a decrease in Richardson number due to an increase in forced-convection effect. Fig. 7.6 also indicates that the buoyancy effect decreases with an increase in γ.

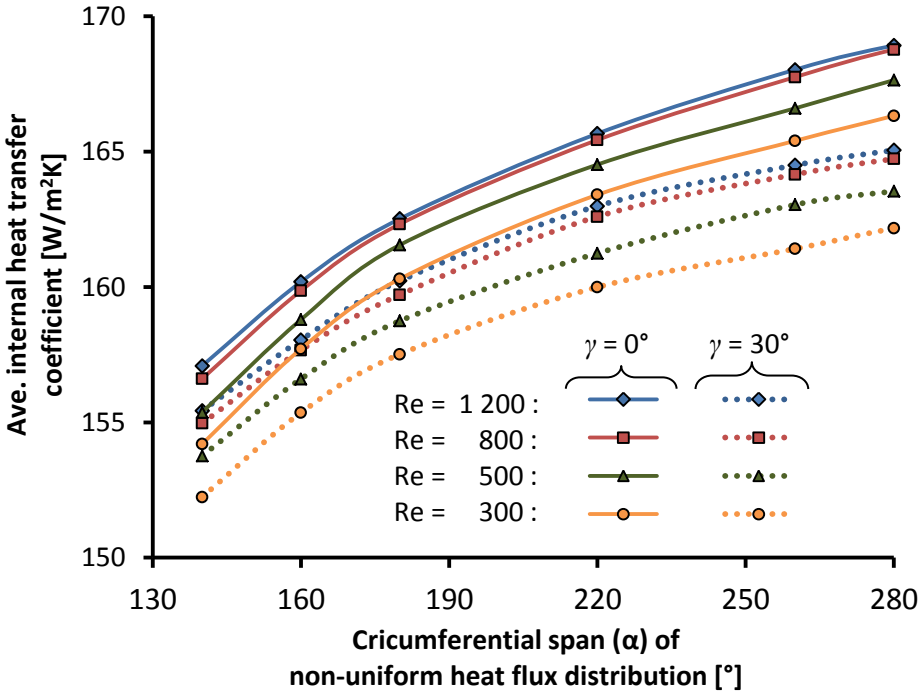

Fig. 7.8 Variation of average internal heat transfer coefficient for different spans (α) of sinusoidal symmetrical and asymmetrical non-uniform heat flux distributions.

Fig. 7.8 shows the influence of different circumferential spans of sinusoidal non-uniform heat flux distributions at different inlet Reynolds numbers on the average internal heat transfer coefficient. The figure allows the average internal heat transfer coefficients to be compared with the cases where the sinusoidal non-uniform heat flux distributions are symmetrical (γ = 0°) and asymmetrical (γ = 30°). The asymmetrical non-uniform heat flux distributions cases are shown with the broken lines. It was found that the average internal heat transfer coefficient for the asymmetrical case is lower than that of the symmetrical case for all angle spans. These differences are higher at larger angle spans. The average internal heat transfer coefficient for the symmetrical case is found to be marginally higher by approximately 3.0% across the Reynolds number range. Fig. 7.8 therefore, reveals that for a circular absorber tube in a horizontal orientation, the average internal heat transfer coefficient is significantly influenced when the non-uniform heat flux distributions are asymmetrical with the heat flux boundaries. It was further found that at Reynolds numbers of 1200 and 800, the average internal heat transfer coefficients are approximately the same for both the symmetrical and asymmetrical non-uniform heat flux boundaries. This indicates that there is no significant increase in the internal heat transfer coefficient at higher Reynolds number with the variation of the circumferential span of the heat flux distributions.

Fig. 7.9 shows the influence of the external loss convective heat transfer coefficient, h_o, on the average internal heat transfer coefficient, for α = 260° sinusoidal non-uniform heat flux distributions with symmetrical (γ = 0°) and asymmetrical (γ = 20°, 30° and 40°) heat flux boundaries. The average internal heat transfer coefficient is coupled to the external heat transfer coefficient due to the impact that the tube wall temperature has on the secondary flow patterns. It was found that the internal heat transfer coefficient decreases with an increase in the external convective heat loss transfer coefficient from 22.3 W/m^{2}K to 75.0 W/m^{2}K. As before, the average internal heat transfer coefficient also decreases with an increase in γ due to the variation of the relative sizes of the fluid circulation vortexes associated with buoyancy effects.

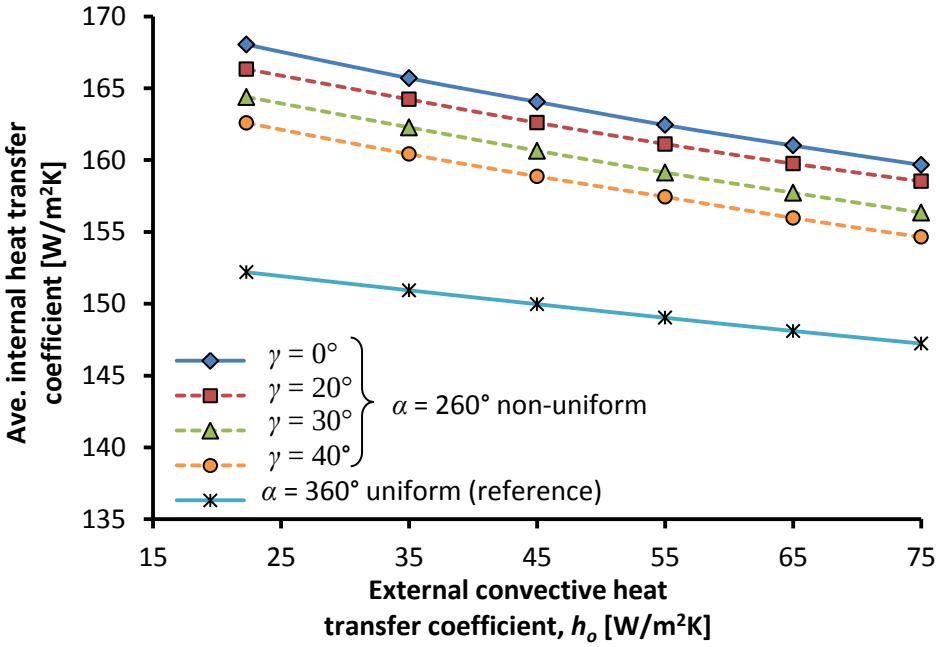

Fig. 7.9 Influence of external loss convective heat transfer coefficient on average internal heat transfer coefficient for symmetrical and asymmetrical non-uniform heat flux distributions, q'' = 7.1 kW/m^2

Fig. 7.9 thus indicates that as the heating becomes more asymmetrical, the one vortex becomes smaller, while the other becomes larger for the symmetrical case and this can be observed in Fig. 7.5(a). The average internal heat transfer coefficient for the symmetrical case is 3.4 % higher than the asymmetrical case of γ = 40°, for the external loss convective heat transfer coefficient of 22.3 W/m^{2}K and 10 % higher than the associated uniform heat flux case.

In Fig.7.10 the influence of the external convective heat loss transfer coefficient on the average internal heat transfer coefficient is shown, for γ = 20° with α = 160°, 220°, and 260°. Similar decreasing behaviour was observed for all angle span cases. The *Ri* number was found to be lower when the *Nu* number was lower due to the impact the tube-wall heat flux distributions boundary has on the buoyancy-driven flow component within the tube. As earlier explained, the external convective heat loss transfer coefficient increases with an increase in the air velocity around the collector receiver tube outer surface. This results in an

increase in the external convective heat loss and a decrease in the heat transfer rate from the external tube-wall surface to the heat transfer fluid in the tube.

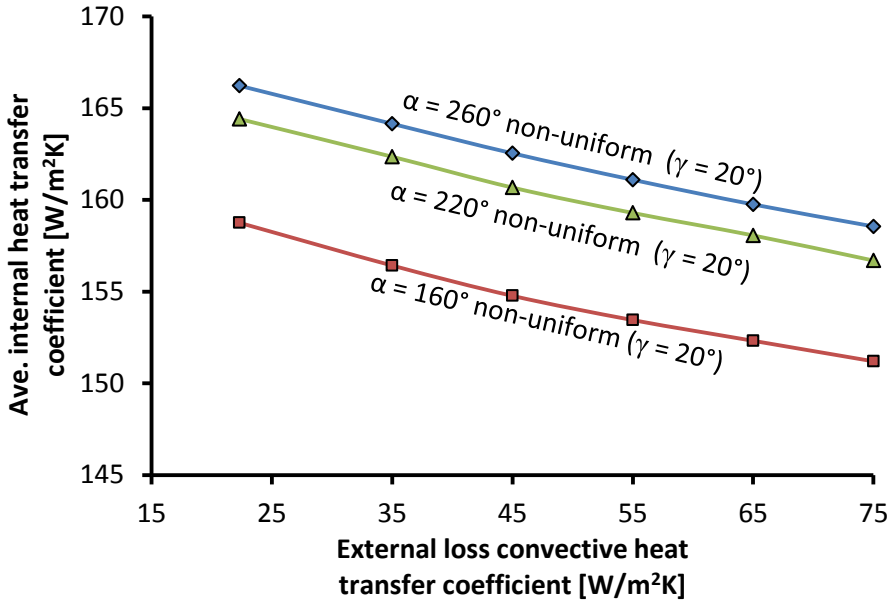

Fig. 7.10 Influence of the external convective heat loss transfer coefficient on the average internal heat transfer coefficient for different values of α at $\gamma = 20°$

Fig.7.11 shows the variations of the average internal heat transfer coefficient for different inlet fluid temperatures, for $\alpha = 260°$ and $\gamma = 0°$ and 40°, for two different heat flux intensities at an inlet Reynolds number of 800. As earlier noted in Fig.6.14, the internal heat transfer coefficient also increases with an increase in the heat flux intensities and the inlet fluid temperatures at the same ambient temperature condition. As in Fig. 7.9, the internal heat transfer also decreases with an increase in γ, due to the relative sizes of fluid circulation vortexes.

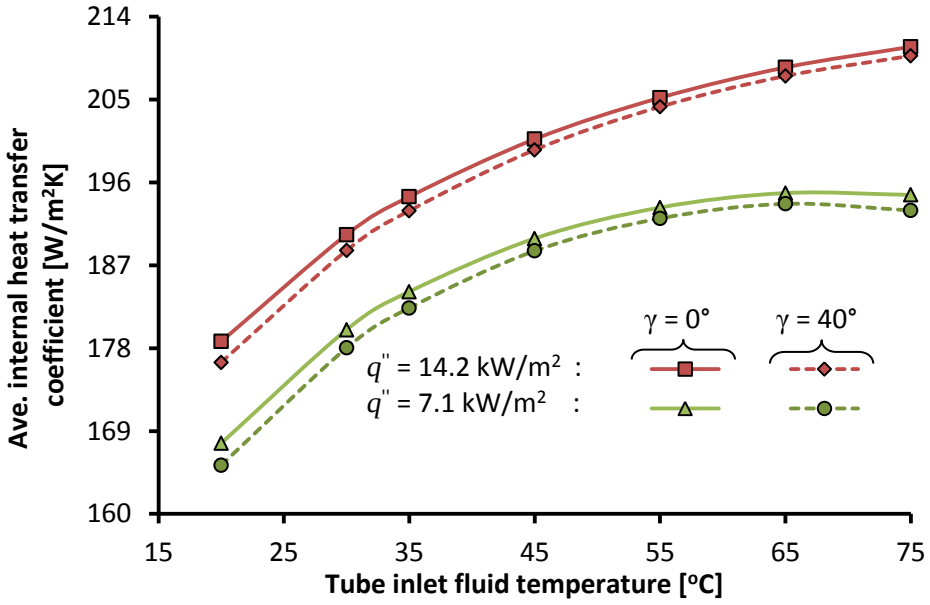

Fig. 7.11 Variation of average internal heat transfer coefficient with fluid inlet temperature for symmetrical and asymmetrical non-uniform heat flux distributions

7.6 Friction Factors for Non-Uniform Heat Flux Boundary

Fig. 7.12 shows the variation of the friction factors with an increase in circumferential spans (α) of sinusoidal non-uniform heat flux distributions cases in Fig.7.8 at different inlet Reynolds numbers. It gives a comparison of the friction factors for symmetrical (γ = 0°) and asymmetrical (γ = 30°) cases. Symmetrical heat flux cases are again represented with solid lines while asymmetrical cases are represented with the broken lines. As it should be expected, the friction factors decrease with an increase in Reynolds number. The friction factors for both cases are nearly constant through-out the angle span range, especially at the higher Reynolds numbers, indicating that friction factor is slightly influenced with an increase in the circumferential angle spans of non-uniform heat flux distributions.

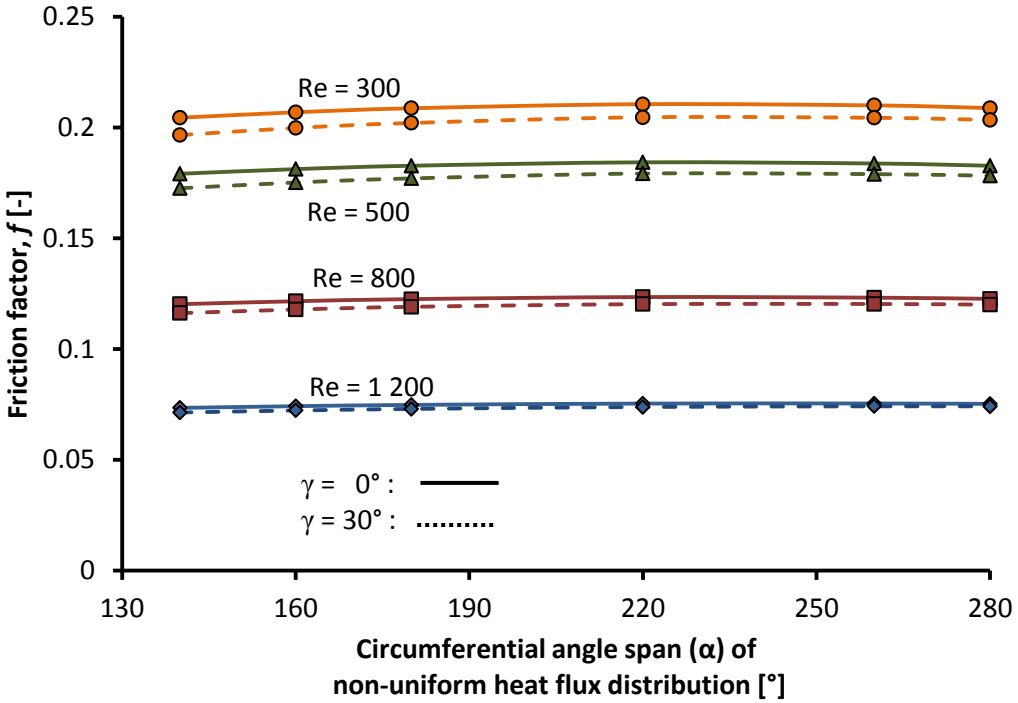

Fig. 7.12 Variation of the friction factors with the different angle spans of symmetrical and asymmetrical sinusoidal non-uniform heat flux distributions.

Similar as with the heat transfer coefficients, the friction factor for the symmetrical heated case is only about 4% higher than for the 30° asymmetrical case at lower angle span for Re = 300. This difference is due to the influence of buoyancy effects, which also decrease with an increase in Reynolds number. The importance of considering secondary flow is once again highlighted in Fig. 7.13, which gives the results obtained with and without buoyancy-driven secondary flow.

It was found that when buoyancy-driven secondary flow is considered, the friction factor is higher by between 39% and 25% for α = 260° and γ = 30°, for the Reynolds number range of 130 to 2000, than when it is neglected. Figs 7.12 and 7.13 reveal that friction factor characteristics of a horizontal circular absorber tube are also sensitive to the orientation of the non-uniform heat flux distributions boundary with the gravitational field, mostly at the lower Reynolds number.

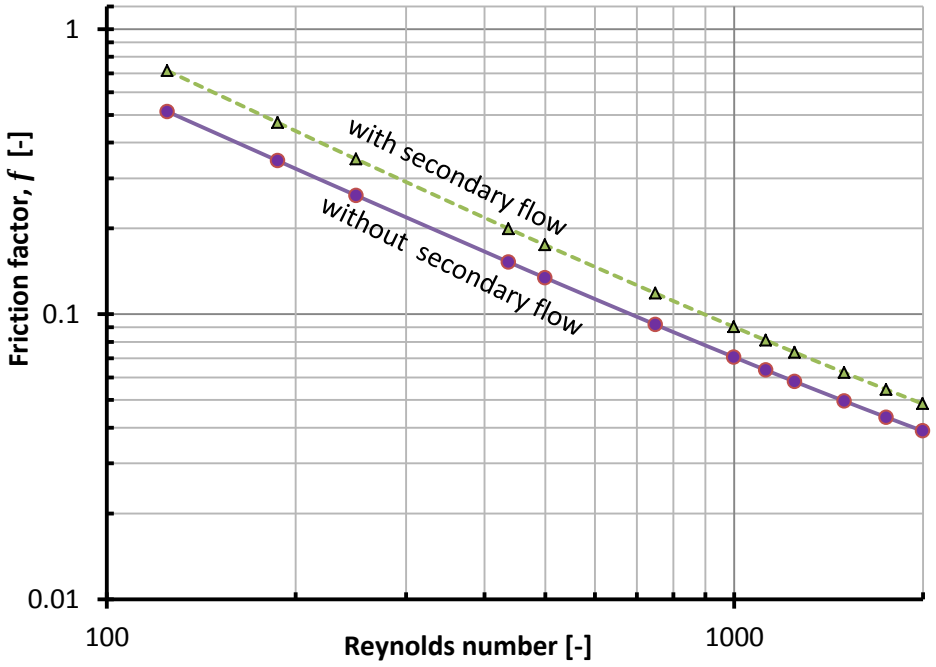

Fig. 7.13 Friction factors for α = 260° and γ = 30° asymmetrical non-uniform heat flux distributions with and without buoyancy-driven secondary flow for an inlet Reynolds number of range of 130 to 2000.

Fig. 7.14 shows the influence of the external convective heat loss transfer coefficient on the friction factor for the non-uniform heat flux distribution case in Fig. 7.9 for α = 260°. Also included are the associated fully uniform heat flux results for the same incident heat transfer rate [W].

It was found that the friction factor for both the symmetrical and asymmetrical cases of the non-uniform heat flux distributions decrease with an increase in the external convective heat loss transfer coefficient. It was also found that the friction factor decreases as the non-uniform heat flux distribution symmetry plane is misaligned with the gravity field. This is due to the impact of conjugate heat transfer in the tube-wall on the secondary flow patterns within the tube. The fully uniform heat flux case had a significantly lower friction factor, indicating that the concentrated non-uniform heat flux profile on the outer tube surface from below had a significant role on the effective pressure drop.

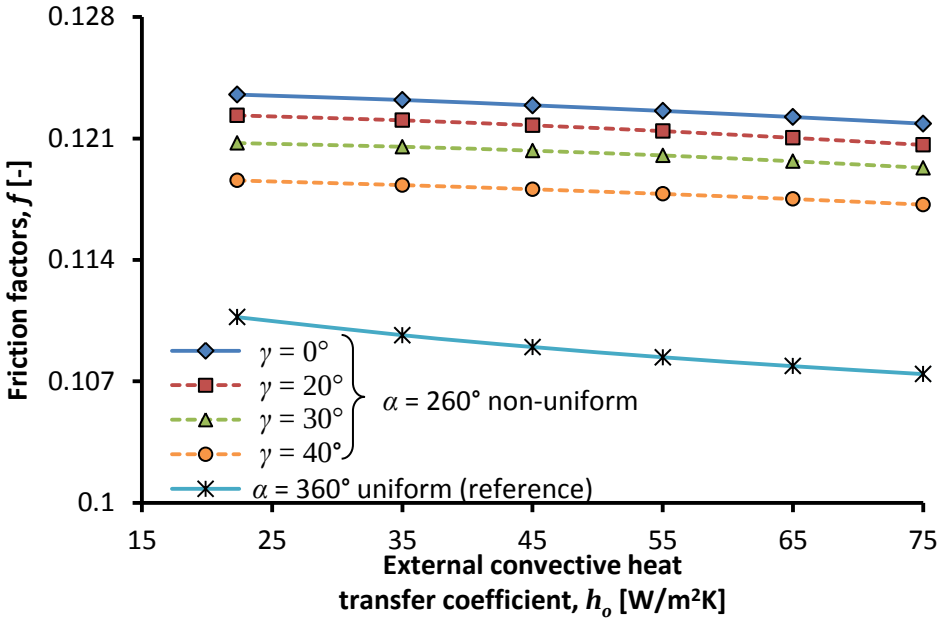

Fig. 7.14 Influence of external convective heat loss transfer coefficient on of friction factor for symmetrical and asymmetrical non-uniform heat flux, q'' = 7.1 kW/m^2

Fig. 7.15 shows the variations of the friction factor for different inlet fluid temperature for the non-uniform heat flux distribution intensities in Fig. 7.11. It was found that the friction factor increases with an increase in the heat flux intensities due to buoyancy effects. It was also found that the friction factor decreases with an increase in the fluid inlet temperature. This could be attributed to a decrease in the fluid density with increase in temperature. As shown in Fig. 7.14, friction factor also decreases with an increase in γ and this could be due to a decrease in buoyancy effect as the heat flux distributions axis deviates from the symmetrical plane. Fig.7.15 indicates that the effect of the asymmetrical non-uniform heat flux boundary on the friction factor for the tube model considered is much higher for the fluid inlet temperature than for the external convective heat loss transfer coefficient shown in Fig. 7.14.

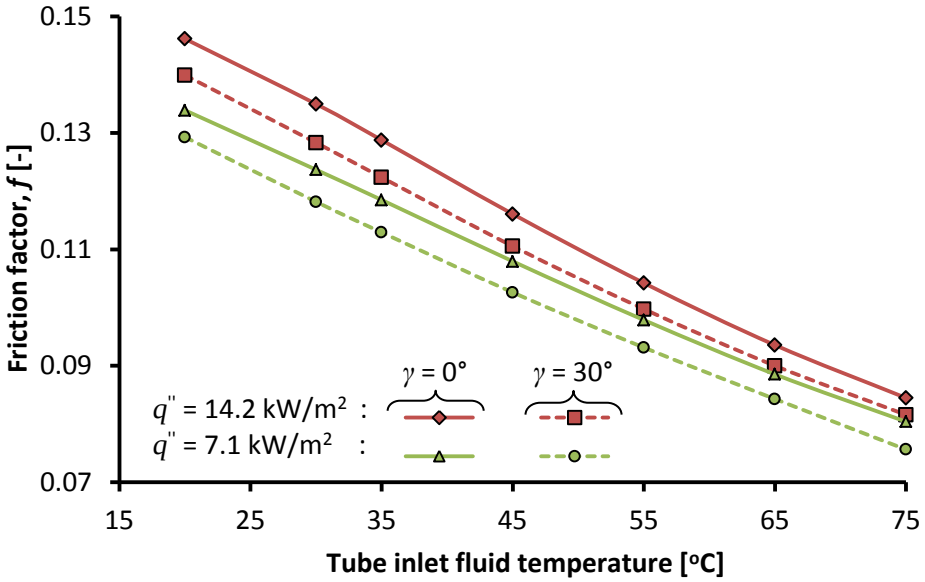

Fig. 7.15 Variation of friction factor with fluid inlet temperature for symmetrical and asymmetrical non-uniform heat flux distributions

7.7 Conclusion

The influence of asymmetrical non-uniform heat flux distributions in terms of the gravitational field on the buoyancy induced secondary flow; internal heat transfer and friction factors for the absorber tube model were determined for the inlet Reynolds number range of 130 to 2200 and compared with the case of symmetrical non-uniform heat flux distributions boundary. The results indicated that the average internal heat transfer coefficient and friction factor decrease as the non-uniform heat flux distribution boundary misaligned with the symmetrical axis of the tube in terms of the gravitational direction. It was also found that the internal heat transfer coefficient increases with an increase in the circumferential span of the symmetrical and asymmetrical non-uniform heat flux distribution boundaries, due to buoyancy effects. However, for cases having the same incident heat transfer rate, the non-uniform concentrated heat flux distributions had much higher significant impact when compared to a fully uniform external heat flux boundary. In such cases the average heat transfer coefficients was up to 15% higher than for the fully uniform heat flux cases for the conditions considered in this study. These differences are due to the buoyancy-induced secondary flow and non-uniformity in the tube wall temperature, indicating that appropriate

heat flux distributions boundary must be considered, otherwise the internal heat transfer coefficient could be underestimated if uniform heat flux is considered where the heat flux distributions is non-uniform. Higher fluid inlet temperatures resulted in higher inner heat transfer coefficients, while increased outer tube wall heat flux losses resulted in lower inner heat transfer coefficients and friction factors.

In the next chapter the influence of non-uniform heat flux boundary distributions for turbulent flow conditions are considered.

CHAPTER EIGHT: NUMERICAL RESULTS AND ANALYSIS FOR NON-UNIFORM HEAT FLUX DISTRIBUTIONS FOR TURBULENT FLOW HEAT TRANSFER

8.0 Introduction

In this chapter, the numerical simulation results are analysed for the influence of symmetrical and asymmetrical sinusoidal non-uniform cases of heat flux distributions boundaries in the turbulent flow regime. The k-ε model was employed to simulate the turbulent flow through the absorber tube model. The inlet Reynolds number range of 3030 to 9200 and 12100 to 202600 are considered to take into consideration the weak turbulent flow regime, where the buoyancy-induced secondary flow phenomenon due to circumferential spans of heat flux distributions boundary, could have significant enhancement on the forced-convection heat transfer of the tube model. However, it would have smaller enhancement on the internal heat transfer coefficients than in the laminar flow regime.

8.1 Symmetrical Non-uniform Heat Flux Distributions for Weak Turbulent Flow Regime

In this section, the influence of circumferential spans of non-uniform heat flux distributions boundaries on the secondary flow, internal heat transfer and friction factors for the tube model are analysed in the weak turbulent flow regime at the inlet Reynolds number range of 3030 and 9200. Also, the influence of different fluid inlet temperatures on the internal surface heat transfer coefficient and the friction factors are presented.

8.1.1 Non-uniform Tube-wall Temperature Contour

Fig 8.1 gives simulation results indicating the tube-wall temperature contours in the weak turbulent flow regime and Reynolds number of 5100. The external wall surface of the tube model was subjected to convective and radiative heat flux losses. The inlet temperature of the heat transfer fluid was 27 °C. The collector absorber tubes are of dimensional case 1 and have an outer diameter of 73 mm and wall thickness of 5.2 mm. The outer-wall surface temperatures of the tubes increase in the direction of the fluid flow and are greater at the outlet of the tubes as shown by the red shade on the temperature scale. It can also be observed that the lower region of

the tubes are warmest than the upper region of the tubes, indicating high temperature differential around the walls of the tubes. This could result in a local overheating due to the concentration of the non-uniform heat flux at the lower region of the tubes.

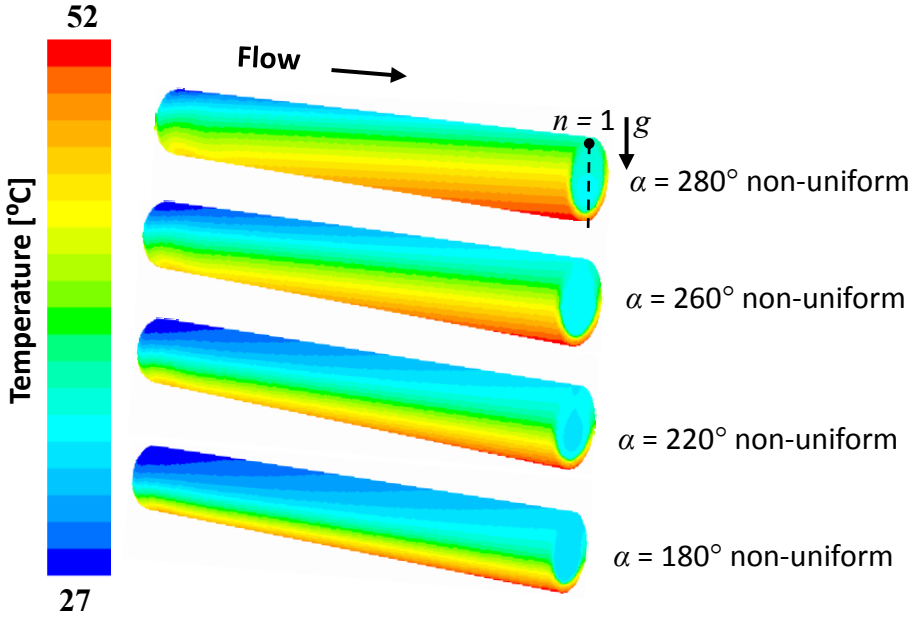

Fig. 8.1 Tube-wall temperature profiles for different circumferential spans of sinusoidal non-uniform heat flux distributions base-level intensity of 7.1 kW/m^2 and Re = 5100

The lower temperatures in the upper regions of the tubes are due to little or no concentrated incident heat flux in those locations and that small amount of heat is conducted to the upper region of the tubes.

8.1.2 Non-Uniform Tube-wall Temperature Factor

The non-uniformity of the tube wall temperature in Figs 8.1 is also demonstrated in Fig. 8.2, where the non-uniform temperature factor, θ_f, defined in Eq. (4.18) is plotted against the circumferential position for different α values. It can be seen that θ_f is maximum at the peak of the profiles ($n \approx 18$ and 19), which corresponds to the lower central portion of the tube with the maximum incident heat flux.

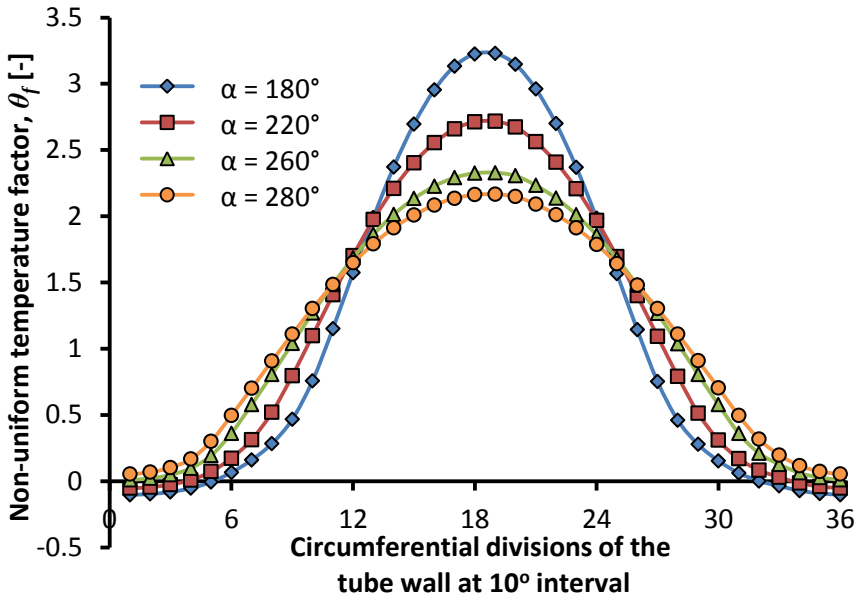

Fig. 8.2 Non-uniform temperature factor for the sinusoidal non-uniform heat flux distributions for a base-level heat flux intensity of 7.1 kW/m^2 and Re = 5100

Eq. (4.18) indicates that for $\theta_f = 0$, the outer-wall temperature is equal to the bulk fluid temperature, which implies no heat transfer from the outer-wall to the fluid at that segment. However, for $\theta_f > 0$, it indicates heat transfer from the outer-wall to the fluid at a particular segment. It can also be observed that towards the two ends of the profiles, $\theta_f < 0$ indicating heat loss from the fluid at segment *n* and this occurred towards upper region of the tube which received little or insignificant heat flux.

8.1.3 Fluid Flow Velocity and Temperature Distributions

In the weak turbulent flow regime, the secondary flow effects could still have distortion effects on the temperature and velocity profiles on pure forced-convection heat transfer. Fig. 8.3 (a) shows the fluid flow in-plane velocity vector at the outlet of the tube for α = 260° at different inlet Reynolds numbers. The figure indicates that the velocity distributions in the fluid varied. The velocity vector arrows indicate the upward buoyancy-driven flow of the less dense fluid and the downward momentum-driven flow of the denser fluid due to buoyancy-effects, as in the case of laminar flow in Chapter six. This results in counter-rotating vortices that are superimposed on

the turbulent forced convection flow. This increases the thermal mixing of the fluid and, thus improves the internal heat transfer performance of the collector tube. It can be seen that the intensity of the upward and downward circulations of the fluid is much higher for Re = 4100, which decreases as the Reynolds number increases and becomes insignificant at Re = 12100.

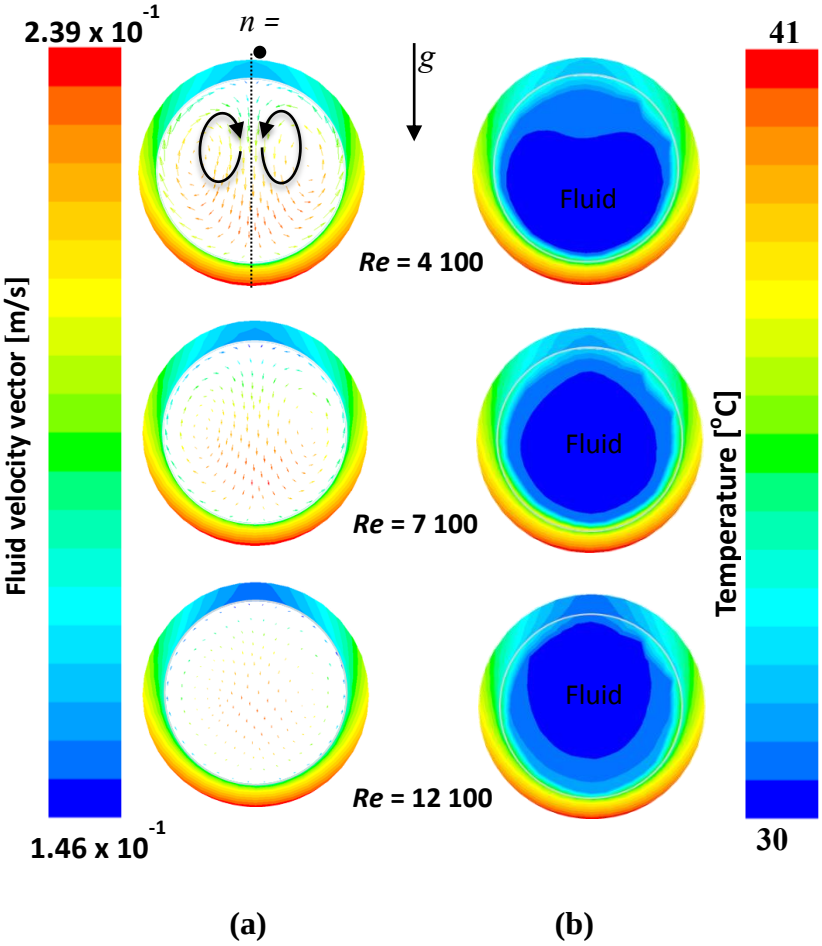

Fig. 8.3 (a) Fluid flow velocity and (b) temperature distribution in the fluid for a symmetrical non-uniform heat flux distribution at an intensity of 7.1 kW/m^2 and for α = 260°

Fig. 8.3 indicates that the secondary flow effects due to non-uniform heat flux boundaries in the weak turbulent flow forced convection is still significant at Reynolds number less than 12 100 and results in a significant internal heat transfer enhancement. This is in line with the findings by Grassi and Testi [120] who experimentally investigated developing turbulent mixed convection in a uniformly heated horizontal circular pipe at Re = 5750. In Fig. 8.3(b), the

temperature distributions in the fluid and around the tube wall also varied. For Re = 4100, it can be observed that the fluid with higher temperature circulated towards the upper region of the tube due to buoyancy effect. Similar results were obtained experimentally for uniform heating cases as presented in Petukhov and Polyakov [156]. However, for Re = 12 100, where buoyancy effect appears insignificant, the fluid with lower temperature appears at the upper region, while the higher temperature fluid is at the lower region of the tube. The blue shade in the inner central region of the tube indicates the lowest temperature region of the fluid.

8.1.4 Richardson Number for Symmetrical Non-Uniform Heat Flux Distributions

Fig.8.4 shows the variation of *Ri* with the symmetrical spans of non-uniform heat flux distributions boundary and Reynolds number ranging from 5100 to 16200.

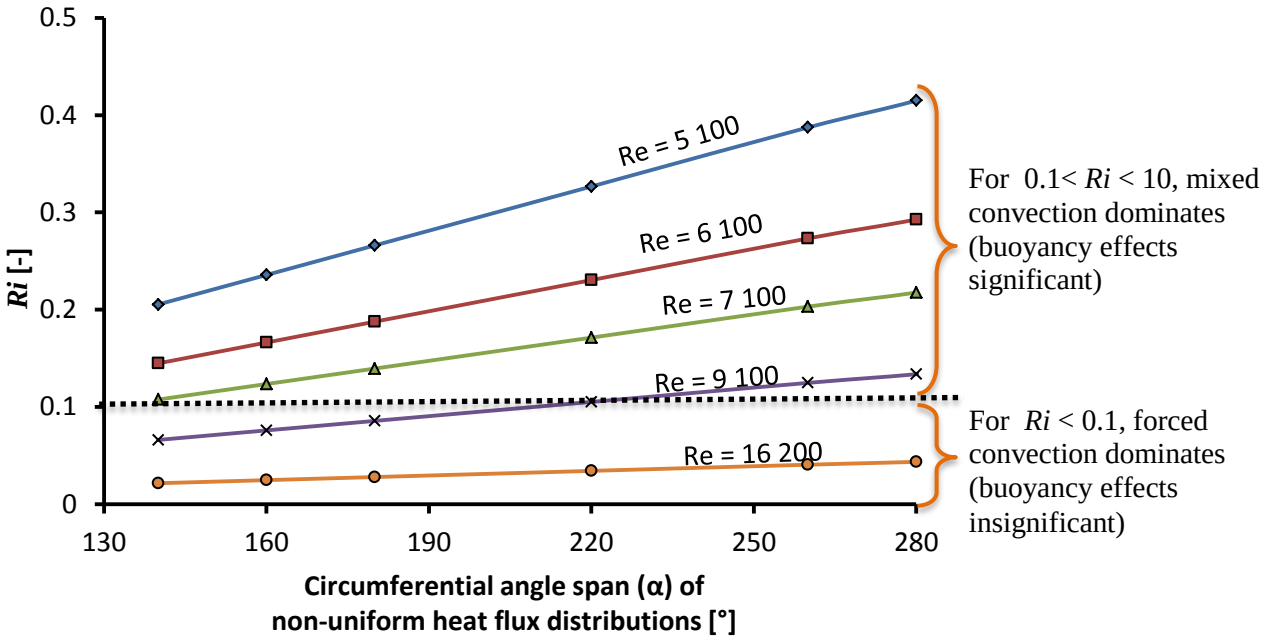

Fig. 8.4 Variation of Richardson number with the circumferential angle spans of the sinusoidal non-uniform heat flux distributions for a heat flux intensity of 7.1 kW/m^2

It can be seen that *Ri* increases with an increase in the circumferential span of the tube-wall with the heat flux distribution boundary and thus an increase in the effective heat input rate. The increase in *Ri* was more pronounced at the lower turbulent Reynolds number. This indicates that the induced secondary flow effect due to the non-uniform on heat flux boundaries has significant effects in the weak turbulent flow regime. It was also found that *Ri* decreases with an increase in Reynolds number, which shows the stronger influence of buoyancy effects at lower Reynolds numbers and the weaker influence of buoyancy effects at higher Reynolds numbers. It can be seen that at Re = 5100, 6100 and 7100 for α = 140° to 280° and Re = 9100 for α = 220° to 280° are all in the range of 0.1< *Ri* <10, which indicated that the turbulent mixed convection heat transfer dominated in this Reynolds number range. For Re = 16 200, it was found that *Ri* is less than 0.1 for all circumferential spans of the heat flux distributions boundaries considered, indicating that buoyancy effect is negligible and that forced-convection dominated the heat transfer processes.

8.1.5 Heat Transfer Coefficients for Symmetrical Non-Uniform Heat Flux Distributions

Fig.8.5 shows the variation of average internal heat transfer coefficient with the inlet Reynolds number for symmetrical α = 260° of different base-level heat flux intensities, where secondary flow effect is present and it is not considered. As it could be expected, average internal heat transfer coefficient increases with the Reynolds number. It was found that there is no significant enhancement of the internal heat transfer coefficients where buoyancy effect is neglected. By contrast, the average internal heat transfer coefficient increases as the non-uniform heat flux base-level intensity is increased.

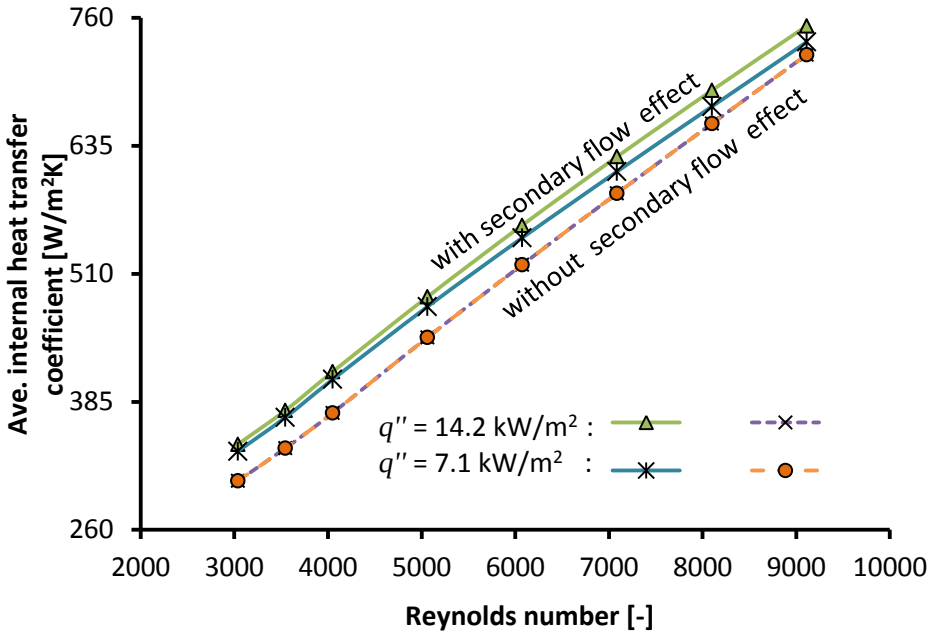

Fig. 8.5 Variation of average internal heat transfer coefficient with the Reynolds number for two different base-level heat flux intensities for α = 260° sinusoidal non-uniform heat flux

It was found that at the inlet Reynolds number of 4000, the average internal heat transfer coefficients for the flux intensities considered, where buoyancy effect is present are 10% and 8% higher than that where buoyancy-effect is neglected. Fig. 8.5 indicates that buoyancy-induced secondary flow still gives a significant internal heat transfer enhancement and therefore cannot be neglected in the Reynolds number range less than 9400. This is also in line with Fig. 8.4 which indicates that the Richardson number for α = 260° to 280^{o} spans of non-uniform distributions in the Reynolds number range less than 9100 are within the turbulent mixed convection regime.

Fig. 8.6 shows the influence of different inlet fluid temperatures on the average internal heat transfer coefficient for α = 260°, with and without buoyancy effects considered. While maintaining the same ambient temperature, it was found that the average internal heat transfer coefficient increases with an increase in the inlet fluid temperature. It was also found that there is no significant enhancement in the average internal heat transfer coefficient for the two heat flux intensities considered, where buoyancy effects are neglected. However, where buoyancy effects are present, the average internal heat transfer coefficients are 8.7% to 15.1 % and 6.4 %

to 11.0% higher than where buoyancy effects are neglected, for the two cases, at the inlet fluid temperature range of 20 ºC to 85 ºC. Also, at the same ambient temperature, the internal heat transfer coefficient increased up to 87% by increasing the fluid inlet temperature from 20 ºC to 85 ºC. This indicates the influence of pre-heating the inlet heat transfer fluid on the internal heat transfer coefficient of a horizontal absorber tube.

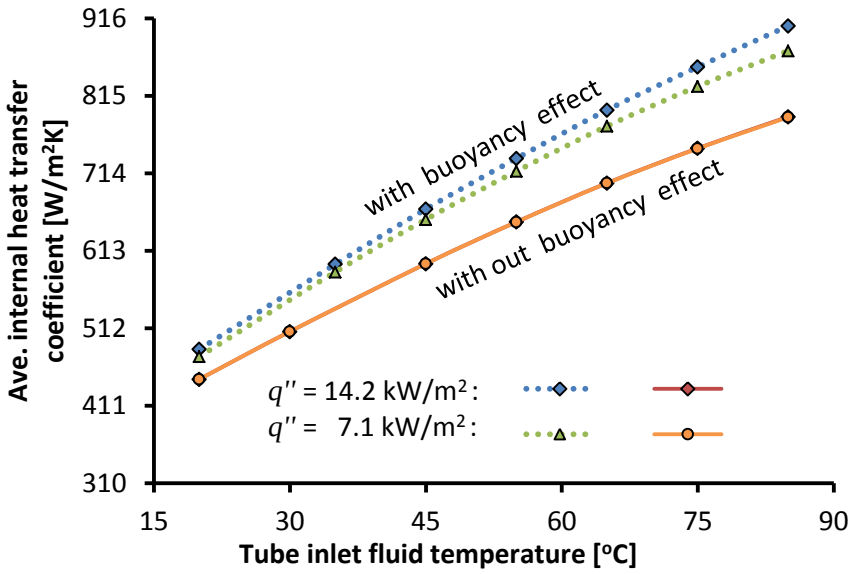

Fig. 8.6 Average internal heat transfer coefficient for α = 260° sinusoidal non-uniform heat flux distributions boundary at different inlet fluid temperatures.

Fig. 8.6 also indicates that with the buoyancy effects present, the internal heat transfer coefficient increases with an increase in heat flux intensities. This agreed with the experimental results of [118] for the case of uniform heat flux distribution boundary.

8.1.6 Friction Factors for Uniform and Non-Uniform Heat Flux Distributions

Fig. 8.7 gives the variation of the friction factors as calculated by Eq. (3.16) for an α = 360° uniform and non-uniform heat flux distributions, with Reynolds numbers, compared with the friction factor correlation, $f = (0.79\ln \mathrm{Re} - 1.64)^{-2}$ [134]. The tube model has an inner diameter, D_i is 73 mm and wall thickness, t is 5.2 mm. The pressure drops for Eq. (3.16) were determined from the numerical model.

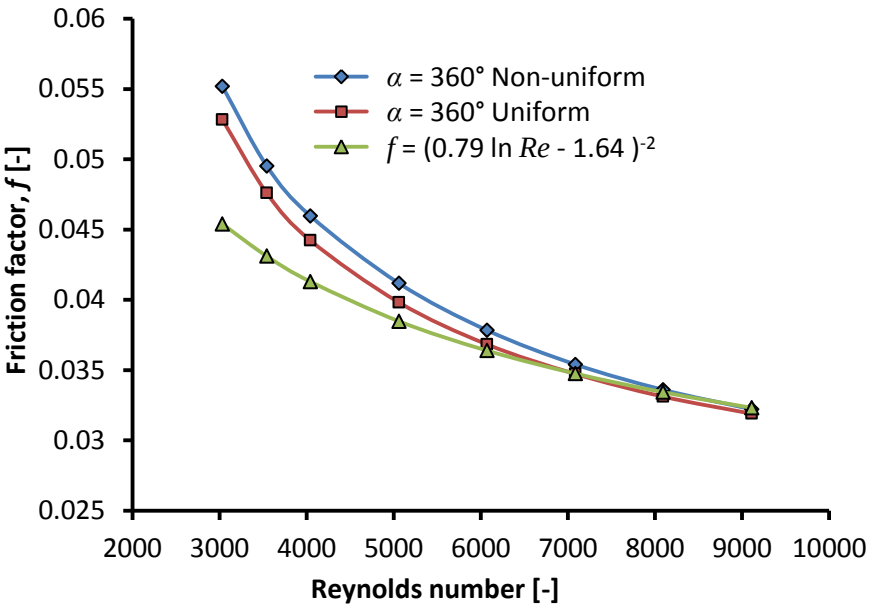

Fig. 8.7 Variation of friction factors for α = 360° uniform and sinusoidal non-uniform heat flux and friction factor correlation with the inlet Reynolds numbers

It can be seen that the friction factors for the three cases decrease with an increase in Reynolds number and became approximately the same towards the Reynolds number of 9100. Fig. 8.7 differentiates between the friction factors for uniform heat flux and non-uniform heat flux distributions boundaries, indicating dependence of friction factor on the heat flux distributions boundary profiles. The friction factor for α = 360° non-uniform was 18% higher than that of $f = (0.79\ln \mathrm{Re} - 1.64)^{-2}$ at Re = 3030 and decreased to 1% at Re = 8100, while α = 360° uniform was 14% higher than that of $f = (0.79\ln \mathrm{Re} - 1.64)^{-2}$ at Re = 3030 and also decreased to 1% at Re = 8100. These revealed that the buoyancy-induced secondary flow is still significant at low turbulent flow regime and should not be neglected at Reynolds number less than 9100.

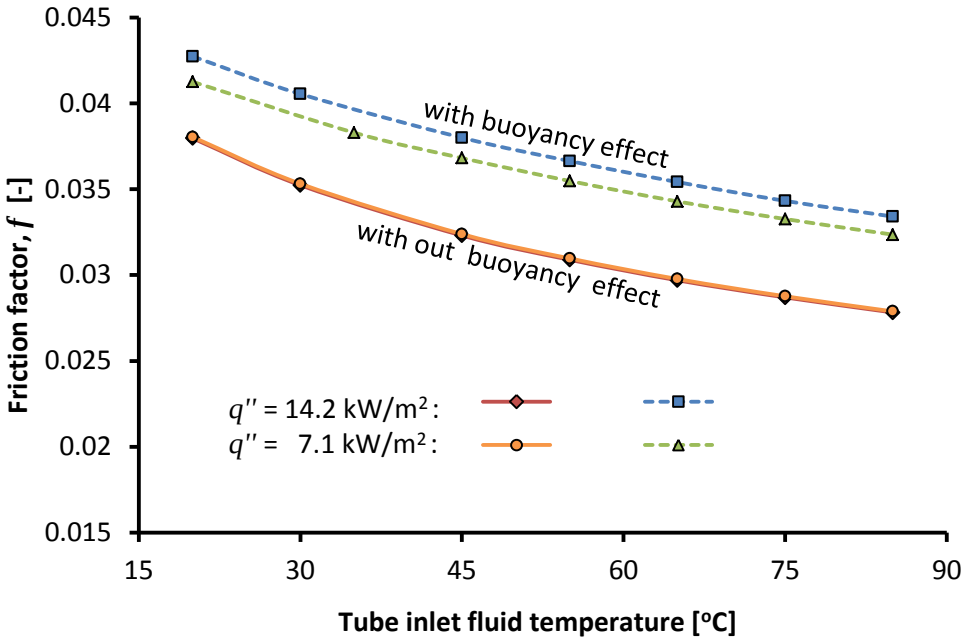

Fig. 8.8 Friction factor for α = 260° spans of non-uniform heat flux distributions intensities and friction factor correlation at different inlet fluid temperature.

Fig. 8.8 shows the influence of different inlet fluid temperature on the friction factor for the two heat flux intensity cases in Fig. 8.6, with and without buoyancy effects considered. The friction factor decreases up to 22% by increasing the fluid inlet temperature from 20 ºC to 85 ºC, at the same ambient temperature and this could be due to decrease in fluid density with an increase in temperature. It can be seen in Fig. 8.8 that there is no significant difference in the friction factors, where buoyancy effects are neglected. It was found that at the inlet fluid temperature range of 20 ºC to 85 °C, the friction factors for the two cases, with buoyancy effects present are 12 % to 20 % and 8% to 16 % higher than where buoyancy effects are neglected.

8.2 Asymmetrical Non-Uniform Heat Flux Distributions

In this section, the influence of asymmetrical non-uniform heat flux distribution boundaries in terms of the gravitational direction on the buoyancy-driven flow field and internal heat transfer coefficient of the tube model are presented for weak turbulent flow regime.

8.2.1 Fluid Flow Velocity and Temperature Distributions

Figs 8.9 (a) and (b) show the influence of asymmetrical non-uniform heat flux boundary (gravity directed at γ = 20° and 40°) on the in-plane velocity vector and temperature distributions in the heat transfer fluid at the outlet of the tube model compared with that of symmetrical non-uniform heat flux case (gravity directed at γ = 0°). The figures, for instance demonstrate a case for an asymmetrical α = 260°, for inlet Reynolds number of 6200. It can be seen that the velocity vector distributions in the fluid are similar for the asymmetrical and symmetrical non-uniform heat flux boundaries. However, it is found that the fluid descending to the lower region through the vertical centre are nearly the same for the case of γ = 0° and 20°, while that of γ = 40° had slightly shifted away from the vertical centre. Similar trends were also obtained for other Reynolds number. This indicates the weak influence of buoyancy-driven flow resulting from the misalignment of the heat flux symmetry plane with the gravity direction (γ) in the turbulent flow regime.

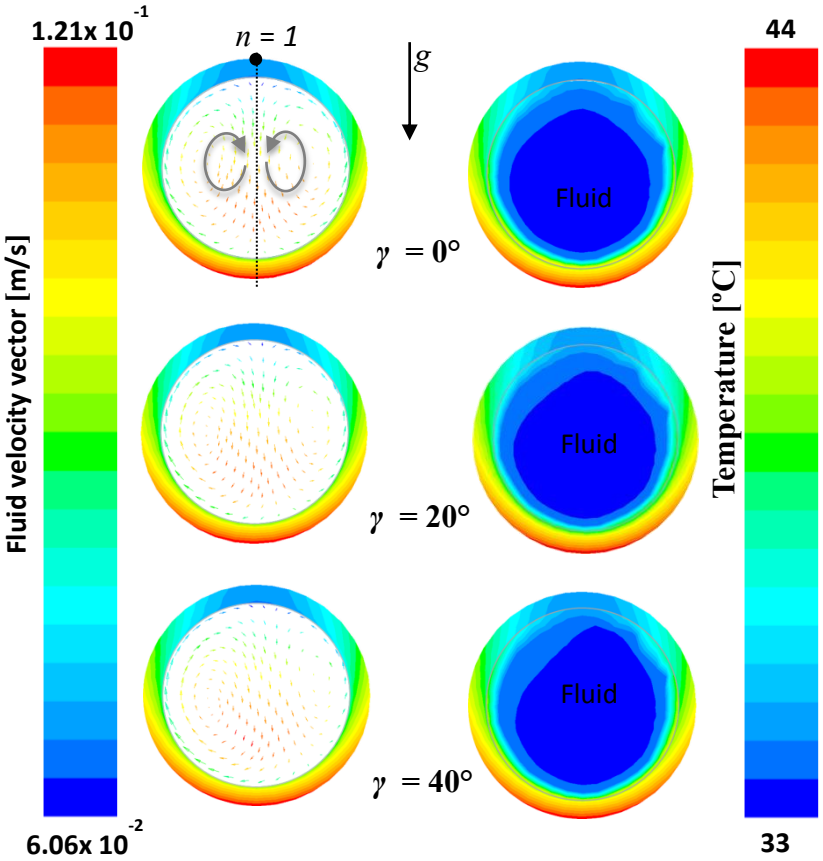

Fig. 8.9(a) Fluid flow velocity, (b) temperature distribution in the fluid for an asymmetrical non-uniform heat flux distribution base-level intensity of 7.1 kW/m^2 for α = 260°

In Fig. 8.9 (b) it can be seen that the fluid layer with lower temperature as indicated by the blue shade are nearly the same for the cases of $\gamma = 0°$ and 20° and the warmer fluid layer appeared towards the upper region of the tube. For the case of $\gamma = 40°$, the fluid layer with lower temperature is slanted, which indicates slight increase in the influence of buoyancy-driven flow due to the misalignment of the non-uniform heat flux boundary with the symmetrical axis of the tube model.

8.2.2 Heat Transfer Coefficient for Asymmetrical Non-Uniform Heat Flux Distribution Boundary

Fig.8.10 shows the internal heat transfer coefficients for asymmetrical non-uniform heat flux boundary (gravity directed at 20°, 30° and 40°) compared with the symmetrical non-uniform heat flux case (gravity directed at 0°) and Reynolds number range of 3030 and 9100. It was found that unlike in the case of laminar mixed convection shown in Fig.7.7, there is only a very slight impact on the internal heat transfer coefficient when the non-uniform heat flux

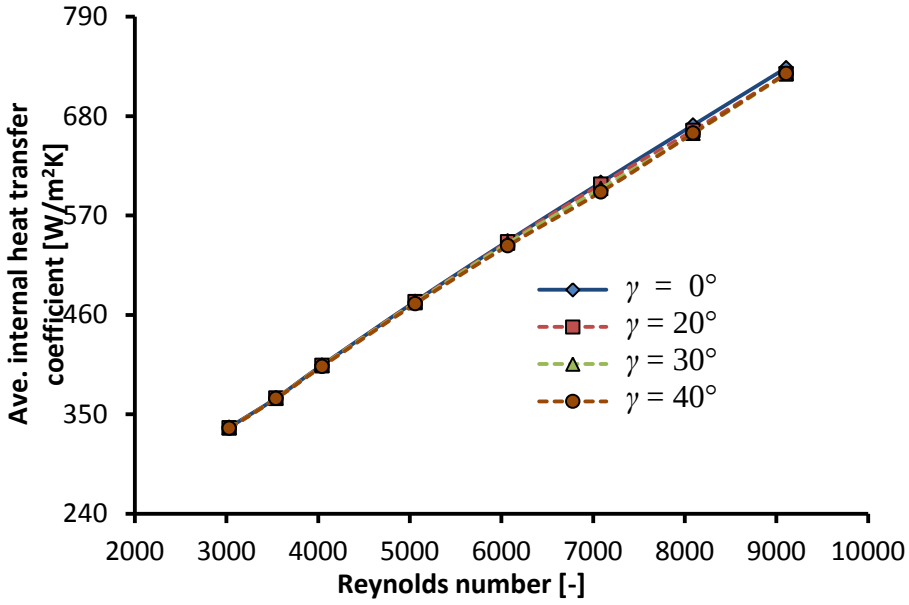

Fig. 8.10 Variation of average internal heat transfer coefficient for symmetrical ($\gamma = 0°$) and asymmetrical ($\gamma = 20°$, 30° and 40°) for $\alpha = 320°$

boundary distribution misaligned with the symmetry plane. This is due to weak influence of buoyancy-induced secondary flow in the turbulent flow regime compared to that of laminar flow case. The asymmetrical non-uniform heat flux distributions in terms of gravitational field could be neglected in the turbulent flow regime in the absorber tube.

8.3 Symmetrical Non-uniform Heat Flux Distributions for Higher Turbulent Flow Regime

In this section**,** the results are analysed for the influence of non-uniform heat flux distributions intensities of 21.3 kW/m^2, 14.2 kW/m^2 and 7.1 kW/m^2 on internal and overall heat transfer coefficients in the turbulent flow regime at the inlet Reynolds number range of 12 100 and 202 600. Also, the internal thermal efficiency for the absorber tube models with different inner diameters and wall thicknesses are analysed for α = 260° and mass flow rate range of 0.15 kg/s and 10 kg/s.

8.3.1 Heat Transfer Coefficients for Different Base-Levels Heat Flux Intensities

As expected, the average internal heat transfer coefficients increases with the Reynolds number due to an increase in heat transfer rate. Unlike in Fig. 8.5, it is found that for the inlet Reynolds numbers ranging from 12 100 to 202 600, the increase in heat flux intensities did not result in any significant increase in the average internal heat transfer coefficient of the absorber tube model. This indicates that at the inlet Reynolds number range of 12100 and above, the average internal heat transfer coefficient is not affected by increasing the solar flux intensities incident on an absorber tube of the same geometry and thermal conductivity. This could be attributed to insignificant secondary flow influences in high turbulent flow regime.

Fig.8.11 shows that the average overall heat transfer coefficient first increases rapidly with the increase in Reynolds number and later remained nearly the same at higher Reynolds number. This indicates that the average overall heat transfer coefficient for the absorber tube model considered had reached the maximum value and that the heat transfer processes from the outer-wall surface of the tube to the heat transfer fluid no longer changes significantly with an increase in Reynolds number. It is also found that the average overall heat transfer coefficient increases with an increase in the heat flux distribution intensities.

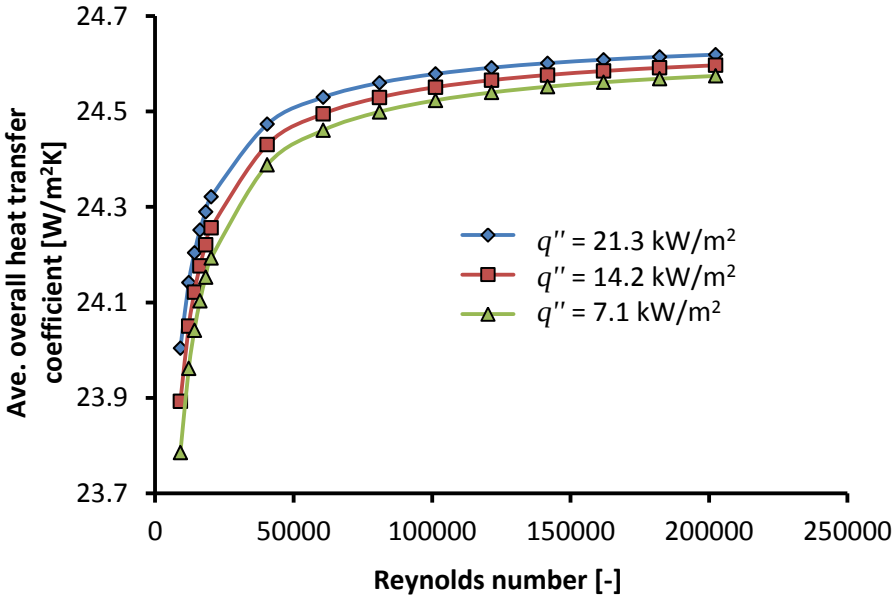

Fig. 8.11 Variations of the average overall heat transfer coefficients with Reynolds number for α = 260° span of different non-uniform heat flux distributions intensities

This could be due to higher overall heat loss coefficient component in Eq. (4.14), which depends on convective and radiative loss coefficients and that the average internal heat transfer coefficient is approximately the same with an increase in Reynolds number. This is especially true since the radiative heat transfer coefficient does not scale linearly.

8.3.2 Heat Transfer Coefficients for Different Circumferential Spans of Non-Uniform Heat Flux Boundary

Fig. 8.12 indicates the variations of the average internal heat transfer coefficients at different circumferential spans of sinusoidal non-uniform heat flux distributions intensity for the inlet Reynolds number range of 12 100 to 202 600. As expected, the average internal heat transfer coefficients increase with the Reynolds number.

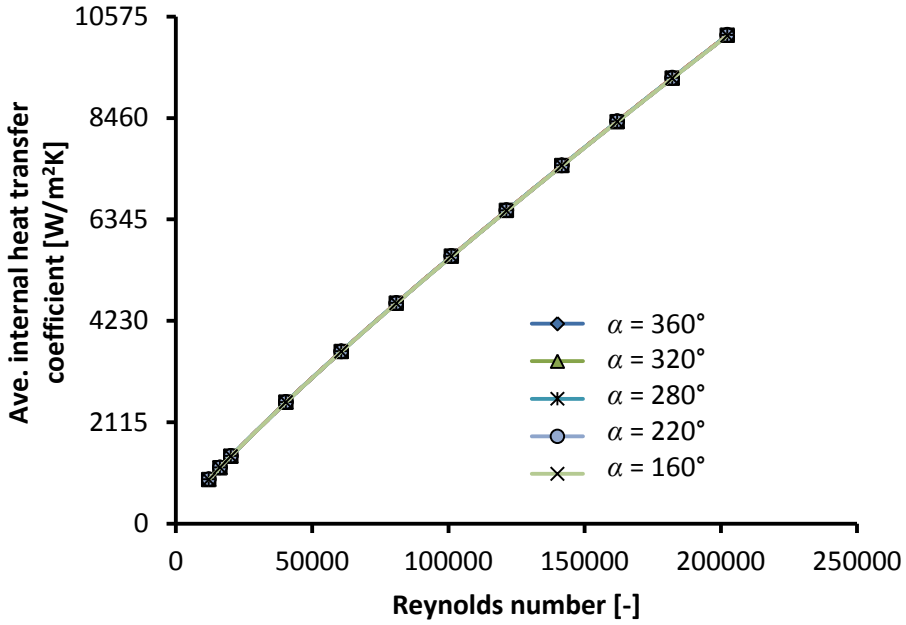

Fig. 8. 12 Variations of average internal heat transfer coefficients for different circumferential spans non-uniform heat flux distributions intensity of 7.1 kW/m^2.

It can be seen that unlike in Fig.6.12, there is no significant difference in the internal heat transfer coefficients with an increase in the circumferential spans of non-uniform heat flux distributions boundary for the Reynolds number cases considered. This is due to weak influence of buoyancy-induced secondary flow in high turbulent flow regime, which resulted in a better mixing of the heat transfer fluid. It was also found that there is no significant difference in the axial local internal heat transfer coefficients with an increase in the circumferential spans of the non-uniform heat flux distributions boundary. These reveal that in a high turbulent flow regime, the internal heat transfer coefficients of the absorber tube model are independent of circumferential span of the heat flux distribution boundary at high Reynolds numbers. Thus, for Reynolds number range of 12 100 and above, the traditional heat transfer correlations given in Table 5.3 could be used without modification to account for circumferential tube-wall temperature variations.

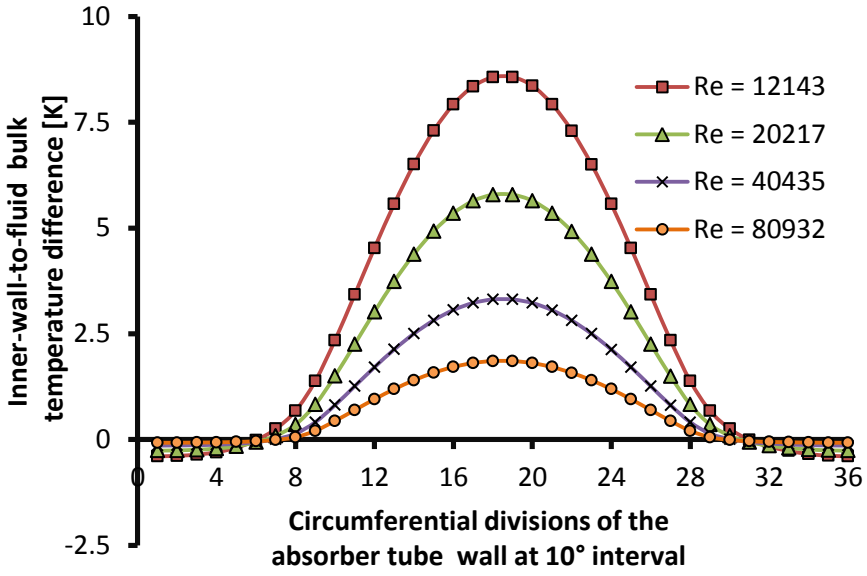

Fig.8.13 Circumferential variation of inner-wall-to-fluid bulk temperature difference at different inlet Reynolds numbers for non-uniform heat flux intensity of 7.1 kW/m^2

Fig. 8.13 indicates non-uniform circumferential variations of the inner-wall-to-fluid bulk temperature difference at different inlet Reynolds numbers for α = 200°. It can be seen that the profile consist of two portions: the portion where the inner-wall-to-fluid bulk temperature difference is positive, which refers to the heat flux into the fluid, and where it is negative, which refers to the heat flux from the fluid. The inner-wall-to-fluid bulk temperature difference decreases with the increase in Reynolds number and is highest at the peak portion of the profile, which corresponds to the most heated lower central portion of the tube. It also decreases down to the portion of the tube with little or no heat flux where it is negative for the thermal conductivity and tube-wall thickness considered in this study. At the portions of the tube where the inner-wall-to-fluid bulk temperature difference is negative, could result in a negative heat transfer coefficient, which indicates that the tube is losing heat from those portions.

8.3.3 Heat Transfer Coefficients and Thermal Efficiency for Absorber Tubes with Different Inner Diameters and Wall Thicknesses

Fig. 8.14 indicates the variations of the average internal heat transfer coefficient for tube models according to the different geometry cases defined earlier in the thesis. Different inner diameters

and wall thicknesses are considered. It is found that the average internal heat transfer coefficient increases with an increase in mass flow rate of the fluid and also increases with a decrease in the inner diameter and wall thickness of the tube.

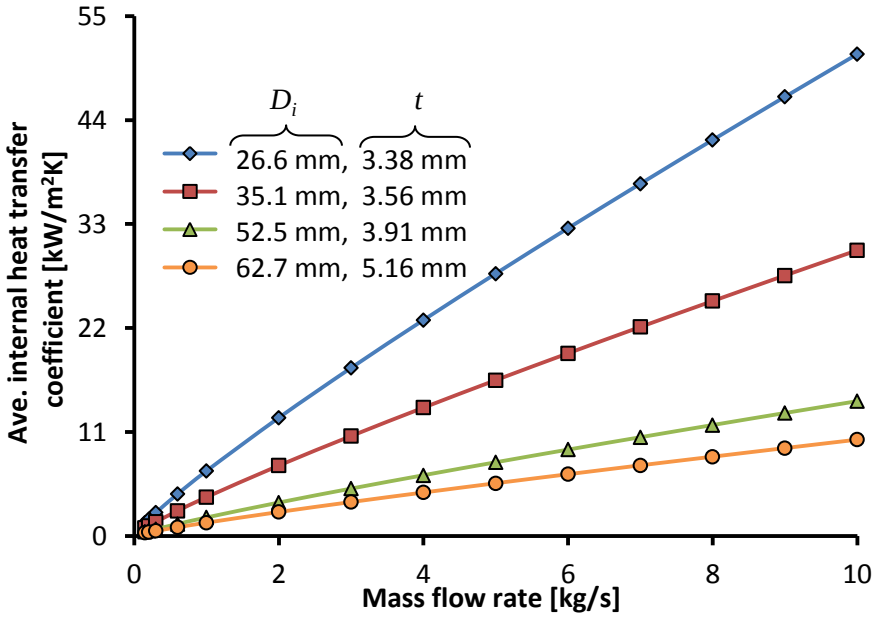

Fig. 8.14 Average internal heat transfer coefficient for tubes with different inner diameters and wall thicknesses and α = 260° span of non-uniform heat flux intensity of 7.1 kW/m^2.

The average internal heat transfer coefficient for the tube with a 26.6 mm inner diameter and 3.36 mm wall thickness is 79%, 71% and 40% respectively higher than that of the tubes with a 40.9 mm inner diameter and 3.68 mm wall thickness, 52.5 mm inner diameter and 3.91 mm wall thickness, and 62.7 mm inner diameter and 5.16 mm wall thickness between the mass flow rate of 0.15 kg/s and 10 kg/s. This variation could be attributed to the difference in their conduction and convection thermal resistances resulting from the differences in their wall thicknesses and inner-wall diameters. This indicates the importance of inner diameter and wall thickness of the tube model and mass flow rate of the heat transfer fluid on the variations of internal heat transfer coefficient of the tube.

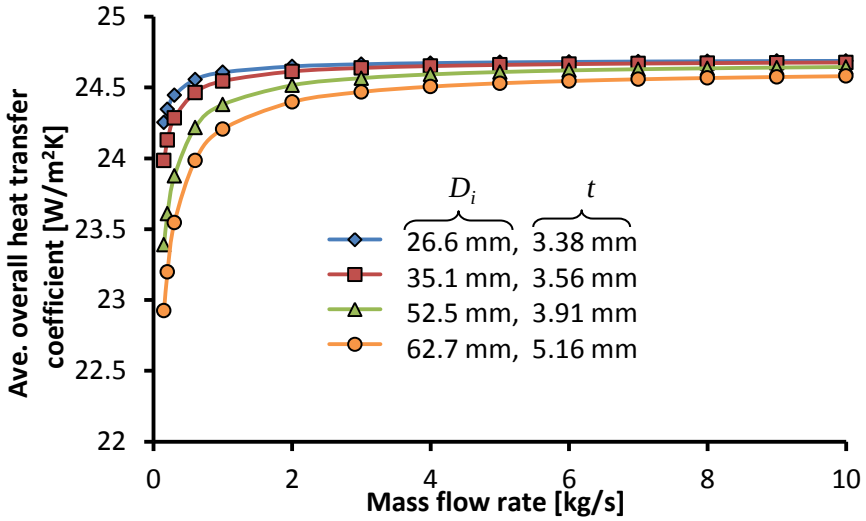

Fig. 8.15 Variation of average overall heat transfer coefficients with mass flow rate for α = 260° case in Fig.8.14.

Fig. 8.15 shows the variations of the average overall heat transfer coefficients with the increase in mass flow rate of the heat transfer fluid for α = 260° case in Fig.8.14. It is found that the variation of the overall heat transfer coefficient of the tubes with an increase in mass flow rate consist of two parts. The first part gives a rapid increase followed by the second part, which is almost horizontal, indicating that there is no significant change in the average overall heat transfer coefficient with the increase in mass flow rate of the fluid. It is also found that the average overall heat transfer coefficient increases with a decrease in the inner diameter and wall thickness of the tube. However, it can be seen in Fig. 8.15 that the difference in the overall heat transfer coefficients of the tubes in the second part decrease as the mass flow rate of the fluid was increasing. This implies that the average overall heat transfer coefficients of the tubes with different inner diameters and wall thicknesses, but with the same thermal conductivity and the same heat flux distribution intensity could become negligible at higher mass flow rate.

Fig. 8.16 indicates that the thermal efficiency of the absorber tubes in Fig. 8.14 increases with an increase in mass flow rate. The lower thermal efficiency for the tube model with higher inner diameter and wall thickness could be due to its higher thermal resistance as a result of its higher wall thickness. It is also found that the variations of thermal efficiency with an increase in mass

flow rate of the fluid consist of two parts. The first part shows a rapid increase, while in the second part it remained nearly horizontal, indicating that the thermal efficiency had reached the maximum value and that the heat transfer processes form the outer wall surface of the tube to the fluid no longer changed significantly with an increase in mass flow rate. However, a decrease in the tube inner diameter and an increase in mass flow rate in order to increase thermal efficiency could result in an increase in pressure drops, since pressure is inversely related to the tube diameter and directly to the square of the velocity of the fluid.

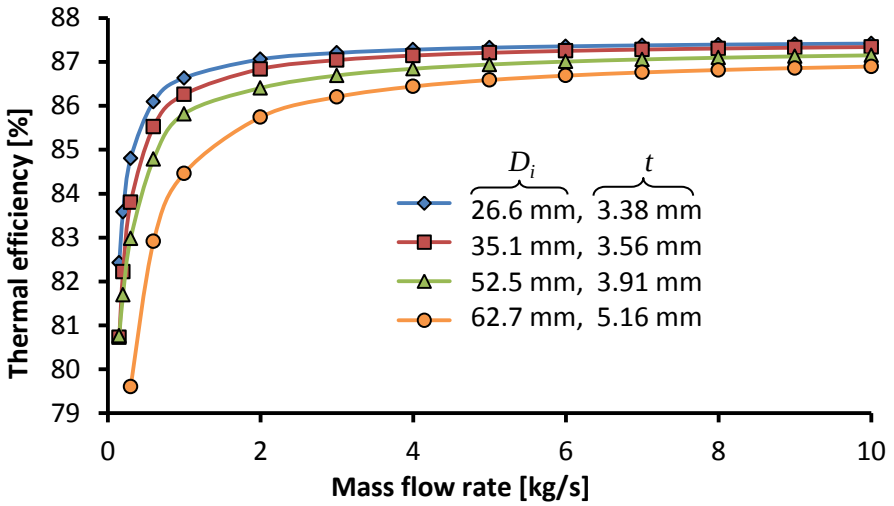

Fig. 8.16 Variations of thermal efficiency with mass flow rate for tubes with different inner diameters and wall thicknesses and heat flux distribution case in Fig. 8.14.

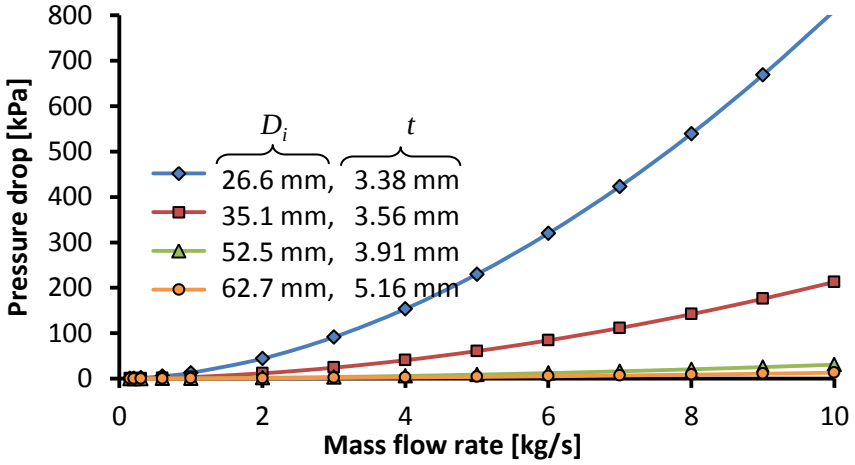

Fig. 8.17 Variations of pressure drops for absorber tubes with different inner diameters and heat flux distribution case in Fig. 8.14

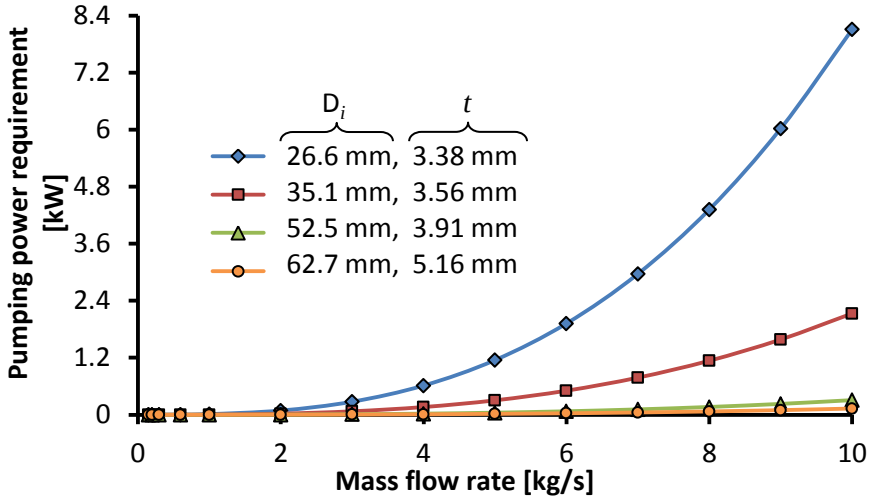

Fig. 8.18 Variations of pumping power for absorber tubes with different inner diameters and heat flux distribution case in Fig. 8.14

The pressure drops for the tube models considered obtained from the simulation results for the mass flow rate in the range of 0.15 kg/s to 10 kg/s are shown in Fig. 8.14. It shows an increase in pressure drop with a decrease in the inner diameter and an increase in pressure drop with an increase in mass flow rate of the fluid.

Fig. 8.18 shows the pumping power required to overcome the pressure drops and turbulent dissipation of the fluid for the tube models considered, determined from Eq. (3.15). It indicates that an increase in pumping power due to pressure drops with a decrease in the tube inner diameter could be a limiting factor to improving thermal efficiency, especially for the case of a linear Fresnel solar collector, which makes use of multiple absorber tubes of a smaller inner diameter.

8.4 Conclusion

In this chapter, the influence symmetrical and asymmetrical sinusoidal non-uniform heat flux distributions boundaries on the secondary flow, internal heat transfer and friction factors are analysed in the turbulent flow regime. In the Reynolds numbers ranging from 3030 to 9200, the circumferential spans of symmetrical non-uniform heat flux distributions boundaries have

significant effects on the buoyancy-driven secondary flow. The Richardson number increases with the span of the heat flux distribution boundary due to buoyancy-effects. Internal heat transfer coefficients and friction factors increase with an increase in heat flux intensities, but there is no significant increase when buoyancy effects are neglected.

The internal heat transfer coefficients enhancement due to buoyancy effects improves the collector thermal efficiency. Internal heat transfer coefficients increase with fluid inlet temperatures, while friction factors decrease with an increase in fluid inlet temperatures. Thus, buoyancy effects cannot be neglected in the weak turbulent flow regime. The influence of the asymmetrical non-uniform heat flux boundary in terms of gravity direction on the internal heat transfer coefficients and friction factors is negligible and could be neglected in the turbulent flow regime.

In the Reynolds numbers range of 12 100 to 202 600, there is no significant increase in the internal heat transfer coefficients with the heat flux intensity and the span of the heat flux distributions boundaries. This indicates that at higher turbulent flow regime, the internal heat transfer coefficients are independent of the heat flux intensity and the span of the heat flux distributions boundaries due to insignificant buoyancy effects. Thus, for Reynolds number range of 12 100 and above, the traditional heat transfer correlations in Table 5.3 could be used without modification to account for circumferential wall temperature variations due to non-uniform heat flux boundary. However, the overall heat transfer coefficients increases with an increase in the heat flux distributions intensities due to an increase in the overall heat loss coefficient. The average internal and overall heat transfer coefficients and thermal efficiency increased with a decrease in the inner diameter and the wall thickness of the tubes of the same thermal conductivity. Also, a decrease in the absorber tube inner diameter to enhance the internal heat transfer coefficient and thermal efficiency would result in an increase in pressure drop.

In the next and last chapter, the main conclusions from this study are presented.

CHAPTER NINE: SUMMARY, CONCLUSIONS AND RECOMMENDATION FOR FUTURE STUDIES

9.1 Summary:

In solar thermal collectors, the absorber tubes are very critical in converting the heat flux into thermal energy absorbed into the heat transfer fluid. In linear focusing solar collectors such as parabolic trough or linear Fresnel solar collectors, concentrated heat flux impinges on the collector tubes from underneath. This results in non-uniform heat flux distributions over the circumferential outer tube-wall and hence non-uniform heat transfer rate to the heat transfer fluid.

A number of previous studies on thermal performance of linear focusing solar collector systems were based on the assumption of uniform heat flux distributions for convenience and this is contrary to the optical ray-tracing designs and simulations results, which revealed that the solar flux distributions around the tubes are non-uniform. Thus, the influence of fully uniform, partial uniform and non-uniform heat flux distributions boundary conditions on the thermal performance were investigated for an absorber tube type of a linear focusing solar collector for a detailed analysis of the impacts of these thermal boundary conditions in both laminar and turbulent flow regimes. Also, the earlier design and development of linear focusing solar concentrators were focused on large-scale applications for steam productions needed for power generations where the collectors are operated in the turbulent flow regime to increase the effective fluid side heat transfer coefficients for efficient thermal performance of the collector system.

The present study considered laminar and weak turbulent flow regimes where the buoyancy-driven secondary flow effects could greatly enhance the internal convective heat transfer rate, by increasing the thermal mixing of the heat transfer fluid, thereby improving the thermal performance of the solar collector system. Also, an indicative first order model thermal performance comparison was conducted for a linear focusing solar collector with a parabolic trough reflector surface for adaption as a viable alternative to a traditional flat-plate solar collector for large volume water heating applications. The improved thermal performance

associated with higher internal heat transfer coefficients due to buoyancy-driven flow could be an acceptable trade-off for a linear focusing solar concentrator, which uses a sun-tracking system when compared to a flat-plate collector. The internal convective heat transfer coefficients and friction factors as well as thermal efficiency for a linear focusing solar collector absorber tubes were determined numerically for different circumferential spans of symmetrical and asymmetrical non-uniform heat flux distributions boundaries in terms of the gravitational field. A three-dimensional steady-state numerical model was implemented in ANSYS Fluent version 14.0 for laminar flow inlet Reynolds numbers range of 130 to 2200 and turbulent flow inlet Reynolds numbers range of 9100 to 225 000, tube diameters of 62.7 mm, 52.5 mm, and 40.9 mm, and for different inlet fluid temperatures. The external tube-wall heat loss was considered via convection and radiation. The heat conduction within the tube wall was also considered since the radial, axial and tangential heat conductions influence the temperature and heat flux distributions on the inner surface of the tube. It should be noted also that the results presented in this study are limited to single-phase liquid water heating applications and considering that the parameters such as heat transfer coefficient and the incident solar heat flux considered are dimensional and as such, the results are only applicable for cases with the same working fluid considered in this study.

9.2 Conclusions:

9.2.1 Laminar Flow Heat Transfer with Symmetrical Heat Flux Distribution Boundary

(i) It was found that with buoyancy-driven secondary flow present, the internal heat transfer coefficients of an absorber tube increases with the heat flux intensity and spans of the non - uniform heat flux distributions boundary. Also, with the secondary flow effect present, the average internal heat transfer coefficient is up to three times higher than the case of pure forced-convection (no secondary flow effect), indicating higher internal heat transfer enhancement and thus, improved thermal performance. The internal heat transfer coefficients for non-uniform heat flux boundary are higher than the uniform heat flux case due to its dominant secondary flow effects.

(ii) It was also found that with the buoyancy effect present, the friction factor value is approximately twice higher than where it was neglected and that it increases with the heat

flux intensity. At the same ambient temperature condition, the friction factor value decreases with an increase in the absorber tube inlet fluid temperature, while the internal heat transfer coefficient increased with an increase in the absorber tube inlet fluid temperature.

(iii) The average internal and overall heat transfer coefficients, as well as thermal efficiency increased with a decrease in the inner diameter and wall thickness of the tubes with the same thermal conductivity. A decrease in the inner diameter of the tube to enhance internal heat transfer coefficients and thermal efficiency would result in an increase in the pressure drop and hence an increase in the pumping power to sustain fluid flow.

(iv) With an enhancement of the internal heat transfer coefficient due to the buoyancy driven secondary flow, the adapted parabolic trough solar collector for hot water production in low mass flow conditions have more favourable heat transfer performances than the standard multi-pass flat plate collector.

9.2.2 Laminar Flow Heat Transfer with Asymmetrical Heat Flux Boundary Compared with the Symmetrical Heat Flux Boundary

(i) The average internal heat transfer coefficient and friction factor decreased as the non-uniform heat flux distribution boundary misaligned with the symmetrical axis of the tube model in terms of the gravitational direction. The internal heat transfer coefficients for both the symmetrical and asymmetrical non-uniform heat flux distribution boundaries increase with an increase in the circumferential spans and heat flux distribution intensities.

(ii) The internal heat transfer coefficients for the symmetrical and asymmetrical non-uniform heat flux distributions increased with an increase in the inlet fluid temperature and decrease with an increase in the external loss convective heat transfer coefficient. The internal heat transfer coefficients for the symmetrical non-uniform heat flux case are higher than that of the asymmetrical case, due to decrease in buoyancy effects.

(iii) Friction factors for the symmetrical and asymmetrical non-uniform heat flux distributions decreased with an increase in the inlet fluid temperature and the external loss convection heat transfer coefficient. The friction factors for the case of symmetrical non-uniform heat flux distributions are higher than that of the asymmetrical case, due to decrease in buoyancy effects.

9.2.3 Turbulent Flow Heat Transfer with Symmetrical and Asymmetrical Heat Flux Distributions Boundary

(i) It was found that the internal heat transfer coefficients and friction factors increase with an increase in the circumferential spans of the heat flux distributions boundary and also with the heat flux intensities for the inlet Reynolds number range of 3030 and 9100, where buoyancy-effect was present, while there was no significant increase, where secondary flow was neglected. However, the impact is significantly smaller than as in the case of laminar flow regime.

(ii) For an inlet Reynolds number higher than 9100, the increase in circumferential spans of the heat flux distributions boundary and heat flux intensities do not have significant effects on the secondary flow, internal heat transfer coefficients and friction factors. This indicated that for Reynolds number range higher than 9100, the buoyancy effects could be neglected and that the traditional heat transfer correlations could be used at higher Reynolds number without modification to account for circumferential wall temperature variations.

(iii) For the asymmetrical non-uniform heat flux distribution boundary, the average internal heat transfer coefficient was very slightly affected when the non-uniform heat flux distribution boundary misaligned with the symmetrical axis of the tube model. This is due to very weak influence of buoyancy-induced secondary flow in the turbulent flow regime compared to that of laminar flow case. Thus, in the turbulent flow regime, the impacts of asymmetrical non-uniform heat flux distributions boundary in terms of gravity direction on the internal heat transfer of a horizontal circular tube could be neglected.

(iv) As in the case of laminar flow heat transfer, the average internal and overall heat transfer coefficients, thermal efficiency increased with a decrease in the inner diameter and the wall thickness for a tube with the same thermal conductivity. Also, a decrease in an inner diameter to enhance the internal heat transfer and thermal efficiency resulted in an increase in pressure drop.

9.3 Recommendations for Future Studies

The linear focusing solar collectors for different thermal applications are still growing and therefore extensive research efforts are needed for improving the general performance of the system. This study has extensively investigated the influence of uniform heat flux boundaries, symmetrical and asymmetrical non-uniform heat flux distributions boundaries on the thermal

performance and friction factors of an absorber tube model for a linear focusing solar collector system, isolating the influence of the receiver envelop on the characteristic performance of the collector tube.

Future studies are recommended to include the impact of the receiver envelop together with influence of the non-uniform circumferential heat flux distributions as well as considering the influence transient nature of solar irradiation flux. Also, the impacts the glass cover might have on the circumferential heat flux distributions boundary on the collector tube wall due to optical refraction, reflection and absorption need to be investigated in details.

REFERENCES

[1] S. F. Larsen, M. Altamirano, and A Hernández, Heat Loss of a Trapezoidal Cavity Absorber for a Linear Fresnel Reflecting Solar Concentrator, Renewable Energy 39 (2012)198-206.

[2] F. Birol, Key World Energy Statistics, OECD/International Energy Agency, 9, rue de la Fédération, 75739 Paris Cedex 15 – France (2016) 6-10.

[3] O. Edenhofer, R. Pichs-Madruga, Y. Sokona, E. Farahani, S. Kadner, K. Seyboth, A. Adler, I. Baum, S. Brunner, P. Eickemeier, B. Kriemann, J. Savolainen, S. Schlömer, C. von Stechow, T. Zwickel and J.C. Minx (eds.) IPCC, 2014: Climate Change 2014: Mitigation of Climate Change. Contribution of Working Group III to the Fifth Assessment Report of the Intergovernmental Panel on Climate Change, Cambridge University Press, Cambridge, United Kingdom and New York, NY, USA (2007) 26-103.

[4] A. Hilbig, Short Compendium on Solar Thermal Applications and the Solar Water Heaters Industry in the Middle East "Solar Thermal Application in Egypt, Jordan, Lebanon, Palestinian Territories & Syria: Technical Aspects, Framework Conditions and Private Sector Needs" Cairo. 23rd - 25th March, 2009.

[5] S. A. Kalogirou, Solar Thermal Collectors and Applications, Progress in Energy and Combustion Science 30 (2004) 231–295.

[6] R. Abbas, M.J. Montes, M. Piera and M. Martinez-Val, Solar Radiation Concentration Features in Linear Fresnel Reflector Arrays," Energy Conversion and Management, 54 (2012)133–144.

[7] R. Grena, Optical Simulation of a Parabolic Solar Trough Collector, Inter. J. of Sustainable Energy, 29(1) (2010)19–36.

[8] R. P. Goswami, B. S. Negi, Sehgal, H. K. and Sootha G. D., Optical Designs and Concentration Characteristics of a Linear Fresnel Reflector Solar Concentrator with a Triangular Absorber, Solar Energy Materials 21 (1990) 237-251.

[9] D. Gielen, Renewable Energy Technologies: Cost Analysis of Concentrating Solar Power, International Renewable Energy Agency, Khalidiyah Street, Abu Dubi, United Arab Emirates 1 (2/5) (2012) 4-7.

[10] R. Abbas, J. Muñoz, J.M. Martínez-Val, Steady-State Thermal Analysis of an Innovative Receiver for Linear Fresnel Reflectors, Renewable Energy 39 (2012) 198-206.

[11] D.R. Mills and G.L. Morrison, Modelling Study for Compact Fresnel Reflector Power Plant. Journal of Phys. IV France 9 (1999) 159-165.

[12] V. K. Jabasingh and G.M. Joselin Herbert, A Review of Solar Parabolic Trough Collector, Renewable and Sustainable Energy Reviews, 54 (2016) 1085 – 1091.

[13] S.A. Kalogirou, Solar Energy Engineering: Processes and Systems, Academic Press Elsevier Inc, First Edition, 2009.

[14] J. A. Duffie and W. A. Beckman, Solar Engineering of Thermal Processes. Second Edition, A Wiley-Interscience Publication, John Wiley & Sons, Inc. New York, 1980.

[15] G. N. Tiwari , Solar Energy Fundamental, Design, Modelling and Applications. Narosa Publishing House, 22 Daryaganj, Delhi, India, 2006.

[16] K. Gasljevic, G. Aguilar, and E. F.Matthys, Buoyancy Effects on Heat Transfer and Temperature Profiles in Horizontal Pipe Flow of Drag-Reducing Fluids International Journal of Heat and Mass Transfer 43(2000) 4267- 4274.

[17] Y. He, J. Xiao, Z. Cheng and Y. Tao, A MCRT and FVM Coupled Simulation Method for Energy Conversion Process in Parabolic Trough Solar Collector, Renewable Energy 36 (2011) 976 – 985.

[18] R. Forristall, Heat Transfer Analysis and Modeling of a Parabolic Trough Solar Receiver Implemented in Engineering Equation Solver National Renewable Energy Laboratory 1617 Cole Boulevard Golden, Colorado (2003) 80401-3393.

[19] K.S. Manikandan , R. Kumaresan, R. Velraj, and S. Iniyan, Parametric Study of Solar Parabolic Trough Collector System. Asian Journal of Applied Sciences, 5 (2012) 384-393.

[20] Z-Y. Li, Z. Huang and W-Q. Tao, Three-Dimensional Numerical Study on Fully-Developed Mixed Laminar Convection in Parabolic Trough Solar Receiver Tube, Energy 113 (2016) 1288-1303.

[21] F. J. Pino, R. Caro, J. R. López, F. Rosa and J. Guerra, Experimental Validation Of An Optical And Thermal Model Of A Linear Fresnel Collector, 2nd European Conference on Polygeneration –Tarragona, Spain (2011)1-8.

[22] F. J. Pino, R. Caro, F. Rosa and J. Guerra, Exp. Validation of an Optical and Thermal Model of a Linear Fresnel Collector System, Appl. Thermal Engineering (2012) 1-9.

[23] N. Velázquez, O. García-Valladares, D. Sauceda and R. Beltrán, Numerical Simulation Of A Linear Fresnel Reflector Concentrator as Direct Generator in a Solar-GAX cycle, Energy Con. and Mgt. 51(2010) 434–445.

[24] R. Abbas, J. Muñoz and J. M. Martínez-Val, Steady-State Thermal Analysis of an Innovative Receiver For Linear Fresnel Reflectors. Applied Energy 92, 503-515 (2012).

[25] A. Häberle, C. Zahler, H. Lerchenmüller, M. Mertins, C. Wittwer, F. Trieb, and J. Dersch, The Solarmundo Line Focussing Fresnel Collector: Optical and Thermal Performance and Cost Calculations, Solar PACES, Switzerland (2002).

[26] M. Eck, R. Uhlig, M. Mertins, A. Häberle and H. Lerchenmüller, Thermal Load of Direct Steam- Generating Absorber Tubes with Large Diameter in Horizontal Linear Fresnel Collectors, Heat Transfer Engineering 28 (1) (2007) 42-48.

[27] R. P. Goswami, B.S. Negi, H.K. Sehgal and G.D. Sootha, Optical designs and concentration characteristics of a linear Fresnel reflector solar concentrator with a triangular absorber. Solar Energy Materials 2 (1990) 237-251.

[28] S. S. Mathur, T.C. Kandpal and B.S. Negi, Optical design and concentration characteristics of linear Fresnel reflector solar concentrators - II. Mirror elements of equal width, Energy Convers. Management 31(3) (1991) 221-232.

[29] J. K. Stynes and B. Ihas, Absorber Alignment Measurement Tool for Solar Parabolic Trough Collectors , ASME 6th International Conference on Energy Sustainability & 10th Fuel Cell Science, Engineering and Technology Conference, San Diego, California, July 23–26, 2012.

[30] J.K. Stynes and B. Ihas, Slope Error Measurement Tool for Solar Parabolic Trough Collectors, World Renewable Energy Forum Denver, Colorado, May 13–17, 2012.

[31] J. M. Christian and C. K. Ho, Finite Element Modeling and Ray Tracing of Parabolic Trough Collector for Evaluation of Optical Intercept Factor with Gravity Loading, Proceedings of the ASME 5th International Conference on Energy Sustainability, 2011.

[32] S.A. Kalogirou, Design and Construction of a One-Axis Sun-Tracking Mechanism. Solar Energy 57 (6) (1996) 465–469.

[33] Y. D. Goswami, Survey of Energy Resources: Solar Energy, World Energy Council (2007) 381- 392.

[34] A. J. Marston, Geometric Optimization of Solar Concentrating Collectors using Quasi-Monte Carlo Simulation, Thesis, Master of Applied Science in Mechanical Engineering Waterloo, Ontario, Canada, 2010.

[35] V. Quaschning, Solar Thermal Power Plants: Technology Fundamentals Renewable Energy World 6 (2003)109-113.

[36] A. Duffie and W. Beckman, Solar Engineering of Thermal Processes, Second Edition. Wiley-Interscience Publication, John Wiley & Sons, Inc. New York, 1980.

[37] P. A. Anil, Compound Parabolic Concentrator M. Tech – Solid Mechanics and Design Roll No.: 10105066 Mechanical Engineering Department Indian Institute of Technology, Kanpur Kanpur – 208016.

[38] P. C. Eames and B. V. Norton, Unified Model for Optics and Heat Transfer in Line-axis Concentrating Solar Energy Collectors, Solar Energy 50 (4) (1993) 339-355.

[39] R. Vallabha, K. Raghavendra and N. A. Kumar, Development of Solar and Wind Power in Karnataka and Tamil Nadu, Asian Development Bank , 6 ADB Avenue, Mandaluyong City, 2013.

[40] V. Kumar, R. Shrivastava and S.P. Untawale, Fresnel lens: A Promising Alternative of Reflectors in Concentrated Solar Power, Renewable and Sustainable Energy Reviews 44 (2015).

[41] K. W. Spinka, Attributes of Renewable Energy: From Nano-possibilities to Solar Power, Yale-New Haven Teachers Institute, Yale University, Volume IV, 2010.

[42] S. Kalogirou, P. Eleftheriou, S. Lloyd and J. Ward, Design and Performance Characteristics of a Parabolic-Trough Solar-Collector System, Appl. Energy 47 (4) (1994) 341–354.

[43] I. A. Thomas and H. M. Guven, Parabolic Trough Concentrators: Design, Construction and Evaluation 2, Energy Convers. Management 34 (5) (1993) 401-416.

[44] National Renewable Energy Laboratory, SkyFuel Parabolic Trough Optical Efficiency Testing, 2010.

[45] J. D. Nixon and P. A. Davies, Cost – Exergy Optimisation of Linear Fresnel Reflectors. Solar Energy 86 (2012) 147-156.

[46] D.R. Mills and G.L. Morrison, Modelling Study for Compact Fresnel Reflector Power Plant. Journal of Phys. IV France 9 (1999) 159-165.

[47] D. R. Mills and G. L. Morrison, Compact Linear Fresnel Reflector Solar Thermal Power Plants, Solar Energy 68 (3) (2000) 263-283.

[48] N. E. Gharbia, H. Derbalb, S. Bouaichaouia and N. Saida, A comparative study between parabolic trough collector and linear Fresnel reflector technologies. Energy Procedia 6 (2011) 565–572.

[49] H. B. Jannet, Combined Solar Power and Desalination Plants: Techno-Economic Potential in Mediterranean Partner Countries, WP1: Technology Review and Selection of CSP and Desalination Configurations adapted for Application in the Southern and Eastern Mediterranean Region Final Report (2009).

[50] A. A. Hachicha, Numerical Modelling of a Parabolic Trough Solar Collector, Doctoral Thesis, Centre Tecnològic de Transferència de Calor Departament de Màquines i Motors Tèrmics Universitat Politècnica de Catalunya, 2013.

[51] F. Lippke, Direct Steam Generation in Parabolic Trough Solar Power Plants: Numerical Investigation of the Transients and the Control of A Once-Through System, J. Sol. Energy Eng. 118 (1996) 9–14.

[52] A. Kumar, S. Chand and O.P. Umrao, Design and Analysis for 1MWe Parabolic Trough Solar Collector plant based on DSG method, International Journal of Engineering Research & Technology (IJERT) 2 (6) 2013.

[53] S. Pawel and M. J. Wagner, CPS: Concentrating Solar Power, Large-Scale Alternatives to Traditional Solar PV. Research Report, Mora Asso. Clean Energy/Clean Technology 2009.

[54] A. Krothapalli and B. Greska, Concentrated Solar Thermal Power, Department of Mechanical Engineering Florida State University, Tallahassee, FL 32310, Sustainable Energy Technologies, LLC St. Cloud, FL 34771 (2011).

[55] M. Eck and E. Zarza Saturated Steam Process with Direct Steam Generating Parabolic Troughs, Solar Energy 80 (2006) 1424–1433.

[56] M. J. Wagner and G. Zhu, A Direct-Steam Linear Fresnel Performance Model For NREL System Advisor Model. Proceedings of the ASME 2012, 6th International Conference on Energy Sustainability & 10th Fuel Cell Science, Engineering and Technology Conference ESFuelCell, San Diego, CA, USA. (2012).

[57] M. Qu, H. Yin and D.H. Archer, A Solar Thermal Cooling and Heating System for a Building: Experimental and Model Based Performance Analysis And Design, Solar Energy 84 (2) (2010) 166–182.

[58] M. Mazloumi, M. Naghashzadegan and K. Javaherdeh, Simulation of a Solar Absorption Cooling System with Parabolic Trough Collector for Sunshine Hours, In: Proceedings of the 47th Conf. on Simulation and Modeling. Helsinki, Finland, SIMS (2006) 188–193.

[59] C. Tzivanidis and E. Bellos, The Use of Parabolic Trough Collectors for Solar Cooling–A Case Study For Athens Climate Case Studies in Thermal Eng. 8(2016) 403-413.

[60] M. Qu, S. Masson and D. Archer, Solar Absorption Cooling / Heating System for the Intelligent Workplace, IWESS Workshop (2006) 1-17.

[61] C. Stanciu, D. Stanciu and A.-T. Gheorghian, Thermal Analysis of a Solar Powered Absorption Cooling System with Fully Mixed Thermal Storage at Startup, Energies 10 (72) (2017) 2-19.

[62] A. Montero, T. Hirsch, H. Schenk, J. C. Bruno, A. Coronas, Performance Analysis of Absorption Cooling Systems Using Linear Fresnel Solar Collectors, Third International Conference on Applied Energy - Perugia, Italy 16-18 May, 2011.

[63] M. Lin, K. Sumathy, Y. J. Dai, R. Z. Wang and Y. Chen, Experimental and Theoretical Analysis on a Linear Fresnel Reflector Solar Collector Prototype with V-Shaped Cavity Receiver, Applied Thermal Engineering 51 (2013) 963-972.

[64] K. A. Sharma, C. Sharma, S. C. Mullicka and T. C. Kandpala, Solar Industrial Process Heating: A Review Renewable and Sustainable Energy Reviews 78 (2017) 124–137.

[65] N. Cottret and E. Menichetti Technical Study Report: On Solar Heat for Industrial Processes, State of the Art in the Mediterranean Region, 14 October, 2015.

[66] D. Pietruschka, R. Fedrizzi, F. Orioli, R. Söll and R. Stauss, Demonstration of Three Large Scale Solar Process Heat Applications with Different Solar Thermal Collector Technologies, Energy Procedia 30 (2012) 755 – 764.

[67] R. Silva, F. J. Cabrera and M. Pérez-García, Process Heat Generation with Parabolic Trough Collectors for a Vegetables Preservation Industry in Southern Spain, Energy Procedia 48 (2014) 1210 – 1216.

[68] S. A. Kalogirou, Parabolic Trough Collectors For Industrial Process Heat in Cyprus, Energy 27(9) 2002.

[69] A. Valan Arasu and S. T. Sornakumar, Theoretical Analysis and Experimental Verification of Parabolic Trough Solar Collector with Hot Water Generation System, Thermal Science 11 (1) (2007)119-126.

[70] S. A. Kalogirou and S. Lloyd, Use of Solar Parabolic Trough Collectors for Hot Water Production in Cyprus, A Feasibility Study, Renewable Energy 2 (2) (1992) 117 -124.

[71] J. Ramesh, J. Kanna Kumar and E. V. Subbareddy, Design, Fabrication and Performance Analysis of a Parabolic Trough Solar Collector Water Heater, International Journal of Innovative Research in Science, Engineering and Technology 4 (7) 2015.

[72] S. K. Singh, A. K. Singh and S. K. Yadav, Design and Fabrication of Parabolic Trough Solar Water Heater for Hot Water Generation, International Journal of Engineering Research & Technology (IJERT) 1(10) 2012.

[73] G. Mokhtar, B. Boussad and S. Noureddine, A Linear Fresnel Reflector as a Solar System for Heating Water: Theoretical and Experimental Study, Case Studies in Thermal Engineering 8 (2016) 176–186.

[74] C. Kutscher, M. Mehos, C. Turchi, G. Glatzmaier and T. Moss, Line-Focus Solar Power Plant Cost Reduction Plan, Milestone Report NREL/TP-5500-48175, National Renewable Energy Laboratory 1617 Cole Boulevard Golden, Colorado 8040 (2010) 8-12.

[75] D. Yogi Goswami, Frank Kreith, Energy Conversion, Taylor & Francis, 2007.

[76] A. Poullikkas, C. Rouvas, I. Hadjipaschalis and G. Kourtis, Optimum Sizing of Steam Turbines for Concentrated Solar Power Plants, International Journal of Energy and Environment 3(1) (2012) 9-18.

[77] R. Pitz-Paal, P. Heller and R. Buck Solar Thermal Power Plants Utilizing Concentrated Sunlight for Generating Energy, BINE-Themeninfo II, Deutsches Zentrum für Luft- und Raumfahrt (DLR) - Institut für Solarforschung (2013) 6-10.

[78] A. C. Ratzel, C. E. Hickox and D. K. Gartling, Techniques for Reducing Thermal Conduction and Natural Convection Heat Losses in Annular Receiver Geometries J. Heat Transfer 101(1) (2010) 108-113.

[79] W. B. Stine and R. W. Harrigan, Solar Energy Systems Design (retitled "Power from the Sun, 2001"), John Wiley and Sons, Inc. 1986.

[80] M. Roesle, V. Coskun and A. Steinfeld, Numerical Analysis of Heat Loss from a Parabolic Trough Absorber Tube with Active Vacuum System ASME, Journal of solar Energy Engineering. 133(031015) (2011) 1-5.

[81] T. L. Bergman, A. S. Lavine, F. P. Incropera and D. P. Dewitt, Fundamentals of Heat and Mass Transfer, Seventh Edition. New York, NY: John Wiley and Sons 2011.

[82] J. D. Pye, G. L. Morrison and M. Behnia, Transient Modelling of Cavity Receiver Heat Transfer for the Compact Linear Fresnel Reflector, Dept. of Mechanical and Manufacturing Engr. University of New South Wales, ANZSES Destination Renewables (2003) 69 – 78.

[83] S. S. Sahoo, S. M. Varghese, A. Kumar and C.S. Kumar, An Experimental and Computational Investigation Of Heat Losses From The Cavity Receiver Used In Linear Fresnel Reflector Solar Thermal System, ICAER (2011).

[84] J. Facão and A. C. Oliveira, Numerical Simulation of A Trapezoidal Cavity Receiver for A Linear Fresnel Solar Collector Concentrator, Renewable Energy 36(2011) 90-96.

[85] A. Mohamad, J. Orfi and H. Alansary, Heat Losses from Parabolic Trough Solar Collectors, International Journal of Energy Research 38(2014) 20–28.

[86] M. Eck, J. F. Feldhoff, and R. Uhlig, Thermal Modelling and Simulation of Parabolic Trough Receiver Tubes Proceedings of the ASME 2010 4th International Conference of Energy Sustainability ES 2010Phoenix, Arizona USA, ES2010-90402, 17-22 May, 2010.

[87] L. Jianfeng, D. Jing and Y. Jianping, Heat Transfer Performance of an External Receiver Pipe under Unilateral Concentrated Solar Radiation, Solar Energy 84 (2010)1879–1887.

[88] W. Heidemann, K. Spindler and E. Hahne, Steady-State and Transient Temperature Field in the Absorber Tube of a Direct Steam Generating Solar Collector, International J. Heat Mass Transfer 35 (3) (1992) 649-657.

[89] I. A. Thomas and H. M. Guven, Effect of Optical Errors on Flux Distribution Around the Absorber Tube of a Parabolic Trough Concentrator, Energy Conversion and Management 35(7) (1994) 575-582.

[90] K. S. Reddy, K. R. Kumar and G. V. Satyanarayana, Numerical Investigation of Energy-Efficient Receiver for Solar Parabolic Trough Concentrator, Heat Transfer Engineering, 29 (11) (2008) 961-972.

[91] Z. D. Cheng, Y. L. He, J. Xiao, Y. B. Tao and R. J. Xu, Three-dimensional Numerical Study of Heat Transfer Characteristics in the Receiver Tube of Parabolic Trough Solar Collector, International Communications in Heat and Mass Transfer 37(2010) 782–787.

[92] Z. D. Cheng, Y.L. He, F.Q. Cui, R.J. Xu and Y.B. Tao, Numerical Simulation of a Parabolic Trough Solar Collector with Non-uniform Solar Flux Conditions by Coupling FVM and MCRT Method, Solar Energy 86 (2012) 1770–1784.

[93] Y. Aldali, T. Muneer and D. Henderson, Solar Absorber Tube Analysis: Thermal Simulation using CFD, International Journal of Low-Carbon Technologies, Advance Access Published, 2011.

[94] M. Yaghoubi, and M. M. Akbari, Three Dimensional Thermal Expansion Analysis of an Absorber Tube in a Parabolic Trough Collector, SolarPACES Conference, Spain, 2011.

[95] J. Muñoz, A. Abánades and J. M. Martínez-Val., A Conceptual Design of Solar Boiler, Solar Energy 83(9) (2009)1713–22.

[96] J. Muñoz, J. M. Martínez-Val and A. Ramos, Thermal Regimes in Solar-Thermal Linear Collectors, Solar Energy 85(5) (2011) 857–70.

[97] C.J. Dey, Heat Transfer Aspects of an Elevated Linear Absorber, Solar Energy, 76 (2004) 243–249.

[98] M. Robledo, J. M. Escano, A. Nunez , C. Bordons and E. F. Camacho, Development and experimental validation of a dynamic model for a Fresnel solar collector, 18th International Federation of Automatic Control (IFAC) World Congress Milano (Italy) (2011) 481- 488

[99] J. Munoz, J. M. Martinez-Val and A. Ruben, Thermal Regimes In Solar-Thermal Linear Collectors, World Renewable Energy Congress – Solar Thermal Applications, Linkoping Sweden 2011.

[100] M. S. Sharma, S. S. Mathur and R. N. Singh, Performance Analysis of A Linear Solar Concentrator under Different Flow Regimes, Appl. Energy 13(1) (1983)77–81.

[101] F. J. Pino, R. Caro, F. Rosa and J. Guerra, Exp. Validation of an Optical and Thermal Model of a Linear Fresnel Collector System, Appl. Thermal Engineering (2012) 1-9.

[102] R. M. Fand and K. K. Keswani, Combined Transfer Natural and Forced Convection Heat from Horizontal Cylinders to Water, Intr. J. Heat Mass transfer 16 (1973) 1175-1191.

[103] A. J. Ghajar and L.-M. Tam, Flow Regime Map for a Horizontal Pipe with Uniform Wall Heat Flux and Three Inlet Configurations, Experimental Thermal and Fluid Science 10(1995) 287-297.

[104] Y. Mori and K. Futagami, Forced Convection Heat Transfer in Uniformly Heated Horizontal Tubes-2nd Report: Theoretical Study, Int. J. Heat Mass Transfer 10 (1967) 1801-1813.

[105] A. Lagana, Mixed Convection Heat Transfer in Vertical, Horizontal, and Inclined Pipes, M. Eng. Thesis, Dept. of Mechanical Engineering, McGill University Montreal, Canada, National Library of Canada, Acquisitions and Bibliographic Services, (1995).

[106] G. S. Barozzi, E. Zanchini and M, Mariotti, Experimental Investigation of Combined Forced and Free Convection in Horizontal and Inclined Tubes, MECCANICA 20 (1985), 18-27.

[107] H. A. Mohammed and Y. K. Salman, Experimental Investigation of Mixed Convection Heat Transfer for Thermally Developing Flow in a Horizontal Circular Cylinder, Applied Thermal Engineering 27 (2007) 1522–1533.

[108] A. E. Bergles and R. R. Simonds, Combined Forced and Free Convection for Laminar Flow in Horizontal Tubes with Uniform Heat Flux, Int. J. Heat Mass Transfer 14(1971) 1989-2000.

[109] J. P. H. Newell and A. E. Bergles, Analysis of Combined Free and Forced Convection for Fully Developed Laminar Flow in Horizontal Tubes, Journal of Heat Transfer 92 (1) (1970) 83-93.

[110] S. Piva, G. S. Barozzi, and M. W. Collins, Combined Convection and Wall Conduction Effects in Laminar Pipe Flow: Numerical Predictions and Experimental Validation under Uniform Wall Heating, Heat and Mass Transfer (30) (1995) 401-409.

[111] J. P. Coutier and R. Greif, Mixed Laminar Convection in a Horizontal Tube Natural Convection around its Boundaries, Int. J. Heat Mass Transfer 29 (3) (1986) 391-402.

[112] S. V. Prayagi and S. B. Thombre, Parametric Studies on Buoyancy Induced Flow through Circular Pipes in Solar Water Heating System, International Journal of Engineering Science and Technology (IJEST) 3 (1) (2011) 616-627.

[113] T. Boufendi and M. Afrid, The Physical Aspect of Three-Dimensional Mixed Convection in a Uniformly Heated Horizontal Pipe, Sciences & Technologies 22 (2004) 39-52.

[114] O. Zeitoun, Heat Transfer for Laminar Flow in Partially Heated Tubes, Alexandria Engineering Journal, Alexandria University, Egypt, 41 (2) (2002) 205-212.

[115] O. Zeitoun, Conjugate Laminar Forced Convection in Partially Heated Tubes ACOMEN: Second International Conference on Advanced Computational Methods in Engineering, Belgium, (2002) 1-25.

[116] Y. Mori, K. Futagami, S. Tokuda and M. Nakamura, Forced Convective Heat Transfer in Uniformly Heated Horizontal Tubes - 1st Report-Experimental Study on the Effect of Buoyancy, International Journal of Heat and Mass Transfer 9(5) (1966) 453-463.

[117] K. Sadik, R. K. Shah, and W. Aung, Handbook of Single-Phase Convective Heat Transfer, A Wiley-Inter-Science Publication John Wiley & Sons New York, 1987.

[118] B. Metais, and E. R. G. Eckert, Forced, Mixed, and Free Convection Regimes, Journal of Heat Transfer 86 (2) (1964) 295-296.

[119] S. M. Peyghambarzadeh, Forced Convection Heat Transfer in the Entrance Region of Horizontal Tube under Constant Heat Flux, World Applied Sciences Journal 15 (3) (2011) 331-338.

[120] W. Grassi and D. Testi, Heat Transfer Correlations for Turbulent Mixed Convection in the Entrance Region of a Uniformly Heated Horizontal Tube, Journal of Heat Transfer, 128 (2006)1103 -1107.

[121] W. Grassi and D. Testi, Evaluation of two RANS Turbulence Models in Predicting Developing Mixed Convection within a Heated Horizontal Pipe, International Journal of Computational Fluid Dynamics 21 (7–8) (2007) 267–276.

[122] F. Bazdidi-Tehrani, M. Aghaamini, and S. Moghaddam, Radiation Effects on Turbulent Mixed Convection in an Asymmetrically Heated Vertical Channel, Heat Transfer Engineering 35(5) (2017) 475-497.

[123] V. V. Satyamurty and R. Repaka, Superposition Relations for Forced Convective Local Nusselt Numbers for Flow through Asymmetrically Heated Parallel-Plate Channels, Heat Transfer Engineering 32(6) (2011)476–484.

[124] W. T. Kim and R. F. Boehm, Laminar Buoyancy-Enhanced Convection Flows on Repeated Blocks with Asymmetric Heating, Numerical Heat Transfer, Part A: Applications International J. of Computation and Methodology 22 (4) (2010) 421-434.

[125] S. Habchi and S. Acharya Laminar Mixed Convection in a Symmetrically or Asymmetrically Heated Vertical Channel, Journal Numerical Heat Transfer 9 (5) (2007) 605-618.

[126] D. G. Osborne and F. P. Incropera, Laminar Mixed Convection Heat Transfer for Flow between Horizontal Parallel Plates with Asymmetric Heating, International Journal of Heat and Mass Transfer 28 (1) (1985) 207-217.

[127] A. A. Badran, M. F. Mustafa, W. K. Dawood, Z. K. Ghazzawi, On the Measurement of Bond Conductance in Solar Collector Absorber Plate, Energy Conversion and Management 49(11) (2008) 3305-3310.

[128] J. Hameury, B. Hay and J-R. Filtz, Measurement of Total Hemispherical Emissivity Using a Calorimetric Technique, Laboratoire National de Métrologie d'Essais (LNE), 29 Avenue Roger Hennequin, 78197 TRAPPES Cedex, France,(2005) 1-14.

[129] L. Theodore, Heat Transfer Applications for the Practicing Engineer, John Wiley & Sons Inc. Hoboken New Jersey, (2011) 187 – 188.

[130] T. A. Moss, and D. A. Brosseau, Final Test Results for the Schott HCE on a LS-2 Collector, Solar Technologies, Sandia National Laboratories Albuquerque, New Mexico 87185 and Livermore, California 94550, NM 87185-1127, 2005.

[131] C.E. Kennedy, Review of Mid- to High-Temperature Solar Selective AbsorberMaterials NREL/TP-520-31267, National Renewable Energy Laboratory, 1617 Cole Boulevard Golden, Colorado 80401-3393, 2002.

[132] J.F. Cerón, J. Pérez-García, J.P Solano, A. García, R. Herrero-Martín, A Coupled Numerical Model For Tube-On-Sheet Flat-Plate Solar Liquid Collectors. Analysis and validation of the heat transfer mechanisms, Applied Energy 140 (2015) 275–287.

[133] T. A. Moss, and D. A. Brosseau, Final Test Results for the Schott HCE on a LS-2 Collector, Solar Technologies, Sandia National Laboratories Albuquerque, New Mexico 87185 and Livermore, California 94550, NM 87185-1127, 2005.

[134] Y. A. Cengel, Heat and Mass Transfer: A Practical Approach, Published by McGraw-Hill Companies, Inc. 1221 Avenue of the Americas, New York, NY 10020; 3rd Edition, 2007.

[135] R. K. Rajput, Heat and Mass Transfer in SI Units. Second Edition, Published by S. Chand and Company Ltd, Ram Nagar, New Delhi, 110 055, 2005.

[136] L. Huang and K. J. Farrell, Buoyancy Effect on Forced Convection in Vertical Tubes at High Reynolds Numbers, Journal of Thermal Science and Engineering Applications 2 (2010) 041003-1-6.

[137] ANSYS Fluent version 14.0, Users' Guide ANSYS, Release 14.0 Incorporated, Southpointe 75 Technology Drive Canonsburg, PA 15317, 2011.

[138] E. Yildiz, S. Dost and M. Yildiz , A Numerical Simulation Study for the Effect of Magnetic Fields in Liquid Phase Diffusion Growth of SiGe Single Crystals, Journal of Crystal Growth 291 (2006) 497–511.

[139] K. Mehmet and K. Tiirkan, Numerical Simulation of a Gaseous Fueled (Methane) Combustor. Mathematical and Computational Applications, © Association for Scientific Research 2 (3) (1997) 101-118.

[140] P. G. Nurnberg, An Experimental and Numerical Investigation of Mixed Convection in Rectangular Enclosures, Open Access Dissertations and Theses, Paper 3956 (1994).

[141] R. B. Lakeh, A. S. Lavine, H. P. Kavehpour, G. B. Ganapathi, and R. E. Wirz, Effect of Laminar and Turbulent Buoyancy-Driven Flows on Thermal Energy Storage Using Supercritical Fluids, Numerical Heat Transfer, Part A 64 (2013) 955–973.

[142] M. Wirz, M. Roesle and A. Steinfeld , Three-Dimensional Optical and Thermal Numerical Model of Solar Tubular Receivers in Parabolic Trough Concentrators, Journal of Solar Energy Engineering, (2012) 134.

[143] S.V. Patankar, Numerical Heat Transfer and Fluid Flow. Hemisphere Publishing Corporation, United States of America, 1980.

[144] J. H. Ferziger and M. Perifi, Computational Methods for Fluid Dynamics, 3 Rev. ed.- Berlin; Heidelberg; Hong Kong; London; Milan; Paris; Tokyo: Springer, 2002.

[145] H. K. Versteeg and W. Malalasekera, An Introduction to Computational Fluid Dynamics: The Finite Volume Method. Longman Scientific and Technical, Longman House, Burnt Mill, Harlow Essex CM20 2JE, England, 1995.

[146] D. Wen and Y. Ding, Experimental Investigation into Convective Heat Transfer of Nanofluids at the Entrance Region under Laminar Flow Conditions, International Journal of Heat and Mass Transfer 47 (2004) 5181- 5188.

[147] M. Hallquist, Heat Transfer and Pressure Drop Characteristics of Smooth Tubes at a Constant Heat Flux in the Transitional Flow Regime, M. Eng. Thesis, Department of Mechanical and Aeronautical Engineering, University of Pretoria, South Africa, 2011.

[148] J. H. Lienhard (IV) and J. H. Lienhard (V), A Heat Transfer Textbook, Published by Phlogiston Press Cambridge Massachusetts, U.S.A; Fourth Edition, 2011.

[149] F. Burkholder and C. Kutscher, Heat Loss Testing of Schott's 2008 PTR70 Parabolic Trough Receiver, National Renewable Energy Laboratory, Technical Report NREL/TP-550-45633, 2009.

[150] T. A. Moss, and D. A. Brosseau, Final Test Results for the Schott HCE on a LS-2 Collector, Solar Technologies, Sandia National Laboratories Albuquerque, New Mexico 87185 and Livermore, California 94550, NM 87185-1127, 2005.

[151] Properties of Syltherm® 800 Heat Transfer Liquid, Midland, MI: Dow Corning Corporation, 1985.

[152] V. E. Dudley, G. J. Kolb, M. Sloan, and D. Kearney, Sand94-1884, Test Results: SEGS LS-2 Solar Collector, Albuquerque, NM, Sandia National Laboratories, 1994.

[153] Z.D. Cheng, Y.L. He, F.Q. Cui, R.J. Xu, Y.B. Tao, Numerical Simulation of a Parabolic Trough Solar Collector with Non-Uniform Solar Flux Conditions by Coupling FVM and MCRT Method, Solar Energy 86 (2012) 1770–1784.

[154] A.V.N. Kapatkar, B. A. S. Padalkar and C. S. Kasbe, Experimental Investigation on Heat Transfer Enhancement in Laminar Flow in Circular Tube Equipped with Different Inserts, AMAE Int. J. on Manufacturing and Material Science, 1(1) (2011)1 - 6.

[155] T. Boufendi and M. Afrid, Three-Dimensional Conjugate Conduction-Mixed Convection with Variable Fluid Properties in a Heated Horizontal Pipe, Rev. Energ. Ren. 8(2005)1-18.

[156] B.S. Petukhov, and A.F. Polyakhov, Heat Transfer in Turbulent Mixed Convection. Hemisphere Publishing Corporation, New York, New York. 1988.